Preparation and Study of High Quality Hydrogenated Silicon Films from Amorphous to Microcrystalline Transition Range for Photovoltaic Applications

A thesis submitted

by

Purabi Gogoi

In partial fulfillment of the requirement for the award of the degree of Doctor of Philosophy

Department of Physics
Indian Institute of Technology, Guwahati
Guwahati- 781 039, Assam, India

March 2010

Statement

The work contained in this thesis entitled **"Preparation and study of high quality hydrogenated silicon films from amorphous to microcrystalline transition range for photovoltaic applications"** has been carried out by me under the supervision of Dr. Pratima Agarwal, Associate Professor, Department of Physics, Indian Institute of Technology, Guwahati, Assam, India. This thesis does not contain any material previously submitted for the award of any degree or diploma.

11th March 2010

(Purabi Gogoi)
Department of Physics
Indian Institute of Technology, Guwahati
Guwahati- 781 039, Assam, India.

Certificate

This is certified that the work contained in this thesis entitled **"Preparation and study of high quality hydrogenated silicon films from amorphous to microcrystalline transition range for photovoltaic applications"** submitted by Ms. Purabi Gogoi, a Ph. D. student in the Department of Physics, Indian Institute of Technology, Guwahati, Assam, India, for the award of the degree of Doctor of Philosophy has been carried out under my supervision. This work has not been submitted elsewhere for the award of any degree or diploma.

11th March 2010

(Dr. Pratima Agarwal)
Associate Professor
Department of Physics
Indian Institute of Technology, Guwahati
Guwahati- 781 039, Assam, India.

Dedicated

to

My Parents & Parents in Laws

Acknowledgements

At the outset, I would like to express my deepest gratitude to my thesis supervisor Dr. Pratima Agarwal for giving me the opportunity for carrying out my Ph. D. thesis work under her supervision. I am grateful not only for her invaluable guidance, but also for her constant encouragement, understanding, patience and support during all years of my studentship. During my thesis work, I learnt a lot from her including condensed matter physics, solar photovoltaics, experimental techniques and other advanced physics topics. Being the first research student of my supervisor, I had the opportunity to set up the laboratory, where she taught me how to tackle a real life problem.

I am grateful to my doctoral committee members, Prof. A. Khare (Chairperson), Dr. P. K. Giri and Prof. J. B. Barua for reviewing my research work regularly and giving valuable suggestions. I am thankful to the earlier heads of the department Prof. A. Srinivasan, Prof. A. Khare and present head Dr. S. Ravi and all the faculty members for their support.

I am fortunate to have Mr. J. Anto Pradeep, Mr. Gouri Sankar Paul and Mr. Himanshu Shekhar Jha as my lab mates. I must thank them for providing an amiable ambience in lab and their help in my research work. I also thank Ms. Bulumoni Kalita, R & D project student, Mr. Taufique A. Ansari and Mr. Apurba Barman, M. Sc. project students for their help in different stages of my work.

I express my sincere thanks to the staff members of Physics department, Dr. Sidanada Sarma, Mr. Lokesh Chakraborty, Mr. Atul Deka, Mr. Bimal Sarma, Mr. Pankaj Goswami, Mr. Basab B. Purakayastha, Mr. Jyoti Borah and Mr. Madan Deka for their support and cooperation during my Ph. D. work.

I am thankful to Mr. Chandan Borgohain, Mr. Kula Senapati and Mr. Madhurjya Borah from Central Instrument Facility, IIT Guwahati, for their help in SEM and TEM studies. I also thank the members of mechanical workshop for fabrication of essential components required for my Ph. D. work.

I am grateful to Dr. P. N. Dixit of NPL, New Delhi and Prof. R. O. Dusane of IIT Bombay for allowing me to use their deposition facilities in the early stage of my work. I express my thanks to Dr. A. Kumbhar of IIT Bombay for her help during film preparation. I would like to thank Prof. D. S. Misra of IIT Bombay and Dr. D. Deva of IIT Kanpur for their help in Raman and AFM studies.

My special thanks go to Mr. S. Pai of M/s Excel Instruments for fabricating the HWCVD chamber as per our design.

I am thankful the research scholars of physics department including Dr. Amal Medhi, Dr. Santanu Sinha, Dr. Munima Borah, Dr. Manos P. C. Kalita, Dr. Sandeep Srivastava, Poulumi Dey, Meera V., Veena Nair, Biswanath Dutta, Arpita Nath for their help and wonderful time they have shared with me. I also thank Jashmini Deka, Monikonkona Sarma, Cosmika Goswami and other hostel friends for making my stay in IITG campus comfortable and memorable.

I am deeply indebted to my parents for their love, understanding, support and encouragement, without which it which it would have been a very hard task to perform. My sincere gratitude goes to my sister and brothers for their help and support. I would like to thank my grandmother for her love and blessings. I am grateful to my parents in laws for their understanding and support and making me free from any family liabilities. I would also like to mention the name of Imon and Sumon, my niece in laws, talking to whom I feel refreshed after the hard work of the day. I am grateful to my best friend cum husband, Pankaj, for his love and support. He not only supported me in the ups and downs of this journey, but also helped me in my research work as well as the preparation of the thesis.

I would like to thank all those who have helped me in whatever manner during my thesis work, some of whom I may have inadvertently forgotten to mention.

Last but not the least, I am grateful to Indian Institute of Technology, Guwahati, Council for Scientific and Industrial Research and Department of Science and Technology, India for providing me the financial support to carry out the present thesis work.

Purabi Gogoi
IIT Guwahati
Guwahati – 781 039
Assam, India

Preface

For last few decades hydrogenated amorphous and microcrystalline silicon (a-Si:H and μc-Si:H) and other silicon alloys like amorphous silicon germanium(a-SiGe:H), amorphous silicon carbon (a-SiC:H) etc. have been gaining attentions from the scientific community as an extensive area of research both from fundamental physics as well as technology point of view. These materials find their applications in solar cells and other optoelectronic device applications such as thin film transistors, liquid crystal displays, radiation detectors etc. Especially, the research on photovoltaic application of these materials carries a lot of significance in context to the present day energy crisis and stands as viable candidate for eco-friendly energy solutions. Solar cells made of amorphous silicon and their alloys have several advantages over their crystalline counterparts such as tunable band gap, high absorption co-efficient, inexpensive preparation, large area deposition, low temperature processing, possibility to use wide range of substrates (including inexpensive plastics) etc. Because of the high absorption co-efficient, solar cells made of these materials need only sub micron thickness thin films unlike the bulk crystalline solar cells. This reduction in amount of material, inexpensive preparation techniques, low process temperature as well as low cost substrates make the thin film solar cells much cheaper compared to the crystalline counter part. Recently, nanostructured silicon (nc-Si:H) and silicon alloys have been gaining importance due to a few unique properties like high band gap, visible photoluminescence, electroluminescence etc. Apart from their application in photovoltaics and thin film transistors, these can also be used in novel applications like light emitters, non volatile memories etc.

The present thesis work focuses on the study of the influence of process parameters on the properties and stability of silicon thin films and optimization of these parameters for high quality films with high deposition rate. The films are prepared by Plasma Enhanced Chemical Vapour Deposition (PECVD) and Hot Wire Chemical Vapour Deposition (HWCVD) methods by varying different deposition parameters and studied extensively for structural, optical and electrical properties. As the HWCVD technique is new and less extensively studied in comparison to PECVD technique, the motivation was to optimize the process parameters of

HWCVD technique for high quality film deposition. Hence, most of the films are prepared by HWCVD method.

The present thesis is divided into ten chapters, *viz.* 1. Introduction 2. Experimental Techniques 3.Fabrication of Experimental Setups 4. Argon dilution of PECVD films 5. Hydrogen dilution of HWCVD films 6. Hydrogen diluted HWCVD film: Effect of Substrate temperature 7. Hydrogen diluted HWCVD film: Effect of Process Pressure 8. HWCVD film: Effect of Silane Flow Rate 9. HWCVD film: Effect of Filament Temperature 10. Conclusion and Scope for future work.

Chapter 1 serves as general introduction to the material of interest i.e., amorphous and micro/nanocrystalline silicon (a-Si:H and μc/nc-Si:H). Here different methods of their deposition, current technology issues related to photovoltaic applications of these materials and motivation of this thesis work have been discussed.

Chapter 2 deals with different experimental techniques used for preparation of the material as well as different structural, optical and transport studies. The analysis details for these measurement techniques are also mentioned in this chapter.

Chapter 3 has been devoted to describe fabrication of experimental set ups developed in house for sample preparation and their characterizations.

In Chapter 4, the effect of combined argon and hydrogen dilution on the properties of PECVD films is discussed. Films ranging from amorphous to nanocrystallites embedded amorphous are deposited from silane and hydrogen mixture (5 % silane in hydrogen) by varying the argon dilution. As PECVD yields films with very low deposition rate, we have used argon dilution to increase the rate. At the same time hydrogen is used to suppress the deleterious effect of argon dilution *viz.* inhomogeneous and columnar growth. The key achievements in these films are high growth rate (1.3-4.5 Å/Sec), high band gap (1.84-2.16eV) compared to regular PECVD films and high photosensitivity ($\sim 10^5$) as well as better stability against exposure to light. The Raman crystalline fraction varies from 1- 54 %. The films are found to be quite homogeneous despite of the use of argon dilution. Presence of hydrogen in the precursor gas prevents the columnar growth. In these films, both Ar* and atomic hydrogen help in the efficient dissociation of silane and in the reconstruction of strong Si-Si bonds thus improving the order. This leads to better stability against light soaking.

Chapter 5 deals with the effect of hydrogen dilution on the film properties prepared by HWCVD method. These films are prepared at low substrate temperature (200^{o}C). The film structure could be tailored from amorphous to nanocrystallites embedded amorphous by varying the hydrogen and silane flow rate. The films possess band gap comparable to regular values (1.7-1.9eV) reported in literature. The deposition rates are also good (0.64-3.22 Å/Sec). The films possess 6.2-12.8 atomic percentage of hydrogen, mostly in the monohydride mode (72-98 %). Monohydride mode of silicon hydrogen is very much appreciated for stable devices, as higher hydrides are believed to be responsible for light induced degradation. Raman studies show that the films range from pure amorphous to maximum 65 % crystalline in nature and possess good short and medium range order (SRO and MRO). These films also suffer very less light induced degradation and the changes could be annealed out by heating at temperature below 100^{o}C. The stability of the films has been attributed to improved order and hydrogen in the monohydride mode.

In Chapter 6, the effect of substrate temperature on the film microstructure and quality of HWCVD films prepared from hydrogen diluted silane (10 % silane in hydrogen) are discussed. The films show transition from amorphous to nanocrystalline when the T_s is raised from 150 to 200^{o}C. These films have very good deposition rate (8-14 Å/Sec), the deposition rate being higher for low T_s amorphous films. For the nanocrystalline films, the crystalline fraction ranges from 50-55 % with average crystallite size of about 4nm. The Raman studies reveal that the films possess good short and medium range order as indicated by rms deviation of tetrahedral angle ($\Delta\theta_B$) of ~ 6.5-7.5^{o} and the ratio of intensity in amorphous TA and TO mode, I_{TA}/ I_{TO} of ~0.3-0.5. Hydrogen content in these films ranges 2.5-7.5 atomic %. The nanocrystalline films have less rms roughness (1.5- 10.8 nm) than the amorphous ones (13.3- 18.4 nm). These films show very high band gap (2.02-2.34eV), attributed to the improvement of order and presence of low density amorphous tissues and microvoids surrounding the nanocrystallites. Films with good adhesion to substrate at T_s as low as 100^{o}C at a deposition rate of 14 Å/Sec is a good achievement towards cost effectiveness of film preparation as well as the feasibility of using the low cost flexible substrates.

Chapter 7 discusses the properties of the HWCVD films prepared by varying the process pressure from hydrogen diluted silane (10 % silane in hydrogen). All these films are nanocrystalline in nature with crystalline fraction of 56-75 % and average crystallite size of about 4nm. These films show very good SRO and MRO ($\Delta\theta_B$ ~4.4-6.7^{o,} I_{TA}/ I_{TO}~0.3-0.5). The films also possess very high band gap (2.2-2.4eV) and good deposition rate (5 to11 Å/Sec). The rms roughness of this series of films ranges 6.5- 11 nm. Stability studies show that the films suffer less light induced degradation.

In Chapter 8, studies on the films prepared from pure silane by varying the silane flow rate (SFR) are reported. The films with higher SFR are amorphous and crystallinity develops at low SFR. The deposition rates are very high (6.5-27.3 Å/Sec). The band gap is slightly higher (1.8-1.98 eV) compared to the regular PECVD films. The hydrogen content in these films ranges ~ 4.6-8.5%, with very high monohydride fraction (70-92%) and the films possess good SRO and MRO. These films show good photosensitivity and less light induced degradation, useful for stable device applications.

Chapter 9 deals with the study of the films prepared with the variation of filament temperature (T_F) in the range of 1600-1900°C. Low T_F films are amorphous and crystallinity develops at T_F of ~ 1800°C. These films also show high deposition rate (8.1-12.4 Å/Sec). The band gaps of the films are also high (1.9-2.2 eV) and show good SRO and MRO ($\Delta\theta_B$ ~3-8^{o}, I_{TA}/ I_{TO}~0.2-0.3). The films possess 4.5-8 atomic % of hydrogen, mostly in the monohydride mode (97-70%) except for the films at 1900°C, where monohydride fraction decreases to 42 %. These films show good photosensitivity and stability against light induced degradation.

In the last chapter, a comparative report and summary of all the films under the present thesis work are mentioned. The thesis work is concluded with the future prospects in this field. The papers published in journals and conference proceedings as well as accepted for presentation in conferences related to this thesis work are listed at the end of thesis.

Table of Contents

Content **Page No**

Chapter 3: Fabrication of Experimental Set ups 47

Chapter 4: Argon dilution of PECVD films 59

Chapter 5: Hydrogen dilution of HWCVD films 79

Chapter6: Hydrogen diluted HWCVD films: Effect of Substrate Temperature 107

Chapter 7: Hydrogen diluted HWCVD films: Effect of Process Pressure 133

Chapter 8: HWCVD films: Effect of Silane Flow Rate 155

List of Figures

Chapter 1: Introduction

Chapter 2: Experimental Techniques

Chapter 3: Fabrication of Experimental Set ups

Chapter 4: Argon dilution of PECVD films

Chapter 5: Hydrogen dilution of HWCVD films

Chapter 6: Hydrogen diluted HWCVD films: Effect of Substrate temperature

Chapter 7: Hydrogen diluted HWCVD films: Effect of Process Pressure

Chapter 8: HWCVD films: Effect of Silane flow rate

Chapter 9: HWCVD films: Effect of Filament Temperature

List of Tables

Chapter 1: Introduction

Chapter 2: Experimental Techniques

Chapter 4: Argon dilution of PECVD films

Chapter 5: Hydrogen dilution of HWCVD films

Chapter 6: Hydrogen diluted HWCVD films: Effect of Substrate temperature

Chapter 7: Hydrogen diluted HWCVD films: Effect of Process Pressure

Chapter 8: HWCVD films: Effect of Silane flow rate

Chapter 9: HWCVD films: Effect of Filament Temperature

Chapter -1

Introduction

Chapter 1

Introduction

Hydrogenated amorphous silicon (a-Si:H) thin films [1-4] have been gaining importance since last three decades among the scientific community as these classes of materials are endowed with a number of remarkable material properties, thus making these ideal for many large area electronic device applications such as solar cells, thin film transistors, radiation detectors etc. [5-6]. Other alloys of silicon like hydrogenated amorphous silicon germanium [7-11], silicon carbon [12-15], silicon nitrogen [16-19] etc., are also drawing attentions for various opto-electronic applications. Recently the nanostructured silicon and silicon alloys have been getting importance as these can be used in novel applications like light emitters [20-23], non volatile memories [24-25] etc. apart from their application in photovoltaics and thin film transistors [26-30]. Studies on amorphous as well as nanocrystalline silicon and their alloys carry significance from both basic physics and technology point of view.

The first a-Si:H film was prepared by Chittick *et al.* in the UK in 1969 [31] by the plasma dissociation of Silane gas (SiH_4), using inductively coupled coiled outside the quartz chamber. However, the material gained attention from amorphous semiconductor research community after the work by Spear et al, who reported that the material thus prepared (by glow discharge or plasma enhanced chemical vapour deposition) had good electrical transport properties along with high carrier mobility [32] and high photoconductivity [33]. In 1975, Spear and LeComber [34] reported the possibility of substitutional doping in amorphous silicon by addition of phosphine or diborane gas in the precursor SiH_4 for n or p type doping respectively, thus enabling the use of a-Si:H films in making thin film devices. These qualities of amorphous silicon prepared by glow discharge decomposition of SiH_4 were not observed in the films prepared by simple evaporation of Si, which were neither photoconducting nor dopable. The role of hydrogen in the improvement in material quality was unclear until the works of Lewis *et al.* [35]. They reported that when hydrogen was introduced in the highly defective amorphous silicon and germanium prepared by sputtering, the material showed improved electronic properties like glow discharge prepared films. It was thus resolved that the improved properties of films prepared by glow discharge were due to the passivation of dangling bonds by hydrogen, which also relaxes the strain in the network, thus making the material less defective. This leads to favorable properties like high photoconductivity and dupability [1]. Fritzsche [36] confirmed that glow discharge material also contained hydrogen. Hydrogen is now regarded as an essential part of amorphous silicon and research turned from amorphous silicon to hydrogenated amorphous silicon (a-Si:H). The amount of hydrogen content in the films plays a very important role in the microstructure formation. Hydrogenation increases the order in amorphous Si in two ways: in the first place, atomic hydrogen suppresses the dangling bonds and secondly, relaxes the network by breaking the weak Si-Si bonds during the film growth. The presence of hydrogen also increases the band gap of the material by the affect of alloying. The band gap increases from 1.1eV of a-Si to 1.7-1.8 eV due to nearly 10 atomic percentage of hydrogen incorporation. The band gap can be tuned by changing the amount of hydrogen present in the material. The fact that hydrogenated amorphous silicon (a-Si:H) is dopable and band gap can be tuned, has made the material a potential area of research from both physics as well as technological point of view. Especially, solar cells made of a-Si:H and alloys like a-SiGe:H have several advantages over the crystalline counterpart. In the former the band gap can be tuned by varying the amount of hydrogen and germanium and other deposition conditions and hence can be used in multi junction solar cells to explore much wider range of solar spectrum. Being a direct band gap semiconductor unlike crystalline silicon (c-Si), a-Si:H possesses high absorption co-efficient $\alpha(h\nu)$. So a-Si:H layer needs much less thickness than c-Si to absorb same amount of energy. Moreover growing crystal is a very expensive and time consuming process. Amorphous silicon film deposition is a low temperature as well as faster process and therefore involves less processing cost. Low substrate temperature processing opens up the possibility to use varieties of substrates for individual applications, including flexible and cheaper plastic substrates [37-39], which further reduces the processing cost. Uniform large area deposition has also made these classes of materials a viable candidate for solar cell applications. However, these materials undergo degradation upon prolonged exposure to light [40], better known as Staebler Wronski effect, which reduces the efficiency of the devices.

The research on photovoltaic applications of these materials carries a lot of significance in context to the present day energy crisis and stands as viable contender for eco-friendly energy solutions. In order to stabilize the CO_2 emission at a reasonable level, it is estimated that we need to install at least a 14TW renewable energy generation capacity by the year 2050 [41]. It has been argued that among the various renewable energy options, only solar energy offers sufficient resources to cover this demand [42]. Also, the depletion of fossil fuel has forced the scientific community to think for alternative energy resources, solar energy being the first choice. Given the large scale needed, the solar cell technologies that are needed to be developed should use earth abundant and preferably nontoxic materials. Among the various options available, wafer based crystalline silicon solar cells are presently dominating the market. At present 85-90 % of the solar PV modules produced world wide are based on c-Si and the relative share of thin film solar cells is about 5-10 % among which more than 90 % is shared by silicon thin film solar cells [43]. Even though Si is the second most abundant material in earth's upper continental crust, high purification that is needed and the indirect absorption of these wafer based solar cells make it an expensive source of material. Therefore, further price reduction has to come from amorphous thin films as well as from the implementation of nanostructured surfaces and materials [44].

All the amorphous semiconductors, including a-Si:H, differ from their crystalline counterparts by the disorder in the atomic structure. The lack of periodicity in the atomic structure unlike the crystalline materials is basically responsible for making these classes of materials different in many aspects from the later such as structural, opto-electronic properties etc. However, the presence of disorder in these materials does not mean that these are completely order-less. There exists short range order up to few atomic distances, which eventually fades away with large atomic distances. Short range order and long range disorder have made these materials similar to crystalline material in some aspects while different in some others. As for example the similarity in the covalent bonding structure results in similar overall electronic structure in both forms of silicon. This leads to comparable band gap in amorphous and crystalline silicon. This is a consequence of short range order. The absence of long rage order occurs due to the variations in bond length (1-2%) and bond angle (8-10%). This variation in bond length and bond angle leads to the broadening of electronic distribution of states and causes electron and hole localization along with strong scattering of carriers. Unlike crystalline semiconductors, amorphous semiconductors do not possess a clean gap. There are electronic states lying in the band gap, called defect states occurring from dangling bonds. Table 1.1 summarizes the defect structure and corresponding electronic properties of amorphous semiconductors in comparison with their crystalline counterparts [1].

Table 1.1: The defect structures and corresponding electronic properties of amorphous semiconductors [1].

Structure	Electronic Properties
Bonding disorder	Broadening of bands, band tails, localization, scattering
Dangling bonds	Electronic states in the band gap
Alternative bonding configuration	Electronically induced metastable states

The structure of amorphous semiconductors with presence of short range order and absence of long range order can be modeled by Continuous Random Network (CRN), originally proposed by Zachariasen in 1932 for glasses like silica [45]. In this model, each atom has a specific number of bonds in its immediate neighborhood. This number is called the coordination number. CRN offers the flexibility to incorporate atoms of different co-ordination. Figure 1.1 shows a CRN with atoms having different coordination. The flexibility of retaining own coordination number of the atoms makes the material less dopable. As CRN model allows any position in the network to be occupied by the atoms, thus the definition of defects in amorphous semiconductors gets modified. Here one has coordination defect when an atom possess too many or too few bonds unlike various point and line defects as in case of crystalline semiconductors. The atomic coordination number is given by Mott '8-N' rule [46].

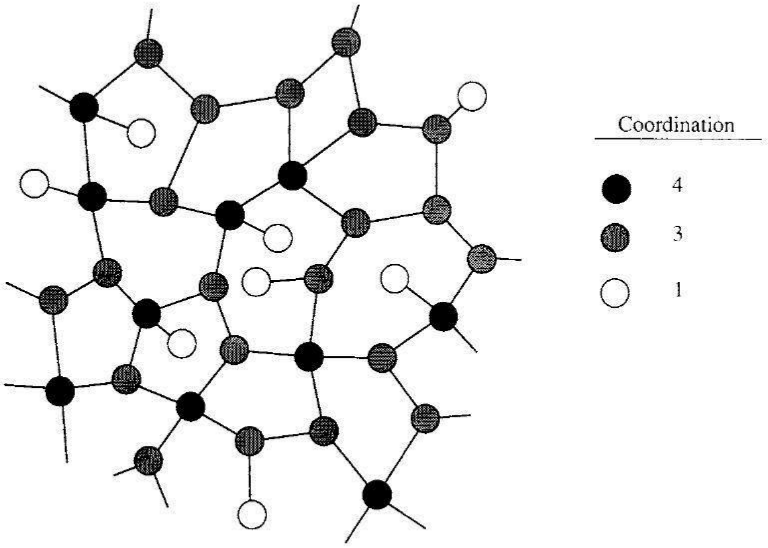

Figure 1.1: Continuous random network (CRN) allowing the constituent atoms to retain their coordination numbers [1].

The information of concentration and distribution of charge carriers in a semiconductor is provided by the energy distribution of states, known as density of state (DOS). In ideal silicon crystal, the conduction band and the valence band are separated by well defined band gap (E_G) and no energy states are allowed in the gap. However, in case of a-Si:H, the lack of long range order gives rise to the formation of defects which manifest in the form of band tails and dangling bonds as mentioned in the table 1.1. The energy states where the charge carriers can be considered as free carriers are called extended state as here the wave function extends over the whole atomic structure, while the tail and defect states are called localized states due to the localized nature of the wave functions. The mobility of the carriers in the localized states is strongly reduced. This feature of a sharp drop in the carrier mobility in the localized states in comparison to the extended states is used to define the band gap in a-Si:H, also called as mobility gap (E_{mob}). This energy gap for a-Si:H (1.7-1.8eV) is larger than the typical band gap of c-Si (1.1eV). Figure 1.2 depicts a standard model for the DOS in a-Si:H [47]. In this model, the valence and conduction band states are represented by parabolic dependence on energy that merge with exponentially decaying band tail states. The dangling bonds have three different charge states, positive (D^+), neutral (D^o) and negative (D^-). These energy states act as trapping and recombination centers and strongly affect the electronic properties of a-Si:H and hence performance of a-Si:H based devices.

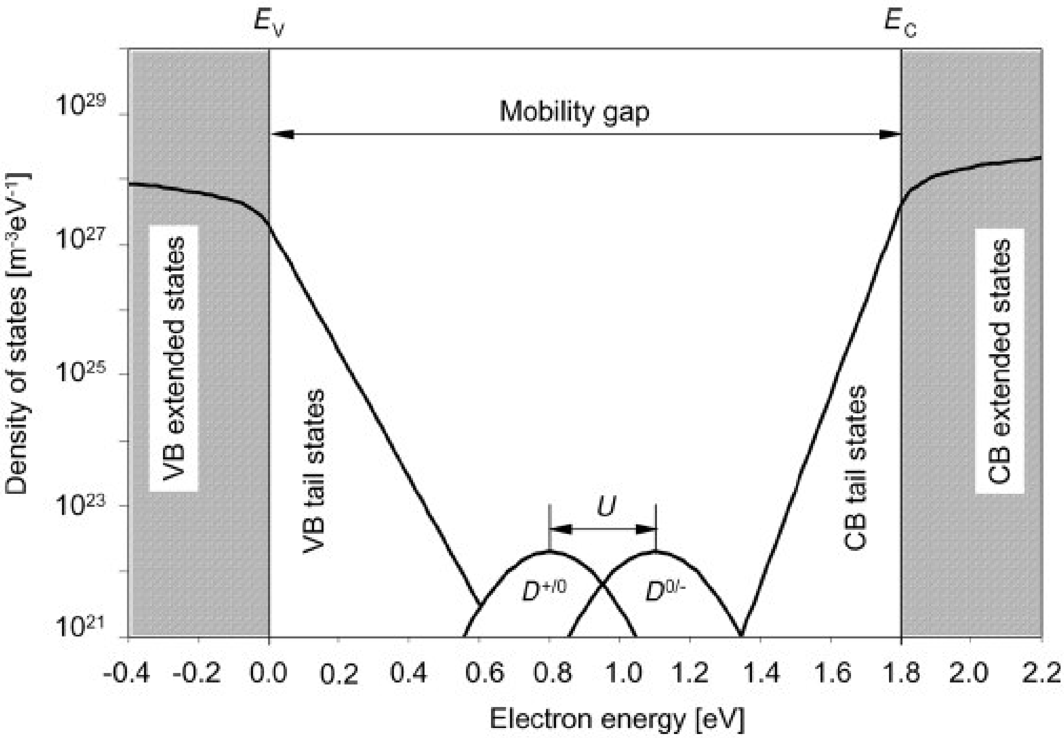

Figure 1.2: Density of states picture for a-Si:H [47]

In case of crystalline solids, the solution of Schrodinger equation which gives the wave functions of energy states are the famous Bloch solutions, which is a consequence of the periodic potential. It is a plane wave whose amplitude is modulated by the periodicity of the crystal lattice.

$$-\frac{h^2}{2m}\nabla^2\Phi+V(r)\Phi=E\Phi \qquad 1.1$$

Where, Φ is the electron wave function, E is the electron energy, $V(r)$ is the potential energy due to the lattice

$$\Phi(r)=\exp(ik.r)U_k(r) \qquad 1.2$$

Where, $U_k(r)$ is the periodicity of the lattice.

The wave function has a well defined momentum, k, extending throughout the crystal and the energy bands are described by energy momentum (E-k) dispersion relation. However, in case of amorphous solids, the potential is not periodic and the weak disorder potential results in a perturbation in the wave function and has the effect of scattering the electrons from one Bloch state to another. As a result, the wave function looses coherency over a distance of one or two atomic spacing. The strong scattering causes a large uncertainty in electron momentum through uncertainty principle.

$$\Delta k = \frac{\hbar}{\Delta x} \approx \frac{\hbar}{a_0} \approx k \qquad 1.3$$

Where Δx is the scattering length, a_0 is inter-atomic spacing. The uncertainty in k is similar to the magnitude of k, thus rendering k not to be a good quantum number. As a result of loss of k-conservation, the conservation of momentum selection rule remains no longer valid in optical transitions. Consequently the distinction between direct and indirect band gap is lost and optical transitions occur between the states overlapping in real space. Hence, silicon, an indirect band gap semiconductor behaves as direct band gap material in amorphous state. This leads to the high optical absorption co-efficient in amorphous silicon [1]. The absence of long range translational symmetry along with the presence of short range bonding disorder make the observation of all vibrational modes possible whose detection in crystalline material is forbidden by selection rules. The basic selection rule in crystalline material is that vibrational modes with inversion symmetry are infrared-forbidden but Raman-allowed. The lack of inversion symmetry occurring in amorphous silicon due to inherent bonding disorder thus allows various vibrational modes to appear in both Raman as well as in IR absorption [48].

1.1 μc-Si:H/ nc-Si:H/proto crystalline silicon :

Microcrystalline silicon is another class of hydrogenated silicon that finds applications in photovoltaic technologies and other opto-electronic devices. These materials were first prepared by Veprek *et al.* [49] in 1968 by chemical transport technique. PECVD deposition of μc-Si:H from silane started around 1980 [50-51] and their application to solar cells was limited to p-type window layer [52]. Fully μc-Si:H thin film solar cell was first demonstrated by the Neuchatel group in 1994 [53]. Microcrystalline silicon can be prepared by the same process as that for amorphous silicon, however heavy hydrogen dilution of precursor gas is required [1]. These are materials with complex microstructure that varies drastically with deposition conditions. These possess indirect band gap of 1.1 eV like crystalline silicon instead of 1.7-1.8eV of amorphous silicon. Hence these materials are useful in the IR range of the solar spectrum and can be used in multijunction solar cells as a replacement of a-SiGe:H, which possess inferior opto-electronic properties. The μc-Si:H are found to possess much milder form of light induced degradation [54] and good opto-electronic properties.

Recently the interest has been focused on nanocrystalline silicon (nc-Si:H) [4,6,55-56], due to its novel properties like high band gap [57-62], visible photoluminescence [27, 62-64] and electroluminescence [64]. The material preparation is similar to that of amorphous and microcrystalline silicon. In these materials small nanocrystallites of silicon of about 10 nm or less are present in the amorphous matrix. Depending on the deposition conditions, more ordered regions in the amorphous matrix gets transformed into nanocrystallites, which grow in size and may result into microcrystalline films. Nanocrystalline films are reported to be more stable than the amorphous films against light induced degradations [57, 65].

The silicon films prepared in the regime of amorphous to microcrystalline transition have attracted a great deal of attention because stable performance solar cells can be prepared at a hydrogen dilution ratio just below the onset of microcrystallinity [28, 66- 68]. These films are also termed as proto crystalline films [69]. The stability of these protocrystalline films is attributed to the improved order [70] and also to the dense homogeneous amorphous network [71]. These transition films also show high efficiency in solar cells [3, 72-73]. These films possess very good opto-electronic properties with improved medium range order and less defect density. These films are endowed with the good qualities of both the amorphous phase (direct band gap, high absorption co-efficient) and microcrystalline phase (improved order, hence high carrier mobility, conductivity, stability etc). This transitions can be achieved with the help of dilution of the precursor gases such as silane (SiH_4), di-silane (Si_2H_6), germane (GeH_4) etc. with different diluent gases like hydrogen and argon as well as varying other deposition parameters. Figure 1.3 depicts the phase diagram for the growth of silicon film with the dilution ratio and thickness [69]. In order to optimize the preparation conditions to make device quality transition films the correlation between the preparation conditions and the structure of the material, the hydrogen configuration and opto-electronic properties as well as stability of the material need to be studied carefully.

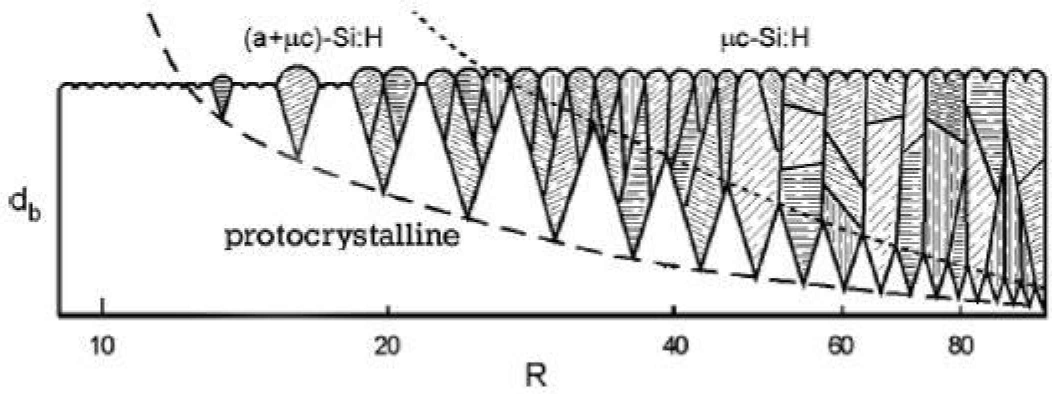

Figure 1.3: Phase diagram for the growth of silicon films with the dilution ratio R and thickness d_b [69].

1.2 Growth model for amorphous and microcrystalline silicon:

The effect of different deposition parameters on growth as well as properties of a-Si:H and μc-Si:H films are extensively studied for PECVD method. In PECVD method the source gas silane is decomposed into different radicals such as SiH_3, SiH_2, SiH, Si, H etc. The radicals with high reaction rate have low concentration and less diffusion length and are less likely to reach the growing surface. Among these radicals, SiH_3 is the least reactive one and has the highest concentration, irrespective of the initial formation rate and thus mainly responsible for the film growth. Figure 1.4 shows the number densities of different radicals in steady state plasma.

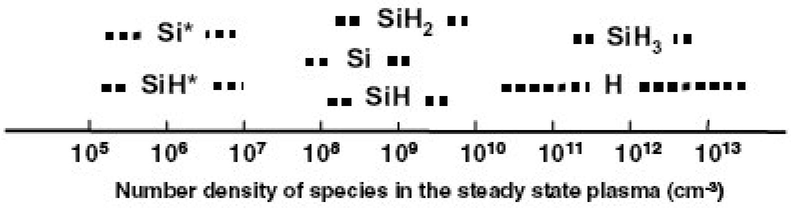

Figure 1.4: Number density of different film forming radicals in steady state plasma [74].

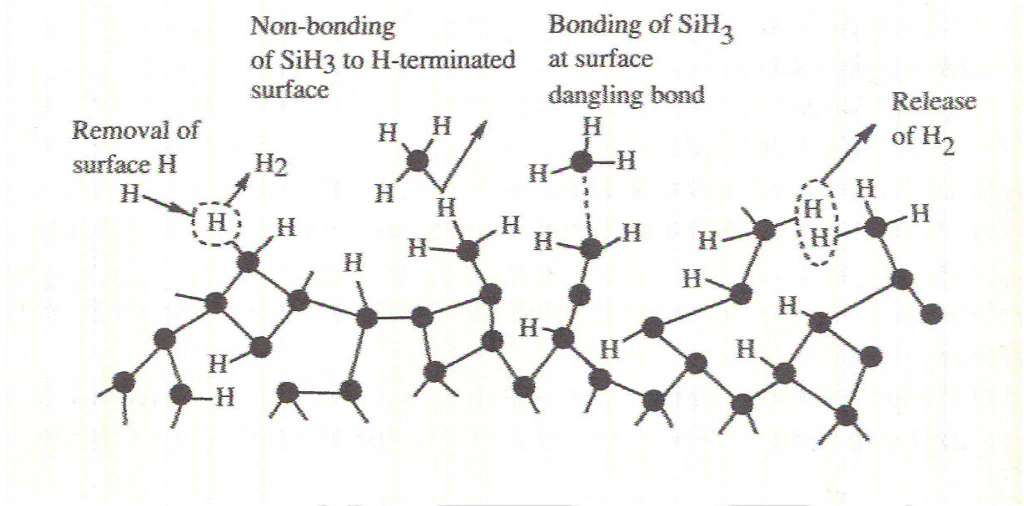

Figure 1.5: Film growth process for a-Si:H [1]

Figure 1.5 illustrates some of the processes involved during the growth of a-Si:H films [1]. The film forming radical SiH_3 reaching the growing film surface starts to diffuse on the film surface to get a favourable site to be bonded [74]. When the growing surface is completely covered by Si-H bond, the most abundant film forming precursor SiH_3 can not be inserted into the film. However, it can be inserted into uncovered Si bonds. Hence the removal of hydrogen from the growing surface is a necessary step for film growth. The hydrogen can be released spontaneously by thermal excitation or stripped of by radicals as illustrated in the figure 1.5, creating unterminated silicon bond, where a new SiH_3 radical can be inserted. The reactions involved are as follows

$$\text{Si-H} + \text{SiH}_3 \rightarrow \text{Si-} + \text{SiH}_4$$

$$\text{Si-H} + \text{H} \rightarrow \text{Si-} + \text{H}_2$$

The silicon dangling bonds thus created may also reconstruct into strong Si—Si bonds. Depending upon the relative fraction of other radicals (SiH_n, where $n \leq 2$), these may also take part in the film growth. Such radicals do not require silicon dangling bonds and result in a void rich material. Hence the final hydrogen content and film structure are set by a delicate balance between the removal of hydrogen into the gas, attachment of radicals into the gas, either SiH_3 which is desirable or other radicals and reconstruction of dangling bonds [1].

In case of microcrystalline silicon growth the same radicals are involved. However in this case abundant hydrogen radicals play a decisive role. Three different models have been proposed to explain the growth of microcrystalline silicon, *viz.*

1. Surface diffusion model [75-76]
2. Etching model [77]
3. Chemical annealing model [78]

According to the surface diffusion model, large amount of atomic hydrogen flux present in the precursor gas mixture (or plasma) covers the surface of the growing film by bonding with the silicon atoms. The hydrogen coverage also produces local heating through hydrogen exchanging reactions. This results in the surface diffusion of SiH_3 radicals, which helps SiH_3 to find energetically favourable sites before getting bonded into the growing film. As a consequence, atomically ordered structures are formed which act as nucleus for epitaxial like growth, with enhanced surface diffusion of SiH_3 [Figure 1.6].

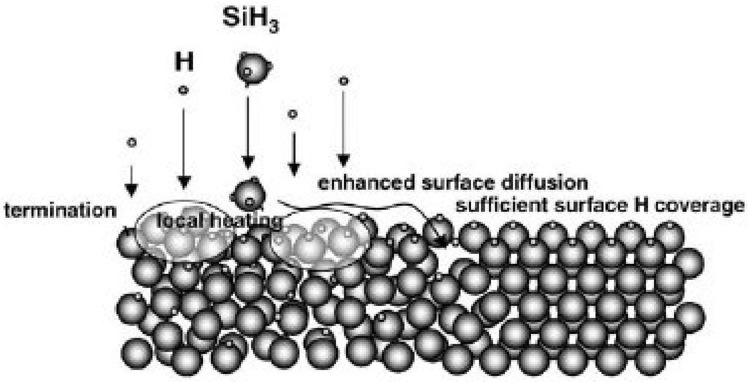

Figure 1.6: Growth of μc-Si:H through surface diffusion of radicals [75]

The etching model is proposed based on the experimental fact that the deposition rate decreases with the increase in hydrogen dilution ratio. The atomic hydrogen breaks the weak bonds on the growing surface and subsurface region which are replaced by new SiH_3 radicals to have strong and rigid bonds. This results in a more ordered structure. Chemical annealing model has been proposed to explain the crystal formation during an alternative layer by layer amorphous film growth and hydrogen plasma treatment. The absence of remarkable reduction in film thickness during hydrogen plasma treatment is hard to be explained by etching model. According to chemical annealing model, the atomic hydrogen permeates the subsurface region and crystallizes the amorphous network through the formation of flexible network with a sufficient number of atomic hydrogen without remarkable removal of Si atoms.

More recently, Cabarrocas *et al.* [79] proposed that the growth of μc-Si:H takes place through four successive and distinct phases. In the early stages of deposition excess atomic hydrogen induces the formation of a porous and hydrogen rich material within which the silicon network starts to rearrange (incubation phase). Once a critical concentration of voids is reached, stable crystallites nucleate (nucleation phase) and then continue to grow at the expenses of a-Si:H (growth phase) until a steady state regime is achieved. The crystallization process induced by surface and subsurface reactions of atomic hydrogen with the silicon network competes with the deposition rate. When the deposition rate is high, the time required for hydrogen to diffuse deep into the layer and to crystallite it decreases resulting in amorphous or partly crystallized layer.

1.3 Different methods of deposition of a-Si:H/ μc-Si:H:

As mentioned earlier, a-Si:H films were first prepared by plasma dissociation of the source gas silane [31]. Till date, radio frequency plasma enhanced chemical vapour deposition (RF PECVD) is the most extensively studied and widely used technique for the preparation of amorphous silicon as well as other alloys of silicon [80-84]. The scientific community has adapted a standard frequency of 13.56MHz for this technique which is used for industrial applications also [3, 55, 85-88]. The advantage of this technique is the high quality films deposited uniformly over a large area. There are other methods also like DC PECVD [89], VHF PECVD [90-94], Microwave PECVD [95-96], Sputtering [29, 97-100], Electron cyclotron resonance (ECR) [101], Remote Plasma CVD [102-103], Arc discharges [104], Photo CVD [105], PLD [106], HWCVD [107-108], etc. However, most of these techniques give poor quality films and hence not used for large scale production. Among these techniques, HWCVD or Cat- CVD is a promising one, as it possesses the ability to yield good quality films at reasonably higher rate than rf PECVD. This is a relatively new technique and was first employed to deposit amorphous silicon films by Wiesmann *et al.* in 1979 [109], though the film quality at that time was poor. Early research by Matsumura *et al.* [110] and Doyle *et al.* [111] helped to understand the deposition process for films prepared using HWCVD. This technique started getting popularity and momentum when Mahan *et al.* revealed the superiority of the Cat-CVD films compared to PECVD films [107]. In this paper as well as their subsequent papers [112-113], they reported the high quality films with hydrogen content below 1 atomic percent deposited at high rate. Their results stimulated the a-Si research community to work on this upcoming technique for the deposition of amorphous as well as microcrystalline silicon and other semiconductors at reasonably low cost. Dusane *et al.* [61], showed that μc-Si:H could be deposited from pure silane by HWCVD process unlike PECVD where heavy hydrogen dilution is required. Due to these developments many laboratories entered in to this field and presently more than 30 laboratories have HWCVD deposition facilities. Using HWCVD technique, the first thin film silicon solar cells were made in 1993 at NREL and University of Kaiserslauter while TFTs were made in 1995 at Utrecht University and JAIST [30]. Still, there are lots of challenges associated with HWCVD like uniform deposition, filament life time, reproducibility of the material etc. The following table (Table 1.2) [114] gives comparative features of different deposition methods.

Table 1.2: Comparative features of different techniques for preparation of a/μc-Si:H

Processes	Advantage	Disadvantage
RF PECVD	High quality, Uniform	Slow
DC PECVD	High quality, Uniform	Slow
VHF PECVD	Fast	Poor uniformity, Less standard generator
Microwave PECVD	Very fast	Quality not as good
HWCVD	Very fast	Large area uniformity is still an issue
Photo CVD	High quality	slow
Sputtering	-------	Poor quality, Slow

1.4 Current issues regarding a-Si:H/ μc-Si:H photovoltaics:

Though amorphous and microcrystalline silicon films have been an active area of research for last few decades, there are still a few issues related with this area. For increasing the share of thin film silicon solar cells in the present energy scenario the following issues have to be taken care of [47].

1. **Increasing the deposition rate**: The most important issue for the production of cost effective solar cells and other devices is the enhancement of deposition rate. Though amorphous silicon based solar cells have many advantages over the crystalline counterpart, the photovoltaic market is mainly dominated by wafer based solar cells. This is because of the fact that amorphous silicon based cells possess low stable efficiency. Hence to compensate this issue, the cells should be prepared at high deposition rate, thus decreasing the processing time and resulting higher throughput. The deposition rate of absorber layer should be about 10-20 Å/Sec in order to limit the investment during deposition. The deposition rate for microcrystalline silicon is further low, typically less than 1 Å/Sec [115]. On the other hand films deposited at high deposition rate possess more defects and suffer more light induced degradation. Dilution of the source gas with inert gases like argon, helium etc. increases the deposition rate, however columnar morphology [115-116] becomes important issue in that case. Very high frequency PECVD, hot wire CVD and expanding thermal CVD are emerging techniques for getting films with high deposition rate. Nowadays most of the efforts are in the development of high growth rate intrinsic absorber layers [94] without compromising the material quality. The deterioration in film quality with increase of deposition rate is because of the competition between surface reaction rate and the deposition rate. When deposition rate is slow, more time is available for surface reaction and hence further structural relaxation of the silicon network is permitted, leading into lower defect density in the film. However, when the deposition rate is high little time is allowed for structural reorientation, which leads to poor film quality [117].
2. **Elimination of light induced degradation (Staebler Wronski effect)**: Light induced degradations of a-Si:H and their alloys have been a serious concern since the observations by Staebler and Wronski [40]. The full understanding of SW effect is necessary for improved stability against light exposure. It is found that nanocrystalline films as well as amorphous films prepared at the onset of crystallinity undergo less light induced degradation [28, 57, 65- 68].

Though this is a topic of interest for long time, the full understanding and complete eradication of SW effect is not completely resolved.

3. **Increasing the conversion efficiency**: The conversion efficiency is the main issue where thin film silicon solar cells lags behind the bulk crystalline silicon solar cells. Till now the stable efficiency is below 15% for small area solar cells [6, 47, 94]. The device performance enhancement is expected from increase in the current in thin film silicon solar cells. This can be achieved by improving the material quality as well as the light management schemes such as light trapping and reduction of light absorption losses. The improvement in material quality includes the improvement in the intrinsic absorber layers (a-Si:H, nc-Si:H, a-SiGe:H etc), doped layers and the interfaces between the doped layers and the intrinsic absorber. Optimization of layer thicknesses for proper matching of current in multijunction solar cells is another important issue for increasing conversion efficiency.

4. **Choice of mass production technology:** The complete manufacturing of solar cells includes several fabrication steps like deposition of TCO front electrode, multilayer back electrode, laser scribing for sub cell series connections, encapsulations and framing. These all contribute to the total cost of the module. The choice of sequence of fabrication steps and processing technique depends on the solar cell structure and design. Most used approaches for depositing the silicon based layers are one chamber batch processsess, multijunction processes and roll to roll processes, each having advantages and disadvantages of their own. The main aim is to deposit the cells on large area in a single run so that the cost per unit area is lowered.

5. **Lowering material cost**: The substrate costs as well as substrate carrier costs have substantial contribution towards the total cost of the module. Cheaper metal as well as polymer foils are preferred for roll to roll processing. Also, cheaper encapsulant is necessary for cost reduction. The choice of precursor gases for the deposition of silicon based layers, its purity, gas utilization etc. also determine the total cost. Low temperature process is much preferred as it involves less processing cost and possible use of low cost substrates such as plastics.

1.5 Motivation for present work:

As mentioned above amorphous and micro/nano-crystalline silicon are promising materials for opto-electronic device applications, especially for solar cells in context to the present scenario of energy crisis and search for eco-friendly energy solutions. However, silicon thin film solar cell technology shares a very small fraction of the total photovoltaic market till date. This is mainly because of the low stable efficiency arising from Staebler Wronski effect and low deposition rate of the thin film silicon cells. Hence the challenge is to prepare films at high deposition rate with better opto-electronic properties which give higher efficiency and can withstand prolonged light exposure. Recent studies have shown that films prepared in the transition region from amorphous to micro-crystalline phase possess very good opto-electronic properties with improved medium range order and less defect density [28, 66, 67, 72]. These films possess the good qualities of both the amorphous phase and crystalline phase. This can be achieved with the help of dilution of the precursor gases such as silane (SiH_4), di-silane (Si_2H_6), germane (GeH_4) etc. with different diluent gases like hydrogen and argon as well as varying other deposition parameters. Though hydrogen dilution improves the material quality, it decreases the deposition rate drastically, especially for the microcrystalline films. Dilution by noble gases such as argon increases the growth rate but it has deleterious effect on the material quality like inhomogeneous and columnar growth [116]. Hence the research on argon dilution did not get much attention in the early years. However, there has been an increased interest on the dilution of source gas with noble gases like argon or helium in the recent years [118-122]. Hamma *et al.* [123] showed that the microcrystalline films prepared with layer by layer (LBL) growth using PECVD technique are better when argon is added to hydrogen during hydrogen plasma treatment. Ray *et al.* [124] also reported the superiority of films prepared with 90% argon dilution than undiluted silane. However, Soppe *et al.* [125] found that the material properties of microcrystalline silicon layers deteriorate if argon dilution is used. Das *et al.* [126], obtained good quality amorphous silicon films with argon dilution at low rf power and low deposition rate (0.16Å/Sec), however the film became columnar at higher rf power though the deposition rate increased a little (0.5 Å/Sec). In subsequent work [115], they showed that addition of hydrogen in the argon diluted gas mixture could improve the material with a reduced deposition rate. We therefore, decided to study the film properties grown by combined argon and hydrogen dilution in PECVD system anticipating good deposition rate due to argon dilution and suppression of columnar growth due to hydrogen dilution. Comparatively new HWCVD technique offers good deposition rate along with reasonably good material properties. However, this technique is not extensively studied and standardized like PECVD technique. Hence there is a need to study the deposition process as well as the effect of different parameters on the material quality. Owing to the viability of this technique lots of research activities are going on around the globe. In Japan, a new NEDO project has been started aiming at 13 % efficient thin film silicon solar cells by HWCVD [30]. A biennial international conference namely "International Conference on Cat-CVD process" was started in November 2000. Films prepared with HWCVD technique show some striking difference with the films by PECVD such as low hydrogen content as well as retaining the quality with hydrogen content below 1 atomic % [107] which manifest in lower Staebler Wronski effect [40], different NMR signature [127], almost complete absence of internal friction [128] etc. Though this technique has been gaining importance, still there are lots of challenges associated with it like, large area uniform deposition, film contamination due to filament, filament life time, reproducibility of the material, substrate heating due to filament etc. Horbach *et al.* [129] reported the observation of film contamination by the filament material for filament temperature, $T_F > 2100^oC$. Brogueria *et al.* [130] reported the burning out of filament at $T_F \sim 2500^oC$. On the other hand at low T_F, the silicon radicals form alloy with the filament. Doyle *et al.* [111] first observed that the evolution of Si from the filament fell below the level of SiH_4 decomposition, indicating possible incorporation of Si into the filament at $T_F < 1450^oC$. Brogueria *et al.* [130] also reported that below 1700^oC, Si gets incorporated into the filament. This alloy so formed (W_5Si_3) is brittle and filament breakage occurs. Duan *et al.* [131] also observed consumption of silane without significant formation of Si containing radicals for T_F up to 1300^oC. The concentration of Si starts rising near 1300^oC and levels off above 1800^oC, while SiH_3 and Si_2H_6 concentration becomes significant at higher temperatures. This problem is more serious in case of undiluted silane. The alloying not only causes breakage of the filament but also increases the power consumption to heat the filament and has adverse effect on the reproducibility of the film quality. For minimizing this silicide formation, other filament elements like graphite, tantalum etc., have been tried by various research groups. Recently Werf et *al.* [132] have shown that annealing the tantalum filament at 2100-2200^oC after silicidation at 1750^oC helps to completely recover the fresh wire. Soni *et al.* [133] made a comparative study of tantalum and tungsten filament and found that tantalum filament yields better growth rate while maintaining the film quality. Another issue in HWCVD system is the substrate heating due to the filament. It is system dependent and function of many factors like filament to substrate distance, power requirements of filament and substrate heater, thermal capacitance of substrate holder etc. This heating can be reduced by using electrostatic chuck [134], increasing filament to substrate distance [135], cooling the substrate during deposition [38] etc. Soler *et al.* [136] studied the effect of filament temperature on the film microstructure using tantalum filament and found that the amorphous to nanocrystalline transition takes place at T_F 1700°C when the films were prepared with pure silane flow of 4SCCM. Fonrodona *et al.* [137], reported the fabrication of amorphous and nanocrystalline TFTs with T_F 1680 and 1610°C. Jadkar *et al.* [138] studied the role of T_F on film properties with T_F in the range of 1400-2200°C using tungsten wire. They found that the transition of film microstructure occurs at T_F 2100°C. These films showed an increase in total hydrogen content and dihydride fraction with the increase in filament temperature. There are reports on the investigations of the effect of substrate (T_s) temperature on film deposition by HWCVD. Soni *et al.* [133] observed that the deposition rate increases with T_s. Low T_s processing of silicon films is a major interest now a days. This not only facilitates the use of variety of substrates like plastic, but also decreases processing cost and increases the possibility to use in biological applications. Alpuim *et al.* [139] could deposit both amorphous and microcrystalline films using rf PECVD and HWCVD method at T_s 100 and 25°C, with the same comparable quality as that of moderate T_s (250°C) prepared in the same chamber. They observed that the HWCVD films become nanocrystalline at lower hydrogen dilution than that required for PECVD films (at T_s 25°C, H_2 dilution required is 99% for PECVD, 87.5% for HWCVD, while at 100°C 98% for PECVD and 85% for HWCVD). Filonovich *et al.* [39] performed a comparative study on the films prepared by both PECVD and HWCVD methods at T_s of 150°C. They found that HWCVD films are of good quality, however PECVD prepared films are better. Brinza *et al.* [38] also reported device quality films with low defect density and good photo response, deposited at 100°C by variation of hydrogen dilution with HWCVD method, however the microcrystalline films thus prepared show lesser quality. Fortmann *et al.* [140] recently demonstrated the possibility of photonic applications of HWCVD deposited silicon films. Mahan *et al.* [113] prepared films with very high deposition rate by HWCVD method using multiple filaments and found that films with deposition rate upto130Å/Sec showed good quality beyond which the quality deteriorated.

Keeping these issues in mind, the present thesis work focuses on the study of the influence of process parameters on the properties and stability of thin silicon films and optimization of the parameters for high quality films with high deposition rate. A few films are prepared by argon dilution of silane by PECVD method while majority of the films are prepared by HWCVD method as HWCVD is new and less extensively studied technique in comparison to PECVD system. Since a detailed study of the influence of process parameters on the film quality and properties is required to set the guideline for optimization of these parameters for making device quality film, several series of the films with varying deposition parameters such as substrate temperature, filament temperature, gas flow rate etc. are prepared and extensively studied. As a part of the thesis work, a few systems, including HWCVD system and characterization setups are also fabricated in house. We are able to achieve films ranging from pure amorphous to nano-crystalline nature by just varying a single deposition parameter at one time. This opens up the possibility of fabricating multi-junction solar cells by varying a single parameter. In the present work good PECVD films are prepared using argon and hydrogen dilution of silane and found to be free from columnar growth. The best films are obtained with argon dilution (Argon flow rate/ silane flow rate) of about 400. These films possess good deposition rate due to argon dilution and are free from columnar growth because of combined effect of hydrogen and argon. It is inferred from the work on HWCVD films that unlike PECVD this method requires less hydrogen dilution for good quality films. The best quality amorphous silicon films are obtained from pure silane or with weakly hydrogen diluted silane. Amorphous films with good adhesion to the substrate could be obtained at substrate temperature as low as 100^{o}C. Also, we could achieve nanocrystalline transition at low substrate temperature like 200^{o}C. The films reported under present work show wide variation of band gap and very good stability along with good photosensitivity. Further, these films possess medium to high deposition rate and hence can be viable candidate for stable and cost effective devices. The process parameters can be fine tuned for further improvement in material quality.

1.6 References:

1. R.A. Street, Hydrogenated Amorphous Silicon, Cambridge University Press, (1992).
2. R.A. Street (Ed.), Technology and Application of Amorphous Silicon, Springer, (1999).
3. P. Kumar, F. Zhu and A. Madan, Int. J. Hydrogen Energy **33** (2008) 3938.
4. C. Song, G. R. Chen, J. Xu, T. Wang, H. C. Sun, Y. Liu, W. Li, Z. Y. Ma, L. Xu, X. F. Huang and K. J. Chen, J. Appl. Phys. **105** (2009) 054901.
5. T. M. Mok and S. K. O' Leary, J. Appl. Phys. **102** (2007) 113525.
6. S. Klein, F.Finger, R. Carius and M. Stutzmann, J. Appl. Phys. **98** (2005) 024905.
7. A. Bhaduri, P. Chaudhuri, D. L. Williamson, S. Vignoli, P. P. Ray and C. Longeaud, J. Appl. Phys. **104** (2008) 063709.
8. P. Agarwal, H. Povolny, S. Han, X. Deng, J. Non-Cryst. Solids **299-302** (2002) 1213.
9. M. Boshta, K. Barner, R. Braunstein, B. Alavi and V. Dalal, Mater. Sci. Eng. B **112** (2004) 69.
10. J. D. Cohen, Sol. Energy Mater. Sol. Cells **78** (2003) 399.
11. A. Matsuda and G. Ganguly, Appl. Phys. Lett. **67** (1995) 1274.
12. J. Koh, Y. Lu, C. R. Wronski, Y. Kuang, R. W. Collins, T. T. Tsong and Y. E. Strausser, Appl. Phys. Lett. **69** (1996) 1297.
13. B. P. Swain, T. K. G. Rao, M. Roy, J. Gupta and R. O. Dusane, Thin Solid Films **501** (2006) 173.
14. D. K. Basa, G. Abbate, G. Ambrosone, U. Coscia and A. Marino, J. Appl. Phys. **107** (2010) 0235032.
15. Th. Nguyen-Tran, V. Suendo and P. Roca i Cabarrocas, Appl. Phys. Lett. **87** (2005) 011903.
16. Z. Lu, P. Santos-Filho, G. Stevens, M. J. Williams and G. Lucovsky, J. Vac. Sci. Technol. A **13** (1995) 607.
17. C. Savall, J. C. Bruyere and J. P. Stoquert, Thin Solid Films **260** (1995) 174.
18. F. L. Martinez, I. Martil, G. Gonzalez-Diaz, B. Selle, I. Sieber, J. Non-Cryst. Solids **227-230** (1998) 523**.**
19. M. T. K. Soh, N. Savvides, C. A. Musca, M. P. Martynjuk and L. Faraone, J. Appl. Phys. **97** (2005) 093714.

20. K. Sato and K. Hirakuri, J. Appl. Phys. **100** (2006) 114303.

21. Z. Cen, J. Xu, Y. Liu, W. Li, L. Xu, Z. Ma, X. Huang and K. Chen, Appl. Phys. Lett. **89** (2006) 163107.

22. M. Wang, K. Chen, L. He, W. Li, J. Xu and X. Huang, Appl. Phys. Lett. **73** (1998) 105.

23. R. J. Walters, G. I. Bourianoff and H. A. Atwater, Nat. Mater. **4** (2005) 143.

24. S. Tiwari, F. Rana, H. Hanafi, A. Hartstein, E. Crabbe and K. Chan, Appl. Phys. Lett., **68** (1996) 1377.

25. B. De Salvo, G. Ghibaudo, P. Luthereau, T. Baron, B. Guillaumot and G. Reimbold, Solid State Electron. **45** (2001) 1513.

26. G. Gracin, A. Gajovic, K. Juraic, M. Ceh, Z. Remes, A. Poruba and M. Vanecek, J. Non-Cryst. Solids **354** (2008) 2286.

27. J. -H. Shim, S. Im and N. -H. Cho, Appl. Surf. Sci. **234** (2004) 268.

28. S. Guha, J. Yang, D. L. Williamson, Y. Lubianiker, J. D. Cohen and A. H. Mahan, Appl. Phys. Lett. **74** (1999) 1860.

29. R. Baghdad, D. Benlakehal, X. Portier, K. Zellama, S. Charvet, J. D. Sib, M. Clin and L. Chahed, Thin Solid Films **516** (2008) 3965.

30. R. E. I. Schropp, Thin Solid Films **451-452** (2004) 455 and references therein.

31. R. C. Chittick, J. H. Alexander and H. F. Sterling, J. Electrochem. Soc. **116** (1969) 77.

32. W. E. Spear and P. G. LeComber, Phys. Rev. Lett. **25** (1970) 509.

33. W. E. Spear, R.J. Loveland and A. Al-Sharbaty, J. Non-Cryst. Solids **15** (1974) 410.

34. W. E. Spear and P. G. LeComber, Solid State Commun. **17** (1975) 1193.

35. A. J. Lewis, G. A. N. Connell, W. Paul, J. R. Pawlik and R. J. Temkin, AIP Conf. Proc. **20** (1974) 27.

36. H. Fritzsche, Proc. 7th Int. Conf. on Amorphous and Liquid Semiconductors, ed. W. E. Spear, (1977) 3.

37. P. Alpuim, V. Chu and J. P. Conde, J. Non-Cryst. Solids **266-269** (2000) 110.

38. M. Brinza, C. H. M. van der Werf, J. K. Rath and R. E. I. Schropp, J. Non-Cryst. Solids **354** (2008) 2248.

39. S. A. Filonovich, P. Alpuim, L. Rebouta, J. E. Bouree and Y. M.Soro, J. Non-Cryst. Solids **354** (2008) 2376.

40. D. L. Staebler and C. R. Wronski, Appl. Phys. Lett. **31** (1977) 292.

41. Ken Caldeira, Atul K. Jain and Martin I. Hoffert, Science **299** (2003) 2052.
42. N. S. Lewis, Scientific challenges in sustainable energy technology, plenary presentation at MRS spring meeting 2007.
43. R. E. I. Schropp, *Amorphous (protocrystalline) and microcrystalline thin film silicon solar cells*, Nanostructured Materials for Solar Energy Conversion, Elsevier, Amsterdam (2006) Ed. T. Soga.
44. R. E. I. Schropp, J. K. Rath and H. Li, J. Cryst. Growth **311** (2009) 760.
45. W. H. Zachariasen, J. Am. Chem. Soc. **54** (1932) 3841.
46. N. F. Mott, Philos. Mag. **19** (1969) 835.
47. M. Zeman, *Advanced amorphous silicon solar cell technologies*, Thin Film Solar Cells: Fabrication, Characterization and Applications, John Wiley and Sons (2006), Ed. J. Poortmans and V. Arkhipov.
48. M. Stutzmann, *Amorphous Semiconductors,* Handbook of Semiconductors, North Holland Vol **3a** (1994), Ed. S. Mahajan.
49. S. Veprek and V. Marecek, Solid State Electron. **11** (1968) 683.
50. R. Tsu, M. Izu, S. R. Ovshinsky and F. H. Pollack, Solid State Commun. **36** (1980) 817.
51. T. Hamasaki, H. Kurata, M. Hirose and Y. Osaka, Appl. Phys. Lett. **37** (1980) 1084.
52. Y. Hattori, T. Kruangam, T. Toyama, H. Okamoto and Y. Hamakawa, Technical Digest of International PVSEC-3, Tokyo, Japan (1987) 171.
53. J. Meier, R. Fluckiger, H. Keppner and A. Shah, Appl. Phys. Lett. **65** (1994) 860.
54. E. V. Sauvain, A. Shah and J. Bailat, *Advances in microcrystalline silicon solar cell technologies*, Thin Film Solar Cells: Fabrication, Characterization and Applications, John Wiley and Sons (2006), Ed. J. Poortmans and V. Arkhipov.
55. Y. He, C. Z. Yin, G. Cheng, L. Wang X. Liu and G.Y. Hu, J. Appl. Phys. **75** (1994) 797.
56. R. E. I. Schropp, H. Li, R. H. Franken, J. K. Rath, C. H. M. van der. Werf, J. W. A. Schuttauf and R. L. Stolk, Thin Solid Films **516** (2008) 6818.
57. G. Viera, M. Mikikian, E. Bertran and P. Roca i Cabarrocas, J. Appl. Phys. **92** (2002) 4684.
58. D. Das, J. Phys. D : Appl. Phys. **36** (2003)2335.
59. M. Konuma, H. Curtins, F. A. Sarott and S. Veprek, Philos. Mag. B **55** (1987) 377.

60. S. Komuro, Y. Aoyagi, Y. Segawa, S. Namba, A. Masuyama, A. Matsuda and K. Tanaka, J. Appl. Phys. **56** (1984) 1658.
61. R. O. Dusane, S. R. Dusane, V. G. Bhide and S. T. Kshirsagar, Appl. Phys. Lett. **63** (1993) 2201.
62. H. Takagi, H. Ogawa, Y. Yamazaki, A. Ishizaki and T. Nakagiri, Appl. Phys. Lett. **56** (1990) 2379.
63. K. Chen, X. Huang, J. Xu and D. Feng, Appl. Phys. Lett. **61** (1992) 2069.
64. D. Han and K. Wang, Sol. Energy Mater. Sol. Cells **78** (2003) 181.
65. T. Itoh, K. Yamamoto, K. Ushikoshi, S. Nonomura and S. Nitta, J. Non-Cryst. Solids **266-269** (2000) 201.
66. R. W. Collins, A. S. Ferlauto, G. M. Ferreira, C. Chen, J. Koh, R. J. Koval, Y. Lee, J. M. Pearce and C. R. Wronski, Sol. Energy Mater. Sol. Cells **78** (2003) 143.
67. W. Du, X. Liao, X. Cao, X. Yang, X. Deng and K. Sun, J. Non-Cryst. Solids **354** (2008) 2155.
68. M. Ito and M. Kondo, Jpn. J. Appl. Phys. **45** (2006) L230.
69. C. R. Wronski, J. M. Pearce, J. Deng, V. Vlahos and R. W. Collins, Thin Solid Films **451-452** (2004) 470.
70. D. V. Tsu, B. S. Chao, S. R. Ovshinsky, S. Guha and J. Yang, Appl. Phys. Lett. **71** (1997) 1317.
71. Jun Yong Ahn, Koeng Su Lim, J. Non-Cryst. Solids **351** (2005) 748.
72. O. Vetterl, F. Finger, R. Carius, P. Hapke, L. Houben, O. Kluth, A. Lambertz, A. Mück, B. Rech, H. Wagner, Sol. Energy Mater. Sol. Cells **62** (2000) 97.
73. T. Roschek, T. Repmann, J. Müller, B. Rech and H. Wagner, J. Vac. Sci. Technol. A **20** (2002) 492.
74. A. Matsuda, J. Non-Cryst. Solids **338-340** (2004) 1.
75. A. Matsuda, J. Non-Cryst. Solids **59-60** (1983) 171.
76. A. Matsuda, Thin Solid Films **337** (1999) 1.
77. C. C. Tsai, G. B. Anderson, R. Thompson and B. Wacker, J. Non-Cryst. Solids **114** (1989) 151.
78. Kenjiro Nakamura, Kunihiko Yoshino, Shinya Takeoka, Isamu Shimizu, Jpn. J. Appl. Phys. **34** (1995) 442.

79. P. Roca i Cabarrocas, Yassine Djeridane, V. D. Bui, Yvan Bonnassieux, Alexey Abramov, Solid State Electron. **52**(2008) 422.
80. A. Matsuda, J. Non-Cryst. Solids **59-60** (1983) 767.
81. R. E. Hollingsworth and P. K. Bhat, Appl. Phys. Lett. **64** (1994) 616.
82. M. Kondo, Y. Toyoshima, A. Matsuda and K. Ikuta, J. Appl. Phys. **80** (1996) 6061.
83. J. H. Zhou, K. Ikuta, T. Yasuda, T. Umeda, S. Yamasaki and K. Tanaka, Appl. Phys. Lett. **71** (1997) 1534.
84. S. J. Jones, Y. Chen, D. L. Williamson, U. Kroll and P. Roca i Cabarrocas, J. Non-Cryst. Solids **164-166** (1993) 131.
85. P. M. Gordo, M. F. F. Marques, C. L. Gil, A. P. D. Lima, G. Lavareda, C. N. D. Carvalho, A. Amaral and Z. Kajcsos, Radiat. Phys. Chem. **76** (2007) 220.
86. Jong Hwan Yoon, J. Non-Cryst. Solids **353** (2007) 4223.
87. S. Alexandrova, P. Danesh and I. A. Maslyanitsyn, Vacuum **69** (2003) 391.
88. P. P. Ray, N. D. Gupta, P. Chaudhuri, D. L. Williamson, S. Vignoli and C. Longeaud, J. Non-Cryst. Solids **299-302** (2002) 123.
89. R. R. Arya and D. E. Carlson, Prog. Photovoltaics **10** (2002) 69.
90. H. Curtins, N. Wyrsch and A. V. Shah, Electronics Lett. **23** (1987) 228.
91. H.Chatham, P. Bhat A. Benson and C. Matovich, J. Non-Cryst. Solids **115** (1989) 201.
92. V. L. Dalal, J. Graves and J. Leib, Appl. Phys. Lett. **85** (2004) 1413.
93. S. Shimizu, A. Matsuda and M. Kondo, Sol. Energy Mater. Sol. Cells **92** (2008) 1241.
94. A. Gordijn, J. K. Rath and R. E. I. Schropp, J. Appl. Phys. **95** (2004) 8290 and references therein.
95. H. Jia, H. Kuraseko, H. Fujiwara and M. Kondo, Sol. Energy Mater. Sol. Cells **93** (2009) 812.
96. Jian-De Gu and Pei-Li Chen, Thin solid Films **498** (2006) 14.
97. T. D. Moustakas, T. Tiedje and W. Lanford, AIP Conf. Proc. **73** (1981) 20.
98. P. G. Lecomber, G. Willeke and W. E. Spear, J. Non-Cryst. Solids **59-60** (1983) 795.
99. N. Maley and J. S. Lannin, Phys. Rev. B **36** (1987) 1146.
100. G. Morell, R. S. Katiyar, S. Z. Weisz, H. Jia, J. Shinar and I. Balberg, J. Appl. Phys. **78** (1995) 5120.

101. T. V. Herak, J. J. Schellenberg, P. K. Shufflebothan and K. C. Kao, J. Appl. Phys. **64** (1988) 688.

102. C. Wang, M. J. Williams and G. Lucovsky, J. Vac. Sci. Technol., A **9** (1991) 444.

103. S. C. Kim, M. H. Jung and J. Jang, Appl. Phys. Lett. **58** (1991) 281.

104. N. Imajyo, J. Non-Cryst. Solids **198-200** (1995) 935.

105. R. E. Rocheleau, S. S. Hegedus, W. A. Buchanan and S.C. Jackson, Appl. Phys. Lett. **51** (1987)133.

106. R. Ayouchi, R. Schwarz, L.V. Melo, R. Ramalho, E. Alves, C.P. Marques, L. Santos, R. Almeida and O. Conde, Appl. Surf. Sci. **255** (2009) 5299.

107. A. H. Mahan, J. Carapella, B. P. Nelson, R. S. Crandall and I. Balberg, J. Appl. Phys. **69** (1991) 6728.

108. S. R. Jadkar, J. V. Sali, A. M. Funde, N. A. Bakr, P. B. Vidyasagar, R. R. Hawaldar and D. P. Amalnerkar, Sol. Energy Mater. Sol. Cells **91** (2007) 714.

109. H. Wiesmann, A. K. Ghosh, T. McMahon and M. Strongin, J. Appl. Phys. **50** (1979) 3752.

110. H. Matsumura and H. Tachibana, Appl. Phys. Lett. **47** (1985) 833.

111. J. Doyle, R. Robertson, G.H. Lin, M. Z. He, A. Gallagher, J. Appl. Phys. **64** (1988) 3215.

112. A. H. Mahan, L. M. Gedvilas and J. D. Webb, J. Appl. Phys. **87** (2000) 1650.

113. A. H. Mahan, Y. Xu, B.P. Nelson, R. S. Crandall, J. D. Cohen, K. C. Palinginis and A. C. Gallagher, Appl. Phys. Lett. **78** (2001) 3788.

114. X. Deng and E. A. Schiff, *Amorphous silicon based solar cells*, Handbook of Photovoltaic Science and Engineering, John Wiley and Sons (2003), Ed. A. Luque and S. Hegedus.

115. M. Jana, D. Das and A. K. Barua, J. Appl. Phys. **91** (2002) 5442.

116. J. C. Knights and R. A. Lujan, Appl. Phys. Lett. **35** (1979) 244.

117. Y. Hishikawa, S. Tsuge, N. Nakamura, S. Tsuda, A. Nakano and Y. Kuwano, J. Appl. Phys. **69** (1991) 508.

118. U. K. Das, P. Chaudhuri and S. T. Kshirsagar, J. Appl. Phys. **80** (1996) 5389.

119. Y. H. Wang, J. Lin and C. H. A. Huan, Mater. Sci. Eng., B **104** (2003) 80.

120. U. K. Das, A. R. Middya, J. K. Rath, C. Longeaud, D. L. Williamson and P. Chaudhuri, J. Non-Cryst. Solids **276** (2000) 46.

121. J. Cárabe, J. J. Gandía, N. González and M. T. Gutiérrez, Sol. Energy Mater. Sol Cells **57** (1999) 97.

122. S. Tchakarov, D. Das, O. Saadane, A. V. Kharchenko, V. Suendo, F. Kail, P. Roca i Cabarrocas, J. Non-Cryst. Solids **338-340**, (2004) 668.

123. S. Hamma and P. Roca i Cabarrocas, J. Non-Cryst. Solids **227-230** (1998) 852.

124. P. P. Ray, P. Chaudhuri and P. Chatterjee, Thin Solid Films **403-404** (2002) 275.

125. W. J. Soppe, C. Devilee, M. Geusebroek, J. Löffler and H.-J. Muffler, Thin Solid Films **515** (2007) 7490.

126. D. Das, M. Jana and A. K. Barua, J. Appl. Phys. **89** (2001) 3041.

127. Y. Wu, J. T. Stephen, D. X. Han, J. M. Rutland, R. S. Crandall and A. H. Mahan, Phys. Rev. Lett. **77** (1996) 2049.

128. X. Liu, B. E. White, Jr., R. O. Pohl, E. Iwanizcko, K. M. Zones, A. H. Mahan, B. P. Nelson, R. S. Crandall and S. Veprek, Phys. Rev. Lett. **78** (1997) 4418.

129. C. Horbach, W. Beyer and H. Wagner, J. Non-Cryst. Solids **137-138** (1991) 661.

130. P. Brogueira, J. P. Conde, S. Arekat and V. Chu, J. Appl. Phys. **79** (1996) 8748.

131. H. L. Duan, G. A. Zaharias and Stacey F. Bent, Thin Solid Films **395** (2001) 36.

132. C.H.M. van der Werf, H. Li, V. Verlaan, C. J. Oliphant, R. Bakker, Z. S. Houweling and R. E. I. Schropp, Thin Solid Films **517** (2009) 3431.

133. S. K. Soni, A. Pathak and R. O. Dusane, Technical Digest of International PVSEC-18, Kolkata, India (2009) 281.

134. K. Ishibashi, Thin Solid Films **395** (2001) 55.

135. J. K. Rath, M. de Jong and R. E. I. Schropp, Thin Solid Films **516** (2008) 751.

136. D. Soler, M. Fonrodona, C. Voz, J. Bertomeu and J. Andreu, Thin Solid Films **383** (2001) 189.

137. M. Fonrodona, D. Soler, J. Escarré, F. Villar, J. Bertomeu, J. Andreu, A. Saboundji, N. Coulon and T. M. Brahim, Thin Solid Films **501** (2006) 303.

138. S. R. Jadkar, J. V. Sali, S. T. Kshirsagar and M. G. Takwale, Thin Solid Films **437** (2003) 18.

139. P. Alpuim, V. Chu and J. P. Conde, J. Appl. Phys. **86** (1999) 3812.

140. C. M. Fortmann, J. Mawyin, R. J. Tonucci and A. H. Mahan, Thin Solid Films **501** (2006) 350.

Chapter -2

Experimental Techniques

Chapter 2

Experimental Techniques

During the course of the thesis work, several experimental techniques have been used to prepare and study the films. This chapter briefly describes the techniques used and also analysis details for estimating different parameters from the raw data obtained from these characterization techniques.

2.1 Film Preparation: Thin films of amorphous as well as nanocrystallites embedded amorphous silicon are prepared using two different deposition techniques *viz.* radio frequency plasma enhanced chemical vapour deposition method (RF-PECVD) and hot-wire chemical vapour deposition (HWCVD) method. These methods are described briefly below.

2.1.1 Radio Frequency Plasma Enhanced Chemical Vapour Deposition (RF-PECVD) method:

This is the most extensively studied and used method for the preparation of amorphous silicon alloy thin films and their devices [1-2]. Capacitatively coupled PECVD method with radio frequency 13.56 MHz is opted among scientific community for preparation of device quality films and also used in industrial applications [2-8]. The system consists of a high vacuum chamber generally connected to a load lock chamber, a gas inlet system and the source for the discharge. The schematic diagram of a regular PECVD system is shown in the Figure 2.1. Different source gases are used for preparation of films such as silane (SiH_4) or disilane (Si_2H_6) in case of silicon films, germane (GeH_4) for germanium films, methane (CH_4) for carbon films etc.

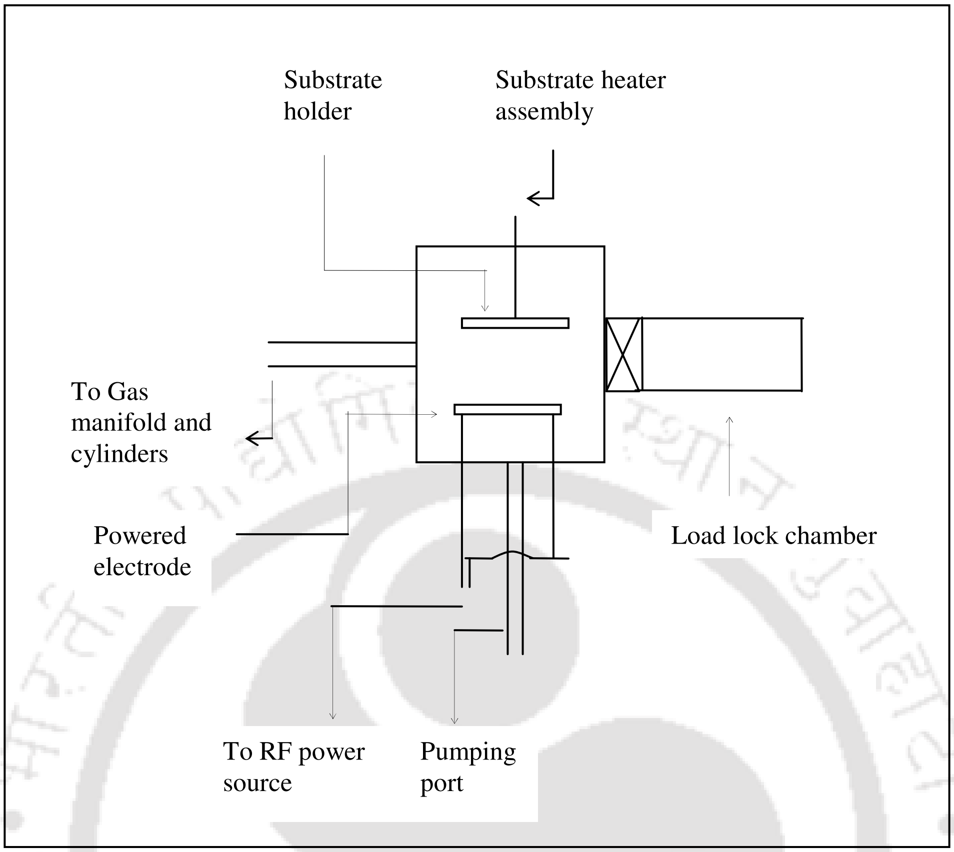

Figure 2.1: Schematic diagram of a general PECVD system

These gases are dissociated into different film forming radicals by inelastic collision with the high energy electrons (about several ten electron volts) present in the plasma, followed by subsequent gas phase reactions. SiH_4 is dissociated into SiH_n ($n \leq 3$) as well as H_2 and H. Hydrogen molecule is also decomposed into atomic hydrogen. As a matter of course, excitation of the ground state electron to the vacuum state gives rise to ionization events, generating new electrons and ions to maintain the plasma [9]. The plasma is confined between two parallel plates, one of which also holds the substrate. Figure 2.2 represents the formation of different radicals by the dissociation of the source gas silane with the help of plasma [9]. The radicals so formed undergo secondary gas phase reactions, mostly with parent SiH_4 and H_2 as mentioned in the Figure 2.3 forming a steady state. The radicals formed in secondary gas phase reactions then get deposited on the substrate, yielding the film. As SiH_3 is the least reactive species, its number density becomes much more (about two orders of magnitude) than the other radicals. Hence the main film forming radical in PECVD method is SiH_3.

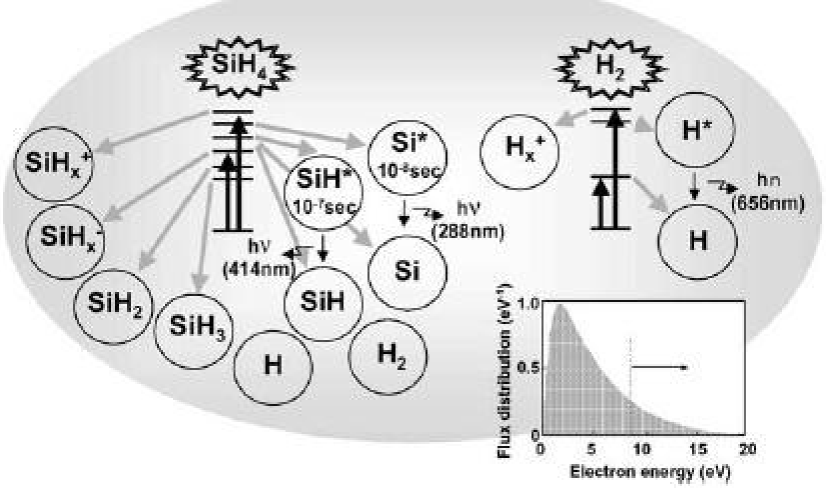

Figure 2.2: Schematic diagram demonstrating the dissociation process of SiH_4 and H_2 into different radicals with the help of plasma through their electronic excited states. Electron energy distribution function is also shown [9].

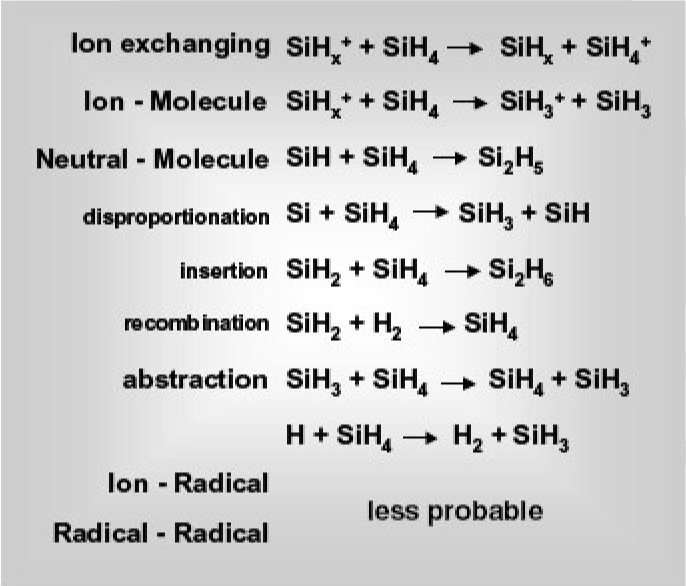

Ion exchanging	$SiH_x^+ + SiH_4 \rightarrow SiH_x + SiH_4^+$
Ion - Molecule	$SiH_x^+ + SiH_4 \rightarrow SiH_3^+ + SiH_3$
Neutral - Molecule	$SiH + SiH_4 \rightarrow Si_2H_5$
disproportionation	$Si + SiH_4 \rightarrow SiH_3 + SiH$
insertion	$SiH_2 + SiH_4 \rightarrow Si_2H_6$
recombination	$SiH_2 + H_2 \rightarrow SiH_4$
abstraction	$SiH_3 + SiH_4 \rightarrow SiH_4 + SiH_3$ $H + SiH_4 \rightarrow H_2 + SiH_3$
Ion - Radical	less probable
Radical - Radical	

Figure 2.3: Representative secondary reactions of the radicals produced from SiH_4 and H_2 by the plasma [9].

2.1.2 Hot Wire Chemical Vapour Deposition (HWCVD) method:

In this method the source gases are decomposed into film forming radicals with the help of a filament heated at high temperatures, generally in the range of 1600-2200 °C [2, 10-12]. The so formed radicals by catalytic cracking may further undergo chain gas phase reactions and get modified before getting deposited at the substrate [13-15]. As the source gas undergoes catalytic cracking reaction over the surface of heated filament this method is also known as catalytic CVD or Cat-CVD [16-17]. Like PECVD, HWCVD system also consists of high vacuum chamber equipped with gas inlet system and substrate heater assembly. The difference between two systems is that instead of rf power source, HWCVD system contains filament assembly and power supply for heating the filament Different metals such as tungsten, tantalum, molybdenum, graphite etc. can be used as filament material [18-19]. The schematic diagram of a general HWCVD system is shown in the Figure 2.4. Unlike PECVD technique, where SiH_3 is the main film forming radical, here Si and H are the primary radicals released from the filament surface [10, 20]. The number density of SiH is two orders of magnitude lower than Si [20]. At very low chamber pressure as studied by Weismann *et al.* [21], radical gas reactions are prevented, resulting poor quality films. At moderate pressure (tens of militorr), the radical - gas reactions yield other film forming radicals like SiH_3 by the following reactions [10]

$$H + SiH_4 \rightarrow H_2 + SiH_3$$

$$\begin{aligned} Si + SiH_4 \rightarrow Si_2H_4^* &\rightarrow 2SiH_2 \\ &\rightarrow SiH + SiH_3 \\ &\rightarrow Si_2H_2 + H_2 \end{aligned}$$

At much higher pressure, however, the radical- radical reaction becomes dominant and desired SiH_3 radicals are consumed before they reach the substrate.

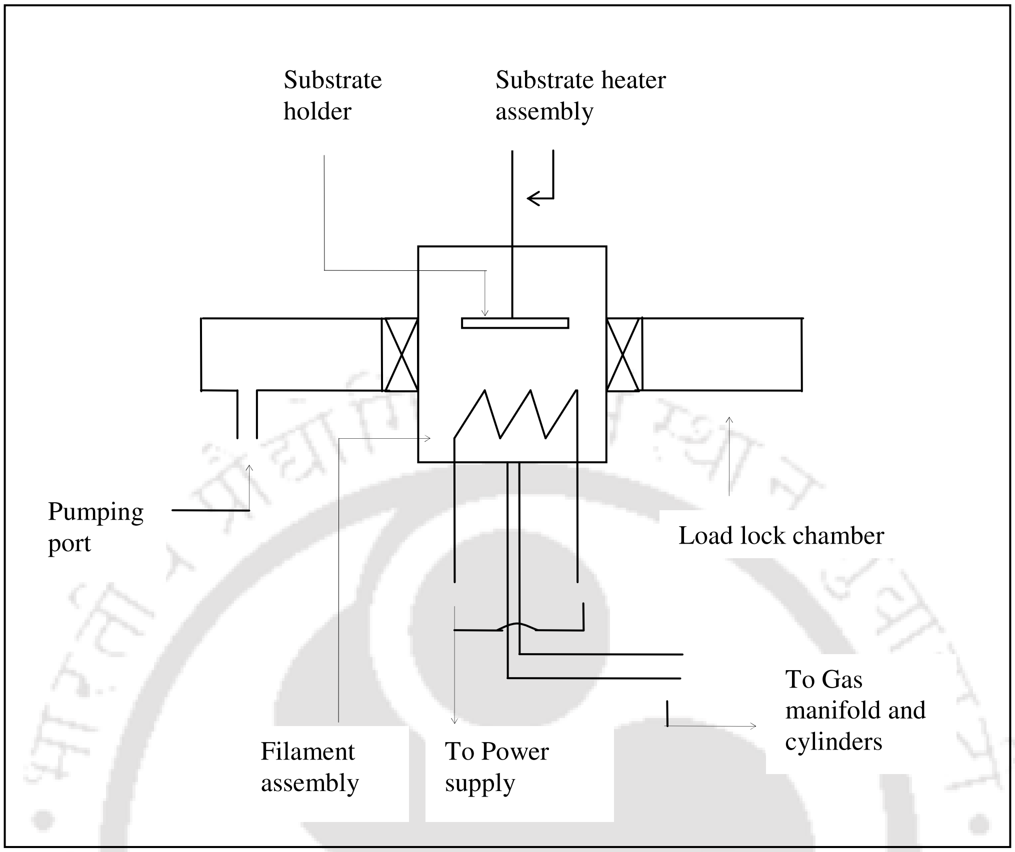

Figure 2.4: Schematic diagram of a general HWCVD system

2.2 Characterization Techniques: The films prepared by any of the above mentioned methods are characterized for different structural, optical and electrical properties using different experimental techniques described below.

2.2.1 Structural Characterizations:

2.2.1.1 X-ray diffraction: X-ray diffractometry (XRD) is used for microstructure investigations of the films. The X-ray diffractometer used in the present work is Seifert 3000 TT with CuK_α radiation of 1.5406 Å. These studies are performed on the films deposited on Corning glass, however some films deposited on (311) oriented c-Si wafer are also used additionally. The measurements are performed in 2θ thin film mode at grazing angle of incidence of 2, 3 and 4°. The films are scanned in the range of 15-60° with a step of 0.05°. In this range, crystalline silicon shows sharp peaks corresponding to (111), (220) and (311) planes near 28.3, 47.6 and 56° respectively. However in case of amorphous silicon the peak broadens and gives the characteristic amorphous hump in the XRD pattern. When the film contains nanocrystallites embedded in the amorphous matrix, peaks corresponding to crystalline silicon appear superimposed on the broad amorphous pattern. The crystallite size can be calculated from Scherrer's formula as follows

$$d_{XRD} = \frac{0.9\lambda}{BCos\theta_{hkl}} \qquad 2.1$$

Where, d_{XRD} is the crystallite size, λ is the wavelength of X-ray, B is the broadening due to crystallite size and θ_{hkl} is the peak position corresponding to the (hkl) plane. The broadening of the first peak i.e., due to (111) plane is estimated by deconvoluting the peak into three components, sharp peak because of the nanocrystalline silicon and a broad peak arising from the amorphous tissue of the film, both centered at 2θ value near 28° and a third broad peak centered at 23° due to the glass substrate.

2.2.1.2 Scanning electron microscopy: Scanning electron microscopy (Leo 1430VP) is used to study the surface morphology of the films. This instrument is also equipped with an energy dispersive spectroscopy (EDS) setup (make Oxford). SEM studies reported in this work are performed under a magnification of 10000-40000X. The films deposited on Corning glass and ITO coated substrates are used in this study. The films are coated with thin gold layer to avoid charging effect during the experiment. The morphology for amorphous silicon films ranges from smooth chonchoidal surface to clustered surface depending on the deposition conditions. EDS measurements give the quantitative constituents in the film by analyzing the characteristic X-Rays from the constituting elements.

2.2.1.3 Raman scattering spectroscopy: Raman scattering spectroscopy is a versatile tool for studying the microstructure of the films. The Raman studies reported here are performed using two different Raman spectrometers *viz.* Olympus BX41 and Witec Alpha with excitation wavelength of 514.532 nm and 514.1 nm respectively depending upon the availability of the instrument. However, for a given series of samples all the measurements are done with the same spectrometer and the same condition. These studies are done on the films deposited on both Corning as well as ITO coated glass and the spectra are recorded in the range of 100-1200 cm^{-1} and 200-1000 cm^{-1} depending upon the instrumental facility. Amorphous silicon Raman spectrum consists of broad peaks near 150 cm^{-1}, 320 cm^{-1}, 440 cm^{-1} and 480 cm^{-1} corresponding to transverse acoustic (TA), longitudinal acoustic (LA), longitudinal optic (LO) and transverse optic (TO) mode respectively, where as crystalline silicon possess sharp peak at 520 cm^{-1} corresponding to TO mode of phonon vibration [22-23]. The short range order (SRO) in the film is conventionally given by the rms deviation in the tetrahedral bond angle ($\Delta\theta_B$). Lower deviation signifies better order in the film. As the bond angle deviation increases the material becomes more disordered with a broadening of the amorphous TO peak. Tsu *et al.* [24] conjectured the broadening of TO peak at 480 cm^{-1} with $\Delta\theta_B$ as follows

$$\Gamma^2 = (32)^2 + (6.75\Delta\theta_B)^2 \qquad 2.2$$

Where, Γ is the FWHM of amorphous TO peak. This equation has been linearised by Beeman *et al.* [25] as

$$\Gamma = 15 + 6\Delta\theta_B \qquad 2.3$$

The medium range order (MRO) is given by the intensity ratio between the amorphous TA peak to the TO peak [23, 26].

$$MRO = \frac{I_{TA}}{I_{TO}} \qquad 2.4$$

In case of nanocrystallites embedded amorphous films the crystalline peak shifts from 520 cm^{-1} towards lower value due to the size limitation of the crystallites, smaller the crystallite size, larger is the shift. Hence the crystallite size can be calculated from the shift of crystalline peak from 520 cm^{-1}. He *et al.* [27] have suggested the relation between the shift and crystallite size as

$$d_{\mathrm{Raman}} = 2\pi\sqrt{\frac{B}{\Delta\omega}} \qquad 2.5$$

Where, $\Delta\omega$ is the shift of the nano crystalline Raman peak corresponding to that of c-Si and B= 2.0 cm^{-1} nm^2 [3].

For the calculation of SRO, MRO, crystallite size and crystalline fraction the Raman spectrum is deconvoluted to different components as mentioned above. It has been observed that while deconvoluting the spectra of nanocrystalline films, an extra peak has to be fitted near 495-505cm^{-1} in order to get the best fitting. This intermediate peak is assigned for bond dilation at grain boundaries by Veprek *et al.* [27], whereas Mavi *et al.* [28], He *et al.* [29] and Jana *et al.* [30] associated the component to be thermodynamically stable grains of size less than 3 nm. Tsu *et al.* [31] also observed this intermediate peak and attributed this to be objects that are intermediate in order between the continuous random network (CRN) and crystalline phase. We associate the intermediate peak to the grain boundaries and include this for the calculation of total crystalline fraction (X_c) along with the nanocrystalline peak, i.e., the total crystalline fraction is estimated as the fraction of integrated intensity under grain boundary peak and nanocrystalline peak with respect to the total intensity under all the TO peaks.

$$X_c = \frac{I_{nc} + I_{int}}{I_{nc} + I_{int} + I_{am}} \tag{2.6}$$

I_{am}, I_{int} and I_{nc} are the integrated intensities under amorphous, intermediate and nanocrystalline TO peaks respectively. The nanocrystalline and grain boundary volume fractions are hence given by the following relations respectively,

$$X_{nc} = \frac{I_{nc}}{I_{nc} + I_{int} + I_{am}} \tag{2.7}$$

$$X_{GB} = \frac{I_{int}}{I_{nc} + I_{int} + I_{am}} \tag{2.8}$$

2.2.1.4 Transmission electron microscopy: JEOL 2100 transmission electron microscope with an accelerating voltage of 200 KeV is used to study the microstructure of the films. This instrument is also equipped with an EDS spectrometer for compositional analysis. For TEM measurements, thin films of about 150-200 nm are deposited on carbon coated copper grids. At low resolution of about 400 KX, the films show different microstructures, while at high resolution of about 5-9 MX, nanocrystalline films show the presence of nanocrystallites embedded in the amorphous matrix with the lattice planes of crystalline silicon. Selected area diffraction (SAD) pattern for amorphous films show diffused rings while for nanocrystallites embedded films the SAD pattern consists of sharp rings along with bright spots on the rings. The position of the diffraction rings in the *k*-space from the center has been converted into real space to get the inter planar spacings.

2.2.1.5 Atomic force microscopy: Atomic force microscopy (Picoplus Molecular Imaging) is used to get the surface morphology of the films. The measurements are performed on the films deposited on Corning glass in acoustic mode using silicon cantilevers with force constant 2.5 N/m and resonance frequency of 80 KHz. Different scan areas *viz.* 500 nm X 500 nm, 1000 nm X 1000 nm, 2500 nm X 2500 nm and 5 μm X 5 μm are used in this study. The rms roughness is calculated using the PicoScan software for different selected areas of 100 nm X 100 nm, 200 nm X 200 nm and 500 nm X 500 nm. For each scan size a statistical average of the roughness is estimated from different scanned regions.

2.2.2 Optical Characterizations:

2.2.2.1 UV-Vis-NIR spectroscopy: UV-Vis-NIR spectroscopy in the transmission mode is performed on the films deposited on corning glass. These measurements are performed with different UV-Vis-NIR spectrometers, *viz.* Shimadzu UV 3101 PC (range 350-3000 nm) and PerkinElmer (range 350-1100 nm) depending upon the availability. The thickness and optical constant of the films are estimated from the interference fringes in the transmission spectrum following Swanepoel [32]. The thickness value thus estimated is used to calculate the deposition rate (r_d) of the films, while the band gap is calculated from the plot of $\sqrt{\alpha h\nu}$ *vs.* $h\nu$ [33-34]. These data are also used to find the energy value E04 at which the absorption coefficient becomes 10^4 cm^{-1}.

2.2.2.2 Fourier Transform Infrared spectroscopy: Fourier transform infrared spectrometer (Perkin Elmer BX) is used to record the IR transmission spectrum of the films deposited on c-Si wafer. Hydrogenated amorphous silicon absorbs the IR radiation due to different modes of bond vibration at the positions listed in the following Table 2.1[35] and also illustrated in figure 2.5.

Table 2.1: Different modes of silicon hydrogen bond vibration and the corresponding peak positions

Bonding Configuration	Vibrational Mode	Peak Position (cm^{-1})
Si-H	Wagging	630
	Stretching	2000
$Si\text{-}H_2$	Rocking	630
$Si\text{-}H_2$	Twist	820
	Wagging	850
	Scissor Bending	880
	Stretching	2100
$Si\text{-}H_3$	Wagging	630
	Symmetric Deformation	862
	Degenerate Deformation	907
	Stretching	2140

Apart from these silicon hydrogen vibrational modes, the IR transmission spectrum may show a dip at 1050 cm^{-1} if the films contain oxygen [36]. The total hydrogen content in the film can be estimated from the following relation [1]

$$N_H = A_W \int_{\omega_W} \frac{\alpha(\omega)}{\omega} d\omega \qquad 2.9$$

Where, A_W = 1.6×10^{19} cm^{-2} for absorption at 630 cm^{-1} and is a proportionality constant [37]. Equation 2.9 can be used for other absorption bands also but the 630cm^{-1} band gives best estimation. To determine the percentage of hydrogen in monohydride mode ($C_{Si\text{-}H}$), the absorption band around 2000-2100 cm^{-1} is deconvoluted into peaks near 2000, 2100 and 2140 cm^{-1} corresponding to different silicon hydrogen bonding configurations. The microstructure factor R* which gives the bonding configuration is given by

$$R^* = \frac{I_{2100} + I_{2140}}{I_{2000} + I_{2100} + I_{2140}} \qquad 2.10$$

Where, I_{2000} and I_{2100} are the integrated intensities under the deconvoluted absorption bands at 2000 and 2100 cm^{-1} respectively. In case of nanocrystalline silicon, there exists an absorption peak near 2080-2090 cm^{-1}. This peak position is attributed to Si-H mode of bond vibration at the inner surface of microvoids, at the surface of crystalline portion and at grain boundaries by several groups [36, 38].

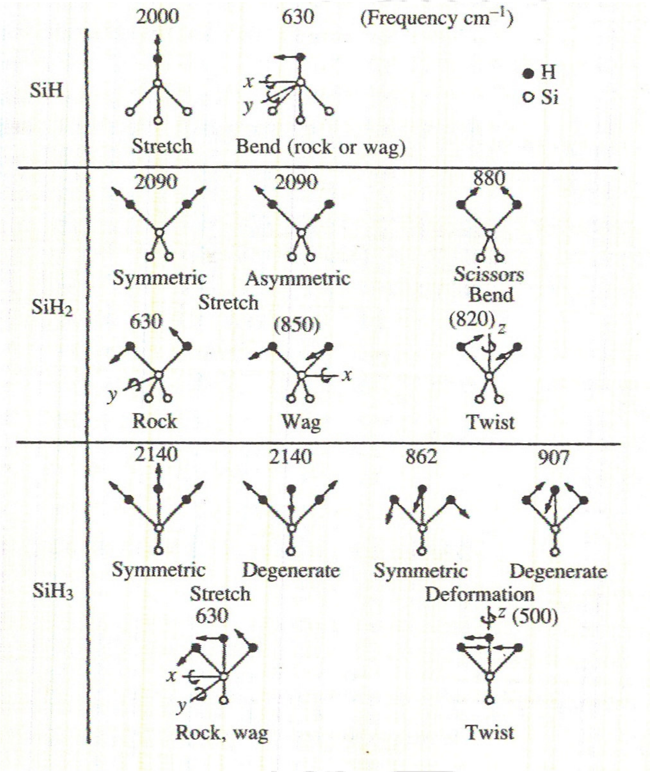

Figure 2.5: Various modes of silicon hydrogen bond vibration in a-Si:H [1].

2.2.2.3 Photoluminescence spectroscopy: Photoluminescence (PL) measurements are performed at room temperature using Aminco Bowman Series 2 Luminescence Spectrometer with different excitation wavelengths *viz.* 250 nm, 300 nm, 350 nm and 375 nm, while the luminescence is recorded in the range 500- 900 nm (2.48-1.38 eV). Films deposited on Corning glass are used for PL studies. The presence of nanocrystallites gives rise to the visible luminescence.

2.2.3 Electrical Characterizations:

2.2.3.1 Temperature dependent Dark and Photoconductivity measurements: The dark and photo conductivity of the films are measured by two probe method. The sample holder is placed inside a vacuum chamber which yields high vacuum of the order of 10^{-5} mbar. The films are heated from room temperature to 200 ^{o}C at high vacuum to measure temperature dependent conductivity. The conductivity of the films on both Corning and ITO coated glass are measured in coplanar and sandwich geometry respectively. For conductivity measurements silver paint electrodes are used. The ohmicity of the film- silver paint electrodes is checked by I-V characteristics. In case of coplanar geometry, if l is the length of electrodes, d is the separation between them, t is the thickness of the film, V is the applied voltage and I is the measured current then the conductivity will be given by the following relation,

$$\sigma = \frac{Id}{Vlt} \qquad 2.11$$

On the other hand for sandwich geometry, if a is the area of the electrode on the film and t is the thickness of the film the conductivity will be as follows,

$$\sigma = \frac{It}{Va} \qquad 2.12$$

A 100 Watt lamp is used for shining the films during photoconductivity measurements. The photoconductivity is calculated from the photocurrent using the equation no 2.11.

The dark conductivity activation energy (E_d) is determined from temperature dependent dark conductivity data using Arrhenius plot. The relation between the dark conductivity σ and activation energy E_d is given by

$$\sigma = \sigma_0 Exp[-\frac{E_d}{kT}] \qquad 2.13$$

Where, σ_0 is the dark conductivity prefactor, k is Boltzmann constant and T is the absolute temperature (in Kelvin).

2.2.3.2 Stability studies: Stability studies of the films are performed by light soaking the films in vacuum and consequent temperature dependent conductivity measurements. The light soaking is done for 12-14 hours by the same lamp used for photoconductivity measurements through a water filter to avoid heating of the film. It is observed that the degradation in both photo and dark conductivities takes place during first few hours of light soaking and then stabilizes; hence the time of light soaking is limited to 12-14 hours. After light soaking the temperature dependent conductivity measurements are carried out to study the stability.

2.2.3.3 Diffusion length measurements by SSPG method: The ambipolar carrier diffusion lengths for the films are measured by steady state photo-carrier grating (SSPG) technique [39-40]. The theory of SSPG technique is described below.

When the two coherent light beams superpose on thin photoconductive film, the resulting light intensity on the sample is modified due to interference thus creating a photograting i.e., periodically varying dark and bright region on the sample. The intensity variation depends on different factors like wavelength of light, angle between the two beams, fringe visibility factor etc. Due to the formation of photo grating on the sample there is subsequent formation of photo carrier grating (periodic variation of carriers). Because of the formation of low and high resistance region photocurrent perpendicular to the grating fringes is less than the case when there is uniform illumination. After the formation of carrier grating, the carriers start diffusing from high concentration region to low concentration region. If the diffusion length (L_d) is less than the grating period (Λ), carrier grating will persist in the sample and in the other case carrier grating will blur resulting uniform concentration. Figure 2.6a shows the formation of photo grating as well as photo carrier grating on the sample while figure 2.6b shows the diffusion of carriers for the cases when the $L_d < \Lambda$ and when $L_d > \Lambda$. Considering one beam to be less intense than the other and measuring the current across the sample when the grating is formed and when there is uniform illumination, one can find out the diffusion length from the ratio of photo current with and without grating as a function of grating period.

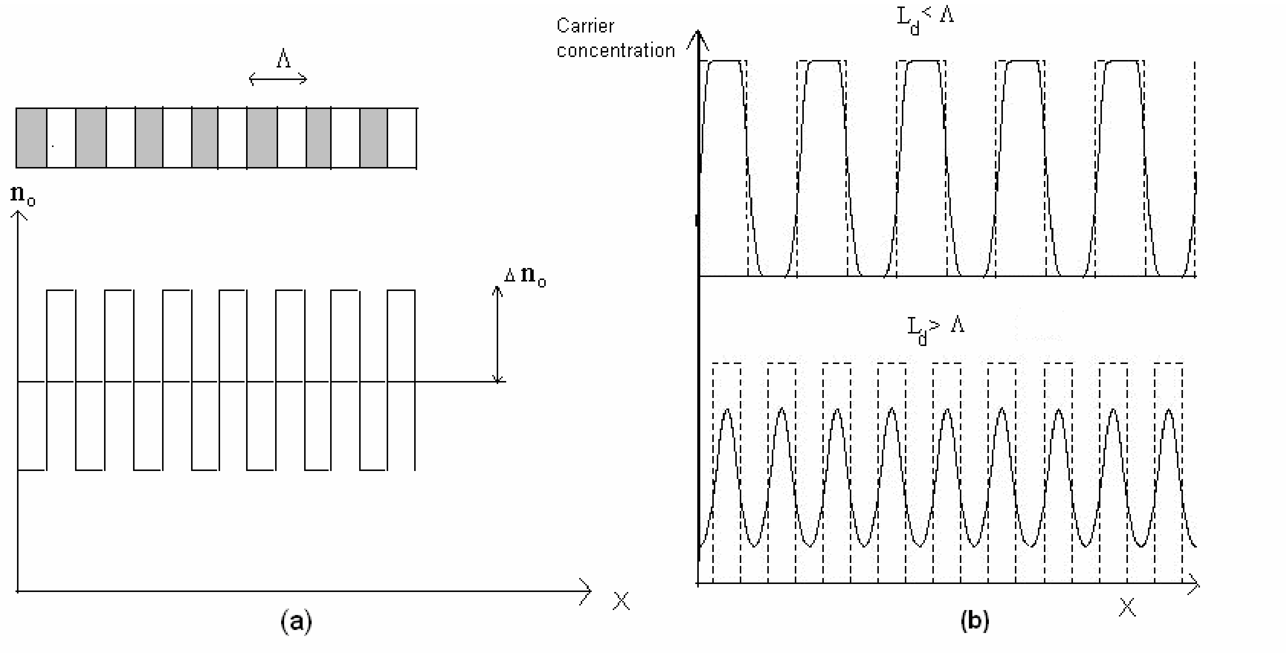

Figure 2.6: (a) photo grating (above) & photo carrier grating (below) (b) blurring of carriers for $L_d < \Lambda$ & $L_d > \Lambda$.

The modified light intensity resulting due to the formation of photo grating is given by the equation,

$$I(x) = (I_1 + I_2)\left[1 + \gamma_0 \frac{2\sqrt{I_1 I_2}}{I_1 + I_2}\cos(\frac{2\pi x}{\Lambda})\right] \qquad 2.14$$

Where $\Lambda = \lambda/(2\sin\delta/2)$ is the grating period, λ is the wavelength of light, δ is the angle between the two beams, γ_0 is fringe visibility factor.

If $I_2 < I_1$, one can solve the diffusion equation 2.14 [39-40] to get the photoconductivity as,

$$\sigma(x) = \sigma(I_1 + I_2)[1 + A\cos(\frac{2\pi x}{\Lambda})] \qquad 2.15$$

Where, $A = 2\gamma\gamma_0\alpha\frac{\sqrt{I_1 I_2}}{(I_1 + I_2)}$ and $\alpha = \frac{1}{1 + (2\pi L_d/\Lambda)^2}$

γ is the exponent of power law dependency of σ_{ph} with light intensity.

The average conductivity perpendicular to the grating fringes σ_g will be,

$$\sigma_g = \Lambda / \int_0^{\Lambda} \frac{dx}{\sigma(x)} \tag{2.16}$$

The parameter β, which is the ratio between the photocurrent in the presence and absence of grating, is related to Λ and L_d as,

$$\beta = \frac{J_{\parallel}}{J_{\perp}} = 1 - [2\phi / (1 + 4\pi^2 L_d^2 / \Lambda^2)^2] \tag{2.17}$$

Where, $\phi = \gamma\gamma_0^2$

A little bit of modification of the equation 2.17 shows that a plot between $\frac{1}{\Lambda^2}$ vs $\sqrt{\frac{2}{(1-\beta)\left(1+\gamma\frac{I_2}{I_1}\right)}}$

gives, $\text{intercept} = -\frac{1}{(2\pi L_d)^2}$ and

$\text{slope} = \frac{\gamma_0\gamma^{0.5}}{(2\pi L_d)^2}$, from where L_d and γ can be found out.

For films with sufficient dark conductivity (σ_d) equation 2.17 gets modified as [41]

$$\beta = \frac{J_{\parallel}}{J_{\perp}} = 1 - [2\phi\gamma_d / (1 + 4\pi^2 L_d^2 / \Lambda^2)^2] \tag{2.18}$$

Where, $$\gamma_d = \frac{\sigma(I_1)}{\sigma(I_1) + \sigma_d} \tag{2.19}$$

In the SSPG set up used for the present thesis work, randomly polarized monochromatic light from a laser source (HeNe 633 nm, 10 mW) is used. The grating period is varied from 500-2000 nm by changing the angle between the superposing beams.

2.3 References:

1. R.A. Street, Hydrogenated Amorphous Silicon, Cambridge University Press, (1992).

2. M. Zeman, *Advanced amorphous silicon solar cell technologies*, Thin Film Solar Cells: Fabrication, Characterization and Applications, John Wiley and Sons (2006), Ed. J. Poortmans and V. Arkhipov.
3. Y. He, C. Z. Yin, G. Cheng, L. Wang X. Liu and G.Y. Hu, J. Appl. Phys. **75** (1994) 797.
4. P. M. Gordo, M. F. F. Marques, C. L. Gil, A. P. D. Lima, G. Lavareda, C. N. D. Carvalho, A. Amaral and Z. Kajcsos, Radiat. Phys. Chem. **76** (2007) 220.
5. J. H. Yoon, J. Non-Cryst. Solids **353** (2007) 4223.
6. S. Alexandrova, P. Danesh and I. A. Maslyanitsyn, Vacuum **69** (2003) 391.
7. P. P. Ray, N. D. Gupta, P. Chaudhuri, D. L. Williamson, S. Vignoli and C. Longeaud, J. Non-Cryst. Solids **299-302** (2002) 123.
8. P. Kumar, F. Zhu and A. Madan, Int. J. Hydrogen Energy **33** (2008) 3938.
9. A. Matsuda, J. Non-Cryst. Solids **338-340** (2004) 1.
10. A. Gallagher, Thin Solid Films **395** (2001) 25.
11. W. Zheng and A. Gallagher, Thin Solid Films **516** (2008) 929.
12. C. Horbach, W. Beyer and H. Wagner, J. Non-Cryst. Solids **137-138** (1991) 661.
13. S. R. Jadkar, J. V. Sali, M. G. Takwale, D. V. Musale and S. T. Kshirsagar, Thin Solid Films **395** (2001) 206.
14. S. Gupta, G. Morell and B. R. Weiner, J. Non-Cryst. Solids **343** (2004) 131 and references therein.
15. M. Heintze, R. Zedlitz, H. N. Wanka and M. B. Schubert, J. Appl. Phys. **79** (1996) 2699.
16. H. Matsumura and H. Tachibana, Appl. Phys. Lett. **47** (1985) 833.
17. H. Matsumura, Jpn. J. Appl. Phys. **25** (1986) L949.
18. H. L. Duan and S. F. Bent, Thin Solid Films **485** (2005) 126.
19. K. Brühne, M. B. Schubert, C. Köhler and J. H. Werner, Thin Solid Films **395** (2001) 163.
20. Y. Nozaki, K. Kongo, T. Miyazaki, M. Kitazoe, K. Horii, H. Umemoto, A. Matsuda and H. Matsumura, J. Appl. Phys. **88** (2000) 5437.
21. H. Wiesmann, A. K. Ghosh, T. McMahon and M. Strongin, J. Appl. Phys. **50** (1979) 3752.
22. M. Stutzmann, *Amorphous Semiconductors,* Handbook of Semiconductors, North Holland Vol **3a** (1994), Ed. S. Mahajan.

23. G. Morell, R. S. Katiyar, S. Z. Weisz, H. Jia, J. Shinar and I. Balberg, J. Appl. Phys. **78** (1995) 5120.
24. R. Tsu, J. G. Hernandez and F. H.Pollak, J. Non-Cryst. Solids **66** (1984) 109.
25. D. Beeman, R.Tsu and M. F. Thorpe, Phys. Rev. B **32** (1985) 874.
26. M. Ito and M. Kondo, Jpn. J. Appl. Phys. **45** (2006) L230.
27. S. Veprek, F. A. Sarott and Z. Iqbal, Phys Rev. **B 36** (87) 3344.
28. H. S. Mavi, A. K. Shukla, S. C. Abbi and K. P. Jain, J. Appl. Phys. **66** (1989) 5322.
29. Y. He, Y. Wei, G. Zheng, M. Yu and M. Liu, J. Appl. Phys. **82** (1997) 3408.
30. M. Jana, D. Das and A. K. Barua, J. Appl. Phys. **91** (2002) 5442.
31. D. V. Tsu, B. S. Chao, S. R. Ovshinsky, S. Guha and J. Yang, Appl. Phys. Lett. **71** (1997) 1317.
32. R. Swanepoel, J. Phys. E: Sci. Instrum. **16** (1983) 1214.
33. D. Das and K. Bhattacharya, J. Appl. Phys. **100** (2006) 103701 and references there in.
34. C. Song, G. R. Chen, J. Xu, T. Wang, H. C. Sun, Y. Liu, W. Li, Z. Y. Ma, L. Xu, X. F. Huang and K. J. Chen, J. Appl. Phys. **105** (2009) 054901.
35. G. Lucovsky, R. J. Nemanich and J. C. Knights, Phys. Rev. B **19** (1979) 2064.
36. D. Han, K. Wang, J. M. Owens, L. Gedvilas, B. Nelson, H. Habuchi and M. Tanaka, J. Appl. Phys. **93** (2003) 3776.
37. C. J. Fang, K. J. Gruntz, L. Ley, M. Cardona, F. J. Demond, G. Müller and S. Kalbitzer, J. Non-Cryst. Solids **35-36** (1980) 255.
38. T. Itoh, K. Yamamoto, K. Ushikoshi, S. Nonomura and S. Nitta, J. Non-Cryst. Solids **266-269** (2000) 201.
39. D. Ritter, E. Zeldov and K. Weiser, Appl. Phys. Lett. **49** (1986) 791.
40. I. Balberg, A. E. Delahoy and H. A. Weakliem, Appl. Phys. Lett. **53** (1988) 992.
41. E. Sauvain and J. H. Chen, J. Appl. Phys. **75** (1994) 5191.

Chapter -3

Fabrication of Experimental Set ups

Chapter 3

Fabrication of Experimental Set ups

The fabrication of experimental set ups for preparation as well as for the study of amorphous and nanocrystalline silicon thin films are an integral part of this thesis work. Details of these set ups developed in our laboratory for this purpose are as explained below.

3.1 HWCVD System Fabrication:

We have indigenously fabricated an HWCVD system in our laboratory for the preparation of Si:H films. The system consists of two stainless steel (SS) chambers separated by a gate valve one of which is the process chamber and the other is the load lock chamber. Other side of the process chamber is connected to a corrosion free turbo molecular pump (TMP) (make Pfieffer, model TPU 261 PC) with a gate valve between them. The TMP is backed by a rotary pump from Pfieffer. The load lock chamber is evacuated with the help of another rotary pump (Vacuum Techniques, model VT-2015). Cold water is supplied to the TMP from a closed cycle chiller. The gate valve separating the TMP and the process chamber is also water cooled to protect the TMP from hot gases. Four fans are attached to the outer wall of the process chamber to keep it cool during deposition. The electrical feed throughs for the filament assembly are also water cooled. Different gauges used for the pressure measurements are Capacitance manometer (Pfieffer, model D-35614 Asslar), Pirani gauge (Vacuum Techniques, model PR-2) and Penning gauge (Vacuum Techniques, model PN-4). Figures 3.1and 3.2 depict top and side view of the system while figure 3.3 depicts the schematic diagram of the process chamber respectively. The process chamber is a cylindrical one with inner diameter 25 cm and height 33 cm. There are three gas inlets to the system. Two annular gas inlets with a number of holes (diameter 0.3 cm) on them are placed above the filament assembly while the third vertical inlet is placed below the filament. The inner diameter of gas inlet pipes used is 4cm, while the inner diameter of the annular portion is about 11 cm. This multi-inlet facility is designed to enable different combinations of gas flow schemes and to study the effect of these on microstructure and other electronic properties of the films. The filament as well as the gas inlets are surrounded by an SS gas confinement cup which facilitates the efficient dissociation of the gases. We have designed two different types of filament assembly; one is horizontal and the other one vertical, either one of them can be used at a time. In the horizontal assembly, filament of total length 30 cm can be put in a zigzag way while in the vertical assembly, coils put in the form of helix can be used; the total length of the filament may vary depending on the helix height and diameter. The filament assembly is powered by a variac through electrical feed through placed at the bottom plate of the process chamber.

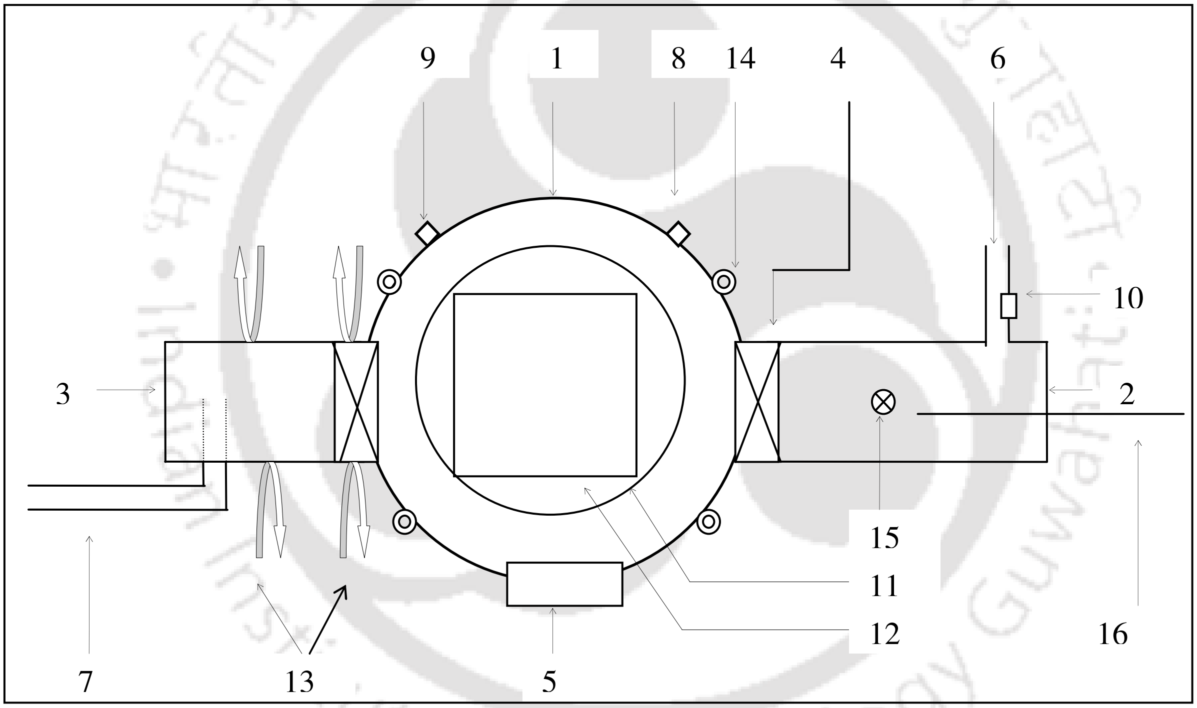

Figure 3.1: Top view of the HWCVD system fabricated in the laboratory. Arabic numbers are used to denote the components as: 1. process chamber, 2. load lock chamber, 3. turbo molecular pump, 4. gate valve, 5. view port, 6. connection of load lock to rotary pump, 7. connection of turbo molecular pump to rotary pump, 8. capacitance manometer, 9. penning gauge, 10. pirani gauge, 11.confinement cup, 12 substrate heater assembly and filament assembly , 13. chilled water line, 14. cooling fan, 15. vent, 16. substrate transferring shaft.

The substrate holder and the heater assembly are connected to the top flange and can be moved up and down to vary the filament to substrate distance (2-6 cm). Substrate holder is made up of copper with dimension of 10 cm x 10 cm whereas substrates are placed within a diameter of 8 cm from the center. The substrate is heated by a PID controlled heater equipped with a K-type thermocouple. A double wavelength pyrometer from IRCON (model MR-OR05-240) with working range of 900-2400^{o}C is used for the measurement of filament temperature.

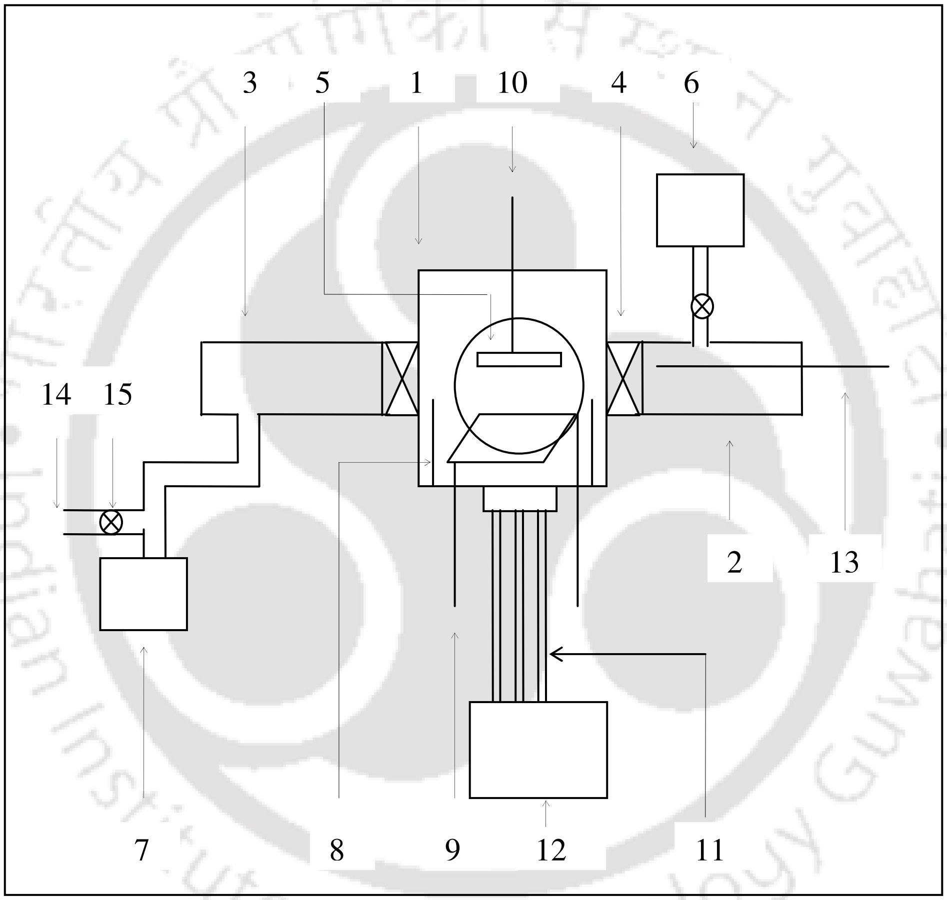

Figure 3.2: Side view of the HWCVD system. Arabic numbers are used to denote the components as: 1. process chamber, 2. load lock chamber, 3. turbo molecular pump, 4. gate valve, 5. view port, 6. rotary pump, 7. rotary pump backing turbo, 8. confinement cup, 9. filament assembly with feed through, 10. substrate heater assembly, 11.gas pipes, 12. gas manifold, 13.substrate transferring shaft, 14. to purge line of the gas manifold, 15.valve.

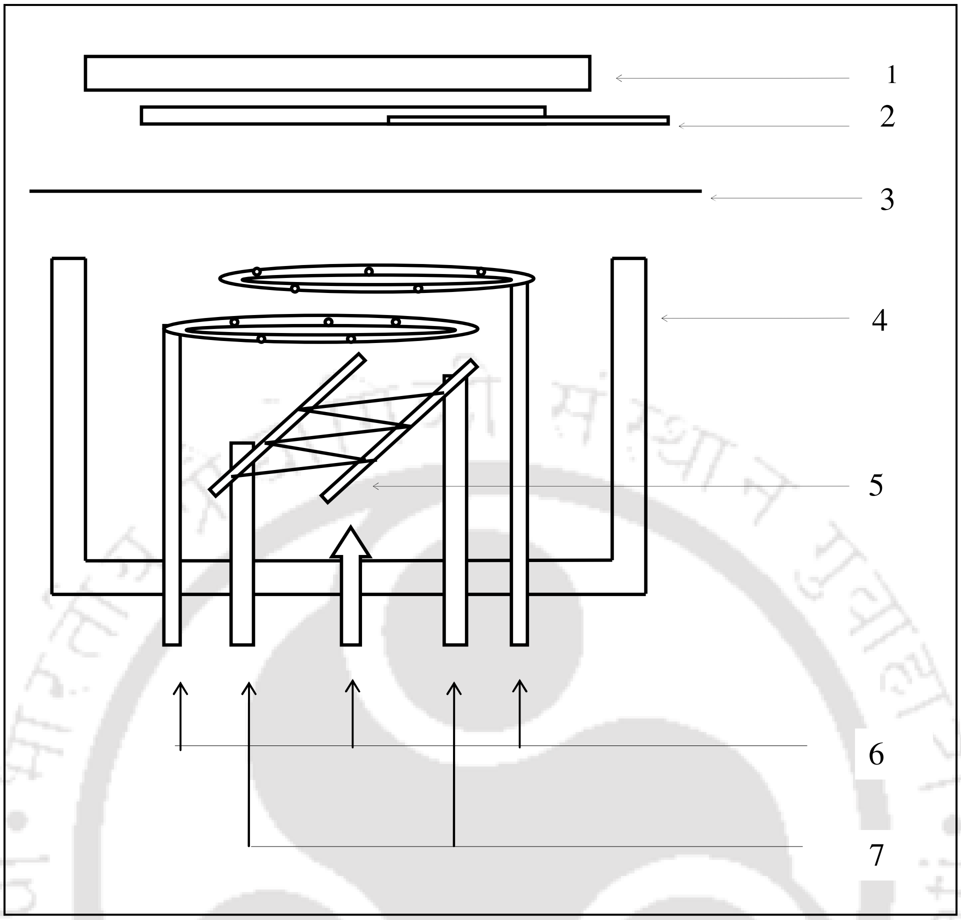

Figure 3.3: Schematic of HWCVD process chamber. Arabic numbers are used to denote the components as: 1. heater, 2. substrate holder with thermocouple, 3. shutter, 4. confinement cup, 5 filament, 6. gas inlet, 7. electrical feed through

The gas manifold is designed in such a way that the gases (SiH_4, H_2, Ar, N_2 and gases to be used in future) can be passed into the chamber through any inlet (figure 3.4). This is fabricated in house by using valves, seamless SS pipes (inner diameter ~ 4 cm) as well as connections from Swagelok and mass flow controllers from Seven Star. Semiconductor grade hydrogen diluted silane (10 % silane in hydrogen), pure silane and hydrogen, all brought from Matheson Inc., argon and nitrogen (99.99 % purity, brought locally from M/s Assam air) are used for deposition of films and purging of the system. Figure 3.5a shows the whole setup while figure 3.5b shows the chamber during deposition

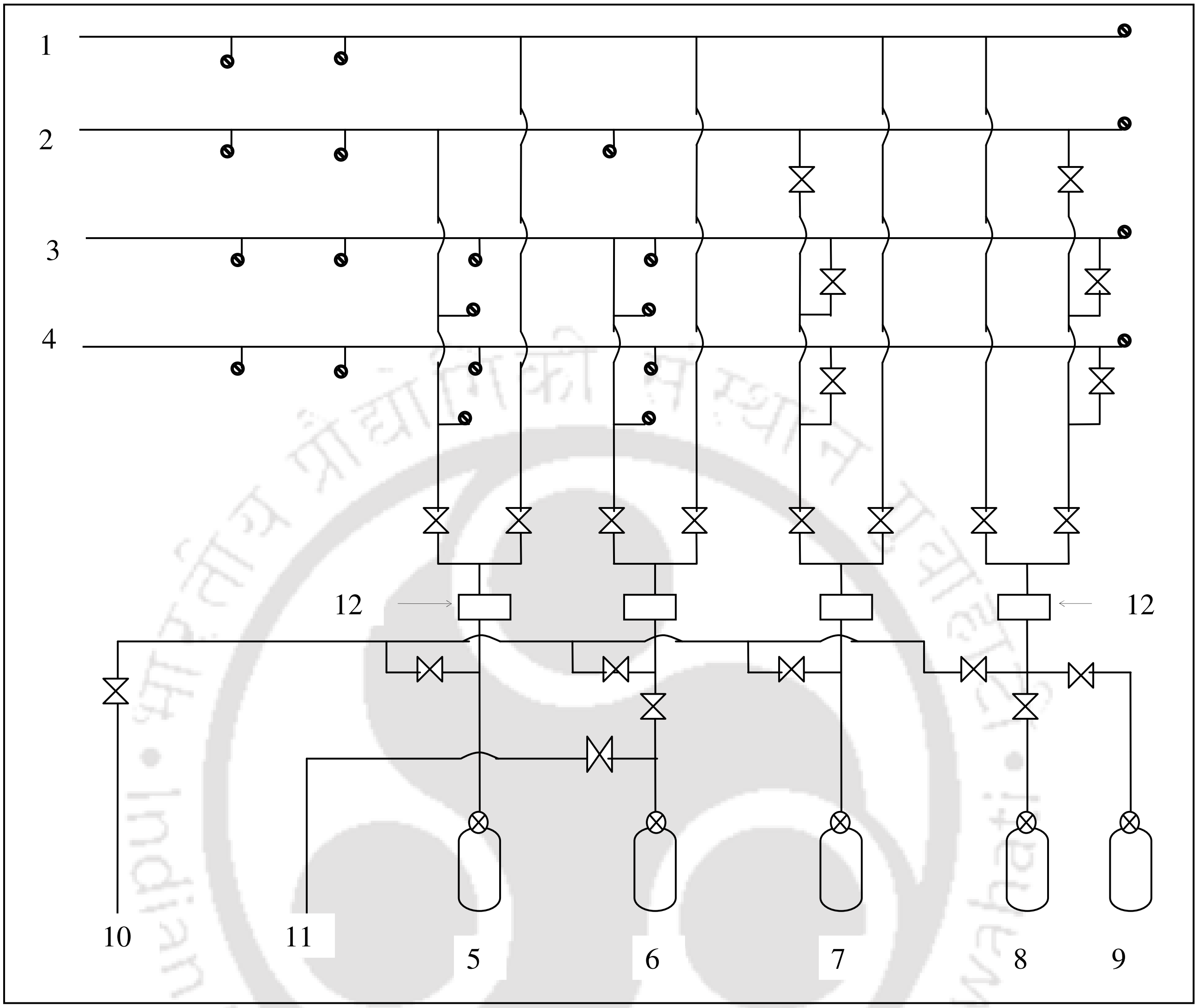

Figure 3.4: Schematic of the gas manifold designed and fabricated in house. Arabic numbers are used to denote the components as: 1. gas inlet to PECVD, 2-4. gas inlet to HWCVD, 5. argon cylinder, 6. nitrogen cylinder, 7. hydrogen cylinder, 8-9. silane cylinder, 10.purge line, 11. to exhaust, 12 valves


(a) (b)

Figure 3.5: (a) The HWCVD setup fabricated in the laboratory (b) deposition chamber during film preparation

3.2 Conductivity measurement set up:

Conductivity measurement gives the idea about the usefulness of the material in the solar cells and other opto-electronic devices. Lower dark conductivity and higher photoconductivity i.e. high photo to dark current ratio is appreciated for solar cells and radiation detectors. Less degradation of the conductivity after prolonged exposure to light is much needed for stable devices.

A diffusion pump based temperature dependent conductivity (σ-T) system is fabricated in house for σ-T and stability studies. This is a two probe set up with quite simple circuit and is shown in figure 3.6. The sample is mounted on an SS sample holder (diameter 9 cm) which can be heated for temperature dependent studies. A thin mica sheet is placed between the sample and the sample holder so that the sample is electrically insulated from the holder but remains in contact thermally. The sample holder is kept inside a vacuum chamber connected to a diffusion pump which yields a vacuum ~ 10^{-6} mbar. The diameter of the chamber is 15 cm while its height is 20 cm. A sealed resistive heater is placed inside the sample holder which can heat the holder to about 300 ^{o}C. Electrical connections for voltage, current and temperature sensor are provided through highly insulated feed throughs connected to a side flange. The upper flange has a glass window (diameter ~ 4cm) which allows light to enter into the chamber for the measurement of photoconductivity and also used for light soaking of the films. The light source is connected to a constant power supply. During dark conductivity measurement this window is blocked. Phosphor bronze probes are used for supplying voltage and for measuring current. The current required for heating the sample is supplied from a constant current source from Scientific (model PSD 3003), with a fuse of 3 Amp to protect the heater from spikes of current. The temperature is measured with the help of a platinum resistance thermometer (PT-100) and a 6 ½ digit multimeter (Agilent, model 34401A). For measuring the conductivity, voltage is supplied from a computer controlled Hioki voltage source (model 7020) while current is measured by Keithley electrometer (model 6514). The working range of the electrometer is pA to 2 mA, when current exceeds the range for nanocrystallites embedded films at high temperature, a general 4 ½ digit DMM is used. The electrical connections are made with highly insulating BNC connectors. Figure 3.7 shows the schematic of the σ-T set up.

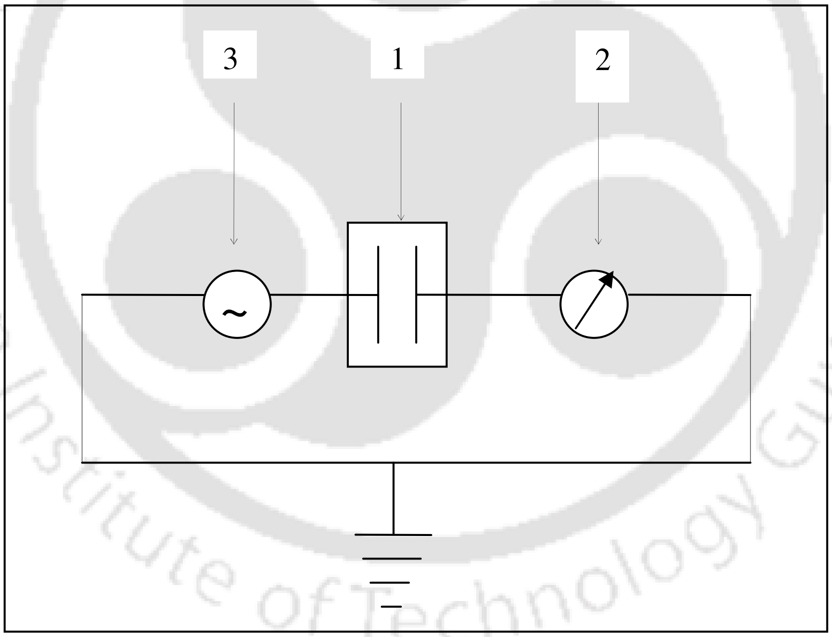

Figure 3.6: Circuit diagram of the two probe conductivity measurement set up. Arabic numbers are used to denote the components as: 1. sample, 2. electrometer, 3. voltage source

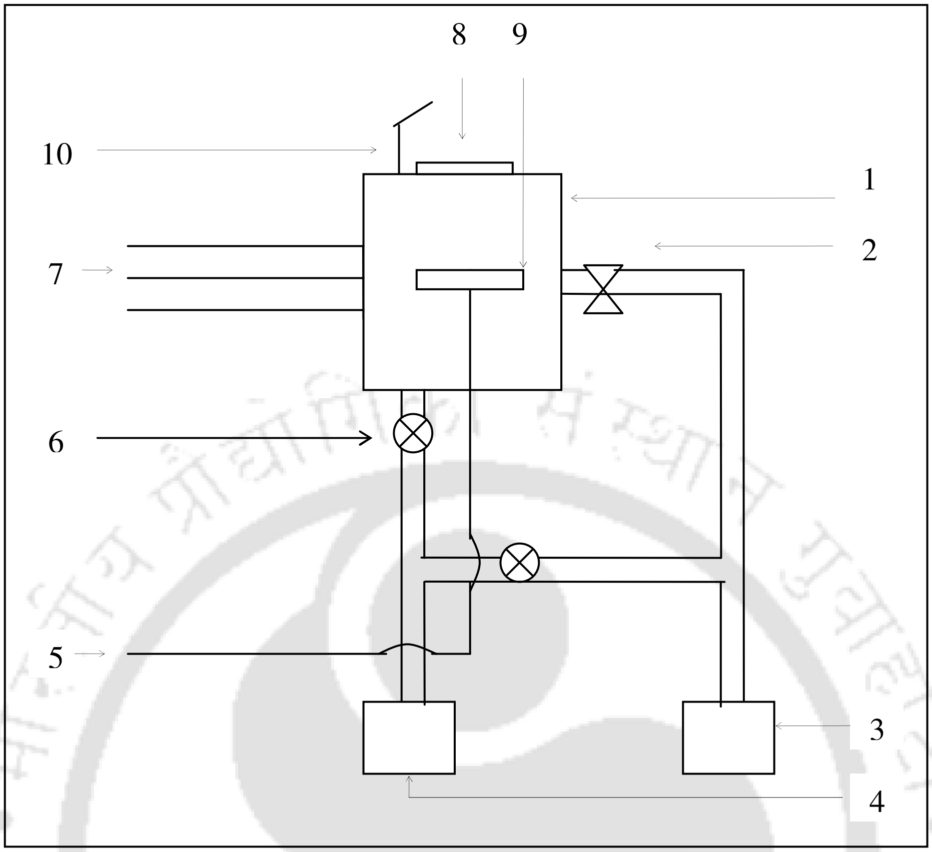

Figure 3.7: Schematic diagram of the conductivity system. Arabic numbers are used to denote the components as: 1. measurement chamber, 2. baffle valve, 3. diffusion pump, 4. rotary pump, 5. supply to heater, 6. gate valve, 7. Electrical feed throughs for voltage, current and thermometer, 8. glass window, 9. heater cum substrate holder, 10. light source.

3.3 Steady State Photo Carrier Grating (SSPG) set up:

The prior knowledge of carrier diffusion length (L_d) in a semiconductor is very necessary in the fabrication of devices like solar cell, thin film transistor etc. for the optimization of device thickness. Especially for hydrogenated amorphous silicon (a-Si:H) and alloys like amorphous silicon germanium (a-SiGe:H), the value of diffusion length is a very good indicator of the material quality for solar cell application. Therefore a number of techniques have been developed for the measurement of L_d; Haynes-Shockley method, surface photo voltage method (SPV) being some of them. Another important method, which is relatively simple, is the steady state photo carrier grating (SSPG) method originally developed by Ritter, Zeldov and Weiser [1]. This is a self consistent and self sufficient [2] method and at the same time it is very simple and versatile for routine characterization of L_d. The detailed theory of SSPG method is explained in section 2.2.3.3.

Figure 3.8 shows the schematic diagram of SSPG set up for the measurement of L_d. The randomly polarized monochromatic light from a laser source (HeNe 633 nm, 10 mwatt) is splitted into two coherent beams (I_1 and I_2) with the help of a beam splitter, which are then reflected by two mirrors in Mczhender geometry and allowed to superpose on the film. The photo grating is created by using two polarizers (P_1 & P_2) in the path of the beams which are in same state of polarization, whereas for uniform illumination, instead of P_2 another polarizer P_3 (cross polarized) is used. We have used one neutral density filter to reduce the intensity of the beam I_2 to 10% of the other beam. The weaker beam is chopped and the change in photoconductivity due to diffusion of carriers is monitored using an optical chopper and a lock-in amplifier (model SR 830 DSP). The signal is fed to the lock in amplifier (LA) across a load resistance. Hence the signal monitored by the LA will be proportional to $\sigma_g - \sigma(I_1)$ when there is grating formation and $\sigma(I_1+I_2) - \sigma(I_1)$ when there is no grating. Thus the ratio of photocurrent β in the presence and absence of grating will be

$$\beta = \frac{\sigma_g - \sigma(I_1)}{\sigma(I_1 + I_2) - \sigma(I_1)} \qquad 3.1$$

In equation 3.1, σ_g is the average conductivity when the grating is present while $\sigma(I_1+I_2)$ and $\sigma(I_1)$ represents the conductivity due to total intensity $(I_1 + I_2)$ in the absence of grating and I_1 respectively. This experimental parameter β is measured as a function of grating period (determined by wavelength of the light and angle between the beams, here solely by the angle) by varying the angle between the beams. This is done by rotating the mirrors. For easy and precise movement of the mirrors they are mounted on gimbal mounts, to enable the rotation of the mirrors in x, y and z directions. The opto-mechanical components used in this set up are from Holmarc while mirrors and beam splitters are from Melles Griot. The intensities during the experiment are monitored by a standard Si photo-diode.

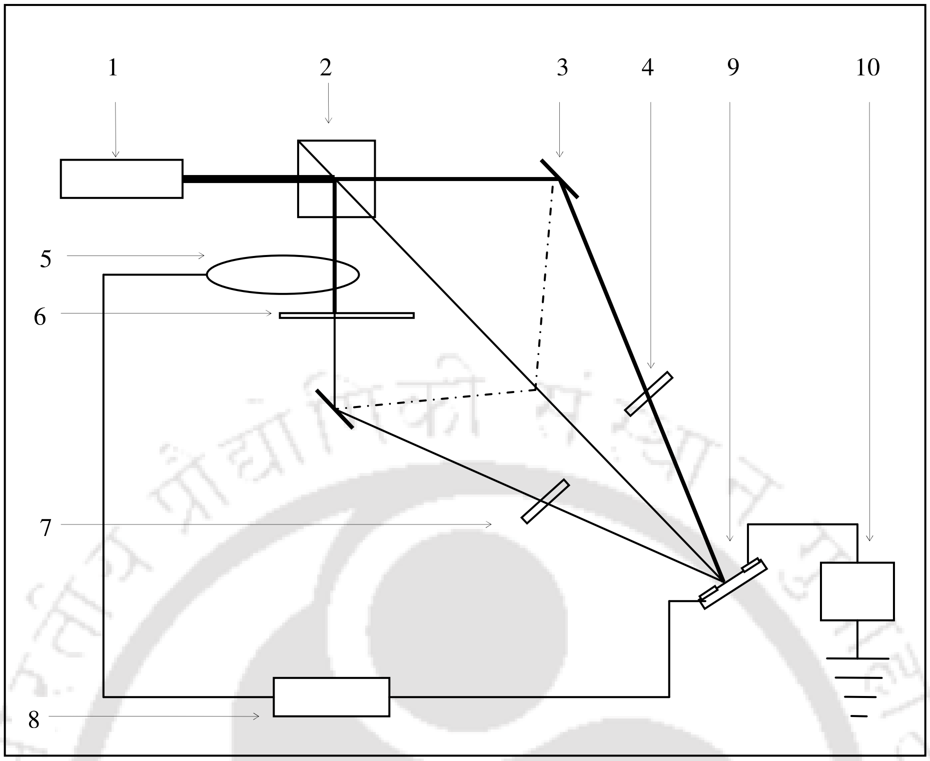

Figure 3.8: Schematic diagram of SSPG set up. Arabic numbers are used to denote the components as: 1. HeNe laser, 2. beam splitter, 3. mirror, 4. polarizer P_1, 5. chopper, 6. ND filter, 7. polarizer P_2/P_3, 8. lock in amplifier, 9. sample, 10.voltage source.

While performing the SSPG measurements a few points are needed to be taken care of. In the first place, because of the difference in the transmittance of the polarizers', intensity of weak beam may be different depending on whether it is crossed polarized or same polarized. So it is very important to ensure that the intensity of the weak beam is same in both the cases. This ensures that the difference in photocurrent is coming from the actual formation of the grating and is not an artifact. Secondly, one beam should be much weak compared to the other since the theory is valid for that approximation only; otherwise large modulation of carrier concentration will cause band bending, which makes the transport drift limited instead of diffusion limited. Another important point is that the bias voltage should be sufficiently small so that the conductivity comes from diffusion of carriers only and not from the drift. We put the polarizers behind the mirrors to avoid the mirror-induced polarization. The load resistance has also to be optimized so as to get good signal and at the same time it should not modify the current in the circuit.

3.4 References:

1. D. Ritter, E. Zeldov and K. Weiser, Appl. Phys. Lett. **49** (1986) 791.
2. I. Balberg, A. E. Delahoy and H. A. Weakliem, Appl. Phys. Lett. **53** (1988) 992.

Chapter -4

Argon dilution of PECVD films

Chapter 4

Argon dilution of PECVD films

Plasma enhanced chemical vapor deposition (PECVD) is most extensively studied and widely used technique for the preparation of silicon thin films and alloys of silicon [1-2]. Though PECVD technique has many variants such as DC PECVD, RF PECVD, VHF PECVD, Microwave PECVD etc., RF PECVD with frequency 13.56 MHz has been standardized for the preparation of thin films of silicon as well as alloys of silicon and used for industrial production of silicon based thin film devices [3-8]. Though RF PECVD method yields device quality films and the uniformity over large area low deposition rate is the main hurdles for the fabrication of cost effective devices. Especially, for preparation of micro/nanocrystalline silicon by this method, where heavy hydrogen dilution is needed, the deposition rate becomes very low, typically <1 Å/Sec [3-4, 9-10]. The deposition rate can be enhanced by the addition of inert gases like helium and argon into the precursor gas mixture [11-13]. However earlier research on noble gas dilution of silane showed that the films developed columnar growth [11]. Due to the columnar growth and resulting formation of voids and rough surfaces, the argon dilution did not gain much attention in earlier days. However, in recent years there is a renewed interest in argon dilution [9, 14-21]. Several groups are working on argon dilution as this yields high deposition rate. They are trying to improve the material quality as well as to understand the role of argon dilution in film growth. Another important issue in PECVD prepared a-Si:H films is the light induced degradation commonly known as Staebler Wronski effect [22]. Though this light induced degradation is known since 1979, and lots of works have been done, the full understanding of this phenomemon and complete eradication of it, have not been achieved yet and still remain a major bottleneck in making stable photovoltaic and other devices. As hydrogen dilution gives better order and hence better quality of the films with less SW effect and argon dilution gives higher deposition rate, we combined both hydrogen and argon dilution of silane to prepare device quality films at moderately good deposition rate.

4.1 Experimental Details:

The films are deposited on Corning 7059 glass substrates using hydrogen diluted silane (5% silane in hydrogen) and argon in a load lock based PECVD chamber. The base pressure of the chamber has been better than 10^{-7} mbar. Prior to deposition, the argon flow rate (AFR) is fixed so that a constant pressure of 0.47 mbar is achieved in the chamber without any silane flow. Silane flow rate (SFR) is then varied from 6.4-40 SCCM to get different argon dilution ratio (R). The substrate temperature (T_s) and rf power are kept constant for all the films at 300^oC and 30 mWatt cm^{-2} respectively. During deposition the process pressure (PP) in the chamber is throttled to 0.92 mbar without disturbing the argon and silane flow rate. The deposition parameters are listed in table 4.1.

Table 4.1: Deposition parameters for the films reported in the present chapter. Here, T_s PP, RFP, SFR, Act. SFR, AFR and R correspond to substrate temperature, process pressure, RF power, silane flow rate (5 % silane in hydrogen), actual SFR, Argon flow rate and argon dilution ratio respectively.

Sample No	T_s (^oC)	PP (mbar)	RFP (mWatt cm^{-2})	SFR (SCCM)	Act. SFR (SCCM)	AFR (SCCM)	R
PE_1	300	0.92	30	40	2	202.8	100
PE_2				20	1		200
PE_3				10	0.5		400
PE_4				6.4	0.32		630

The films are structurally characterized by XRD and SEM using Siefert XRD 3003 TT and Leo 1430 VP scanning electron microscope respectively. XRD measurements are done in 2θ mode (scanning range $15-60^o$) at grazing angle of incidence 3^o. Raman scattering experiments are done using Olympus BX41 Raman spectrometer with excitation wavelength of 514.532 nm. Transmission measurements are performed in the range of 400-1100 nm using PerkinElmer UV-Vis-NIR spectrometer. The photoluminescence studies are performed at room temperature using Aminco Bowman Series 2 Luminescence Spectrometer with different excitation wavelengths *viz.* 250 nm, 300 nm, 350 nm and 375 nm, while the luminescence is recorded in the range 450- 900 nm. Transport studies are performed by temperature dependent dark and photo conductivity measurements, stability studies and ambipolar diffusion length measurements. The conductivity measurements are performed in the temperature range of room temperature to 200^0C in vacuum better than 10^{-5} mbar. A 100 W halogen lamp is used for photoconductivity measurements and also for light soaking in vacuum through an optical window. The carrier diffusion lengths (L_d) is measured by Steady State Photocarrier Grating (SSPG) technique [23] using wavelength of 633 nm from a HeNe laser source. More details of the experimental procedures are given in Chapter 2.

4.2 Results and Discussions:

4.2.1 X-ray diffraction studies:

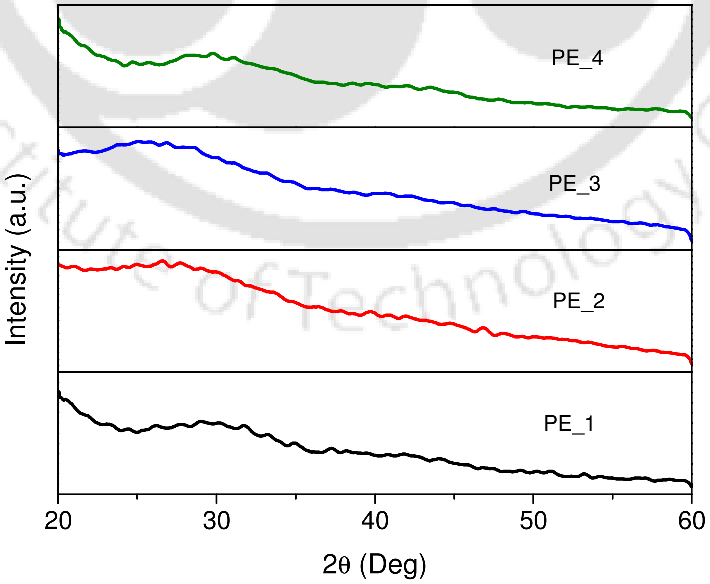

Figure 4.1: XRD patterns of the films deposited by using combined hydrogen and argon dilution.

Figure 4.1 shows the XRD pattern for the films reported in the present chapter. All the films show amorphous nature with a broad hump around 28^o. No peaks are observed corresponding to the formation of nanocrystallites.

4.2.2 Raman scattering spectroscopy:

Figure 4.2 shows the Raman scattering spectra for the films in the scanning range of 200-1000 cm^{-1}. It is observed that though the films show amorphous nature in XRD studies, Raman studies show the formation of nanocrystallites in the amorphous matrix. It is observed from the Raman spectra that the film with the lowest argon dilution (R= 100) is almost amorphous with the broad hump centered about 480 cm^{-1}. This spectrum also contains a very small peak near 520 cm^{-1} corresponding to nanocrystallites superimposed on the broad amorphous hump. This indicates that there exist small crystallites in the film in a very less amount though the film is mostly amorphous. As the dilution is further increased, the film crystallinity increases at the expense of the amorphous tissues up to dilution ratio 400. However, further increase in argon dilution reduces the crystallinity to some extent as can be seen from figure 4.2.

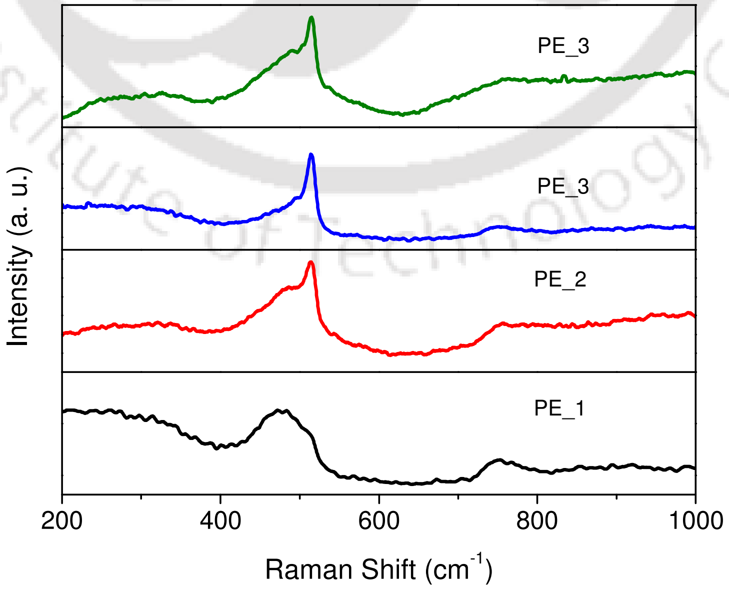

Figure 4.2: Raman scattering spectra for the samples prepared using combined argon and hydrogen dilution.

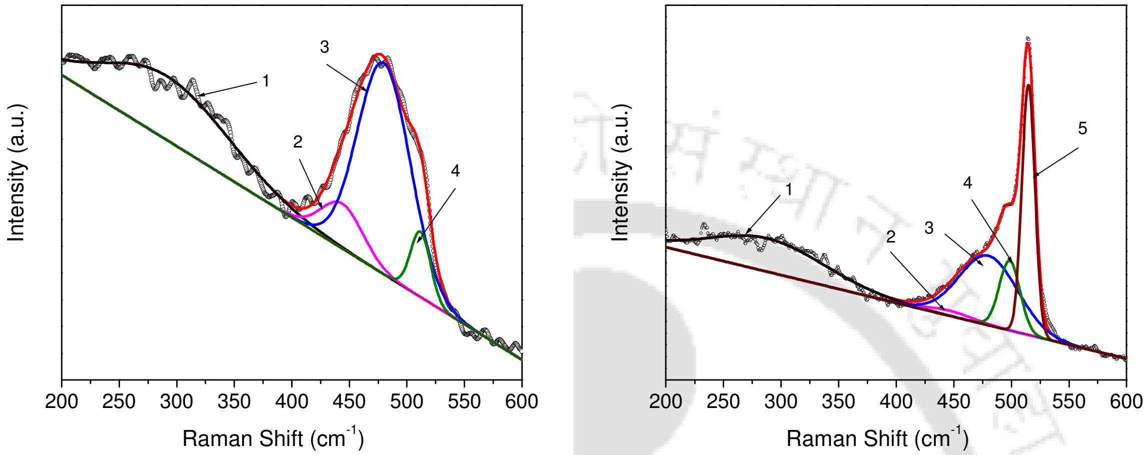

(a) (b)

Figure 4.3: Deconvoluted Raman spectra for films (a) PE_1 (amorphous) and (b) PE_3 (nanocrystallites embedded amorphous). For the film PE_1, the deconvoluted peaks 1, 2 and 3 correspond to amorphous LA, LO and TO mode while 4 correspond to nanocrystalline peak respectively. In case of the film PE_3, peaks 4 and 5 correspond to grain boundary and nanocrystalline TO peak, while others are like the film PE_1.

For the quantitative estimation of different parameters like total crystalline fraction (X_c), crystallite size (d_R), rms deviation of tetrahedral angle ($\Delta\theta_B$) etc., the Raman spectra are deconvoluted in the range 200-600 cm^{-1} into different components as mentioned in chapter 2. The TA mode at about 150 cm^{-1} could not be recorded due to instrumental limitation. Figures 4.3a and 4.3b show deconvoluted spectra for two different films, PE_1 and PE_3 (amorphous and nanocrystallites embedded amorphous). The parameters thus estimated are mentioned in the table 4.2. It is observed that as the argon dilution increases, the crystallinity fraction (X_c) in the films increases except for the highest dilution film (PE_4) where X_c is lower than the previous film (PE_3) of the series. It is further observed that with increase in argon dilution the size of the nano crystallites (d_R) increases along with a decrease in the grain boundary fraction (X_{GB}), which could be attributed to the improvement of MRO. The rms bond angle deviations ($\Delta\theta_B$) for the films up to R = 400 are below 8^o suggesting that the films are of device quality [24-25], however the film with highest dilution (R=600) possess little high $\Delta\theta_B$ of ~11. 6^o. At the highest dilution, the depletion of silane and increased concentration of argon may lead to defective structure, thus reducing short range order (SRO) and hence increasing $\Delta\theta_B$ which could be the reason for lesser crystallinity of the film with highest dilution compared to the previous one. Another possible reason for reduced crystallinity of the film with highest argon dilution could be the less thickness of that film compared to the other films. As the crystallinity develops with film thickness along the growth direction this less thickness film is expected to be less crystalline with isolated nanocrystalline nuclides in the amorphous matrix. The observed mismatch of the XRD and Raman data may be occurring due to two reasons, first, because of the small crystallite size, nanocrystallites are difficult to be detected in XRD studies and second, the crystallites plans are not parallel to the surface of the films.

Table 4.2: Total crystallinity fraction (X_c), grain boundary fractions (X_{GB}), nanocrystalline fraction (X_{nc}), Raman crystallite size (d_R) and rms deviation of bond angle ($\Delta\theta_B$) from the tetrahedral configuration.

Sample No	X_c (%)	X_{GB} (%)	X_{nc} (%)	d_R (nm)	$\Delta\theta$ (Deg)
1	1.04	0	1.04	3.12	6.49
2	49.29	35.59	13.69	3.62	7.46
3	53.83	16.49	37.34	3.88	7.38
4	29.81	12.65	17.16	3.88	11.61

4.2.3 Scanning Electron Microscopy:

Figures 4.4a and 4.4b show the Scanning electron micrographs of two representative films, one amorphous (PE_1) and the other nanocrystallite embedded amorphous (PE_3) respectively. SEM studies show smooth conchoidal surface morphology for all the films except for sample PE_3, where clusters of about 100 nm are found. These clusters are formed due to the aggregation of amorphous or nanocrystalline tissues [26]. No columnar growth is observed in these films.

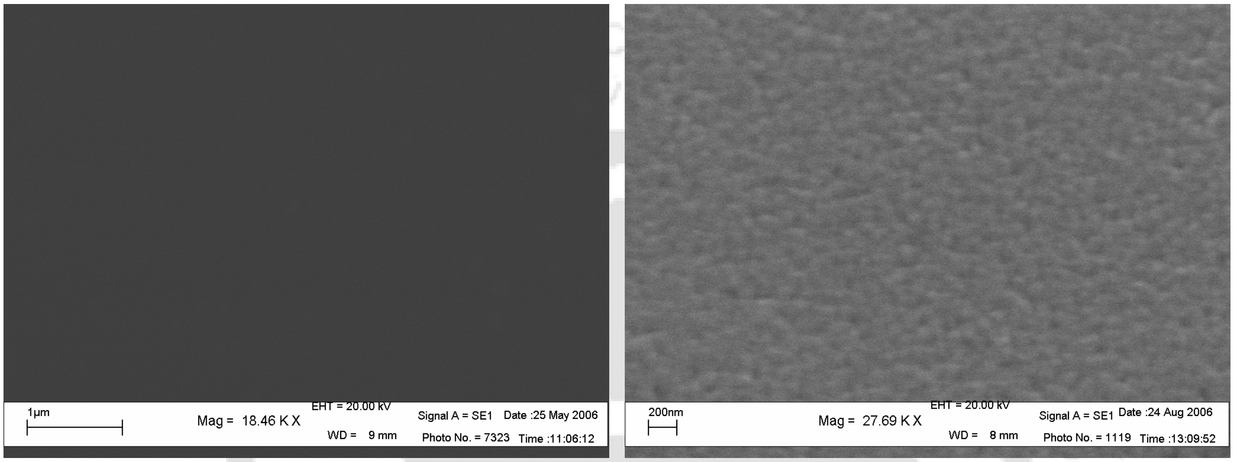

(a) (b)

Figure 4.4: SEM micrograph for films (a) PE_1 (amorphous) and (b) PE_3 (nanocrystallites embedded amorphous).

4.2.4 Thickness, optical constants and optical band gap calculation:

The UV-Vis-NIR transmission spectra for the films are shown in figure 4.5. The thickness of the films as calculated from the interference fringes is found to be around 460-540 nm which gives the high deposition rate (r_d) of about 4-5 Å/sec for argon dilution ratio $R \leq 400$. As R is further increased, the r_d decreases drastically (1.3 Å/sec, for R=630), resulting in a very low thickness of the film for the same deposition time (20 minutes). The r_d decreases with the increase in argon dilution because of the depletion of silane concentration in the gas mixture. Even the lowest r_d for our argon diluted films is found to be much higher compared to that reported in the literature (0.5-0.83 Å/Sec) [9] for argon diluted microcrystalline films. The band gap (E_G) of the films, calculated by plotting $\sqrt{\alpha h\nu}$ *vs* $h\nu$ [figure 4.6], is estimated to be in the range of 1.85-2.16 eV, which is slightly higher compared to regular a-Si:H films (~ 1.7-1.8 eV) prepared without argon dilution. E_G is found to be nearly independent (1.85-1.90 eV) of argon dilution (for R≤400) except when the argon dilution is the highest (E_G =2.16eV for R=630). These results are summarized in table 4.3.

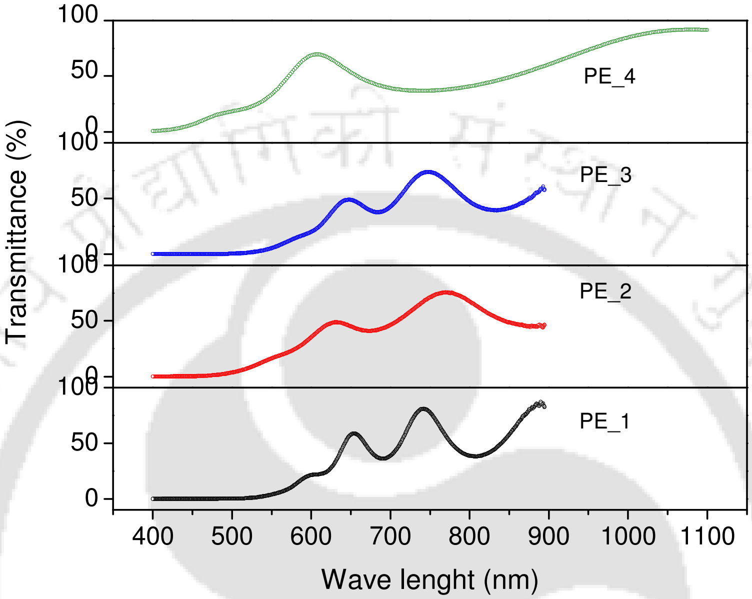

Figure 4.5: UV-Vis-NIR transmission spectra for the films reported in the present chapter.

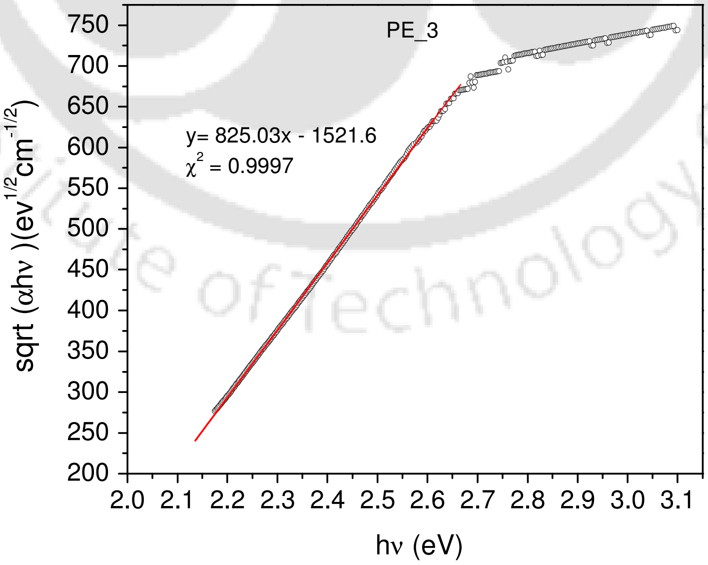

Figure 4.6: $\sqrt{\alpha h\nu}$ *vs* $h\nu$ curve for a representative film (PE_3) for the determination of optical band gap, E_G.

Table 4.3: Thickness, deposition rate (r_d) and optical band gap (E_G) for the films as estimated from UV-Vis-NIR transmission data along with the argon dilution ratio (R).

Sample No	R	Thickness (nm)	E_G (eV)	r_d (Å/Sec)
PE_1	100	535	1.87	4.46
PE_2	200	494	1.90	4.12
PE_3	400	461	1.84	3.84
PE_4	630	160	2.16	1.32

4.2.5 Photoluminescence studies:

Figure 4.7 shows the photoluminescence spectra for the films with excitation wavelength 375 nm. We have observed very weak intensity broad PL peaks in the visible range of 500-700 nm with the peak centered at ~ 600nm. The peak positions and intensity vary slightly with the excitation wavelengths; generally the higher excitation wavelength shifts the peak position to the higher wavelength side. The sharp peak with smaller intensity centered at ~765 nm is due to the instrument. Figure 4.8 shows PL spectra of film PE_3 corresponding to different excitation wavelengths. The PL emission from a-Si:H in the infra red regime is a well known phenomenon [19, 27]. Yue *et al.* [27] reported the low energy PL (0.84-1.4eV) on the films prepared in transition from amorphous to microcrystalline silicon prepared by HWCVD method. They suggested the PL to be originating from small volume of two dimensional grain boundary regions. Yoon *et al.* [14] have studied the luminescence of the PECVD deposited samples prepared with argon dilution. They observed PL peaks composed of three sub bands at 0.89, 0.92 and 1.0 eV and described 1.0 eV PL band as the band tail to band tail transition in the crystallites. Though visible PL is not observed in a-Si:H, there have been reports of PL in the visible range in case of nanocrystalline silicon [28-29]. The PL signal in visible range suggests that the films contain nanocrystallites.

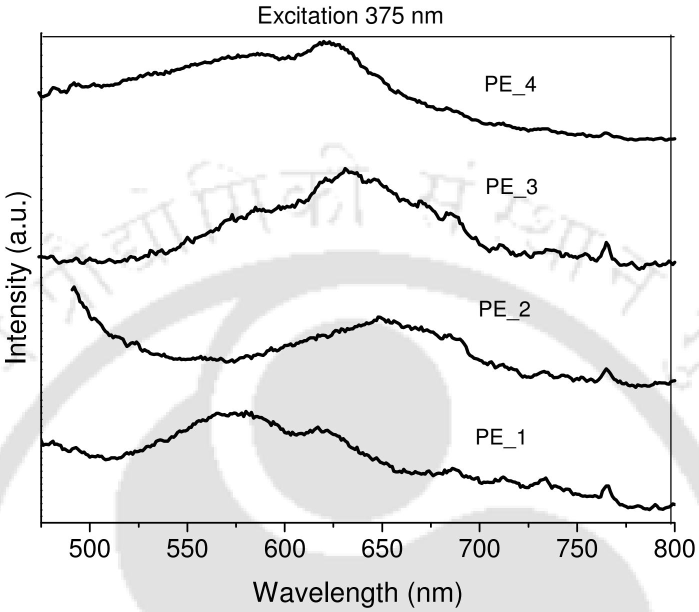

Figure 4.7: Photoluminescence spectra with excitation wavelength of 375 nm for the films reported in the present chapter.

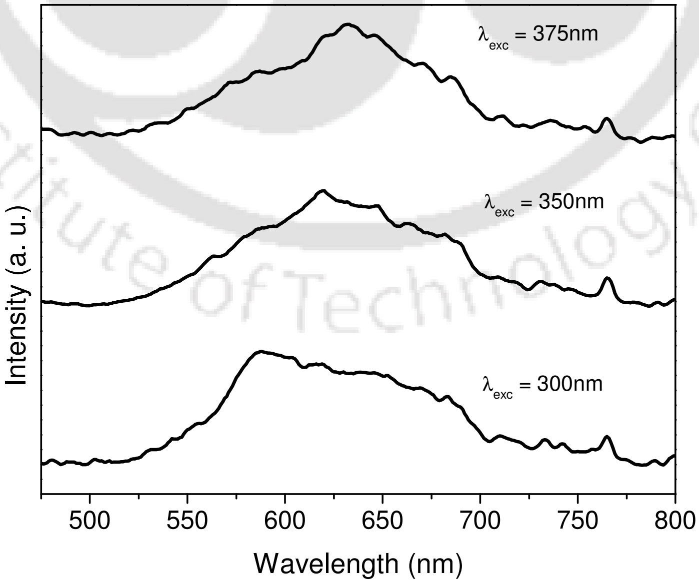

Figure 4.8: Photoluminescence spectra for a representative film PE_3 with different excitation wavelengths.

4.2.6 Temperature dependent Conductivity and Stability studies:

The room temperature dark conductivity of the annealed films ranges from 10^{-10} to 10^{-6} $\Omega^{-1}cm^{-1}$, while photoconductivity varies from ~10^{-7} to 10^{-5} $\Omega^{-1}cm^{-1}$. Figures 4.9a -4.9d show the temperature dependent dark conductivity (σ_d) as well as photo conductivity (σ_{ph}) curves for both in the annealed and then slow cooled (Annld) as well as the light soaked states (LS). The results of conductivity studies are summarized in table 4.4. The Arrhenius plot (log σ vs $10^3/T$ curve) for these films could be best fitted with two activation energies. This is because the films are not purely amorphous but have nanocrystallites embedded in the amorphous matrix. Films prepared with the least argon dilution (R =100) show a small value of σ_d with σ_{ph} /σ_d ratio of more than 4 orders of magnitude, characteristic of a-Si:H films prepared with no dilution or small hydrogen dilution. When R is increased to 200, the formation of nanocrystallites begins and the films exhibit higher σ_d and lower photosensitivity (with σ_{ph}/ σ_d ~10 only). For the films with R =400 which shows the maximum crystallinity fraction, σ_d becomes very low, thus giving σ_{ph} / σ_d ~ $2x10^5$. The σ_d curve in this case has a nearly single activation energy E_d~0.88 eV. These values correspond to very good quality a-Si:H films. Further increase in argon dilution increases σ_d considerably along with decrease in activation energy. In this case σ_d is close to the microcrystalline films, which is also supported by drastic decrease in the deposition rate. It is seen that the films undergo very less light induced degradation. After light soaking for 12 hours (LS) σ_d and σ_{ph} for these films are not affected much; the maximum change is one order of magnitude for the films corresponding to the lowest argon dilution. Figure 4.10 shows the room temperature dark and photo conductivity of the films in the annealed and LS state. The two $\sigma(T)$ curves in the annealed and the LS states meet at T_E and for T >T_E , $\sigma(T)$ is same for both the states (Fig 4.9a-4.9d). The changes in σ_d due to light soaking and also T_E, for these films are much lower compared to that reported in literature (more than 3 orders of magnitude decrease and ~ 200°C respectively) for undoped a-Si:H films. It is also observed that as the argon dilution increases, T_E decreases systematically. This could be due to the improvement in structural order of these films. Figure 4.11 shows the variation of T_E and E_d with argon dilution ratio. Conductivity measurements and stability studies suggest that the best quality a-Si:H films are produced when R is close to 400. The deposition rate for these samples is 3.84 Å/sec and these films are suitable for making cost effective stable solar cells.

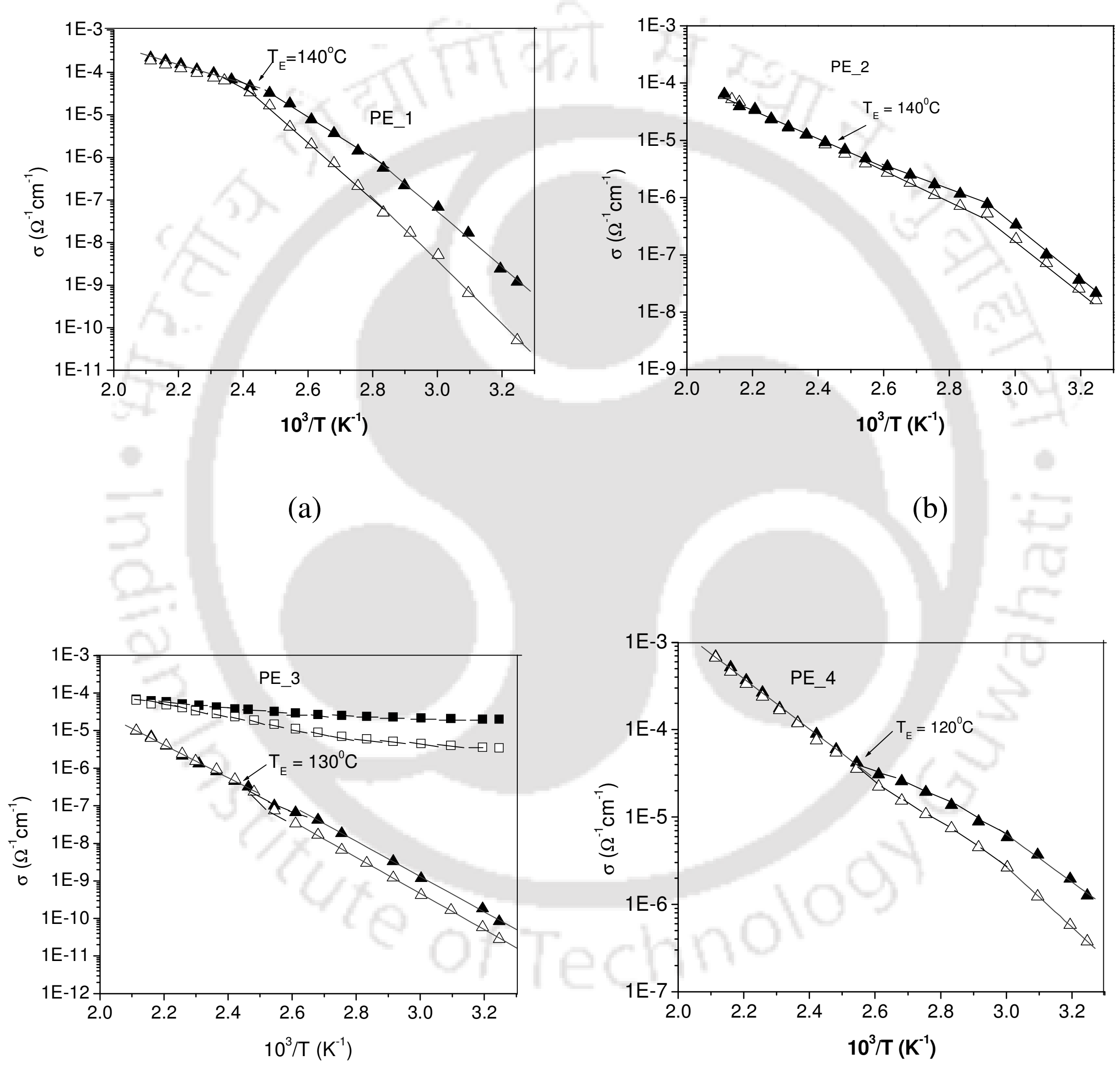

(a) (b)

(c) (d)

Figure 4.9: Variation of dark (triangles) conductivity with temperature for the films (a) PE_1, (b) PE_2, (c). PE_3 and (d) PE_4. Figure (c) shows the photo (rectangles) conductivity for film

PE_3 in addition. For both dark and photo conductivity the filled symbols are for annealed state while the empty symbols are for light soaked state.

Table 4.4: Conductivity and stability studies results for the films reported in this chapter.

Sample No	State	σ_d ($\Omega^{-1}cm^{-1}$) (35^0C)	σ_{ph} ($\Omega^{-1}cm^{-1}$) (35^0C)	E_d (eV) $T<100^oC$	E_d (eV) $T>T_E$	T_E (^0C)
PE_1	Annld	$1.19x10^{-9}$	$4.35x10^{-5}$	1.22	0.44	140
	LS	$5.10x10^{-11}$	$4.76x10^{-6}$	1.45		
PE_2	Annld	$5.40x10^{-8}$	$5.00x10^{-7}$	0.77	0.56	140
	LS	$2.16x10^{-8}$	$4.73x10^{-7}$	0.80		
PE_3	Annld	$8.30x10^{-11}$	$1.99x10^{-5}$	0.93	0.86	130
	LS	$2.84x10^{-11}$	$3.44x10^{-6}$	0.96		
PE_4	Annld	$1.27x10^{-6}$	$1.84x10^{-5}$	0.49	0.57	120
	LS	$3.80x10^{-7}$	$9.87x10^{-6}$	0.58		

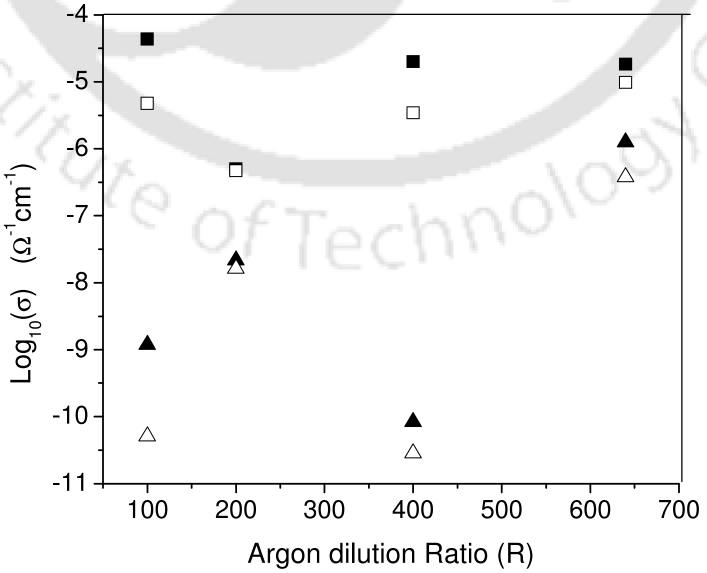

Figure 4.10: Variation of dark (σ_d) and photo conductivity (σ_{ph}) as a function of argon dilution ratio R in both annealed state as well as LS state. Triangles are for dark conductivity while squares are for photo conductivity. Filled symbols are for annealed and open ones for LS state. Error bars are included in the size of the symbols.

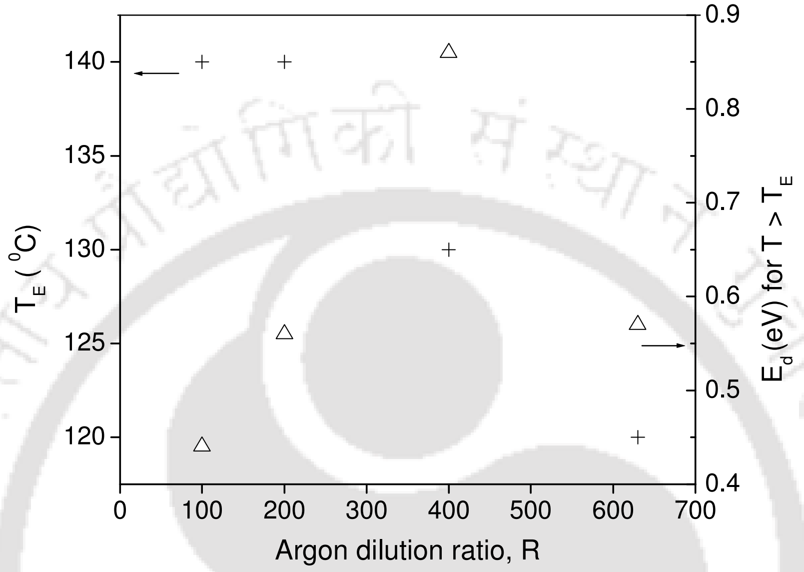

Figure 4.11: Variation of T_E and E_d (for $T>T_E$) with argon dilution ratio. Error bars are included in the size of the symbols.

4.2.7 Diffusion length measurements by SSPG method:

The SSPG measurements are performed for the determination of carrier diffusion length L_d by varying the optical grating period Λ in the range of 360-1560 nm. Figure 4.12 shows the variation of experimental parameter β, which is the ratio of photocurrents in the presence and absence of grating, with Λ. The curves can be fitted with a polynomial of power 4 (β= 1-[$2\phi/(1+\gamma F_2/F_1)(1+4\pi^2L^2/\Lambda^2)^2$]). A plot of $1/\Lambda^2$ Vs Sqrt[$2/\{(1-\beta)(1+\gamma F_2/F_1)\}$] is (Figure 4.13) used for the determination of the diffusion length L_d, where γ is the exponent of power law dependence of photocurrent with intensity of light and F1 and F2 are the intensities of strong and weak beams superposing on the sample. The measurements give the diffusion length to be 70-80 nm. We did not observe any considerable change in L_d of the films after light soaking with a laser light of 633 nm for 12 hours.

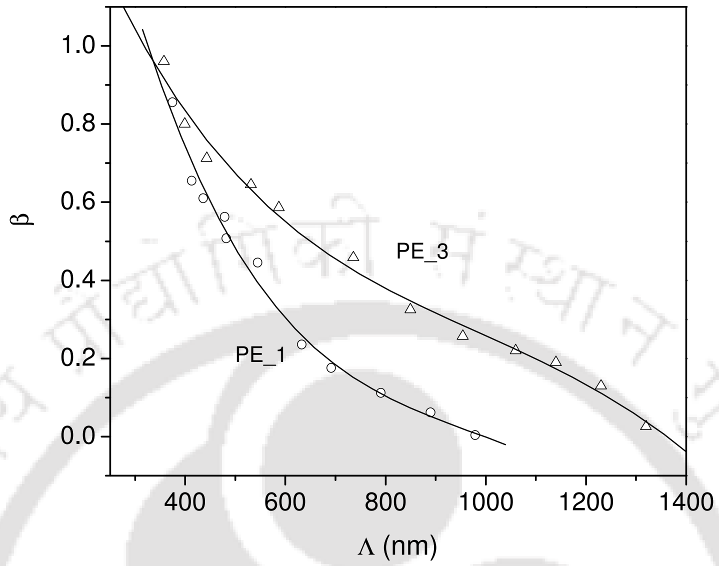

Figure 4.12: Variation of experimental parameter β with the grating period Λ.

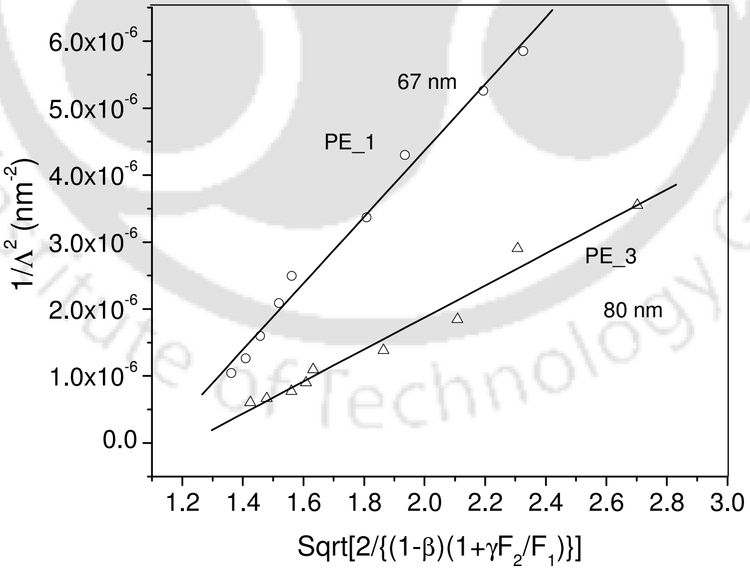

Figure 4.13: Plot for the determination of carrier diffusion length L_d.

The growth of Si:H films using hydrogen dilution as well as argon dilution of SiH_4 is understood as follows. In case of heavily hydrogen diluted silane, main film forming precursor is SiH_3, which is a very less reactive species having a long diffusion length. During the growth, SiH_3 does not find a Si site on the surface, well covered by hydrogen which passivates all the bonds on the surface, and hence traverses a long distance before it finds an un-terminated silicon bond on the surface of the growing film [30]. However, lower radicals (SiH_x, $x<3$), can be bonded with hydrogen terminated surface, resulting in weak bonds. The figure 1.6 in the chapter 1 illustrates some of the processes occurring at the growing surface of a-Si: H films. For bonding of SiH_3 on the growing surface, the removal of hydrogen from the surface is necessary. This can occur spontaneously from weakly bonded Si-H sites by thermal excitation or hydrogen can be stripped off by gas radicals or ions, which then form strong bond with SiH_3. Atomic hydrogen also can traverse in the subsurface region and scavenges weak Si-Si and Si-H bonds, which subsequently forms strong Si-Si bonds or gets passivated by hydrogen. This way it results in homogeneous film (CVD like growth), but the deposition rate is hindered a lot as atomic hydrogen reaching the film growing surface breaks the weak Si-Si bonds and surface etching is significant. On the other hand, in argon diluted silane, the energy released in the de excitation of Ar* is used in the dissociation of the source gas to produce highly reactive radicals like Si, SiH, SiH_2. Each of the radicals has high sticking co-efficient and less surface mobility and is able to react directly with hydrogen-terminated surface, inserting into Si-H bonds [1, 17]. This results in an accelerated growth process, however films prepared using only argon dilution are reported to have columnar structure (PVD like growth) [1, 11 17]. Recently, Das *et al.* [15] reported less defective high C_H films prepared by argon dilution compared to hydrogen diluted or pure silane films. They found that the structural heterogeneities in the films decreased for argon dilution up to 90%, after which heterogeneities increased again. Another work by Das *et al.* showed that argon dilution up to 95 % led to the improvement in structural homogeneity while beyond that structural heterogeneity increases [31]. In case of argon dilution, a large amount of energy is transferred to the growth zone by bombardment of Ar^+ and Ar* in the plasma. Since, Ar* ($^3P_{0,2}$) has life time >1.3 sec, this plays an important role compared to other excited states of argon. It helps in the process of dissociation of the silane. The amount of energy transferred to the growth zone depends on the equilibrium concentrations of Ar* and Ar^+ in the plasma and their interaction with the growth zone. RF power increases the concentration of both Ar* and Ar^+

while dilution increases Ar*. The formation energy of Ar* (11.5-11.7eV) is less than Ar^+ (15.76eV), so for low to moderate power density, bombardment of Ar* is more probable. Also, Ar^+ is less reactive than Ar*, the reaction rate is about one order of magnitude lower. The reaction probabilities are listed below. Energy transfer by Ar^+ depends on the Coulomb attraction by the anode which is normally at a few hundred negative potential, so the Ar^+ ions have sufficient energy to sputter the growing film, thus increasing the roughness and the voids. On the other hand Ar* impinges the growing film only with thermal velocity and hence the energy transfer is much softer in this case. The energy released by Ar * is used to break the weak Si-Si bonds and also loosely bound hydrogen from SiH_2 sites. The dangling bonds so formed form strong Si- Si bonds or are terminated by hydrogen. This way the voids and microstructures are lowered in the films. In this process the hydrogen bonded in amorphous matrix gets removed from the film and thus the hydrogen depleted region with strong Si-Si bonds forms nanocrystals in the matrix.

$$Ar + e \rightarrow Ar^+ + 2e \ (j = 1.05 \times 10^{-11}\ cm^3/s)$$
$$Ar + e \rightarrow Ar^* + e \ (j = 1.2 \times 10^{-12}\ cm^3/s)$$
$$Ar^* + SiH_4 \rightarrow SiH_3 + H + Ar \ (j = 1.4 \times 10^{-10}\ cm^3/s)$$
$$SiH_2 + H + H + Ar \ (j = 2.6 \times 10^{-10}\ cm^3/s)$$

$$Ar^+ + SiH_4 \rightarrow Si^+ + H_2 + H_2 + Ar \ (j = 1.184 \times 10^{-11}\ cm^3/s)$$
$$SiH^+ + H + H_2 + Ar \ (j = 4.2 \times 10^{-12}\ cm^3/s)$$
$$SiH_2^+ + H_2 + Ar \ (j = 1.66 \times 10^{-12}\ cm^3/s)$$
$$SiH_3^+ + H + Ar \ (j = 2.4 \times 10^{-12}\ cm^3/s)$$

We have observed higher deposition rate for films prepared using combined argon and hydrogen dilution. The deposition rates are significantly higher than those reported in literature for hydrogen diluted [2] and argon diluted [9] silane. The high deposition rate of our films is due to the efficient dissociation of silane by Ar* and atomic hydrogen. At the same time the diffusion of film forming precursor radicals are enhanced due to the hydrogen coverage on the growing surface which helps these radicals to reach energetically favorable sites thus preventing columnar growth and improving the short and medium range order of the films. Sufficient number of atomic hydrogen present in the plasma can etch out weak Si-Si bonds at the growing surface as well as in the bulk and thereby help in the formation of strong Si-Si bonds and thus improving the stability of these films against light soaking. The excited argon atoms (Ar*) also release energy that is used in breaking weak Si-Si bonds [9] and reconstructing strong Si-Si bond thus further improving the medium range order. Hence the role of Ar* in Ar diluted plasma is analogous to that of atomic H during chemical annealing in H_2 diluted plasma. The absence of crystalline peak in XRD data and at the same time the presence of a peak corresponding to nano-crystallites in Raman spectrum can be understood as the presence of small nano-crystallites embedded in the amorphous network. This could also be the possible reason for the relatively high band gap of these films. When argon dilution is extremely high, the surface of the growing film is less covered by hydrogen. The bombardment of Ar* on the growing surface leads to structural reorientation and therefore promotes improvement in order and micro/ nanocrystalline formation. As the density of SiH_n species becomes very low in this case, the deposition rate is reduced significantly.The improved opto-electronic properties, better stability against light soaking and lower T_E for these is due to the improved microstructure as can be seen from Raman data. With the increase in argon dilution, we observe a systematic decrease of T_E, which indicates the lowering of defect annealing energy. The metastable changes after light soaking are believed to be due to the presence of potential fluctuations caused by inhomogeneous growth [32]. A mixture of hydrogen and argon dilution of silane possibly causes the homogeneous growth and thus less potential fluctuations in these films, which results in the reduction in the degradation of these films after exposure to light.

4.3 Conclusion:

In this chapter, we have reported the high deposition rate (~ 4-5 Å/sec) as well as improved transport properties and stability against exposure to light of a-Si:H films prepared by argon and hydrogen dilution of silane. The columnar growth, otherwise observed in films prepared by only argon-diluted silane is prevented by the presence of hydrogen in the precursor gas mixture. In our case, both Ar* and atomic hydrogen help in the efficient dissociation of silane and in the reconstruction of strong Si-Si bonds thus improving the short and medium range order and thus leads to better stability against light soaking. The best quality films are obtained for samples with argon dilution ratio around 400 for silane diluted with hydrogen. The films prepared under these conditions are best suited for stable device applications.

4.4 References:

1. R.A. Street, Hydrogenated Amorphous Silicon, Cambridge University Press, (1992).
2. G. Morell, R. S. Katiyar, S. Z. Weisz, H. Jia and J. Shinar, J. Appl. Phys. **78** (1995) 5120.
3. M. Zeman, *Advanced amorphous silicon solar cell technologies*, Thin Film Solar Cells: Fabrication, Characterization and Applications, John Wiley and Sons (2006), Ed. J. Poortmans and V. Arkhipov.
4. S. Guha, Sol. Energy Mater. Sol. Cells. **78** (2003) 329.
5. P. Kumar, F. Zhu and A. Madan, Int. J. Hydrogen Energy **33** (2008) 3938.
6. Y. He, C. Z. Yin, G. Cheng, L. Wang X. Liu and G.Y. Hu, J. Appl. Phys. **75** (1994) 797.
7. P. M. Gordo, M. F. F. Marques, C. L. Gil, A. P. D. Lima, G. Lavareda, C. N. D. Carvalho, A. Amaral and Z. Kajcsos, Radiat. Phys. Chem. **76** (2007) 220.
8. P. P. Ray, N. D. Gupta, P. Chaudhuri, D. L. Williamson, S. Vignoli and C. Longeaud, J. Non-Cryst. Solids **299-302** (2002) 123.
9. M. Jana, D. Das and A. K. Barua, J. Appl. Phys. **91** (2002) 5442.
10. J. Yang, B. Yan and S. Guha, Thin solid Films **487** (2005) 162.
11. J. C. Knights and R. A. Lujan, Appl. Phys. Lett. **35** (1979) 244.
12. C. C. Tsai, J. C. Knights, G. Chang and B. Wacker, J. Appl. Phys. **59** (1986) 2998.
13. S. T. Kshirsagar, N. R. Khaladkar, J. B. Mamdapurkar and A. P. B. Sinha, Materials Chemistry and Physics **15** (1987) 433.
14. S. Hamma and P. Roca i Cabarrocas, J. Non-Cryst. Solids **227-230** (1998) 852.
15. U. K. Das, A. R. Middya, J. K. Rath, C. Longeaud, D. L. Williamson and P. Chaudhuri, J. Non-Cryst. Solids **276** (2000) 46.
16. W. M. M. Kessels, J. P. M. Hoefnagels, M. G. H. Boogaarts, D. C. Schram and M. C. M. van de Sanden, J. Appl. Phys. **89** (2001) 2065.
17. D. Das, M. Jana and A. K. Barua, J. Appl. Phys. **89** (2001) 3041.
18. P. P. Ray, P. Chaudhuri and P. Chatterjee, Thin Solid Films **403-404** (2002) 275.

19. J. H. Yoon, J. Y. Lee and D. H. Park J. Non Cryst. Solids **338-340** (2004) 465.
20. W. J. Soppe, C. Devilee, M. Geusebroek, J. Löffler and H.-J. Muffler, Thin Solid Films **515** (2007) 7490.
21. A. Bhaduri, P. Chaudhuri, D. L. Williamson, S. Vignoli, P. P. Ray and C. Longeaud, J. Appl. Phys. **104** (2008) 063709.
22. D. L. Staebler and C. R. Wronski, Appl. Phys. Lett. **31** (1977) 292.
23. D Ritter, K Weiser and E. Zeldov, J. Appl Phys. **62** (1987) 4563.
24. M. Stutzman, *Amorphous Semiconductors,* Handbook of Semiconductors, North Holland Vol **3a** (1994), Ed. S. Mahajan.
25. M. Ito and M. Kondo, Jpn. J. Appl. Phys. **45** (2006) L230.
26. B. Yan, C. –S. Jiang, C. W. Teplin, H. R. Moutinho, M. M. A. Jassim, J. Yang and S. Guha, J. Appl. Phys. **101** (2007) 033712.
27. G. Yue, J. D. Lorentzen, J. Lin, D. Han and Q. Wang, Appl. Phys. Lett. **75** (1999) 492.
28. H. Takagi, H. Ogawa, Y. Yamazaki, A. Ishizaki and T. Nakagiri, Appl. Phys. Lett. **56** (1990) 2379.
29. J. -H. Shim, S. Im and N. -H. Cho, Appl. Surf. Sci. **234** (2004) 268.
30. A. Matsuda, J. Non-Cryst. Solids 338-**340** (2004) 1 and references therein.
31. U. K. Das, P. Chaudhuri and S. T. Kshirsagar, J. Appl. Phys. **80** (1996) 5389.
32. P Agarwal and S.C. Agarwal, Philos. Mag. B **80** (2000) 1327.

Chapter -5

Hydrogen dilution of HWCVD films

Chapter 6

Hydrogen diluted HWCVD films: Effect of Substrate Temperature

This chapter presents the studies on the HWCVD films prepared by substrate temperature (T_s) variation. The substrate temperature plays a decisive role on the microstructure and quality of the films for both PECVD and HWCVD films [1-3]. Deposition of device quality amorphous and microcrystalline silicon films at low substrate temperature is of major interest as this not only facilitates the use of variety of substrates like plastic, but also decreases processing cost and increases the possibility to use in biological applications. Recent reports suggest that good quality amorphous and microcrystalline silicon films can be deposited at a substrate temperature as low as 100^{o}C [2, 4]. Filonovich *et al.* [3] have performed a comparative study on the films prepared by both PECVD and HWCVD method at low T_s of 150^{o}C. They found that HWCVD films are of good quality, however PECVD prepared films are better. A detailed understanding of the role of substrate temperature in case of HWCVD is still required. With this motivation, we prepared a series of films with T_s in the range of 100-350 ^{o}C keeping the other deposition parameters fixed. In this chapter we report the structural, optical and transport studies on amorphous as well as nanocrystallites embedded amorphous films prepared from hydrogen diluted silane (10% silane in hydrogen) by varying the T_s in the range of 100- 350^{o}C keeping T_F fixed at 1800^{o}C.

6.1 Experimental Details:

The films are prepared using semiconductor grade hydrogen diluted silane (10 % silane in hydrogen) from Matheson Inc. The films are deposited on Corning 1737, ITO coated glass, c-Si wafer and carbon coated Cu grids for different studies. Tungsten filament in the horizontal filament assembly is used for film preparation. During deposition filament temperature (T_F) is kept constant at 1800^{o}C. Generally, for T_F< 1700^{o}C, the silicon radicals get incorporated into tungsten filament forming silicides and affecting the life time of filament as well as reproducibility of the material [5]. On the other hand for T_F> 2100^{o}C, the films get contaminated due to the evaporation of filament material [6]. Hence we have chosen an intermediate T_F for film preparation. The filament to substrate distance is kept fixed at 6 cm. The detailed deposition conditions are listed in Table 6.1.

Table 6.1: Deposition details of the studied films. Here T_F, SFR, PP and T_s represent filament temperature, silane flow rate, process pressure and substrate temperature respectively.

Sample No.	T_F (^oC)	SFR (10% SiH_4 in Hydrogen) (SCCM)	PP (mbar)	T_s (^oC)
HW_Ts_1	1800	10	0.5	100
HW_Ts_2				150
HW_Ts_3				200
HW_Ts_4				250
HW_Ts_5				300
HW_Ts_6				350

The films are structurally characterized by X- ray diffraction (XRD), Scanning electron microscopy (SEM), Transmission electron microscopy (TEM), Raman spectroscopy and Atomic force microscopy (AFM). The details of the experimental techniques are discussed in Chapter 2. XRD measurements are done in scanning range of 15-60^o in 2θ mode at grazing angle of incidence 3^o using Siefert XRD 3003 TT while SEM studies are performed by Leo 1430 VP scanning electron microscope. Raman studies are performed by Witec Alpha Raman spectrometer with excitation wavelength of 514.1 nm in the scanning range of 100-1000 cm^{-1}. TEM studies are performed using JEOL TEM while AFM studies are performed by Picoplus Molecular Imaging in acoustic mode using silicon cantilevers with force constant 2.5N/m and resonance frequency of 80 KHz. All these measurements are performed on the films deposited on Corning glass except TEM studies where films deposited on Cu grids are used. The optical studies are performed by UV-Vis-NIR and FTIR transmission spectroscopy. UV-Vis-NIR transmission spectra are recorded by Shimadzu UV 3101 PC in the range 3000- 350 nm while

FTIR transmission spectra are recorded in the range of 400- 4000 cm^{-1} using Perkin Elmer BX II FTIR spectrometer. The transport studies are done by temperature dependent dark and photoconductivity measurements and stability studies. For photoconductivity and stability studies, a white light source of 100 Watt is used.

6.2 Results and Discussions:

6.2.1 X-ray diffraction studies:

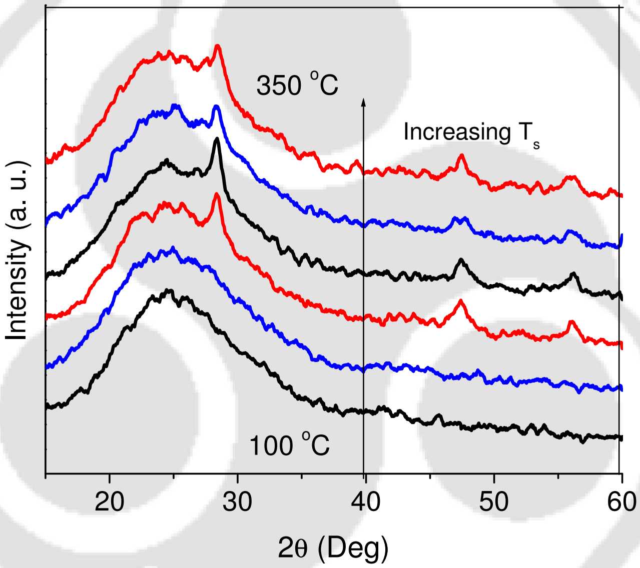

Figure 6.1: XRD pattern for the films prepared with substrate temperature variation. Films become nanocrystalline embedded at T$_s$ ~ 200°C. The XRD patterns are vertically shifted for the sake of clarity.

Figure 6.1 shows the XRD pattern for the studied films. It is observed that the films deposited at low T$_s$ are amorphous while nanocrystallites develop in the amorphous matrix as T$_s$ is increased (T$_s$ $\geq$ 200°C). This is revealed by the emergence of small intensity peaks corresponding to (111), (220) and (311) planes of crystalline silicon superimposed on the broad amorphous peak. The XRD pattern has been deconvoluted in to a broad amorphous peak and a narrow peak corresponding to the presence of nanocrystallites as discussed in Section 2.2.1.1. The FWHM of the nanocrystalline peak varies in 2θ value from 0.97 to1.54^{o} giving the size of nanocrystallites (d_{XRD}) of about 5-9 nm (listed in Table 6.2) whereas that corresponding to amorphous peak, it remains in the range 9.75-10.55^{o}. It is observed that there is no systematic variation of amorphous peak FWHM with $T_{s.}$

6.2.2 Raman scattering spectroscopy:

For information regarding the crystalline fraction (X_c), crystallite size (d_R) and short range order (SRO), Raman measurements are performed on the films deposited on Corning 1737 and are shown in figure 6.2. Like the XRD results, Raman spectra also show low temperature films to be amorphous in nature while crystallinity develops for $T_s \geq 200$ ^{o}C. The low T_s films show a peak centered near 480 cm^{-1} corresponding to TO mode of amorphous silicon; while the films deposited at $T_s \geq 200$ ^{o}C are characterized by sharp peak corresponding to TO mode of crystalline silicon near 520 cm^{-1} in addition to the amorphous peak. This observation suggests that the films grown at elevated T_s develop crystallinity, with the nanocrystallites embedded in the amorphous matrix. For calculation of various parameters the Raman spectra are deconvoluted as mentioned in Section 2.2.1.3. The TA mode which occurs near 150 cm^{-1} could not be recorded due to instrumental limitations. Figures 6.3a and 6.3b show the deconvoluted spectra for film HW_Ts_1 (amorphous) and HW_Ts_4 (nanocrystalline) respectively. The rms bond angle variation $\Delta\theta_B$ from the tetrahedral angle of 109^{o}28″, which is a measure of SRO in the films, is estimated from FWHM (Γ) of the TO peak at 480 cm^{-1} as described in Section 2.2.1.3 and is mentioned in the table 6.2. It is observed that the $\Delta\theta_B$ for the films are ~ 6.5-7.5^{o}, corresponding to good quality silicon films [7]. This reduction in the values of $\Delta\theta_B$ indicates the improvement in SRO. It is observed that the SRO is more for the films with higher T_s. At low T_s the film forming radicals do not acquire sufficient energy to diffuse to the energetically favorable site. Hence they stick to the growing surface wherever they strike i.e. the growth is PVD like resulting in films with strained network having lower SRO. When T_s is increased, the radicals become more mobile to diffuse on the growing surface and find energetically favorable site; thus the film growth becomes more CVD like [2] resulting in better SRO.

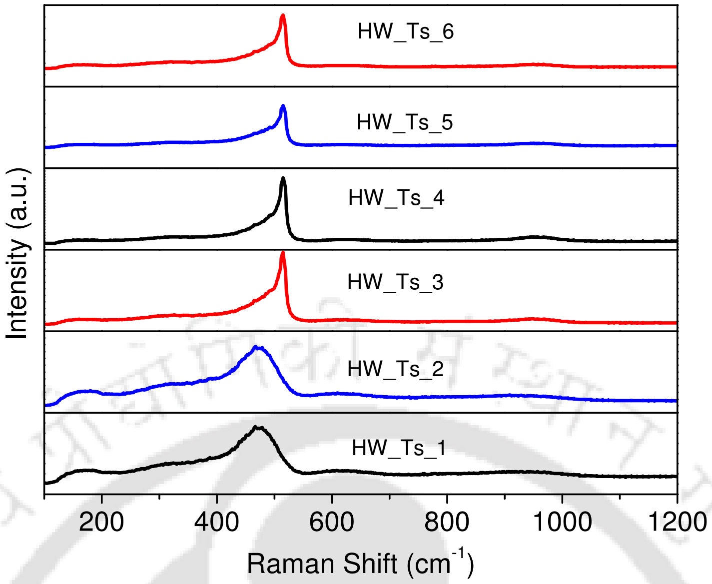

Figure 6.2: Raman scattering spectra for the films prepared with varying T_s.

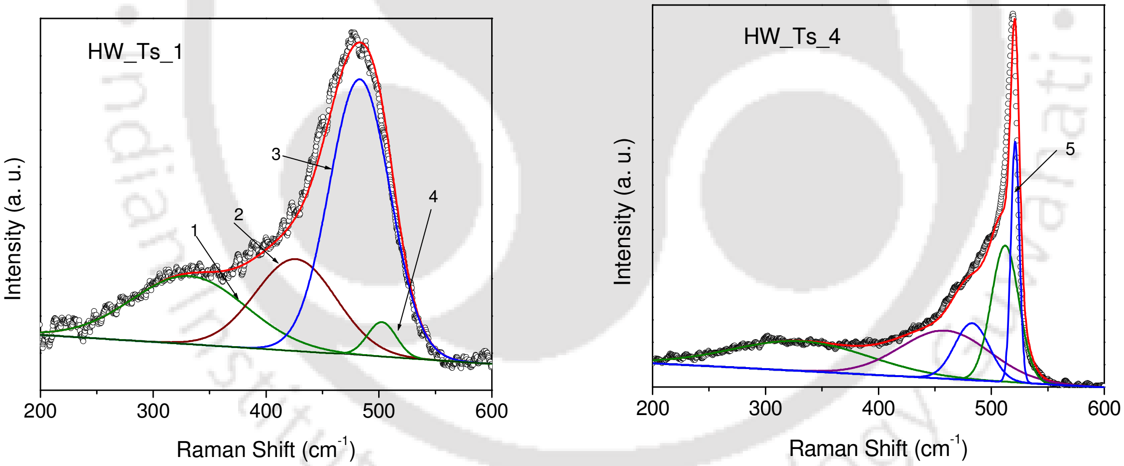

(a)

(b)

Figure 6.3: Deconvoluted Raman spectra for (a) an amorphous film (HW_Ts_1) and (b) a nanocrystallites embedded film (HW_Ts_4) in the range 200-600cm^{-1}. The peaks labeled 1, 2, 3 correspond to amorphous LA, LO and TO mode respectively while peak 4 and 5 correspond to grain boundaries and nanocrystallites.

The total crystalline fraction (X_c), nanocrystalline fraction (X_{nc}) and grain boundary fraction (X_{GB}) in these films are calculated from the deconvoluted intensities of the TO modes of amorphous, grain boundary as well as nano rystalline component as mentioned in Section 2.2.1.3 and listed in table 6.2. The X_c for the films ranges from 0 (amorphous) to 56 % (nano-crystallites embedded amorphous). It is observed that the increase in the X_c of the films is due to the increase in grain boundary fraction, whereas the nanocrystalline volume fraction remains almost constant (Figure 6.4). The medium range order (MRO) for the films is estimated from the I_{TA}/I_{TO} ratio and found to agree with the device quality films as reported in literature [8-9]. The crystallite size (d_R) is calculated from the shift of the nanocrystalline peak from 520 cm^{-1} due to size limitation using the procedure mentioned in Section 2.2.1.3. The films with improved SRO exhibit higher crystallinity, since better SRO leads to the formation of bigger crystallites hence also gives larger X_c. The d_R values calculated from Raman data are found to be ~ 4nm, slightly lower than those calculated from XRD data. The variation of X_c, $\Delta\theta_B$, $I_{TA}/I_{TO,}$ d_R and d_{XRD} with T_s is also plotted in figure 6.5.

Table 6.2: Total crystalline fraction (X_c), nanocrystalline fraction (X_{nc}) grain boundary fraction (X_{GB}), rms deviation of tetrahedral bond angle ($\Delta\theta_B$), MRO (I_{TA}/I_{TO}), crystallite size estimated from Raman and XRD measurements (d_{Raman}, d_{XRD}) respectively .

Sample No	T_s (^oC)	X_c (%)	X_{nc} (%)	X_{GB} (%)	$\Delta\theta_B$ (^{o})	MRO, I_{TA}/I_{TO}	d_{Raman} (nm)	d_{XRD} (nm)
HW_Ts_1	100	-----		----	7.3	0.45	-----	----
HW_Ts_2	150	----		----	7.5	0.40	----	----
HW_Ts_3	200	55.3	24.9	30.4	6.84	0.38	3.94	8.47
HW_Ts_4	250	55.9	21.8	34.1	6.47	0.32	4.25	6.82
HW_Ts_5	300	49.4	26.1	23.3	7.48	0.27	4.16	8.39
HW_Ts_6	350	55.2	25.3	29.9	7.07	0.35	3.97	5.32

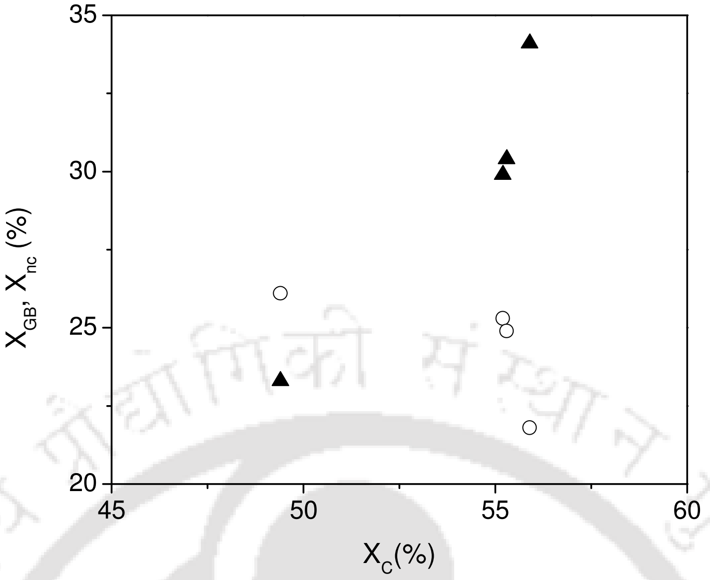

Figure 6.4: Plot of X_{GB} (triangles) and X_{nc} (circles) with X_c. The error bars are included in the size of the symbols.

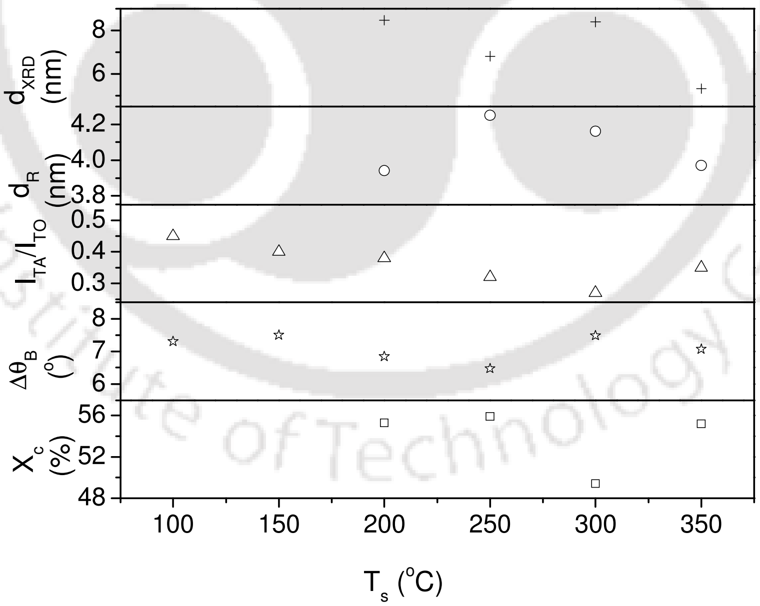

Figure 6.5: Variation of total crystalline fraction (X_c), rms deviation of tetrahedral bond angle ($\Delta\theta_B$), ratio of intensity between the amorphous TA and TO peak (I_{TA}/I_{TO}), crystallite size

calculated from Raman and XRD data (d_R and d_{xrd}) respectively as a function of the substrate temperature.

6.2.3 Transmission electron microscopy:

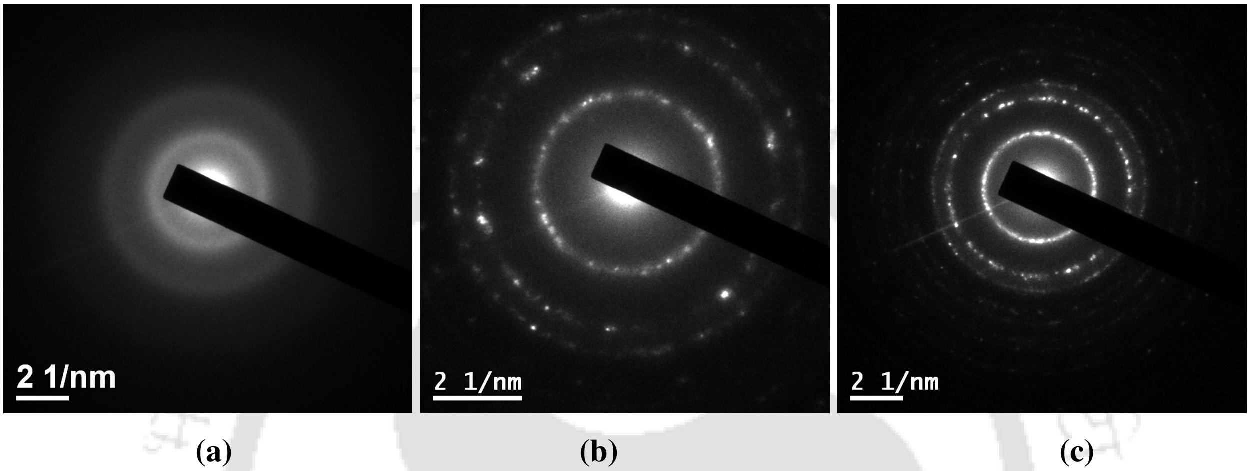

(a) **(b)** **(c)**

Figure 6.6: SAD pattern for (a) HW_Ts_1 (amorphous film), (b) HW_Ts_3 (less nanocrystalline film) and (c) HW_Ts_4 (more nanocrystalline film).

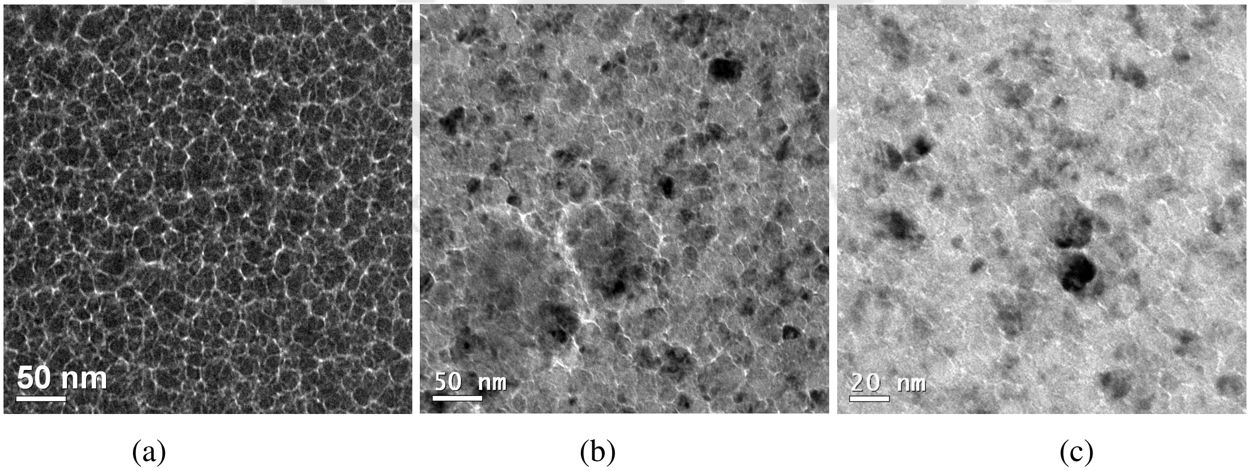

(a) (b) (c)

Figure 6.7: Low resolution TEM images for films (a) HW_Ts_1 (b) HW_Ts_3 and (c) HW_Ts_4 .

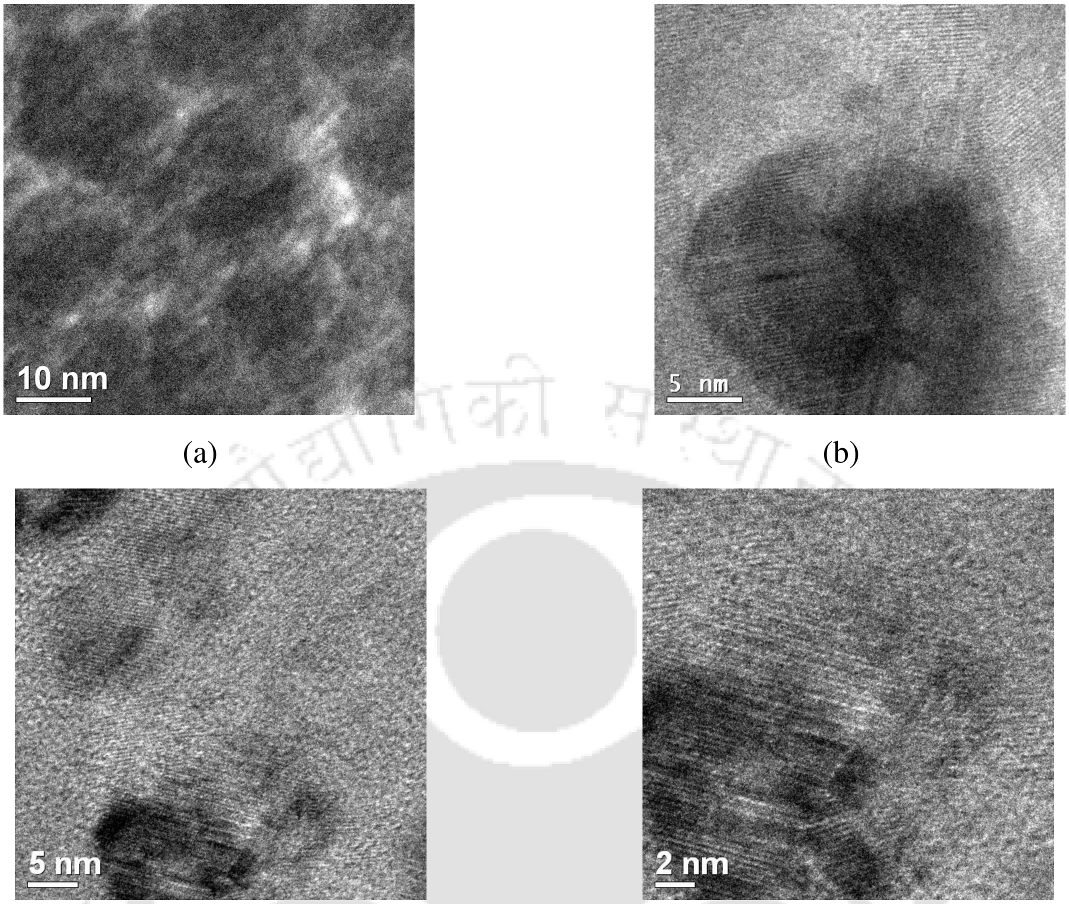

(a) (b)

(c) (d)

Figure 6.8: High resolution TEM images for (a) HW_Ts_1 (b) HW_Ts_3 (c) HW_Ts_4 (d) HW_Ts_4. Figure (c) and (d) show the same nanocrystallite at two different scales.

The selected area diffraction (SAD) patterns for a few samples are shown in the figures 6.6a-6.6c. It is observed from the SAD patterns that the films deposited at low T_s *viz.* 100 and 150^{o}C are completely amorphous with diffused diffraction rings (figure 6.6a). As T_s increases, the diffraction pattern becomes sharper with the appearance of bright spots on the rings (Figures 6.10b and 6.10c). The most intense ring is observed for (111) plane. Rings corresponding to (220) and (311) planes are also sufficiently bright. However the rings corresponding to higher planes such as (400), (331), (422) etc. diminish slowly. The appearance of sharp spotty rings in the SAD pattern is an indication of the formation of nanocrystallites in the amorphous matrix. Low magnification TEM images show grains of average size 20 nm separated from others by thread like structures (Figure 6.7 a-6.7c). These white thread like structures are identified as low density amorphous regions [3]. High resolution TEM (HRTEM) images for a few representative films are shown in figures 6.8a- 6.8d. In these images while low T_s films (which are amorphous) do not show any formation of crystallites, high T_s films clearly reveal the formation of silicon nanocrystallites with lattice spacing ~ 0.3 nm. The crystallites of about 5-10 nm are randomly distributed in the amorphous matrix. Hence the results show consistency in all the XRD, Raman and TEM studies. The films are amorphous up to T_s ~ 150°C while the transition from amorphous to nanocrystalline occurs in the T_s range 150- 200°C as evident in XRD, TEM and Raman studies.

6.2.4 Atomic force microscopy:

Figures 6.9a-6.9d show the AFM images (surface topography) of a few representative samples. As the T_s increases the film develops crystallinity and undergoes a change in the surface morphology. It is observed that the films deposited at high T_s are densely packed with less rms roughness (r_{rms}) whereas for films at low T_s, scattered clusters are seen. The rms roughness (r_{rms}) is found to decrease with increasing T_s. As T_s increases the film forming radicals become more mobile to find energetically favourable site before getting absorbed into the film. Hence the surface roughness decreases with the increase in T_s. The values of rms roughness of the films are listed in Table 6.3.

Table 6.3: The rms roughness (r_{rms}) of the films as calculated from AFM data.

Sample No	HW_Ts_1	HW_Ts_2	HW_Ts_3	HW_Ts_4	HW_Ts_5	HW_Ts_6
r_{rms} (nm)	13.3	18.4	10.8	6.5	1.5	3.6

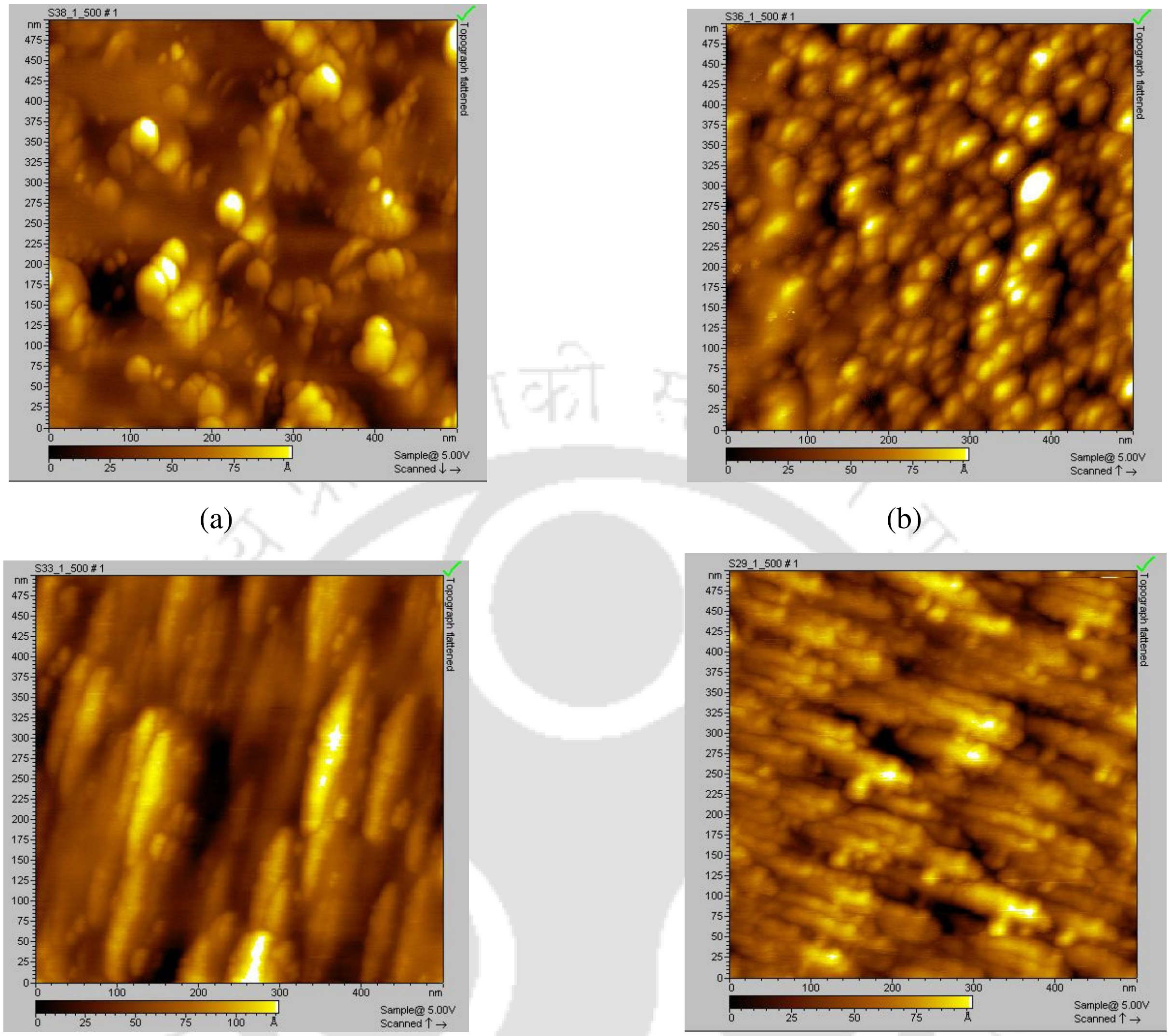

(a) (b)

(c) (d)

Figure 6.9: AFM images showing the surface topography of a few films (a) HW_Ts_1 (b) HW_Ts_3 (c) HW_Ts_4 and (d) HW_Ts_6.

6.2.5 Scanning electron microscopy:

SEM images for a few films under present study show smooth surface morphology while some others show formation of grains or clusters of about 150-200 nm. The formation of clusters occurs irrespective of whether the films are amorphous or nanocrystalline. Figures 6.10a and 6.10b show SEM micrographs for film HW_Ts_2 (amorphous) and HW_Ts_4 (nanocrystalline).

The aggregation of nanocrystallites as well as amorphous tissues results the cluster formations in these films [10].

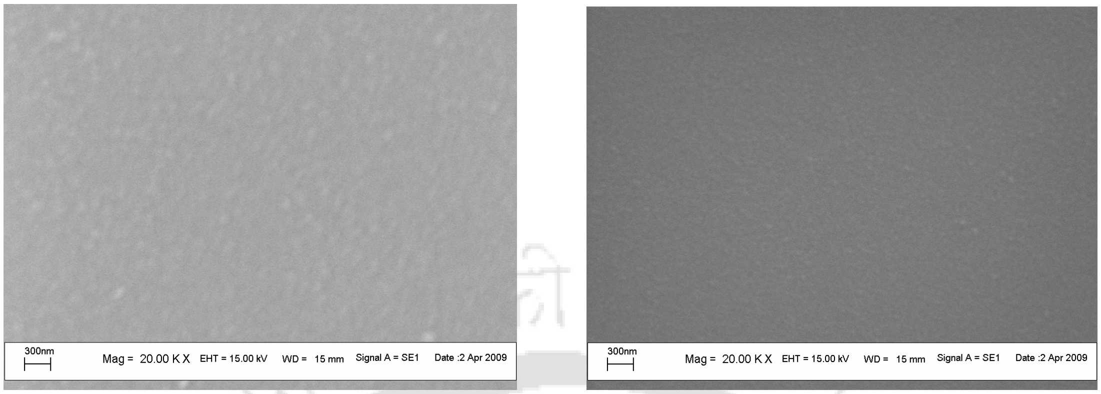

(a) (b)

Figure 6.10: SEM image of two films (a) HW_Ts_2 and (b) HW_Ts_4

6.2.6 Thickness, optical constants and optical band gap calculation:

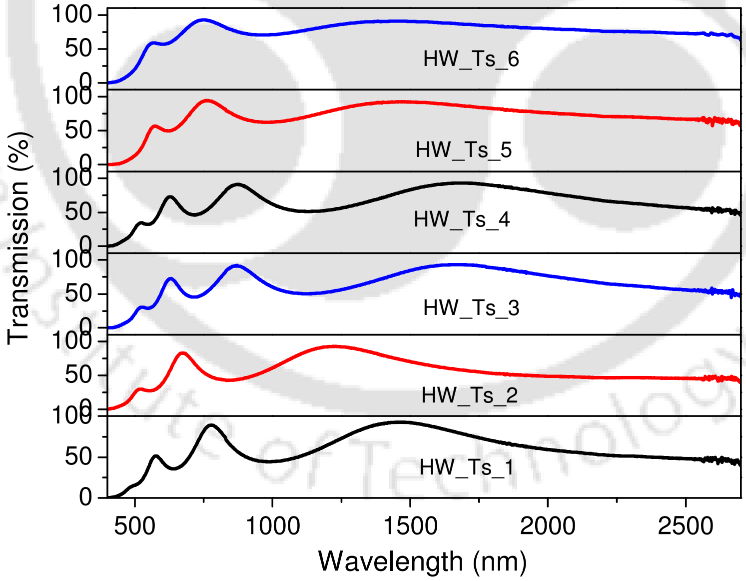

Figure 6.11: UV-Vis-NIR transmission spectra for the films reported in the present chapter

Figure 6.11 shows the UV-Vis-NIR transmission spectra of the films reported in the present chapter. The thickness, deposition rate (r_d) and optical constants of the films are estimated from the interference fringes in the UV-Vis-NIR transmission spectrum, while the band gap (E_G) is estimated from the $\sqrt{\alpha h\nu}$ vs $h\nu$ plot (Figure 6.12) in high absorption region of the spectra as discussed in Section 2.2.2.1. The results are listed in Table 6.4. It is observed that as the T_s increases from 100 to 350°C, r_d decreases from about 14 to 8 Å/Sec. This can be attributed to the temperature dependence of reaction probability and increase of silane desorption from the film surface. The surface mobility of the radicals is low at low T_s with high sticking co-efficient. So, the radicals get easily incorporated into the film. As the T_s increases, the surface mobility of the radicals increases. This facilitates the surface diffusion of the radicals to get energetically favourable sites, thus decreasing the deposition rate [1]. Also, higher T_s helps the spontaneous thermal breaking of weak Si-Si and Si-H bonds in the film surface thus reducing the film growth rate.

It is observed that E_G for these films lies in the range of 2.0-2.4 eV, which is higher compared to commonly reported values for Si:H films. The values of E04, i.e., energy for which the absorption is 10^4 cm^{-1} are found to be higher than the E_G, however, they follow the same trend with the deposition parameter like the values of E_G do. Figure 6.13 shows the variation of E_G and E04of the films as a function of T_s. We will elucidate the high E_G in the light of Raman and FTIR studies.

Table 6.4: Thickness, deposition rate (r_d), optical band gap (E_G) and energy value E04 calculated from UV-Vis-NIR transmission data.

Sample No.	T_s (°C)	Thickness (nm)	r_d (Å/Sec)	E_G (eV)	E04 (eV)
HW_Ts_1	100	325	13.5	2.04	2.29
HW_Ts_2	150	291	12.1	2.02	2.23
HW_Ts_3	200	296	12.3	2.34	2.38
HW_Ts_4	250	288	9.6	2.28	2.34
HW_Ts_5	300	194	8.03	2.24	2.37
HW_Ts_6	350	234	7.8	2.33	2.42

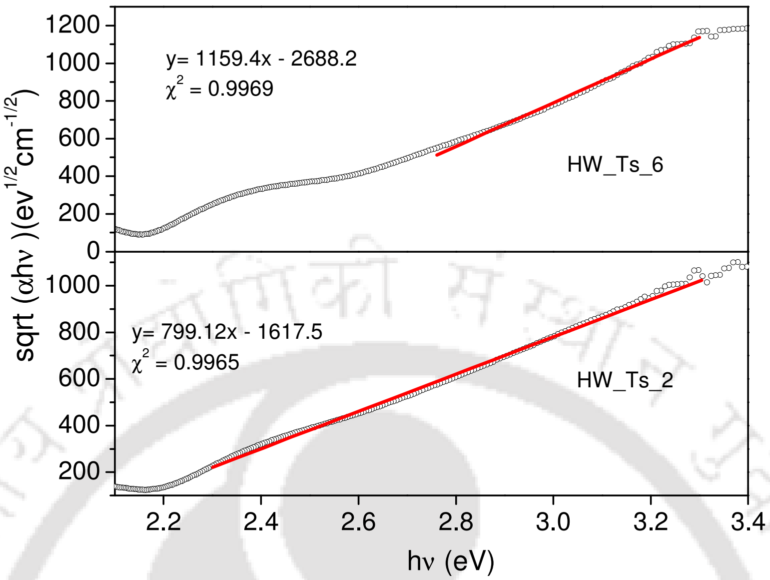

Figure 6.12: Plot of $\sqrt{\alpha h\nu}$ vs $h\nu$ for two different films (HW_Ts_2 and HW_Ts_6) to calculate the band gap.

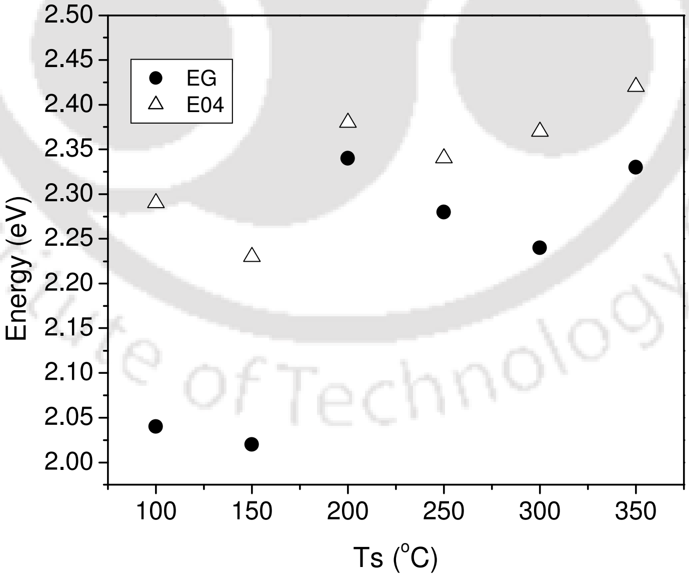

Figure 6.13: Variation of optical band gap (E_G) and E04 with substrate temperature. The error bars are included in the size of the symbol.

6.2.7 Infrared absorption studies:

Figure 6.14 shows the IR transmission spectra of the films, while figures 6.15a and 6.15b show the absorption band due to the wagging mode of vibration around 630 cm^{-1} and stretching mode of vibration around 2000-2100 cm^{-1} respectively. The hydrogen content, C_H in the films is estimated from the total IR absorption intensity under the peak corresponding to the wagging mode of silicon hydrogen bond as discussed in the Section 2.2.2.2. The percentage of hydrogen in monohydride mode and hence the microstructure factor R* are calculated by deconvoluting the stretching mode to the contributing monohydride and dihydride mode. Figure 6.16 shows the deconvoluted spectrum for a film (HW_Ts_2). The values of C_H and R* are listed in the Table 6.5. The values of C_H are found to be within the range of ~2.5-4.75 atomic % and agree well with the typical values for HWCVD films [11]. It is observed that the C_H content of amorphous films is more than 4 atomic % while nanocrystalline films possess C_H less than that (Figure 6.17).

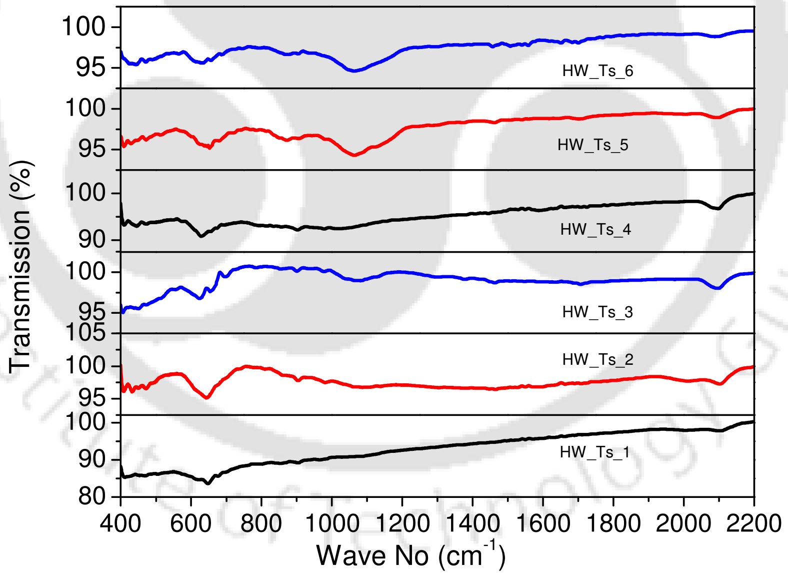

Figure 6.14: IR transmission spectra for the films reported in the present chapter.

The transition from amorphous to nanocrystalline is within T_s range of 150-200^{o}C and indicated by the sharp change in the values of C_H and R*. It is found that amorphous films have less R* than the nanocrystalline films. It is also observed that whether the films are amorphous or nanocrystalline, R* increases with increase in T_s. As the films become more ordered with the increase of T_s, the hydrogen content decreases. Like the films reported in the previous chapter, for these films also we have observed that the wagging mode bands are also not symmetric around the peak positions. This may be due to the presence of microstructure and variations in local bonding configurations. This is in agreement with Zhang *et al.* [12], Halindintwali *et al.* [13] and Han *et al.* [14] who also reported the deviation of the peak from symmetric shape with the development of crystallinity.

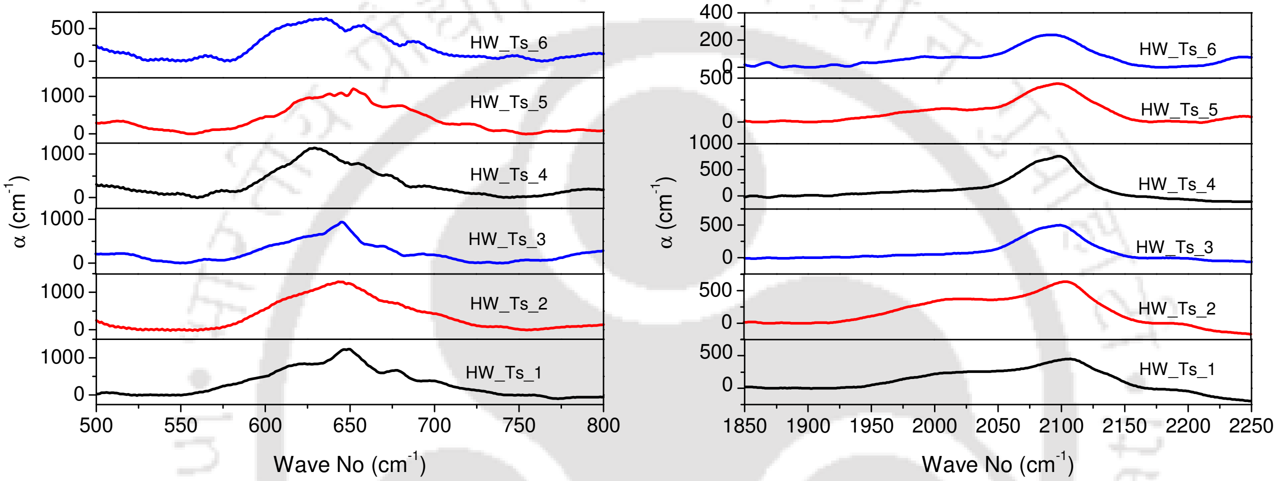

(a) (b)

Figure 6.15: Absorption coefficient at (a) wagging mode and (b) stretching mode of vibration for the films.

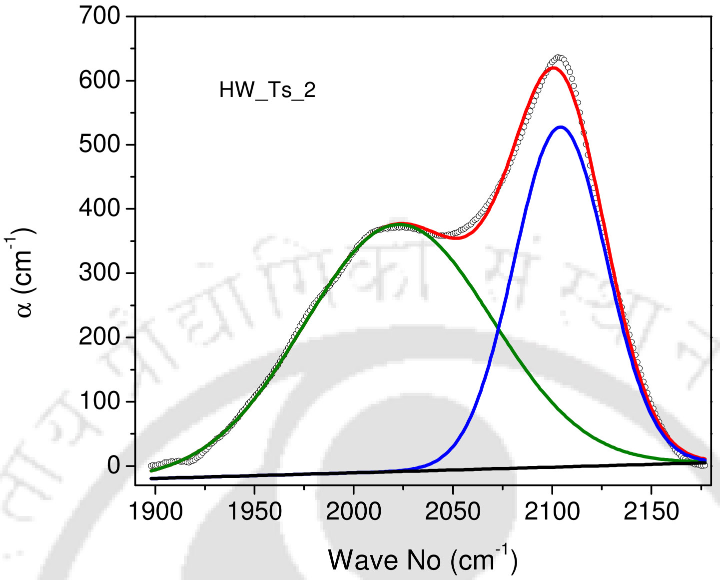

Figure 6.16: Deconvoluted IR absorption co-efficient in the stretching mode for a representative film (HW_Ts_2). The spectrum can be fitted with two peaks, one at 2000 cm^{-1} and the other at 2100 cm^{-1} corresponding to different modes of silicon hydrogen bonding.

Table 6.5: The hydrogen content C_H and microstructure factor (R*) for the films as estimated from IR transmission data.

Sample No	C_H (%)	R*
HW_Ts_1	4.33	0.515
HW_Ts_2	4.75	0.405
HW_Ts_4	2.59	0.79
HW_Ts_4	3.68	0.74
HW_Ts_5	3.59	0.69
HW_Ts_6	2.54	0.73

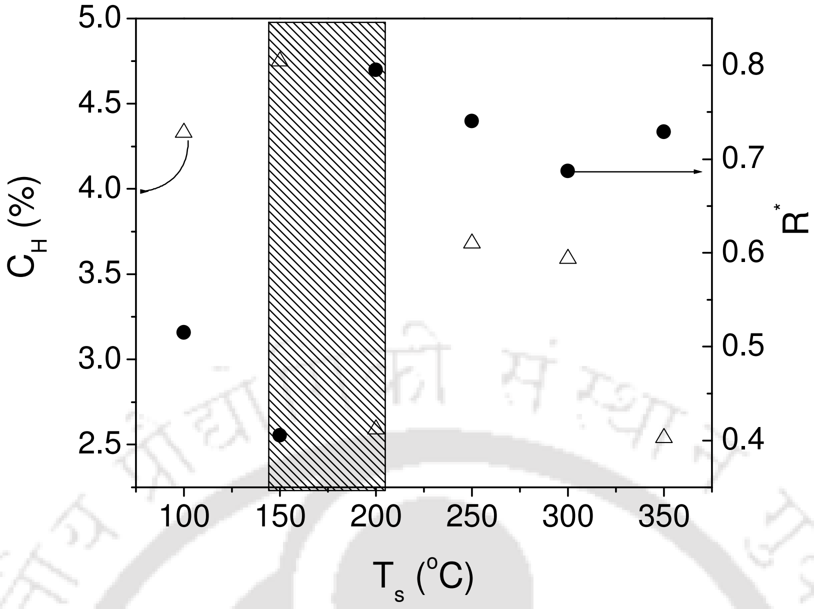

Figure 6.17: Variation of atomic percentage of hydrogen content (C_H) and microstructure factor (R*) with substrate temperature. Triangles represent C_H while circles represent R*.

It may appear at first sight that the films prepared under present study have hydrogen mainly bonded in dihydride and poly hydride mode. However it may not be so. It has been reported that for μc-Si:H films the stretching mode peak corresponding to Si-H bonds at the inner surface of microvoids, at the surface of crystalline portion and at GB appear at 2100 cm^{-1} [14-15] rather than 2000 cm^{-1} which is due to Si-H mode in amorphous tissues. However, the wag mode frequencies for these clustered Si-H do not shift much. John *et al.* [16] theoretically predicted that the small change in bond length produces sizeable changes in both the stretch mode peak frequency and FWHM, while leaving both wag mode peak frequency and FWHM virtually unchanged. This difference in response to the changes in the local environment may possibly be due to the fact that the stretch mode is dipole active whereas the wag mode is not. In our case, we observe that for amorphous films where GB is almost absent, the intensity under the 2100 cm^{-1} peak (i.e., R^*) in IR spectra is less. The value of R* increases as the GB fraction increases (figure 6.18). This implies that peak at 2100 cm^{-1} is at least partially related to the hydrogen bonded in the GBs. We also observe the peaks in the range 850-890 cm^{-1} which again are assigned to the silicon in dihydride and polyhydride modes as well due to the monohydride in GBs. Compared to PECVD films, HWCVD films exhibit higher structural inhomogeneity and larger percentage of clustered hydrogen [17-18], which results in high R*. Though the FTIR absorption spectra in as deposited films do not show any signature of the Si-O peaks, the feature appears in the nanocrystallites embedded films when the films are kept for a couple of weeks at room temperature under ambient conditions. This is the result of porous and less dense GBs of the nanocrystllites embedded films. When kept in ambient, atmospheric oxygen gets absorbed in the surfaces of micro-voids.

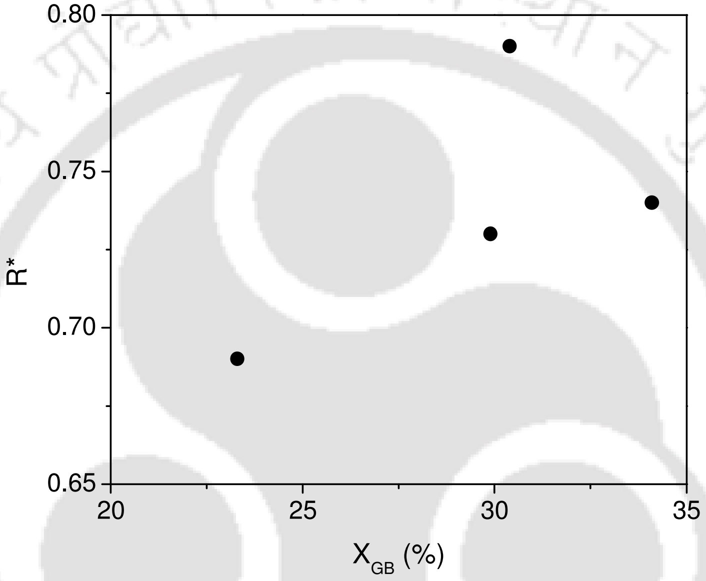

Figure 6.18: Variation of microstructure factor (R*) with the grain boundary fraction (X_{GB}).

In PECVD films the main film forming radical is SiH_3 which has less sticking coefficient; since it can only bond with dangling Si bonds and hence diffuses over the growing surface before it gets an energetically favorable site. This results in homogeneous structure, thereby making the growth CVD like [19]. In case of HWCVD, the primary radicals are atomic Si and H [6, 20] and hence depending on the gas phase reaction main film forming radical may be atomic Si which has high sticking coefficient. This results in PVD like growth and inhomogeneous as well as void rich material with large microstructure factor R* [21], especially at low T_s. At low T_s the film forming radicals do not acquire sufficient energy to diffuse to the energetically favourable site. Hence they stick to the growing surface wherever they strike resulting in a PVD like growth. This yields strained network with lower SRO and higher surface roughness. When T_s is increased, the radicals become more mobile to diffuse on the growing surface and find energetically favorable site. Hence the film growth becomes more CVD like with the improvement in SRO and smoother surface topography. An improvement in SRO leads to the formation of bigger crystallites and also larger X_c. The transition from amorphous to nanocrystalline in the T_s range 150- 200°C is evident from XRD, TEM and Raman studies and is also reflected in the variation of E_G, C_H, R* as well as rms roughness.

Now we elucidate on high E_G of the films under present study. The widening of the band gap of Si:H films has been attributed by various researchers to the presence of hydrogen, improvement of short and medium range order and also to the presence of the nanocrystallites. Si-H films with band gap larger than the normally observed 1.7-1.8 eV for films deposited by PECVD technique have been prepared by other researchers also. However, in most of the cases the band gap is around 2.0 eV except for the films prepared by Furukawa *et al.* [22] and Das *et al.* [23]. Furukawa *et al.* reported microcrystalline Si:H films with band gap lying in the range of 2.4 eV using magnetron sputtering technique. They discussed the high band gap in the light of quantum confinement occurring due to small sized crystallites. Das *et al.* reported high band gap PECVD films prepared by argon dilution and high rf power. However, they did not explain the origin of high band gap. It is interesting to note that in the case of HWCVD films where the hydrogen content is relatively much less compared to the PECVD films, the band gap is higher when the films have improved SRO and the formation of nanocrystallites. Mahan *et al.* [24] reported high band gap of HWCVD films (1.8-1.99 eV) and attributed the increased band gap to the improvement in both SRO and MRO (medium range order) after carefully subtracting the contribution of alloying due to hydrogenation. It has been argued that the widening of band gap is due to narrowing of band tail width because of the improvement in order as evident from the narrowing of Urbach edge for the films with low C_H. The observed increase in E04 which is related to the direct band gap of c-Si is also related to the improvement in order, which results in increase in splitting of bonding-antibonding states [22]. Since E04 is intimately related to the optical absorption, it is closely linked to the direct gap rather than the indirect gap of c-Si. With improving order the bonding-antibonding splitting of electronic states increases and direct gap or E04 is expected to increase [24]. Maley *et al.* also observed an increase in the band gap when the film SRO is improved [25]. They suggested that improved SRO widened the band gap by sharpening the valence band and possibly the conduction band tails. However, in our films under present studies, both E_G and E04 are found to be higher than reported by Mahan *et al.* Though Raman studies show improvement in order, this cannot be the only reason for the higher E_G. We attribute the high E_G of the films to the presence of low density amorphous tissues and microvoids in addition to the improvement of SRO. Generally nanocrystalline films prepared by HWCVD consist of silicon nanocrystallites surrounded by porous grain boundaries [26]. In the TEM micrograph of the studied films low density amorphous tissues surrounding high density grains are also clearly visible. The presence of low density tissues is also reflected by the high microstructure factor R*. As can be seen from the figure 6.19, R* seems to have correlation with the E_G; films with higher E_G show higher R*. This indicates that the high band gap is probably due to the presence of low density tissues and micro-voids in the films which reduce the effective density of the material and increase the average Si-Si distance. This also lowers the absorption in the films and shifts the transmission curve towards higher photon energy [1] thus increasing the optical band gap. If seen carefully, it is observed that the high band gap films reported by Das *et al.* [23] possess high R*. Hence we attribute the high band gap of the films under present studies to the presence of low density amorphous tissues and microvoids along with the improvement in short and medium range order of the films.

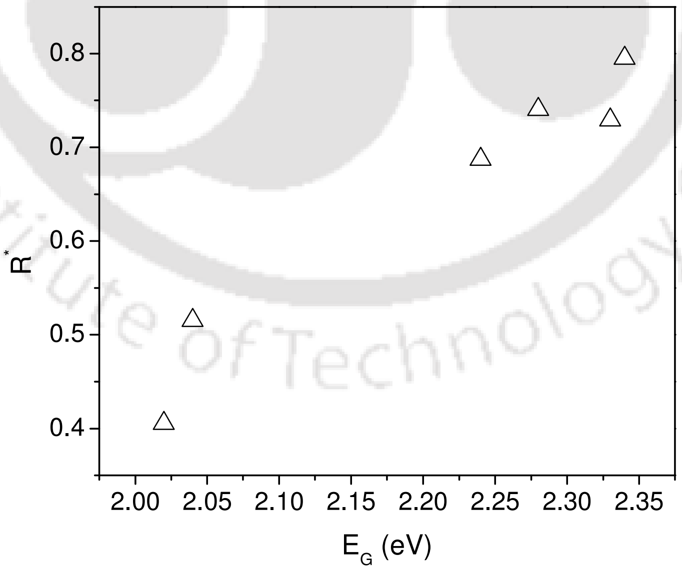

Figure 6.19: Variation of microstructure factor (R*) with the optical band gap (E_G) of the films.

6.2.8 Temperature dependent Conductivity and Stability studies:

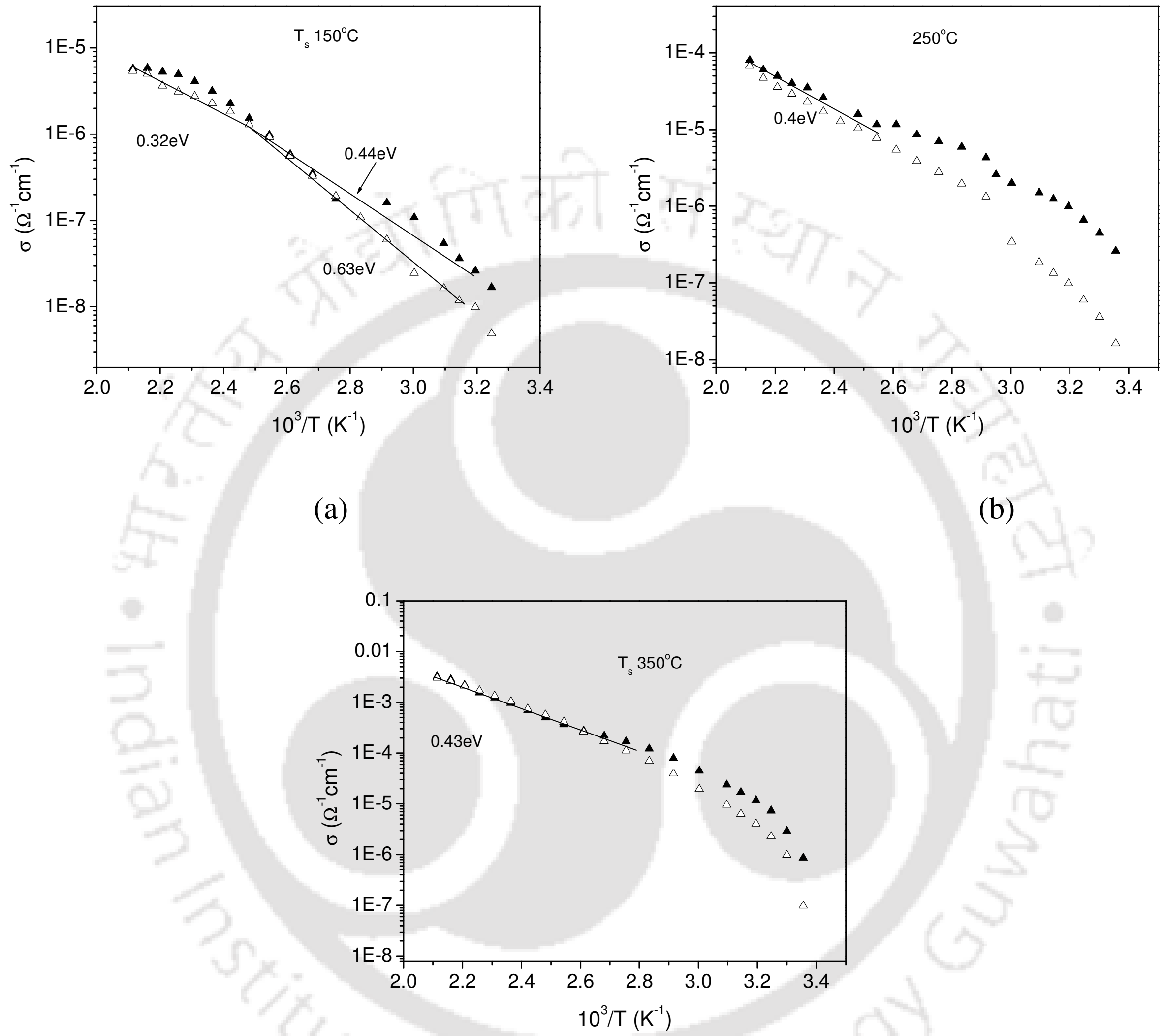

(a) (b)

(c)

Figure 6.20: Arrhenius plot for films (a) HW_Ts_2 (T_s 150^{o}C) (b) HW_Ts_4 (T_s 250^{o}C) (c) HW_Ts_6 (T_s 350^{o}C). Filled triangles are for annealed and empty triangles are for light soaked state

Figures 6.20a-6.20c show the temperature dependent dark conductivity in the annealed and light soaked state.The dark conductivities of the annealed films are of the order of 10^{-7}-10^{-8} Ω^{-1}cm^{-1} while photo conductivities are little higher than dark conductivities. Hence, the photosensitivities of the films are not very good. This is because of the nanocrystalline nature; the dark conductivities are high and of the order of photoconductivities. The films show very high activation energies at low temperature range (25-45°C) while the high temperature activation energies are lower (100-200°C). Stability studies show that the films are quite stable; the maximum decrease of conductivity is about one order of magnitude and can be annealed out at low equilibrium temperature (T_E), around 100°C. The conductivity and stability studies data are listed in Table 6.6.

Table 6.6: Conductivity and stability studies data for a few films in the annealed (annld) and light soaked state (LS) reported in the present chapter.

Sample No	T_s (°C)	σ_d (30°C) ($\Omega^{-1}cm^{-1}$)		σ_{ph} (30°C) ($\Omega^{-1}cm^{-1}$)		σ_{ph}/s_{ph} (annld)	E_d (eV)
		Annld	LS	Annld	LS		
HW_Ts_2	150	$1.66x10^{-8}$	$4.9x10^{-9}$	$2.95x10^{-8}$	$1.47x10^{-8}$	1.76	0.32
HW_Ts_4	250	$2.61x10^{-7}$	$1.62x10^{-8}$	$9.33x10^{-7}$	$1.09x10^{-7}$	3.58	0.40
HW_Ts_5	300	$2.22x10^{-7}$	$9.28x10^{-8}$	$4.79x10^{-7}$	$2.47x10^{-7}$	2.16	0.41
HW_Ts_6	350	$8.5x10^{-7}$	$9.77x10^{-8}$	$1.22x10^{-6}$	$2.44x10^{-7}$	1.43	0.43

6.3 Conclusion:

In this chapter the effect of substrate temperature on film microstructure and optoelectronic properties are studied. The deposition rate (r_d) obtained for the films are reasonably high (8-14 Å/Sec). We have achieved the transition of film microstructure from amorphous to mixed phase (nanocrystallites embedded amorphous) in the T_s range of 150-200 °C. It is observed that the crystallinity in the films increases with T_s. Amorphous films with good adhesion to the substrates are prepared at T_s as low as 100°C. We have observed high E_G (2.02-2.34 eV) though hydrogen content of the films is low (2.54-4.75 atomic %). The high E_G of the films are attributed to the improved order in the film microstructure as well as to the presence of voids and low density amorphous tissues surrounding the grain boundaries. Raman studies reveal good short range ($\Delta\theta_B$~ 6.5-7.5^o) and medium range (I_{TA}/I_{TO}~ 0.3-0.45) order of the films. The films are found to be very stable against prolonged light soaking and can be useful for stable devices.

6.4 References:

1. S. R. Jadkar, J. V. Sali, A. M. Funde, Nabeel Ali Bakr, P. B. Vidyasagar, R. R. Hawaldar and D. P. Amalnerkar, Sol Energy Mater. Sol. Cells **91** (2007) 714.
2. P. Alpuim, V. Chu and J. P. Conde, J. Appl. Phys. **86** (1999) 3812.
3. S. A. Filonovich, P. Alpuim, L. Rebouta, J. E. Bouree and Y. M.Soro, J. Non-Cryst. Solids **354** (2008) 2376.
4. M. Brinza, C. H. M. van der Werf, J. K. Rath and R. E. I. Schropp, J. Non-Cryst. Solids **354** (2008) 2248.
5. P. Brogueira, J. P. Conde, S. Arekat and V. Chu, J. Appl. Phys. **79** (1996) 8748.
6. C. Horbach, W. Beyer and H. Wagner, J. Non-Cryst. Solids **137-138** (1991) 661.
7. M. Stutzmann, *Amorphous Semiconductors,* Handbook of Semiconductors, North Holland Vol **3a** (1994), Ed. S. Mahajan.
8. M. Ito and M. Kondo, Jpn. J. Appl. Phys. **45** (2006) L230.
9. G. Morell, R. S. Katiyar, S. Z. Weisz, H. Jia, J. Shinar and I. Balberg, J. Appl. Phys. **78** (1995) 5120.
10. B. Yan, C. –S. Jiang, C. W. Teplin, H. R. Moutinho, M. M. A. Jassim, J. Yang and S. Guha, J. Appl. Phys. **101** (2007) 033712.
11. A. H. Mahan, J. Carapella, B. P. Nelson, R. S. Crandall and I. Balberg, J. Appl. Phys. **69** (1991) 6728.
12. S. Zhang, X. Liao, L Raniero, E. Fortunato, Y. Xu, G. Kong, H. Aguas, I. Ferreira and R. Martins, Sol. Energy Mater. Sol Cells **90** (2006) 3001.
13. S. Halindintwali, D. Knosen, R. Swanepoel, B. A. Julies, C. Arendse, T. Muller, C. C. Theron, A. Gordjin, P. C. P. Bronsveld, J. K. Rath and R. E. I. Schropp, Thin Solid Films **515** (2007) 8040.

14. D. Han, K. Wang, J. M. Owens, L. Gedvilas, B. Nelson, H. Habuchi and M. Tanaka, J. Appl. Phys. **93** (2003) 3776.
15. T. Itoh, K. Yamamoto, K. Ushikoshi, S. Nonomura and S. Nitta, J. Non-Cryst. Solids **266-269** (2000) 201.
16. P. John, I. M. Odeh, M. J. K. Thomas, M. J. Tricker and J. I B. Wilson, Phys. Status Solidi **B 103** (1981) K141.
17. Y. Wu, J. T. Stephen, D. Han, J. M. Rutland, R. A. Crandall and A. H. Mahan, Phys. Rev. Lett. **77** (1996) 2049.
18. D. Han, J. Baugh, G. Yue and Q. Wang, Phys. Rev. B **62** (2000) 7169.
19. A. Matsuda, J. Non-Cryst. Solids **338-340** (2004) 1.
20. J. Doyle, R. Robertson, G. H. Lin, M. Z. He and A. Gallagher, J. Appl. Phys. **64** (1988) 3215.
21. K. F. Feenstra, R. E. I. Schropp and W. F. Van der Weg, J. Appl. Phys. **85** (1999) 6843.
22. S. Furukawa and T. Miyasato, Phys. Rev. B **38** (1988) 5726.
23. D. Das, M. Jana and A. K. Barua, J. Appl. Phys. **89** (2001) 3041.
24. A. H. Mahan, R. Biswas, L. M. Gedvilas, G. D. Williamson and B. C. Pan, J. Appl. Phys. **96** (2004) 3818.
25. N. Maley and J. S. Lannin, Phys. Rev. B **36** (1987) 1146.
26. M. Fonrodona, D Soler, J.M. Asensi, J. Bertomeu and J. Andreu, J. Non-Cryst. Solids **299-302** (2002) 14.

Chapter -7

Hydrogen diluted HWCVD films: Effect of Process Pressure

Chapter 7

Hydrogen diluted HWCVD films: Effect of Process Pressure

In this chapter we report the studies of high optical band gap (E_G) silicon films prepared by varying the process pressure (PP) keeping the substrate temperature fixed at 250°C. The films are prepared by HWCVD method using hydrogen diluted silane (10% silane in hydrogen). The films are studied for structural, optical and electronic properties by various tools. All of these films are found to contain nanocrystallites randomly distributed in the amorphous network with 56-75 % crystalline fraction. The E_G of the films are found to be higher (2.21-2.37 eV) compared to those reported in literature. The films show good deposition rate (r_d ~ 3-11 Å/Sec) which is useful for the fabrication of cost effective devices.

7.1 Experimental Details:

The films are prepared using semiconductor grade hydrogen diluted silane (10 % silane in hydrogen) from Matheson Inc. The films are deposited on Corning 1737, ITO coated glass, c-Si wafer and carbon coated Cu grids for different studies by using a tungsten filament in the horizontal filament assembly. Prior to deposition, the chamber is evacuated to a base pressure of about 10^{-6} mbar and then 10 SCCM of silane is introduced into the chamber. The required process pressure (PP) is reached and maintained by throttling the chamber outlet. During deposition, filament temperature (T_F) and substrate temperatures are kept constant at 1800°C and 250° respectively, while the filament to substrate distance is kept fixed at 6 cm. Detailed deposition conditions are listed in Table 7.1.

The films are structurally characterized by X- ray diffraction (XRD), Raman spectroscopy, Transmission electron microscopy (TEM) and Atomic force microscopy (AFM). The details of the experimental techniques are discussed in the Chapter 2. XRD measurements are done using Siefert XRD 3003 TT in 2θ mode at grazing angle of incidence of 3° while SEM studies are performed by Leo 1430 VP scanning electron microscope. Raman scattering spectra are recorded by Witec Alpha Raman spectrometer with excitation wavelength of 514.1 nm in the scanning range of 100-1000 cm^{-1}. TEM studies are performed using JEOL TEM while AFM studies are performed by Picoplus Molecular Imaging in acoustic mode using silicon cantilevers with force constant 2.5 N/m and resonance frequency of 80 KHz. All these measurements are performed on the films deposited on Corning glass except TEM studies where films deposited on Cu grids are used. For optical characterization UV-Vis-NIR transmission spectra are recorded by Shimadzu UV 3101 PC in the range 3000- 350 nm on the films deposited on Corning 1737, while IR transmission spectra are recorded on the films deposited on c-Si wafer in the range of 400-4000 cm^{-1} using Perkin Elmer BXII FTIR spectrometer. The transport studies are done in coplanar geometry by temperature dependent dark and photoconductivity measurements and stability studies by light soaking. For photoconductivity measurements and light soaking a light source of 100 Watt is used.

Table 7.1: Deposition details of the films under present study. Here, T_F, SFR, T_s and PP mean filament temperature, silane flow rate, substrate temperature and process pressure respectively. The only intentional variable in these films is the PP.

Sample No.	T_F (^oC)	SFR (10% SiH_4 in Hydrogen) (SCCM)	T_s (^oC)	PP (mbar)
HW_PP_1	1800	10	250	0.02
HW_PP_2				0.05
HW_PP_3				0.08
HW_PP_4				0.2
HW_PP_5				0.5
HW_PP_6				0.8

7.2 Results and Discussions:

7.2.1 X-ray diffraction studies:

Figure 7.1 shows the XRD pattern for the films under present study. All the films reported in this chapter are found to be nanocrystallites embedded amorphous in nature as indicated by the emergence of sharp peaks corresponding to (111), (220) and (311) planes of crystalline silicon superimposed on the broad amorphous pattern. The nanocrystalline nature is expected as the films are deposited at an intermediate substrate temperature (T_s) of 250°C. We have seen in the earlier chapter that the films deposited at T_s ≥200°C are nanocrystalline. The crystallite sizes (d_{XRD}) for these films are calculated using Scherrer formula as mentioned in the Section 2.2.1.1 and found to be ~ 6-11 nm. These values are listed in the table 7.2 along with the Raman results. The FWHM of the broad (111) amorphous peak remains in the range 8.79-10.56°. More crystalline films possess low values of FWHM for the broad peak corresponding to amorphous phase, which is a result of the structural improvement in these films.

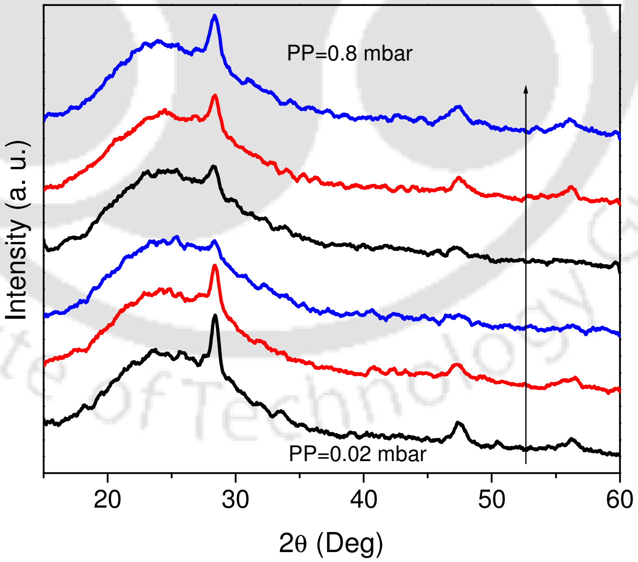

Figure 7.1: X-ray diffraction pattern of the films prepared by varying the process pressure (PP).

7.2.2 Raman scattering spectroscopy:

Raman scattering spectra for the films discussed in the present chapter are shown in the Figure 7.2. Like XRD studies, Raman measurements also show mixed phase (nanocrystallites embedded amorphous) nature of the films with the appearance of sharp peak near 520cm^{-1} superimposed on the broad amorphous peak at 480 cm^{-1}. For the estimation of different parameters like total crystalline fraction (X_c), grain boundary fraction (X_{GB}), both short range and medium range order (SRO and MRO) given by rms deviation of tetrahedral bond angle ($\Delta\theta_B$) and intensity ratio of amorphous TA and TO peak (I_{TA}/I_{TO}), crystallite size (d_R) etc., the spectra are deconvoluted (Figure 7.3) into different contributing peaks as mentioned in the Section 2.2.1.3. These parameters are listed in table 7.2.

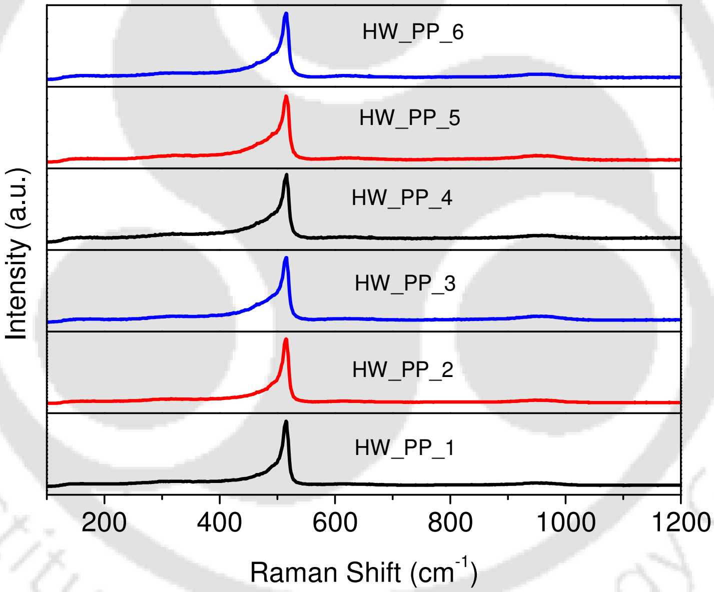

Figure 7.2: Raman scattering spectra for the films prepared with varying PP.

The total crystalline fraction (X_c) for these films ranges from 56 to 75%. It is observed that the X_c decreases as the PP increases upto 0.5mbar and again increases (Figure 7.4). This increase in X_c is due to the increase in both grain boundary fraction (X_{GB}) as well as nanocrystalline fraction (X_{nc}), as evident from figure 7.5. This is unlike the films reported in the previous chapter, where X_{nc} was almost constant and the increase in total crystalline fraction was mainly due to increase in contribution from the grain boundaries. The films show good SRO characterized by low rms deviation of bond angle ($\Delta\theta_B$) of 4.38- 6.75^o from the tetrahedral angle of 109^{o}28″ [1]. The films also possess good medium range order (MRO), inferred from low I_{TA}/I_{TO} values (0.3-0.5) and matches well with that of device quality films [2-3]. The crystallite sizes as calculated from Raman data (d_R) are ~ 4 nm. This crystallite sizes estimated from Raman data are almost constant, however those from XRD data increases with the increase in X_c. Figure 7.6 shows the variation of the FWHM of the amorphous XRD (111) peak with X_c. It is observed that as the X_c increases the FWHM decreases, hence the lowering of amorphous XRD peak FWHM is an indication of the ordered structure. This is in agreement with the findings of Mahan *et al.* [4].

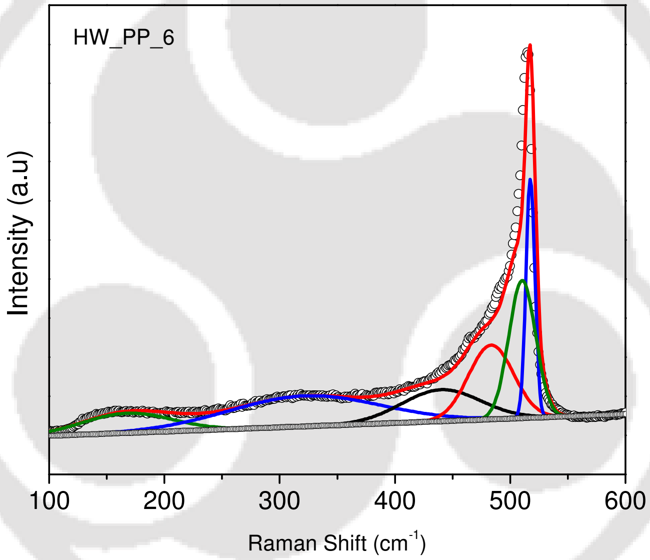

Figure 7.3: Deconvoluted Raman scattering spectrum for the film prepared with PP 0.8mbar (HW_PP_6).

Table 7.2: Total crystalline fraction (X_c), grain boundary fraction (X_{GB}), rms deviation of tetrahedral bond angle ($\Delta\theta_B$), medium range order parameter (I_{TA}/I_{TO}), crystallite size calculated from Raman and XRD data (d_R and d_{XRD}) respectively.

Sample No.	PP (mbar)	X_c (%)	X_{nc} (%)	X_{GB} (%)	$\Delta\theta_B$ (°)	MRO (I_{TA}/I_{TO})	d_R (nm)	d_{XRD} (nm)
HW_PP_1	0.02	74.8	31.4	43.4	4.44	0.5	3.94	10.99
HW_PP_2	0.05	75.2	30.9	44.3	4.38	0.48	3.97	8.71
HW_PP_3	0.08	59.8	27.6	32.2	6.22	0.29	3.98	5.83
HW_PP_4	0.2	59.8	26.1	33.7	6.75	0.39	4.02	7.23
HW_PP_5	0.5	55.9	21.8	34.1	6.47	0.32	4.25	6.82
HW_PP_6	0.8	63.7	23.5	40.2	5.31	0.49	3.95	7.93

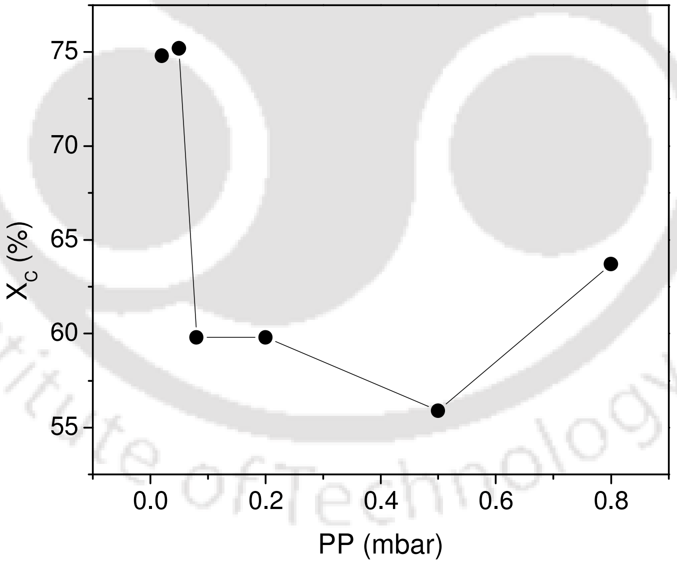

Figure 7.4: Variation of total crystalline fraction (X_c) with process pressure (PP). Error bars are included in the size of the symbols.

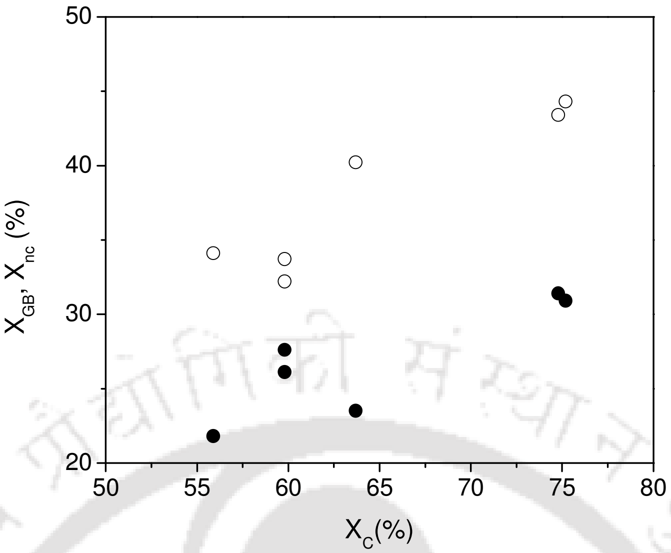

Figure 7.5: Plot of grain boundary fraction (X_{GB}) and nanocrystalline fraction (X_{nc}) with the total crystalline fraction (X_c). The empty symbols correspond to X_{GB} while filled symbols correspond to X_{nc}. Error bars are included in the size of the symbols.

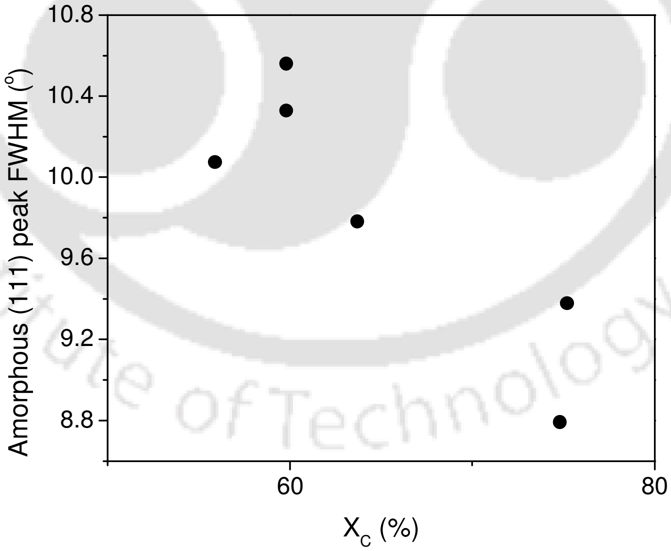

Figure 7.6: Variation of FWHM of the amorphous (111) peak with total crystalline fraction (X_C). Error bars are included in the size of the symbols.

7.2.3 Transmission electron microscopy:

The selected area diffraction (SAD) patterns for two representative films are shown in the figures 7.7a and 7.7b. For all the films sharp rings with bright spots are observed. The most intense ring is observed for (111) plane. Rings corresponding to (220) and (311) planes are also sufficiently bright, whereas the rings corresponding to higher planes *viz.* (400), (331), (422) have diminishing intensity. The appearance of sharp spotty rings in the SAD pattern indicates of the formation of nanocrystallites in the amorphous matrix. The low resolution TEM images for these films are shown in figures 7.8a and 7.8b. The images show three different types of tissues *viz.* randomly distributed dark spots of about 10 nm, the lighter region which form the matrix of the film and white thread like surrounding the lighter region of a diameter of about 20 nm. Under high magnification, the dark spots and nearby regions show the formation of crystallites as evident from the high resolution TEM (HRTEM) image in figure 7.9. The size of such crystallites are about 5-10 nm with lattice spacing ~ 0.3 nm corresponding to silicon crystals. Hence it is inferred that the nanocrystallites (dark regions) are randomly distributed in the amorphous network (lighter regions). The amorphous matrix also contains low density amorphous tissues (white threads like structures) in it [5].

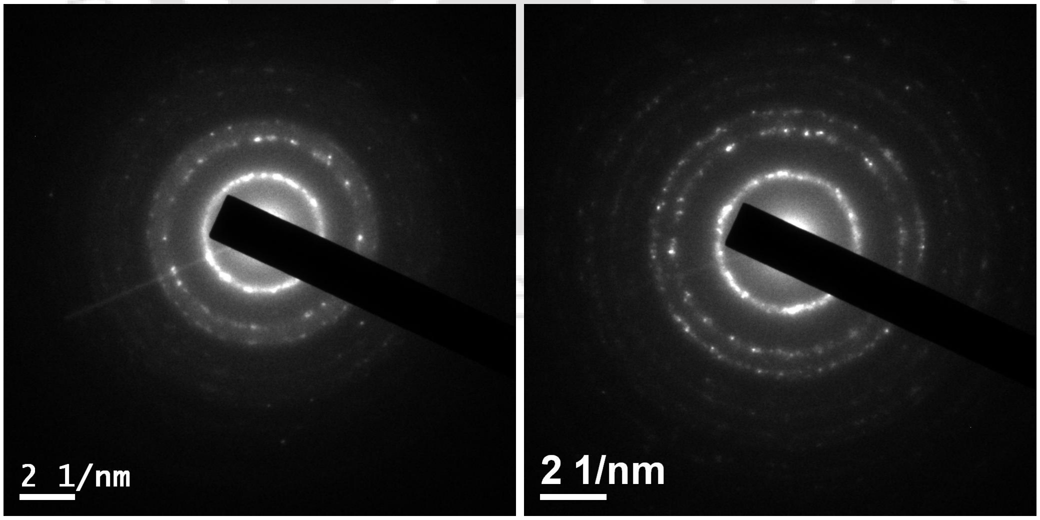

(a) (b)

Figure 7.7: SAD pattern for films (a) HW_PP_4 and (b) HW_PP_6

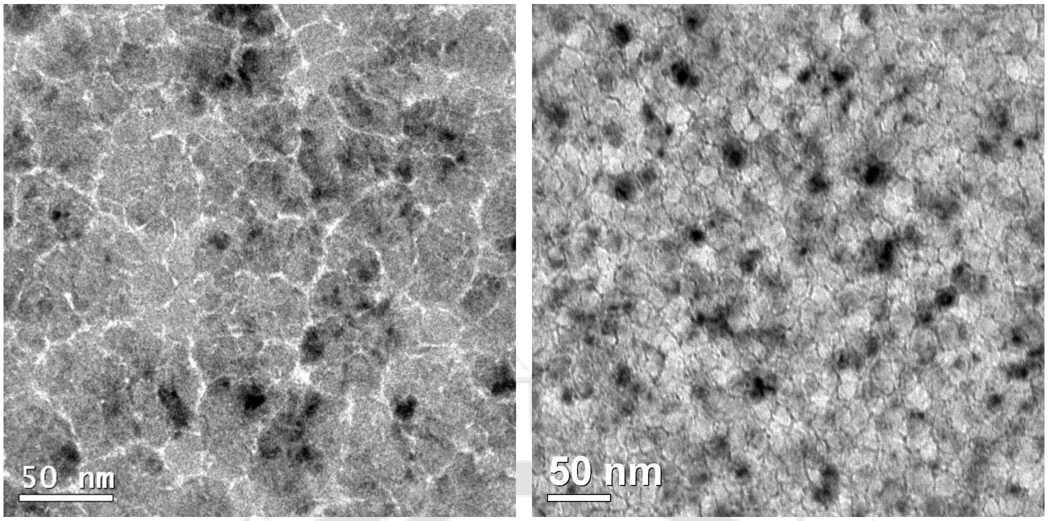

(a) (b)

Figure 7.8: Low resolution TEM image for films (a) HW_PP_4 and (b) HW_PP_6

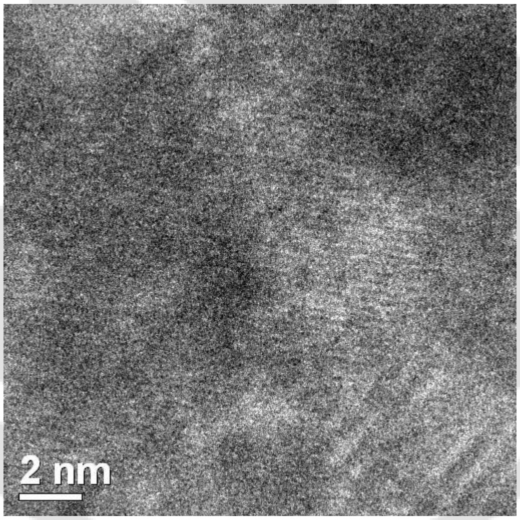

Figure 7.9: HRTEM image of a film (HW_PP_6) showing the formation of nanocrystallites.

7.2.4 Atomic force microscopy:

Figures 7.10a- 7.10d show the AFM images (surface topography) of a few representative films. Though all the films are nanocrystallites embedded amorphous in nature, there is large variation in their surface morphology. However, it is observed that the films possess almost constant rms roughness (r_{rms}) of about 9±3 nm except for the film with PP of 0.2 mbar, which is too high (33nm). This film has very less thickness (125nm) compared to others. The r_{rms} values for different films are listed in Table 7.3. Figure 7.11 shows the variation of r_{rms} with the film thickness.

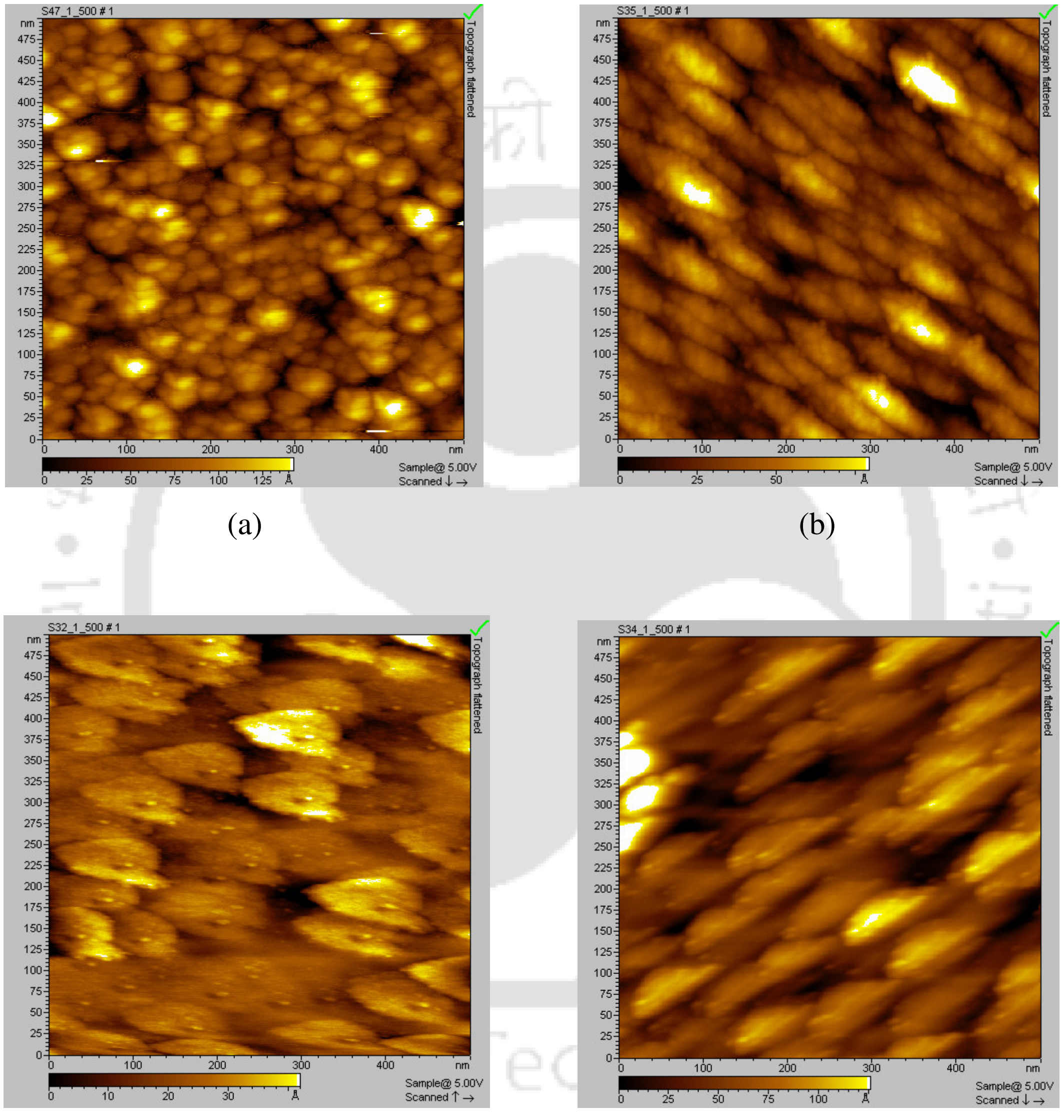

(a) (b)

(c) (d)

Figure 7.10: AFM images showing the surface topography of films (a) HW_PP_1 (b) HW_PP_3 (c) HW_PP_4 (d) HW_PP_6

Table 7.3: rms roughness (r_{rms}) of the films as calculated from AFM data.

Sample No	HW_PP_1	HW_PP_2	HW_PP_3	HW_PP_4	HW_PP_5	HW_PP_6
r_{rms} (nm)	12	7.4	11	33	6.5	10

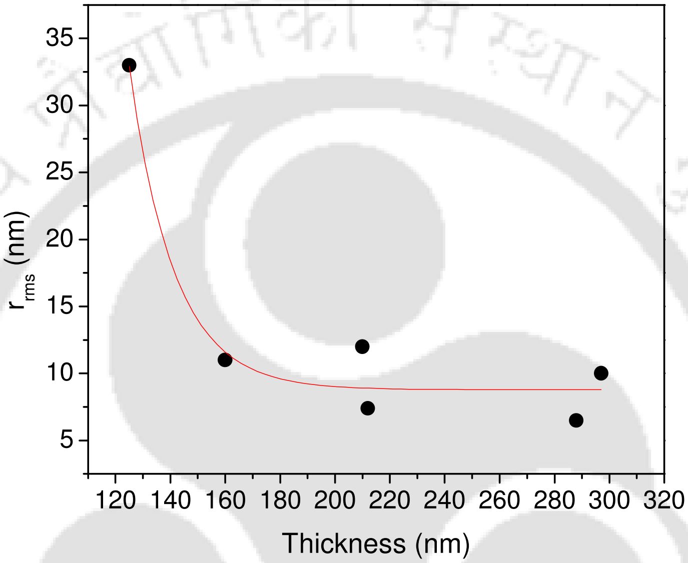

Figure 7.11: Plot of rms variation of surface roughness (r_{rms}) with the thickness of the film. The error bars are included in the size of the symbol.

7.2.5 Thickness, optical constants and optical band gap calculation:

Figure 7.12 shows the UV-Vis-NIR transmission spectra of the films reported in the present chapter. The thickness and optical constants are estimated from the interference fringes in the UV-Vis-NIR transmission spectrum as discussed in Section 2.2.2.1, while deposition rate (r_d) is calculated from the estimated thickness and are listed in table 7.4. The r_d estimated from the thickness is found to be in the range of 2.5-11 Å/Sec. The r_d increases with the increase in process pressure (PP). This is expected as with the increase in PP the growing film receives more film forming radicals which results in higher r_d. The E_G of the films are calculated from the plot of $\sqrt{\alpha h\nu}$ *vs* $h\nu$ as shown in the figure 7.13. The E_G thus estimated for the present films are found to be 2.21-2.37eV, which is much higher than the E_G of 1.7-1.8eV for the regular PECVD. The energy values for which absorption coefficient becomes 10^4 cm^{-1}(E04) for these films are also very high. These values are like the films prepared from 10 % silane in hydrogen by varying the substrate temperature as mentioned in Chapter 6. Like those films, we attribute the high band gap values to the improved order, formation of nanocrystallites and the existence of low density amorphous tissues surrounding the grain boundary regions as supported by Raman and TEM studies.

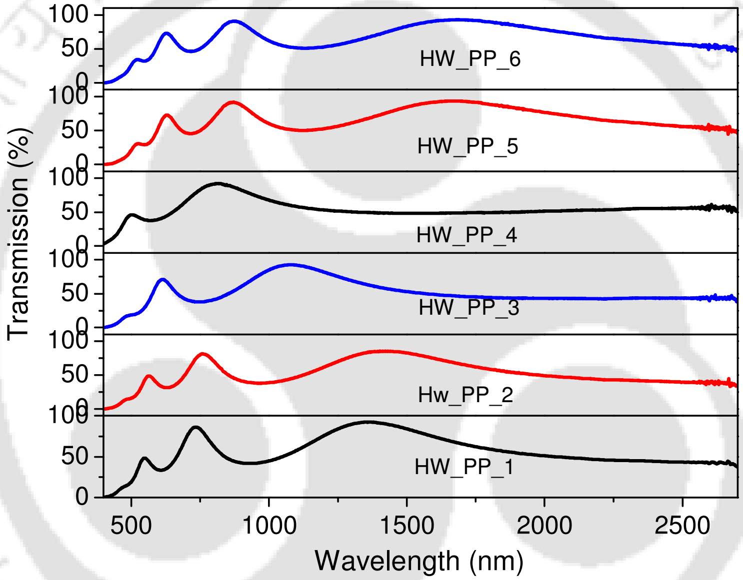

Figure 7.12: UV-Vis-NIR transmission spectra for the films reported in the present chapter

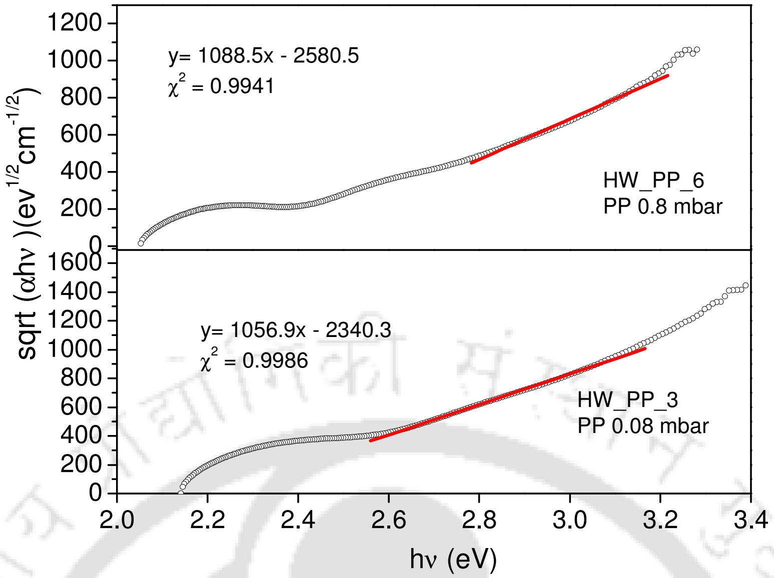

Figure 7.13: Plot of $\sqrt{\alpha h\nu}$ *vs* $h\nu$ for two representative films to calculate the band gap

Table 7.4: Thickness, deposition rate (r_d), optical band gap (E_G), energy E04, for which absorption coefficient becomes 10^4 cm^{-1}determined from UV-Vis-NIR transmission spectra.

Sample No.	PP (mbar)	Thickness (nm)	r_d (Å/Sec)	E_G (eV)	E_{04} (eV)
HW_PP_1	0.02	210	2.5	2.29	2.46
HW_PP_2	0.05	212	3.53	2.25	2.51
HW_PP_3	0.08	160	4.4	2.21	2.48
HW_PP_4	0.2	125	5.2	2.31	2.56
HW_PP_5	0.5	288	9.6	2.28	2.34
HW_PP_6	0.8	297	11	2.37	2.37

7.2.6 Infrared absorption spectroscopy:

Figure 7.14 shows the IR transmission spectra of the films reported in the present chapter. The spectra consist of absorption bands due to wagging mode and stretching mode of silicon hydrogen bond vibration at 630cm^{-1} and 2000-2100 cm^{-1} respectively. Figures 7.15a and 7.15b show the absorption coefficients in the wagging and stretching mode respectively. A few films show the presence of oxygen (absorption band in the range of 1000-1100 cm^{-1}) also. The hydrogen content, C_H, in the films is estimated from the total IR absorption intensity under the peak corresponding to the wagging mode of silicon hydrogen bond vibration, where as the microstructure factor R* is calculated from the intensity ratio between the monohydride and polyhydride stretching mode (figure 7.16) as discussed in the Section 2.2.2.2 and are listed in table 7.5. The values of C_H (3.3-5 atomic %) agree well with the typical values for HWCVD films [6]. Like the films reported in the previous chapter, here also the wagging mode peak is not symmetric around the peak position which may be due to the presence of microstructure and variations in local bonding configurations. This is in agreement with reports of Halindintwali *et al.*[7] and Zhang *et al.*[8] These films possess high values of R* as also observed in the films reported in chapter 6 prepared from heavily hydrogen diluted silane (10% silane in hydrogen) and by varying the substrate temperature. However high R* may not necessarily indicate the dihydride and poly hydride mode as discussed in Chapter 6. It has been reported that for μc-Si:H films, the stretching mode peak corresponding to Si-H bonds at the inner surface of microvoids, at the surface of crystalline portion and at GB appear at 2100 cm^{-1} [9-10] rather than 2000 cm^{-1} occurring for amorphous tissues. John *et al.* [11] theoretically predicted that the small change in bond length produces sizeable changes in both the stretch mode peak frequency and FWHM, while leaving both wag mode peak frequency and FWHM virtually unchanged. This difference in response to the changes in the local environment may possibly be due to the fact that the stretch mode is dipole active whereas the wag mode is not. The value of R* increases as the GB fraction increases (Figure 7.17). This implies that the peak at 2100 cm^{-1} is at least partially related to the hydrogen bonded in the GBs. We also observe the peaks in the range 850-890 cm^{-1} which again are assigned to the silicon in dihydride and polyhydride modes as well due to the monohydride in GBs [10]. The porous and less dense GBs also results in the oxygen absorption as observed in some films and also after storing these for a couple of weeks at room temperature under ambient conditions.

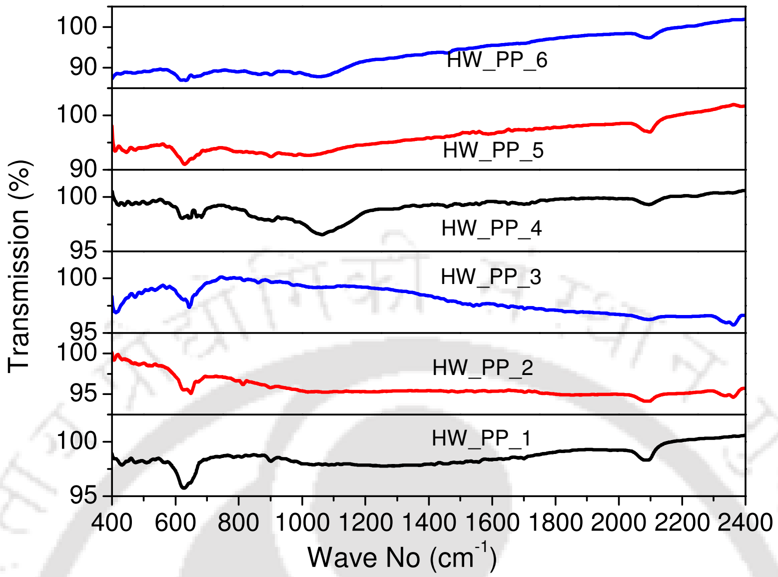

Figure 7.14: Infrared transmission spectra of the films prepared with varying PP.

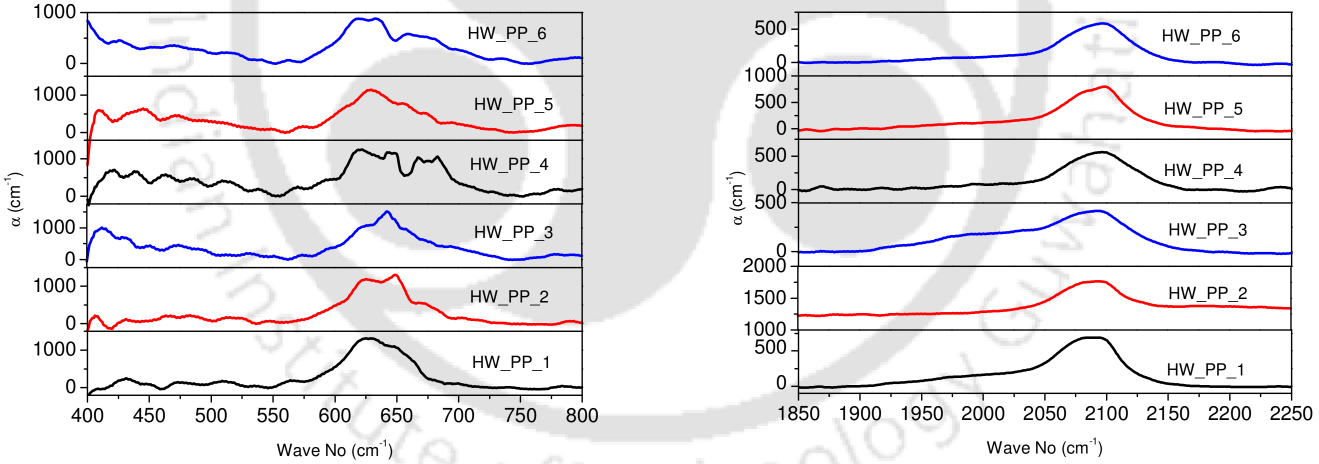

(a) (b)

Figure 7.15: Absorption coefficients in the (a) wagging mode and (b) stretching of silicon hydrogen bond vibration.

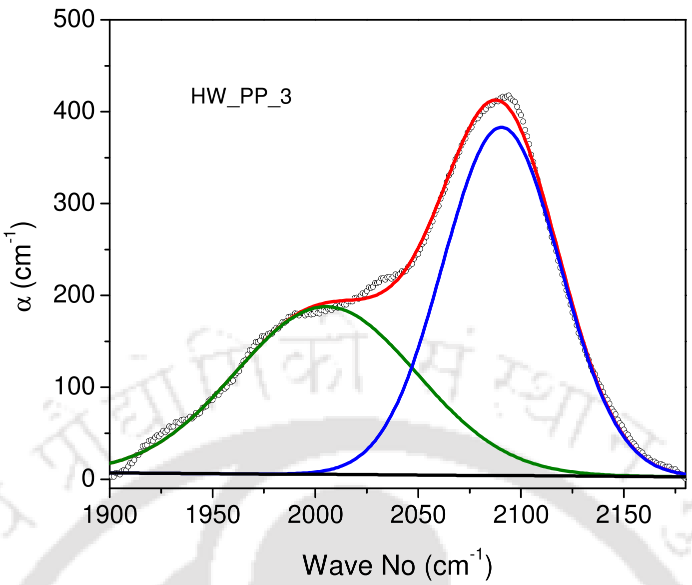

Figure 7.16: Deconvoluted absorption coefficients in the stretching mode of silicon hydrogen bond vibration for the film with PP 0.08 mbar (HW_PP_3).

Table 7.5: Atomic percentage of hydrogen content (C_H) and microstructure factor (R*) in the films.

Sample No.	C_H (%)	R*
HW_PP_1	4.89	0.69
HW_PP_2	4.94	~1
HW_PP_3	4.36	0.57
HW_PP_4	4.99	0.88
HW_PP_5	3.68	0.74
HW_PP_6	3.26	0.8

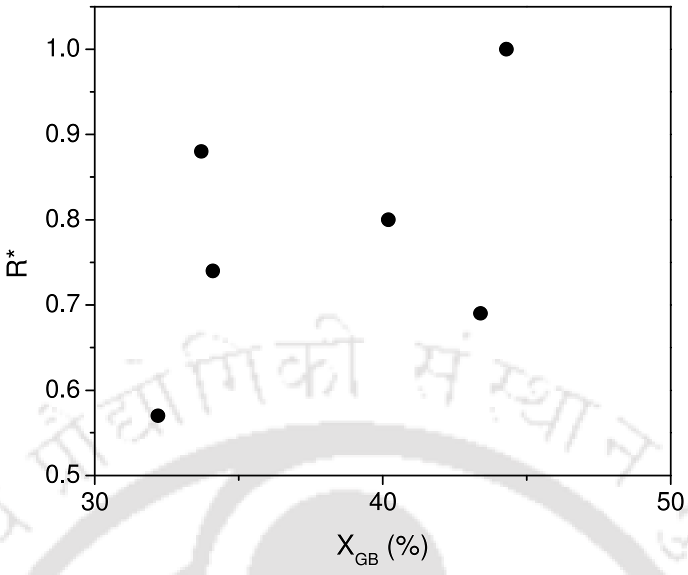

Figure 7.17: Variation of microstructure factor (R*) with the grain boundary fraction (X_{GB}). The error bars are included in the size of the symbols.

The high values of E_G of the films under present study are attributed to the presence of low density amorphous tissues surrounding the GB regions in addition to the improvement in short and medium range order and also the presence of nanocrystallites like the films reported in the previous chapter. The films reported in both the chapters are prepared from the same source gas (10% silane in hydrogen) and both types of films show very high band gap (up to 2.4eV). Generally, nanocrystalline films prepared by HWCVD consist of silicon nanocrystallites surrounded by porous grain boundaries [5]. In the TEM micrograph of the studied films, low density amorphous tissues surrounding high density grains are also clearly visible. The presence of low density tissues is also reflected by the high microstructure factor R*. As can be seen from the figure 7.18, R* seems to have correlation with the E_G, films with higher E_G show higher R* like the films reported in the Chapter 6. This indicates that the high band gap is probably due to the presence of low density tissues and micro-voids in the films which reduces the effective density of the material and increases the average Si-Si distance. This lowers the absorption in the films and shifts the transmission curve towards higher photon energy [12], thus increasing the optical band gap.

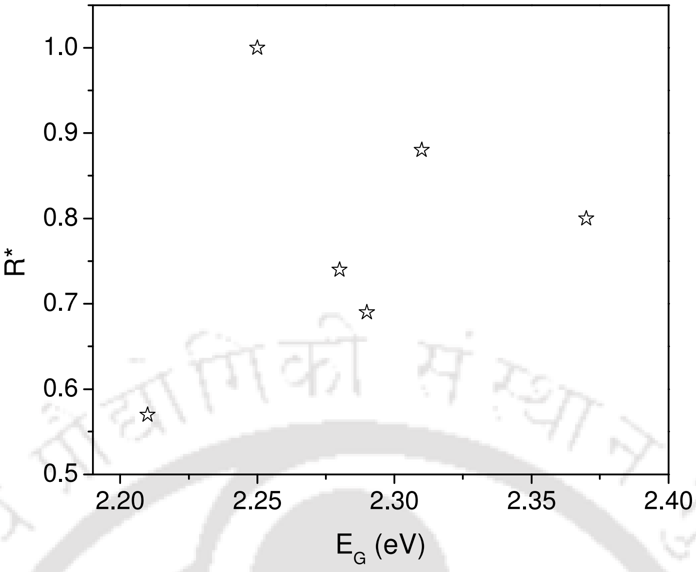

Figure 7.18: Variation of microstructure factor (R*) with optical band gap (E_G).

7.2.7 Temperature dependent Conductivity and Stability studies:

Figures 7.19a and 7.19b show Arrhenius plot in the range from room temperature to 200^{o}C for two representative films HW_PP_3 and HW_PP_5 respectively. The dark conductivities of the annealed films are of the order of 10^{-7}-10^{-8} $\Omega^{-1}cm^{-1}$ while photo conductivities are about double of dark conductivities yielding low photo-sensitivity. These films show thermally activated conduction with very high activation energies at low temperature (25-45^{o}C) and low activation energies at high temperature (100-200^{o}C) range. The dual activation energy is the result of mixed phase nature of the films. The conductivity and stability studies data are listed in Table 7.6. The conductivity of the films do not degrade much after light soaking of 12 hours with illumination from a 100W lamp. The light is water filtered during the light soaking experiment to avoid heating of the films and the light soaking is limited to 12 hours as the changes saturates after a few hours of illumination. The maximum decrease of conductivity is about one order of magnitude and can be annealed out at low equilibrium temperature (T_E), around 100^{o}C. We associate the high stability of the films with their ordered structure as can also be seen in structural studies like XRD, Raman and TEM.

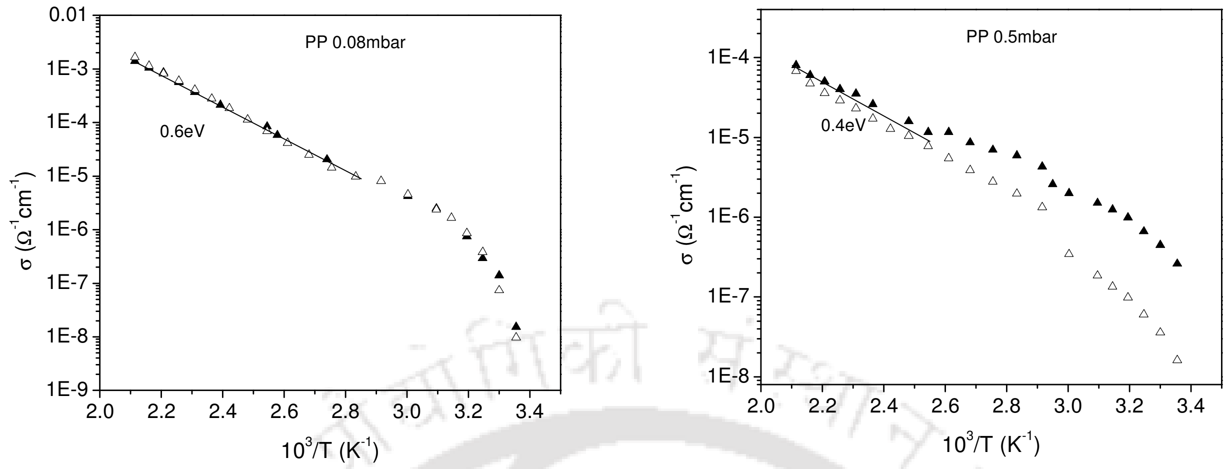

(a) (b)

Figure 7.19: Arrhenius plot for the films (a) HW_PP_3 (PP=0.08mbar) and (b) HW_PP_5 (PP=0.5mbar). Filled triangles are for annealed and empty triangles are for light soaked state.

Table 7.6: Conductivity and stability studies data in the annealed and light soaked state for few films under present study.

Sample No	PP (mbar)	σ_d (30^o) (Ω^{-1}cm^{-1})		σ_{ph} (30^o) (Ω^{-1}cm^{-1})		σ_{ph}/σ_d (Annld)	E_d(eV)
		Annld	LS	Annld	LS		
HW_PP_3	0.08	1.53x10^{-8}	9.72x10^{-8}	3.19x10^{-8}	2.5x10^{-8}	2.1	0.60
HW_PP_5	0.05	2.61x10^{-7}	1.62x10^{-8}	9.33x10^{-7}	1.09x10^{-7}	3.58	0.40

7.3 Conclusion:

In this chapter the structural, optical and electrical studies on nanocrystallites embedded amorphous silicon films prepared from hydrogen diluted silane by varying the process pressure are presented. The films are deposited at reasonably high deposition rates (3-11Å/Sec). All of these films are found to contain nanocrystallites randomly distributed in the amorphous network with 56 to 75 % crystalline fraction. The films possess good short and medium range order

($\Delta\theta_B$~ 4.38-6.75°, I_{TA}/I_{TO} ~ 0.3-0.5). The E_G of the films are found to be higher (2.21-2.37 eV) compared to those reported in literature, even though the hydrogen content is low (3.3-5 atomic %). The high E_G of the films is attributed to the nanocrystallite formation as well as to the presence of voids and low density amorphous tissues surrounding the grain boundaries. The films suffer very less light induced degradation under prolonged illumination. The light induced changes could be annealed out at temperature around 100°C, called equilibrium temperature (T_E). Less light induced degradation of the films are attributed to the improved order as supported by structural studies.

7.4 References:

1. M. Stutzmann, *Amorphous Semiconductors,* Handbook of Semiconductors, North Holland Vol **3a** (1994), Ed. S. Mahajan.
2. M. Ito and M. Kondo, Jpn. J. Appl. Phys. **45** (2006) L230.
3. G. Morell, R. S. Katiyar, S. Z. Weisz, H. Jia, J. Shinar and I. Balberg, J. Appl. Phys. **78** (1995) 5120.
4. A. H. Mahan, R. Biswas, L. M. Gedvilas, G. D. Williamson and B. C. Pan J. Appl. Phys. **96** (2004) 3818.
5. M. Fonrodona, D Soler, J.M. Asensi, J. Bertomeu and J. Andreu, J. Non-Cryst. Solids **299-302** (2002) 14.
6. A. H. Mahan, J. Carapella, B. P. Nelson, R. S. Crandall and I. Balberg, J. Appl. Phys. **69** (1991) 6728.
7. S. Halindintwali, D. Knosen, R. Swanepoel, B. A. Julies, C. Arendse, T. Muller, C. C. Theron, A. Gordjin, P. C. P. Bronsveld, J. K. Rath and R. E. I. Schropp, Thin Solid Films **515** (2007) 8040.
8. S. Zhang, X. Liao, L Raniero, E. Fortunato, Y. Xu, G. Kong, H. Aguas, I. Ferreira and R. Martins, Sol. Energy Mater. Sol Cells **90** (2006) 3001.
9. D. Han, K. Wang, J. M. Owens, L. Gedvilas, B. Nelson, H. Habuchi and M. Tanaka, J. Appl. Phys. **93** (2003) 3776.

10. T. Itoh, K. Yamamoto, K. Ushikoshi, S. Nonomura and S. Nitta, J. Non-Cryst. Solids **266-269** (2000) 201.
11. P. John, I. M. Odeh, M. J. K. Thomas, M. J. Tricker and J. I B. Wilson, Phys. Status Solidi **B 103** (1981) K141.
12. S. R. Jadkar, J. V. Sali, A. M. Funde, Nabeel Ali Bakr, P. B. Vidyasagar, R. R. Hawaldar and D. P. Amalnerkar, Sol Energy Mater. Sol. Cells **91** (2007) 714.

Chapter -8

HWCVD films: Effect of Silane Flow Rate

Chapter 8

HWCVD films: Effect of Silane Flow Rate

This chapter presents the studies on the HWCVD films prepared from pure silane by varying the silane flow rate (SFR). The microstructures of the films are varied from pure amorphous to nanocrystallites embedded amorphous just by decreasing the SFR. The effect of SFR on the film growth and quality are studied extensively using different techniques.

8.1 Experimental Details:

The films are prepared using semiconductor grade pure silane from Matheson Inc. on various substrates *viz.* Corning 1737, ITO coated glass, c-Si wafer and carbon coated Cu grids for different studies. A tungsten filament in the horizontal filament assembly is used for film preparation. Prior to deposition the chamber was evacuated to a pressure of about 10^{-6} mbar and then silane is passed into the chamber. The only intentional variable is the silane flow rate (SFR). During deposition, a constant process pressure (PP) of 0.05 mbar is maintained by throttling the chamber outlet while the substrate temperature (T_s) and filament temperature (T_F) are kept constant at 250°C and 1800°C respectively. The filament to substrate distance is kept fixed at 6 cm. Detailed deposition conditions are listed in Table 8.1.

The films are structurally characterized by X- ray diffraction (XRD), Raman spectroscopy, Transmission electron microscopy (TEM) and Atomic force microscopy (AFM). XRD measurements are performed by Siefert XRD 3003 TT X-ray diffractometer in 2θ mode at grazing angle of incidence of 3°. Raman studies are performed by Witec Alpha Raman spectrometer with excitation wavelength of 514.1 nm in the scanning range of 100-1000 cm^{-1}. TEM studies are performed using JEOL TEM while AFM studies are performed by Picoplus Molecular Imaging in acoustic mode using silicon cantilevers with force constant 2.5 N/m and resonance frequency of 80 KHz. TEM studies are done on the films deposited on Cu grids whereas XRD, Raman and AFM studies are performed on the films deposited on Corning 1737.

The optical studies are performed by UV-Vis-NIR and IR transmission spectroscopy. The UV-Vis-NIR transmission spectra are recorded in the range 3000- 350 nm on the films deposited on Corning 1737 using Shimadzu UV 3101 PC spectrometer while IR transmission spectra are recorded in the range of 400-4000 cm^{-1} on the films deposited on c-Si wafer using Perkin Elmer BX II FTIR spectrometer respectively. The transport studies are done by temperature dependent dark and photoconductivity measurements in co planner geometry. The stability studies are performed by light soaking the film. The details of the measurements and analysis are mentioned in Chapter 2.

Table 8.1: Deposition details of the films reported in the present chapter. Here T_s, T_F, PP and SFR represent the substrate temperature, filament temperature, process pressure and silane flow rate respectively.

Sample No.	T_s (^oC)	T_F (^oC)	PP (mbar)	SFR (SCCM)
HW_SFR_1	250	1800	0.05	10
HW_SFR_2				5
HW_SFR_3				3
HW_SFR_4				2

8.2 Results and Discussions:

8.2.1 X-ray diffraction studies:

Figure 8.1 shows the XRD patterns for the films under present study. The films prepared with high SFR (10 and 5 SCCM) are amorphous with a broad hump around 28° while nanocrystallites develop as the SFR is decreased. In the XRD pattern for 3 and 2 SCCM films, sharp peaks corresponding to (111), (220) and (311) planes of crystalline silicon appear, superimposed on the amorphous hump. This indicates the formation of silicon nanocrystallites in the amorphous matrix. The crystallite sizes (d_{XRD}) for these two films are calculated using Scherrer formula as mentioned in the Section 2.2.1.1 and listed in the table 8.2 along with the Raman results.

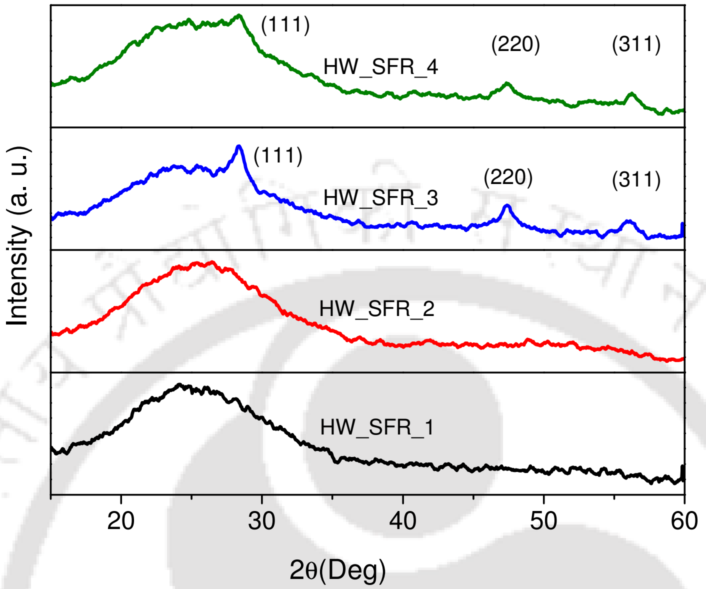

Figure 8.1: X-ray diffraction patterns for the films prepared with varying SFR.

8.2.2 Raman scattering spectroscopy:

Figure 8.2 shows the Raman scattering spectra for the films. The high SFR films (10 and 5 SCCM) show a broad peak centered at 480 cm^{-1} indicating the amorphous nature while the low SFR films possess sharp peak near 520 cm^{-1} corresponding to nanocrystallites of silicon in addition to the 480 cm^{-1} peak. This further reveals the formation of nanocrystallites in amorphous matrix for the films deposited at low SFR supporting the XRD results. For estimation of total crystalline fraction (X_c), crystallite size (d_R), short and medium range order (SRO and MRO), the Raman spectra are deconvoluted (Figures 8.3a and 8.3b) into different components as mentioned in Section 2.2.1.3. Different parameters estimated from Raman spectra are listed in table 8.2. The crystalline fraction of film with SFR 3SCCM is found to be more than that with 2SCCM. XRD studies also show that the 3SCCM film is more crystalline than 2SCCM film, though we expected lowest SFR film to have the highest crystallinity as also reprted by Dusane *et al.* [1]. This could be the result of too much depletion of silane during the deposition at very low SFR condition which affected the film growth and microstructure. The rms deviations ($\Delta\theta_B$) of the tetrahedral bond angle for these films are found to be quite good (~7°). The film with highest crystalline fraction, i.e., with SFR 3SCCM shows much better $\Delta\theta_B$ (3.13°). The lower values of $\Delta\theta_B$ (< 10°) suggest better short range order even in amorphous films [2-3]. The medium range order (MRO) in the films calculated as the intensity ratio between the TA and TO phonon vibration of amorphous component is found to be of device quality [4-5]. The crystallite sizes as calculated from Raman studies (d_R) match well with those estimated from XRD data.

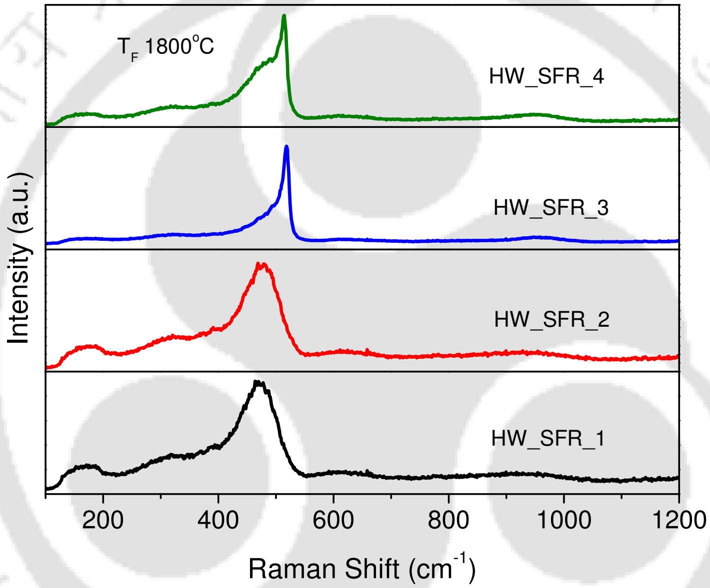

Figure 8.2: Raman scattering spectra for the films prepared with varying SFR.

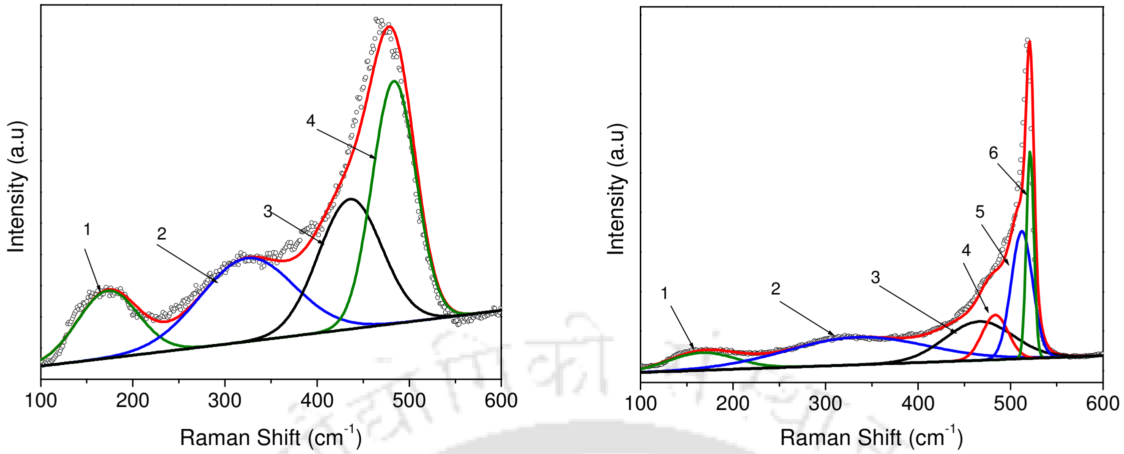

(a) (b)

Figure 8.3: Deconvoluted Raman scattering spectra for (a) amorphous film (HW_SFR_1) and (b) nanocrystallites embedded amorphous film (HW_SFR_3). Black circles are raw data while the red line is for fitted data. The peaks 1, 2, 3 and 4 correspond to amorphous TA, LA, LO and TO peak respectively while peak 5 and 6 correspond to grain boundary and nanocrystalline peak.

Table 8.2: Total crystalline fraction (X_c), fraction of nanocrystallites (X_{nc}), grain boundary fractions (X_{GB}), rms bond angle deviation of tetrahedral angle ($\Delta\theta_B$), MRO (I_{TA}/I_{TO}), crystallite size estimated from Raman (d_R) and XRD (d_{XRD}) studies respectively.

Sample No	X_c (%)	X_{nc} (%)	X_{GB} (%)	$\Delta\theta_B$ (^{o})	MRO (I_{TA}/I_{TO})	d_R (nm)	d_{XRD} (nm)
HW_SFR_1	---		---	6.94	0.37	---	
HW_SFR_2	---		---	7.80	0.25	---	
HW_SFR_3	78	28	50	3.13	0.20	7.68	6.83
HW_SFR_4	35	15	20	7.25	0.23	3.89	4.77

8.2.3 Transmission electron microscopy:

The selected area diffraction (SAD) patterns for the films are shown in the figure 8.4. The high SFR films (10 and 5 SCCM) show diffused diffraction rings which confirm the amorphous nature of these films. The SAD pattern for low SFR films show intense sharp rings corresponding to (111), (220) and (311) planes and weak rings corresponding to higher order planes of silicon. The appearance of bright spots on the sharp rings for these films is an indication of the formation of nanocrystallites in the amorphous matrix.

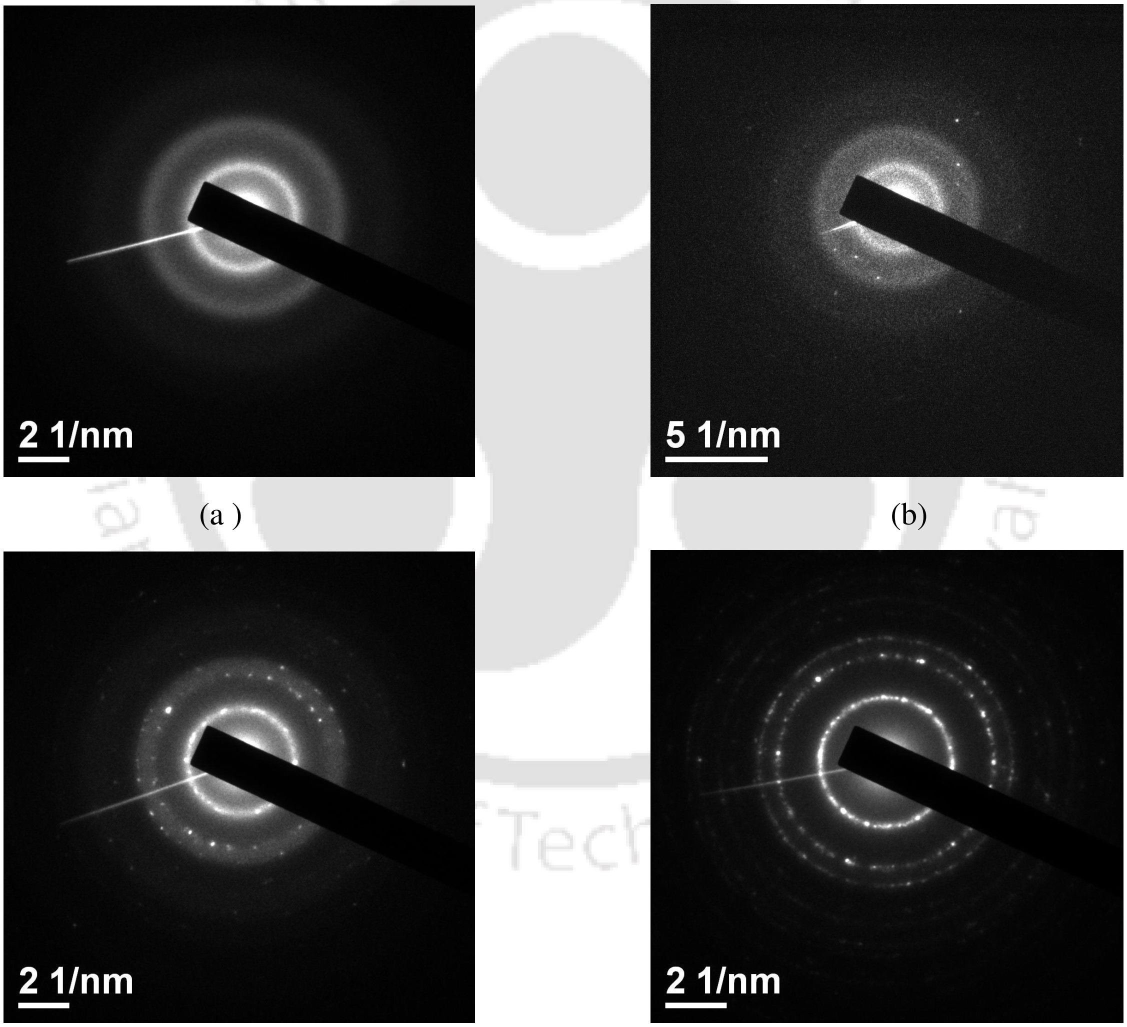

(a) (b)

(c) (d)

Figure 8.4: SAD pattern for the films (a) HW_SFR_1, (b) HW_SFR_2, (c) HW_SFR_3 and (d) HW_SFR_4.

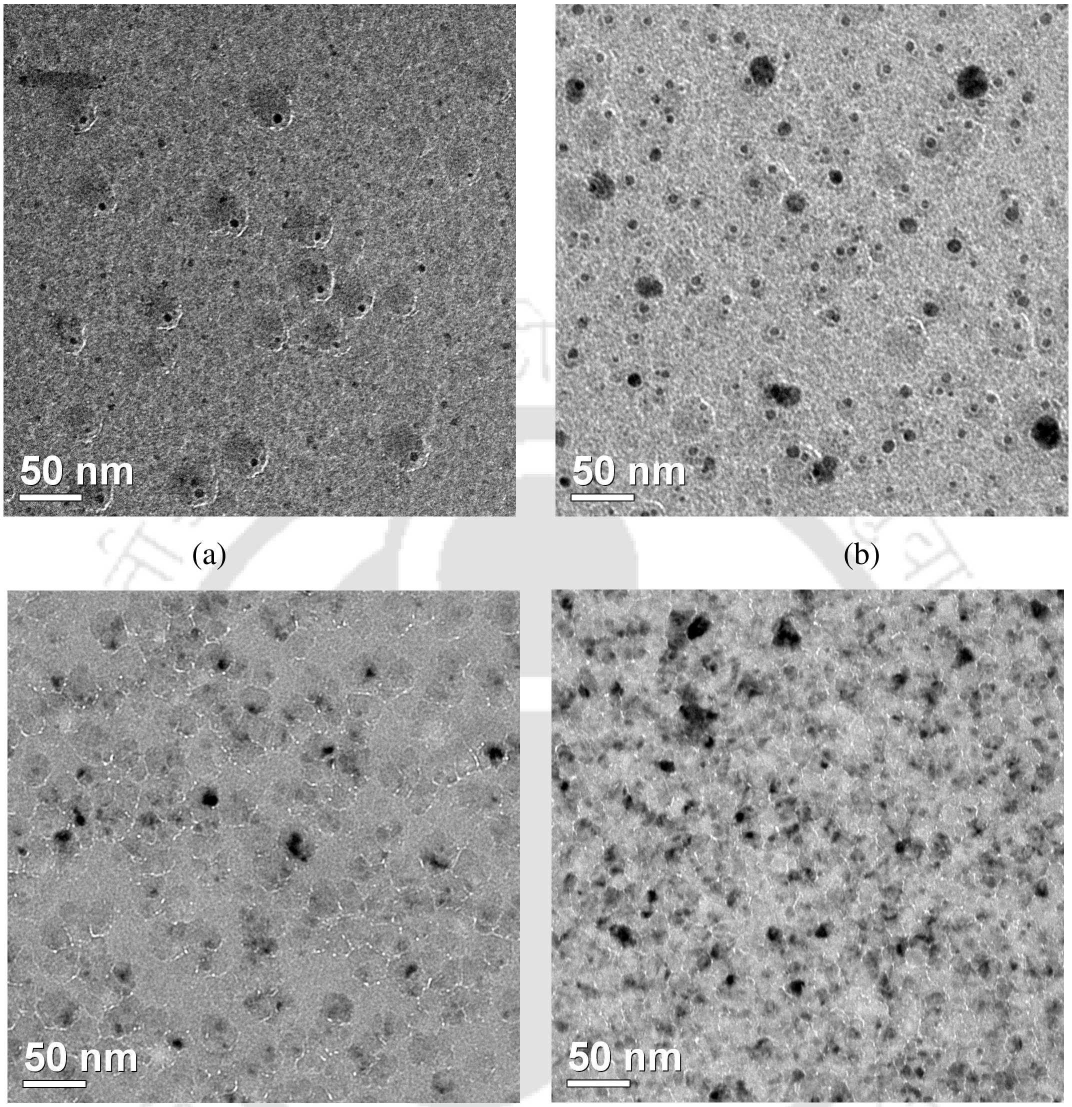

(a) (b) (c) (d)

Figure 8.5: Low resolution TEM images for films (a) HW_SFR_1 (b) HW_SFR_2 (c) HW_SFR_3 and (d) HW_SFR_4, prepared with varying SFR.

The low resolution transmission electron micrographs for the films are shown in figure 8.5. It is observed that the films with high SFR contain some dark regions scattered randomly in the homogeneous bright matrix. These regions are also seen in the films with low SFR; however in these films white thread like structures surrounding the brighter regions of about 20 nm diameter are observed in addition. These white thread like structures are believed to be low density amorphous tissues, mainly surrounding the grain boundaries [6]. The high resolution TEM images of high SFR films do not show the formation of nanocrystallites (Figure 8.6a). These films reveal amorphous nature in XRD and Raman analyses as well. But in case of nanocrystallites embedded films deposited with low SFR, the dark spots and nearby regions generally reveal the formation of nanocrystallites with the lattice spacing of silicon (0.3nm) under high resolution (Figure 8.6b). Probably the dark regions in films deposited at high SFR are the nucleation sites with more ordered network which transform to nanocrystallites as the SFR is reduced. Thus the XRD, Raman and TEM studies are all consistent, revealing the films to be amorphous for high SFR and transition of the film microstructure to nanocrystallites embedded amorphous for low SFR. At low SFR, the film forming radicals get more time to diffuse over the growing surface to find energetically favourable sites and hence a more ordered structure is formed. This leads to the formation of nanocrystallites. When the SFR is high, the growing surface receives the radicals before the earlier radicals diffuses out to find an energetically favourable site and bury those radicals giving a less ordered i.e., amorphous structure.

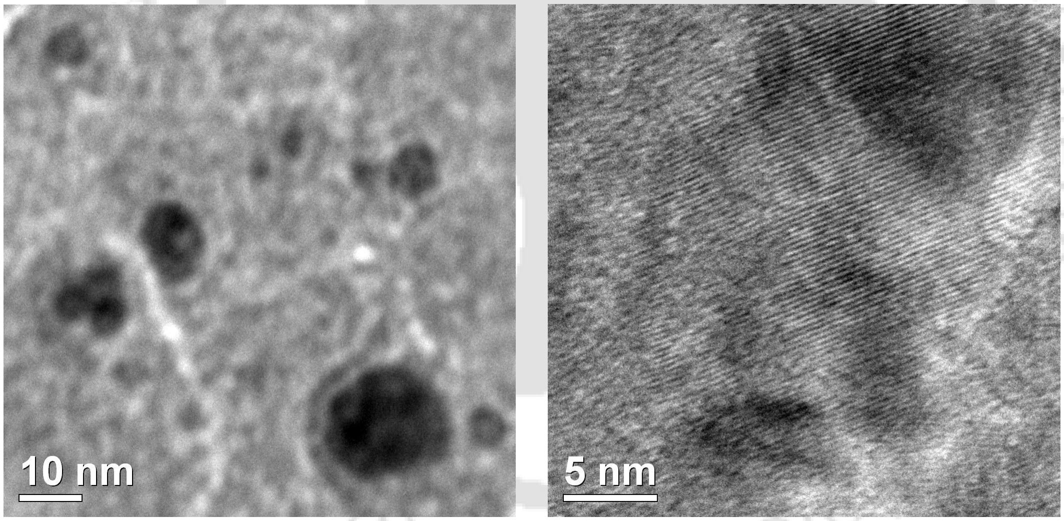

(a) (b)

Figure 8.6: High resolution TEM (HRTEM) images for (a) an amorphous (HWH_SFR_1) and (b) nanocrystallites embedded amorphous (HWH_SFR_4) film.

8.2.4 Atomic force microscopy:

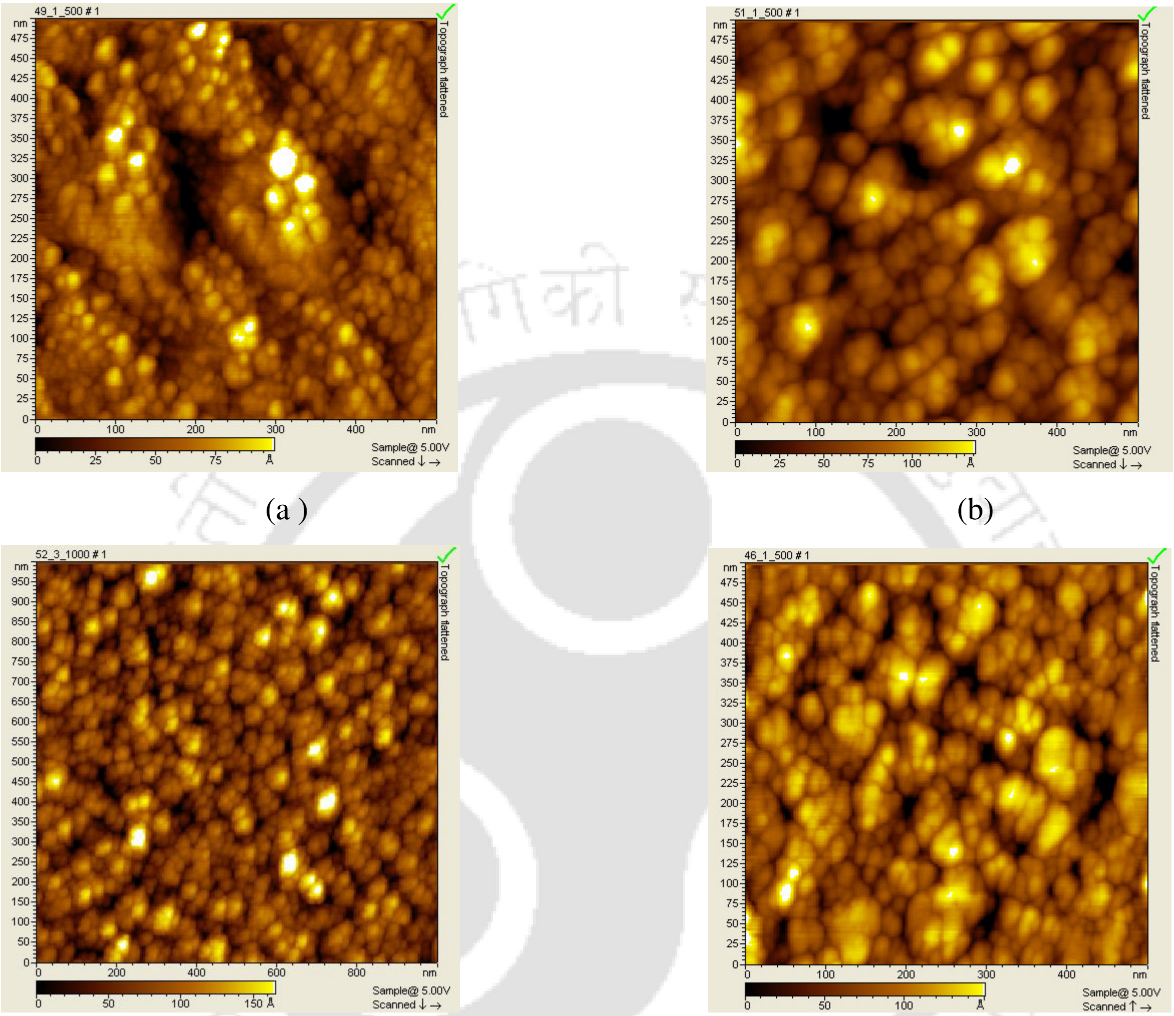

(a)

(b)

(c)

(d)

Figure 8.7: AFM images for the films (a) HW_SFR_1 (b) HW_SFR_2 (c) HW_SFR_3 and (d) HW_SFR_4 showing their surface morphology.

Figures 8.7a- 8.7d show the AFM images of the films depicting the surface morphology. The surface morphologies of the films are almost similar though the film microstructure varies from amorphous to nanocrystallites embedded amorphous in nature. The films are densely packed with small grains grouped into bigger clusters. It is observed that the films possess very small rms roughness (r_{rms}) of about 3-6 nm. The r_{rms} of the films are listed in Table 8.3.

Table 8.3: The rms roughness (r_{rms}) of the films estimated from AFM images.

SFR (SCCM)	10	5	3	2
r_{rms} (nm)	5.6	3.3	2.8	6

8.2.5 Thickness, optical constants and optical band gap calculation:

Figure 8.8 shows the UV-Vis-NIR transmission spectra of the films reported in the present chapter. The thickness and optical constants of the films are estimated from the interference fringes in the UV-Vis-NIR transmission spectra while the deposition rate (r_d) is calculated from the thickness thus estimated. The E_G of the films are calculated from the plot of $\sqrt{\alpha h\nu}$ *vs* $h\nu$ as shown in the figure 8.9. The estimated values of thickness, r_d and E_G are listed in table 8.4.

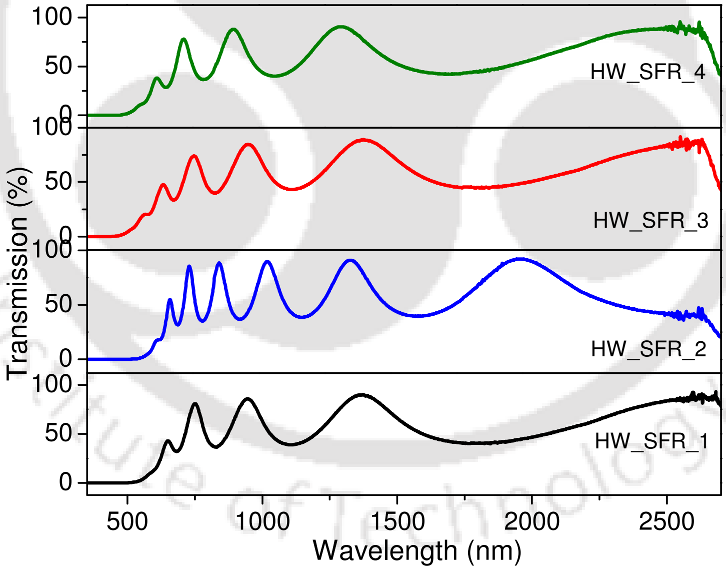

Figure 8.8: UV-Vis-NIR transmission spectra for the films reported in the present chapter.

It is observed that r_d increases with the increase in SFR. This is expected, as with the increase in SFR, the growing film surface receives more film forming radicals and hence the film grows faster. The increase in r_d with SFR is steeper for lower SFR while the rate decreases for higher SFR as can be seen from figure 8.10. This is probably because as the SFR becomes higher (10 SCCM in this case), the number of radicals that can be absorbed in the surface gets saturated. The values of E_G for the present films are found to be in the range of 1.8-1.98 eV and are slightly higher than the E_G of 1.7-1.8 eV for the regular PECVD films [7]. It is observed that the band gap decreases with the increase in SFR except for the film with SFR 3SCCM, which is higher than that with 2SCCM. Incidentally this film is found to possess the highest crystallinity in different studies. Hence variation of band gap is not directly related to SFR, but related to the microstructure which in turn is related to the SFR. Comparing with the Raman data, it is evident that E_G is more for more crystalline films. Figure 8.11 shows the variation of E_G with the medium range order (I_{TA}/I_{TO}) of the films. From the plot it is clearly seen that as I_{TA}/I_{TO} increases i.e., MRO decreases, the E_G also decreases. Hence it can be concluded that the E_G is related to the MRO, i.e., films with improved MRO possess higher E_G. These findings are in agreement with Mahan *et al.* who also observed that improvement in order leads to increased band gap [8].

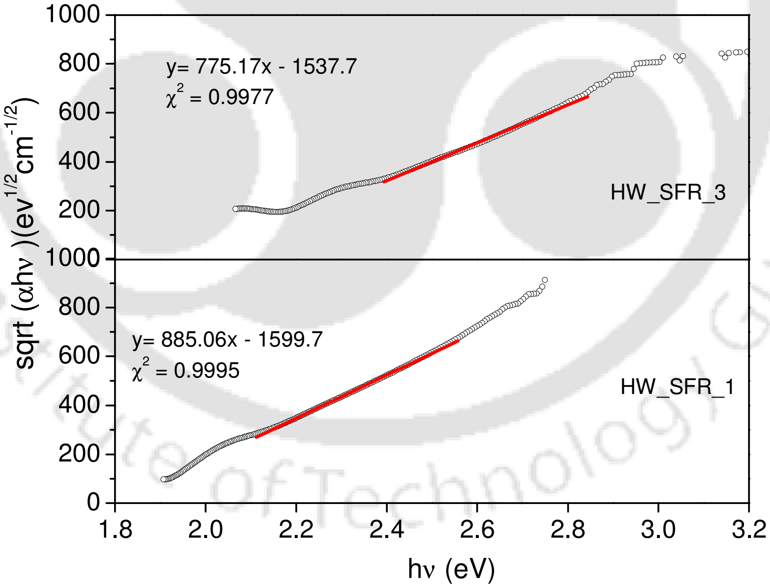

Figure 8.9: Plot of $\sqrt{\alpha h\nu}$ *vs* $h\nu$ for two representative films to calculate the band gap

Table 8.4: Thickness, deposition rate (r_d), optical band gap (E_G) determined from UV-Vis-NIR transmission spectra.

Sample No.	SFR (SCCM)	Thickness (nm)	r_d (Å/Sec)	E_G (eV)
HW_SFR_1	10	410	27.3	1.81
HW_SFR_2	5	590	17.9	1.82
HW_SFR_3	3	442	10.5	1.98
HW_SFR_4	2	393	6.55	1.92

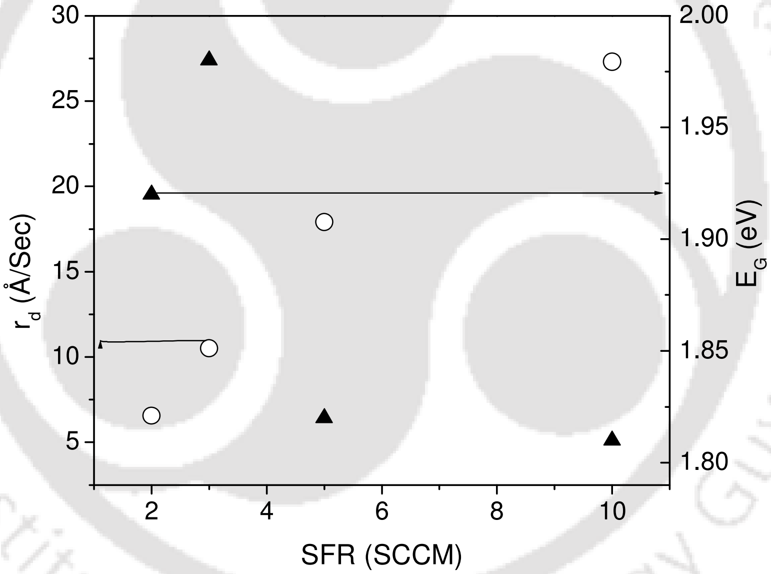

Figure 8.10: Variation of deposition rate (r_d) and band gap (E_G) with the silane flow rate (SFR). The circles denote the r_d while triangles denote the E_G. Error bars are included in the size of the symbol.

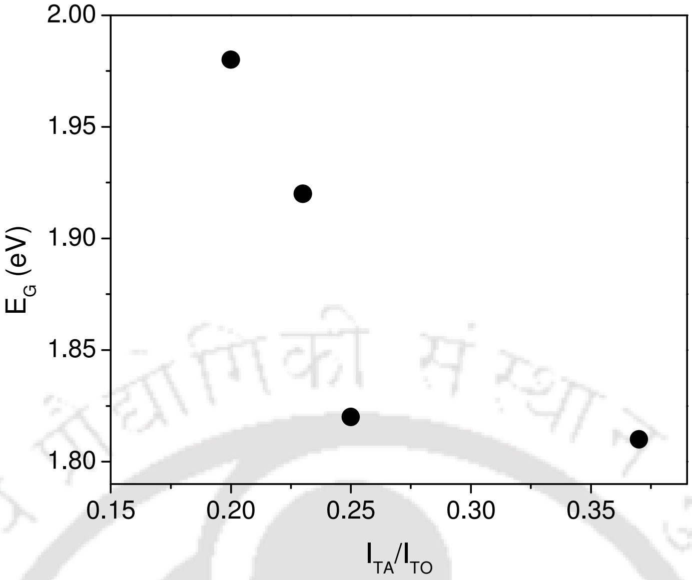

Figure 8.11: Variation of E_G with I_{TA}/I_{TO}. Error bars are included in the size of the symbol.

8.2.6 Infrared absorption studies:

The IR transmission spectra for the films are recorded for estimation of total hydrogen content and silicon hydrogen bonding configuration. Figure 8.12 shows the IR transmission spectra for the films consisting of absorption band near 630 cm^{-1} and 2000 cm^{-1} corresponding to wagging and stretching mode of silicon hydrogen bond vibrations. The spectra do not show any signature of oxygen in the films. Figures 8.13a and 8.13b show the absorption coefficients of the films in the wagging and stretching mode of vibrations. It is observed that the wagging band of amorphous films is more or less symmetric, while that for nanocrystallites embedded films the band shows deviation from symmetric shape with the appearance of sub bands. This feature is also observed by Halindindwali *et al.* and Zhang *et al.* [9-10] and also observed for other nanocrystallites embedded films reported in this thesis. In these films, the local environment of the silicon hydrogen bond in amorphous and nanocrystalline phase is expected to be different. Also, TEM studies of these films show some thread like low density amorphous regions. The local environment of silicon hydrogen bonding in these regions is different than other amorphous regions. This leads to the shift in the peak position and hence the deviation of the band from its symmetric shape occurs.

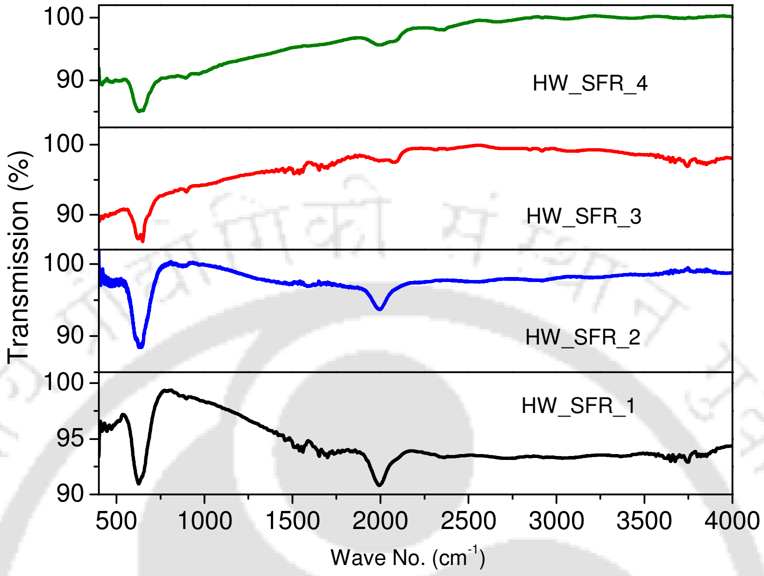

Figure 8.12: IR transmission spectra for the films under present study.

The hydrogen content (C_H) in the films is estimated to be 4.6- 8.5 atomic % considering the same force constant. The C_H in the films agrees well with the films reported by Mahan *et al.* [11-12]. The deconvolution of absorption spectra due in the stretching mode shows (Figure 8.14) that the hydrogen is mostly bonded in monohydride mode (71-92%). This is encouraging as monohydride bonding is very much appreciated for stable device quality films. The weak polyhydride bonding is believed to be responsible for light induced degradation of the films. Table 8.5 shows the hydrogen content and microstructure factor (R*) of the films. It is observed that the amorphous films possess more hydrogen and also more monohydride bonding. The ordered structure inside the nanocrystals makes the region hydrogen depleted and forces the hydrogen to be bonded in the GB regions, where hydrogen gets bonded in polyhydride as well as clustered monohydride mode to passivate the GB surfaces. Both poly hydride and clustered monohydride in the GB region give rise to absorption around 2100 cm^{-1} [13 Han] as discussed in Chapter 6 in details.

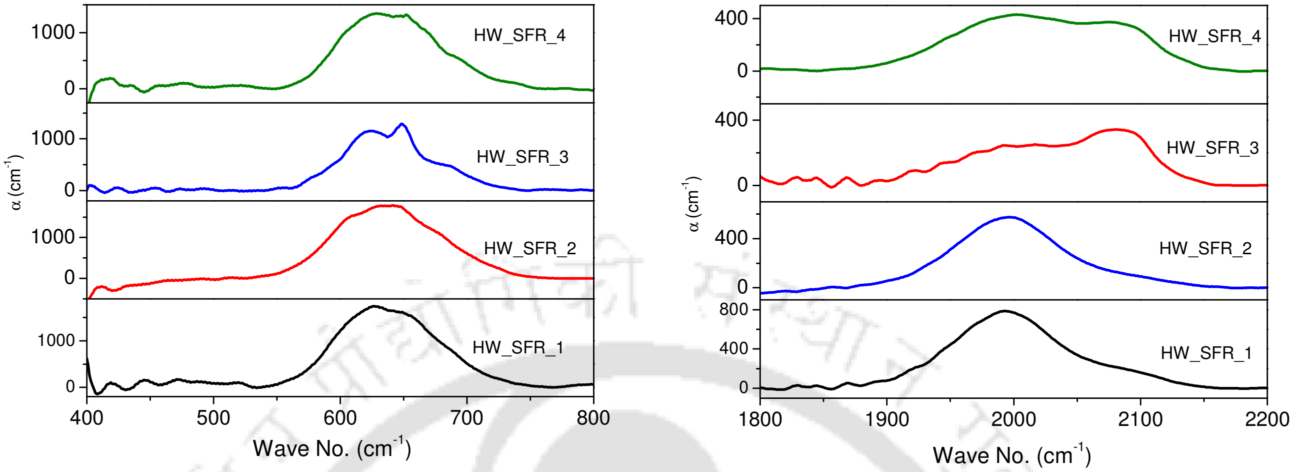

(a) (b)

Figure 8.13: Absorption coefficients of the films in the (a) wagging and (b) stretching mode of silicon hydrogen bond vibrations.

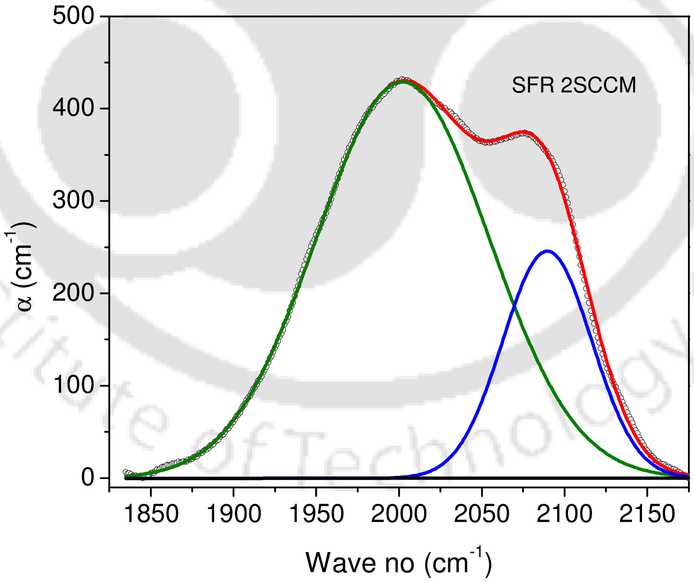

Figure 8.14: Deconvoluted absorption coefficient of a representative film (SFR 2 SCCM, HWH_4) in the stretching mode of vibration for the determination of microstructure factor R*. Black line corresponds to raw data while red line corresponds to the fitted data. The green and blue lines are for the bands at 2000 and 2100 cm^{-1} respectively.

Table 8.5: Atomic percentage of hydrogen content (C_H) and microstructure factors (R*) for the films.

Sample No.	C_H (%)	R*
HW_SFR_1	7.87	0.10
HW_SFR_2	8.53	0.08
HW_SFR_3	4.64	0.29
HW_SFR_4	6.00	0.23

8.2.7 Temperature dependent Conductivity and Stability studies:

Figures 8.15a-8.15d show the temperature dependent conductivity and stability studies data in the temperature range of room temperature (25 or 30 ^oC) to 200 ^oC. In all the figures the variation of dark conductivity in the annealed state and light soaked state are shown while in figure 8.15c the photoconductivity data (filled and empty rectangles) are also included, since we consider this film to be the best among all. The as deposited films show dark conductivity below 10^{-11} $\Omega^{-1}cm^{-1}$, while photo conductivity lies between $3x10^{-7}$ to $3x10^{-6}$ $\Omega^{-1}cm^{-1}$; thus giving a high photosensitivity ratio of $>10^4$ except for the film with SFR 3SCCM. This film contains high fraction of nanocrystallites (X_c ~ 80 %) and possess high dark conductivity. Hence the photosensitivity is not very good. After annealing at 200 ^oC for 2 hours both dark and photoconductivity increase. However the photosensitivity decreases, the decrease being less for the amorphous films and the highest for the film with 2SCCM, which is nanocrystalline in nature. As this film is already nanocrystalline, annealing could make this film more ordered, thus increasing the dark conductivity and hence decreasing the photosensitivity. Table 8.6 shows the summarized results of conductivity studies. The films show thermally activated conduction with different activation energies (E_d) in different temperature ranges. Generally, the values of E_d at low temperatures (room temperature to 45^{o}C) are very high, low at high temperatures (160-

200^{o}C) and at intermediate temperatures E_d values lie in between. More than one E_d for these films can be associated with complex microstructures consisting of amorphous tissues, nanocrystallites and grain boundaries. As the conductivity measurements are performed in coplanar geometry, perpendicular to the growth direction, the grain boundaries and internal microvoids play a major role in determining the E_d of the films.

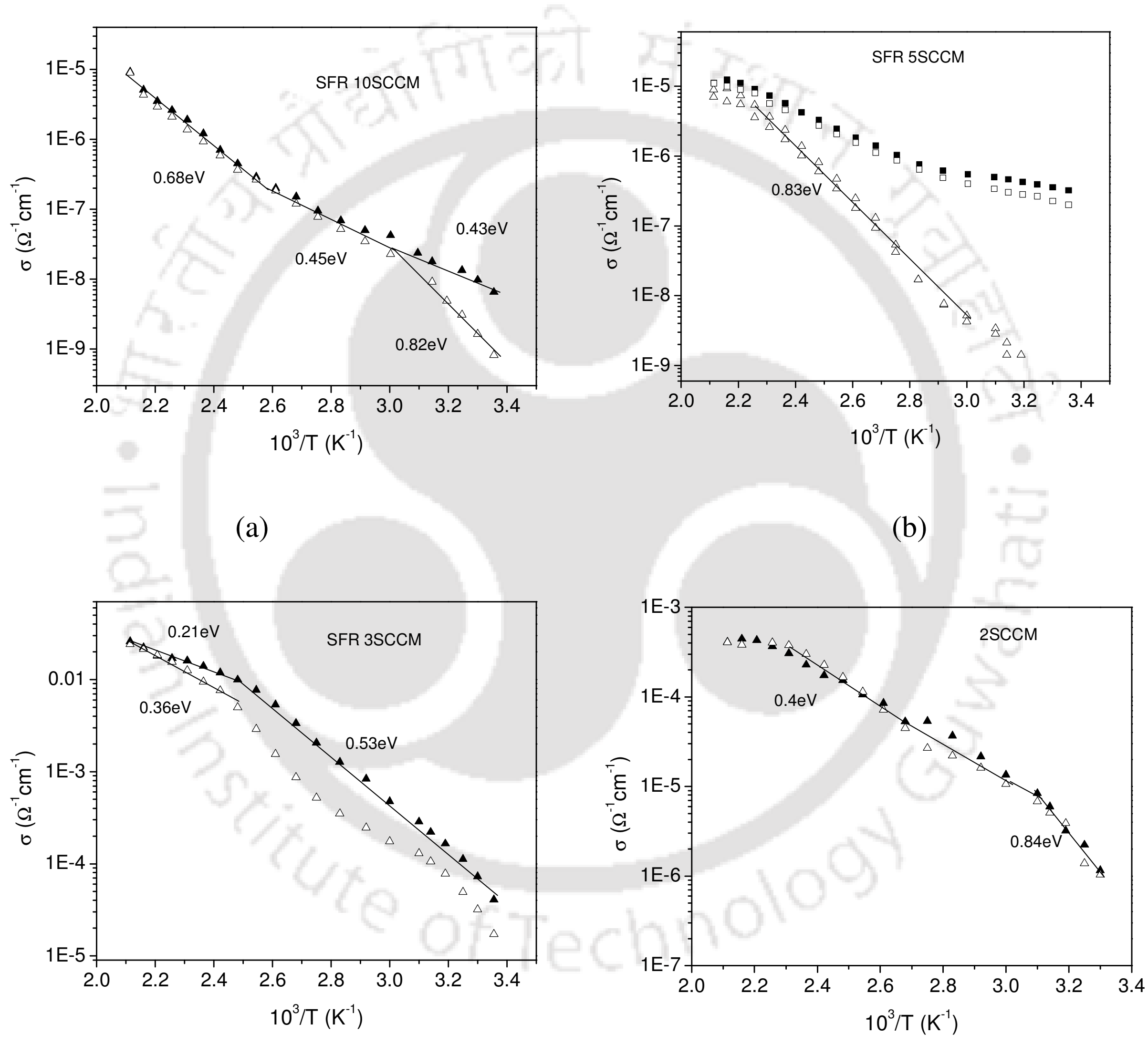

(a) (b)

(c) (d)

Figure 8.15: Variation of dark conductivity for the film with SFR (a) 10 SCCM (HWH_1) (b) 5 SCCM (HWH_2) (c) 3 SCCM (HWH_3) and (d) 2 SCCM (HWH_4) in the temperature range

25-200^{o}C. The filled symbols are for annealed sample while the empty symbols are for light soaked sample. The triangles and rectangles indicate dark and photo conductivity data respectively.

All the films seem to suffer very less light induced degradation under exposure of 100 Watt light for 12 hours. The degradation occurs in first few hours of light exposure and then saturates, hence the light soaking time is fixed to 12 hours. It is observed that the film with highest SFR suffers the highest degradation, a decrease of about one order of magnitude in dark conductivity while the photoconductivity reduces to half of the original value. Other films suffer very less decrease in both dark and photoconductivity as can be seen from table 8.6. We attribute the less light induced degradation to the improved order as supported by Raman studies and also hydrogen preferably bonded in the monohydride bond. There are reports of less Staebler Wronski (SW) effect suffered by HWCVD films [14-15]. Mahan *et al.* associated lower C_H with the reduction in SW effect [16]. Lower C_H is a manifestation of better lattice ordering. As discussed earlier, the ordered network forces the region to be hydrogen deficient though the vice versa may not be true. The better ordered (crystalline or crystalline like) regions can tolerate the recombination events without much damage more easily than the regions which are less ordered and hence suffer less light induced degradation [16]. The film with SFR 5SCCM is found to have good photosensitivity and at the same time suffers very less light induced degradation (ratio of conductivity between annealed and light soaked state being 1.6). Hence we consider this film to be the best among all the films discussed in this chapter. This film is prepared in the onset of crystallinity. According to Feenstra *et al.*, low C_H HW film is expected to result in improved stability against light induced degradation of amorphous silicon [17] as SW- effect is related to hydrogen content. Guha [18] reported these types of, on the edge of crystallinity, films to be best suited for solar cell applications. These types of films are also called protocrystalline films and more stable because of dense homogeneous amorphous network [19]. These films possess good photosensitivity because of amorphous nature while at the same time suffers less light induced degradation because of ordered structure.

Table 8.6: Room temperature (at 30^{o}C) dark and photoconductivities (σ_d and σ_{ph}) in the as deposited (As dep), annealed (annld) and light soaked (LS) states, photosensitivity ratio (σ_{ph}/σ_d) in the as deposited and annealed states and activation energies (E_d) in low and high temperature ranges.

Sample No (HW_SFR_)	σ_d (30^o) ($\Omega^{-1}cm^{-1}$)			σ_{ph} (30^o) ($\Omega^{-1}cm^{-1}$)			σ_{ph}/σ_d (As dep)	σ_{ph}/σ_d (Annld)	E_d (eV)	
	As Dep	Annld	LS	As Dep	Annld	LS			High Tmp	Low Tmp
1	<10^{-11}	$6.5x10^{-9}$	$8.13x10^{-10}$	$3.62x10^{-6}$	$6.18x10^{-6}$	$3.14x10^{-6}$	>10^4	$9.51x10^2$	0.68	
2	<10^{-11}	$5.1x10^{-10}$ (extrpl)	$3.15x10^{-10}$ (extrpl)	$3.9x10^{-6}$	$3.56x10^{-7}$	$2.26x10^{-7}$	>10^4	$6.98x10^2$	0.83	
3	$1.8x10^{-5}$	$7.28x10^{-5}$	$3.18x10^{-5}$	$3.91x10^{-5}$	$1.9x10^{-4}$	$1.11x10^{-4}$	2.17	2.61	0.21	0.53
4	<10^{-11}	$1.16x10^{-6}$	$1.04x10^{-6}$	$5.08x10^{-7}$	$2.43x10^{-6}$	$2.11x10^{-6}$	>10^4	2.09	0.40	0.84

8.3 Conclusion:

In this chapter the effects of silane flow rate on film microstructure and optoelectronic properties are studied. The deposition rates (r_d) for the films are found to be very good (6.55-27.3 Å/Sec). The band gap is little higher than the regular PECVD films and can be varied in the range of 1.8-2eV. The film microstructure could be tailored from pure amorphous to nanocrystallites embedded amorphous just by decreasing the gas flow rate without using any hydrogen dilution of precursor gas. Raman studies reveal good short and medium range order ($\Delta\theta_B$~ 3-8^o and I_{TA}/I_{TO} ~ 0.2-0.37) of the films. The hydrogen content agrees with the reported values for HWCVD films and hydrogen is preferably bonded in the monohydride mode. The films are found to possess good photosensitivity and are very stable against prolonged light soaking. We attribute the stability of the films to the improved order, monohydride bonding and also low hydrogen content in the films. The stability and variation of band gap make these films suitable contender for multijunction solar cells and other optoelectronic devices.

8.4 References:

1. R. O. Dusane, S. R. Dusane, V. G. Bhide and S. T. Kshirsagar, Appl. Phys. Lett. **63** (1993) 2201.
2. D. Beeman, R. Tsu and M. F. Thorpe, Phys. Rev. B **32** (1985) 874.
3. M. Stutzmann, *Amorphous Semiconductors,* Handbook of Semiconductors, North Holland Vol **3a** (1994), Ed. S. Mahajan
4. M. Ito and M. Kondo, Jpn. J. Appl. Phys. **45** (2006) L230.
5. G. Morell, R. S. Katiyar, S. Z. Weisz, H. Jia, J. Shinar and I. Balberg, J. Appl. Phys. **78** (1995) 5120.
6. M. Fonrodona, D. Soler, J. M. Asensi, J. Bertomeu and J. Andreu, J. Non-Cryst. Solids **299-302** (2002) 14.
7. E. V. Sauvain, A. Shah and J. Bailat, *Advances in microcrystalline silicon solar cell technologies*, Thin Film Solar Cells: Fabrication, Characterization and Applications, John Wiley and Sons (2006), Ed. J. Poortmans and V. Arkhipov.
8. A. H. Mahan, R. Biswas, L. M. Gedvilas, D. L. Williamson and B. C. Pan, J. Appl. Phys. **96** (2004) 3818.
9. S. Halindintwali, D. Knoesen, R. Swanepoel, B. A. Julies, C. Arendse, T. Muller, C. C. Theron, A. Gordjin, P. C. P. Bronsveld, J. K. Rath and R. E. I. Schropp, Thin Solid Films **515** (2007) 8040.
10. S. Zhang, X. Liao, L. Raniero, E. Fortunato, Y. Xu, G. Kong, H. Aguas, I. Ferreira and R. Martins, Sol. Energy Mater. Sol. Cells **90** (2006) 3001.
11. A. H. Mahan, J. Carapella, B. P. Nelson, R. S. Crandall and I. Balberg, J. Appl. Phys. **69** (1991) 6728.
12. A. H. Mahan, L. M. Gedvilas and J. D. Webb, J. Appl. Phys. **87** (2000) 1650.
13. D. Han, K. Wang, J. M. Owens, L. Gedvilas, B. Nelson, H. Habuchi and M. Tanaka, J. Appl. Phys. **93** (2003) 3776.
14. A. H. Mahan and M. Vanecek, AIP Conf. Proc. **234** (1991)195.
15. M. Heintze, R. Zedlitz, H. N. Wanka and M. B. Schubert, J. Appl. Phys. **79** (1996) 2699.
16. A. H. Mahan, J. Yang, S. Guha and D. L. Williamson, Phys. Rev. B **61** (2000) 1677.
17. K. F. Feenstra, R. E. I. Schropp and W. F. Van der Weg, J. Appl. Phys. **85** (1999) 6843

18. S. Guha, Sol. Energy **77** (2004) 887.

19. J. Y. Ahn and K. S. Lim, J. Non-Cryst. Solids **351** (2005) 748.

Chapter -9

HWCVD films: Effect of Filament Temperature

Chapter 9

HWCVD films: Effect of Filament Temperature

This chapter presents the studies on the HWCVD films prepared from pure silane by varying the filament temperature (T_F). The filament temperature plays a decisive role in cracking the source gas into film forming radicals. The efficiency of cracking the source gas as well as the concentration of particular radical explicitly depend on the T_F. Higher T_F results in more efficient cracking of the source gas, thus enhancing the deposition rate; however, there are reports of film contamination by filament material at high T_F. Horbach *et al.* [1] reported observation of film contamination by the filament material for $T_F > 2100$ °C. Brogueria *et al.* [2] reported the burning out of filament at $T_F \sim 2500$ °C. On the other hand at lower T_F, the source gas gets incorporated into the filament thus forming silicide alloy and reducing the filament life time as well as reproducibility of the films. Doyle *et al.* [3] first observed that the rate of evolution of Si from the filament fell below the SiH_4 decomposition rate indicating possible incorporation of Si into the filament at $T_F < 1450$ °C. Brogueira *et al.* [2] also reported the incorporation of Si into the filament below 1700 °C. Duan *et al.* [4] also observed consumption of silane without significant formation of Si containing radical for T_F up to 1300 °C. The concentration of Si starts rising near 1300 °C and levels off above 1800°C, while SiH_3 and Si_2H_6 concentration becomes significant at higher temperatures. For these reasons intermediate T_F range (1600- 1900°C) is chosen for the deposition of films reported in this work. The effect of T_F on the material properties and microstructures are studied. The structural studies have shown that the film microstructure can be varied from amorphous to nanocrystallites embedded amorphous just by increasing the T_F keeping other deposition parameters constant.

9.1 Experimental Details:

The films are prepared using semiconductor grade pure silane from Matheson Inc. Thoroughly cleaned Corning 1737, ITO coated glass, c-Si wafer and carbon coated Cu grids are used as substrates for film preparation. Tungsten filament is used in the horizontal filament assembly. Prior to deposition, the chamber was evacuated to a pressure of about 10^{-6} mbar. The deposition is performed by keeping substrate temperature (T_s) and silane flow rate (SFR) fixed at 250°C and 3SCCM respectively for all the films while filament temperature (T_F) is varied in the range of 1600- 1900°C. During deposition, a constant process pressure (PP) of 0.05 mbar is maintained by throttling the chamber outlet. The filament to substrate distance is kept fixed at 6 cm like all other HWCVD films reported in this thesis. This distance is chosen so that the substrate heating due to the filament is negligible. Detailed deposition conditions are listed in Table 9.1.

Table 9.1: Deposition details of the films reported in the present chapter. Here, PP, SFR, T_s and T_F correspond to process pressure, silane flow rate, substrtae temperature and filament temperature respectively.

.

Sample No.	Base Pressure (mbar)	PP (mbar)	SFR (SCCM)	T_s (°C)	T_F (°C)
HW_TF_1	10^{-6}	0.05	3	250	1600
HW_TF_2					1700
HW_TF_3					1800
HW_TF_4					1900

The films are structurally characterized by X- ray diffraction (XRD), Transmission electron microscopy (TEM), Raman spectroscopy and Atomic force microscopy (AFM). X- ray diffraction studies are performed in thin film mode in the scanning range of $2\theta \sim 15\text{-}60^{o}$ using CuKα radiation. Transmission electron microscopy is done on the films deposited on Cu grids using JEOL TEM. Raman studies are performed by Witec Alpha Raman spectrometer with excitation wavelength of 514.1 nm in the scanning range of 100-1000 cm^{-1}. Atomic force microscopy is performed in the acoustic mode with silicon cantilevers having force constant 2.5 N/m and resonance frequency of 80 KHz using Picoplus Molecular Imaging. For optical studies, UV-Vis-NIR transmission spectra are recorded in the range 3000- 350 nm using Shimadzu UV 3101 PC spectrometer while IR transmission spectra are recorded in the range of 400-4000 cm^{-1}

using Perkin Elmer BXII FTIR spectrometer. The transport studies are done by temperature dependent dark and photoconductivity measurements and stability studies by light soaking. For photo conductivity measurements and stability studies by light soaking, a white light source of 100 Watt is used. The more details of the experimental procedure and estimation of different parameters are explained in Chapter 2.

9.2 Results and Discussions:

9.2.1 X-ray diffraction studies:

Figure 9.1 shows the XRD pattern for the films under present study. It is clearly seen from the figure that the films prepared at lower T_F (1600 and 1700^{o}C) are amorphous in nature with a broad hump around 28^o while for the films at higher T_F nanocrystallites develop in the amorphous matrix. For the films prepared at higher T_F, sharp peaks corresponding to (111), (220) and (311) planes of crystalline silicon, superimposed on the broad amorphous hump are observed. The crystallinity increases as the T_F is increased. The crystallite sizes (d_{XRD}) for these two films are calculated using Scherrer formula as explained in Section 2.2.1.1 and listed in table 9.2 along with the Raman results.

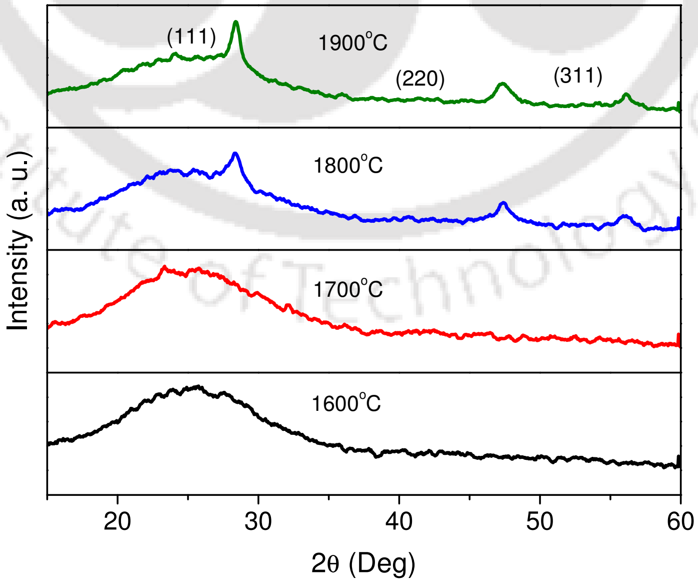

Figure 9.1: X-ray diffraction pattern for the films prepared with varying T_F.

9.2.2 Raman scattering spectroscopy:

Figure 9.2 shows the Raman scattering spectra of the films. Like the XRD pattern, Raman scattering spectra also show that the films at lower T_F are completely amorphous while nanocrystallites develop in the amorphous matrix as the T_F is increased. The low T_F films (1600 and 1700 ^{o}C) show a broad peak centered at 480 cm^{-1} indicating the amorphous nature. The high T_F films show a sharp peak near 520 cm^{-1} corresponding to nanocrystallites in addition to the broad 480cm^{-1} peak. This reveals the formation of nanocrystallites in amorphous matrix for the films deposited at high T_F.

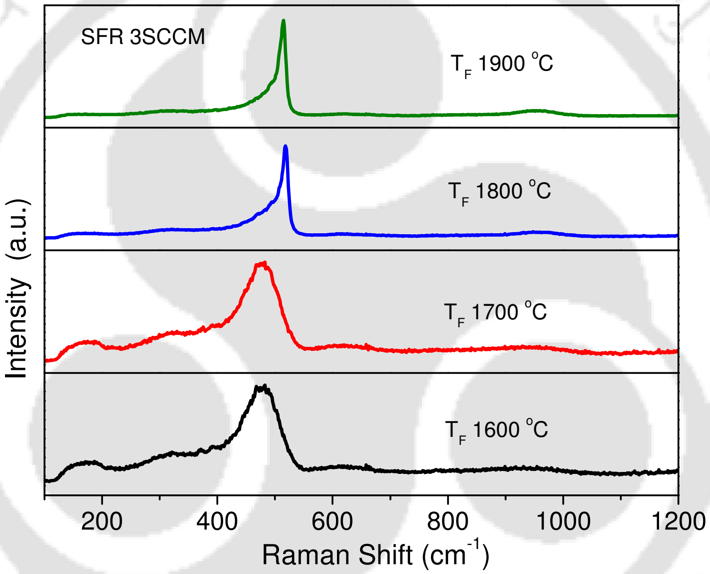

Figure 9.2: Raman scattering spectra for the films prepared with varying T_F.

For estimation of total crystalline fraction (X_c), crystallite size (d_R), short and medium range order (SRO and MRO), the Raman spectra are deconvoluted (Figures 9.3a and 9.3b) into different components corresponding to amorphous, nanocrystallites and grain boundaries, as mentioned in Section 2.2.1.3. Different parameters estimated from Raman spectra are listed in Table 9.2. The rms deviations ($\Delta\theta_B$) of the tetrahedral bond angle for the amorphous films are found to be ~8^{o}, while for nanocrystalline films, it is ~ 3^{o}. The low values of $\Delta\theta_B$ (< 10^{o}) suggest better short range order even in amorphous films [5-6]. The medium range order (MRO) in the films calculated as the intensity ratio between the transverse acoustic to transverse optic phonon vibration of amorphous component is also listed in Table 9.2 and is found to be of device quality [7-8].

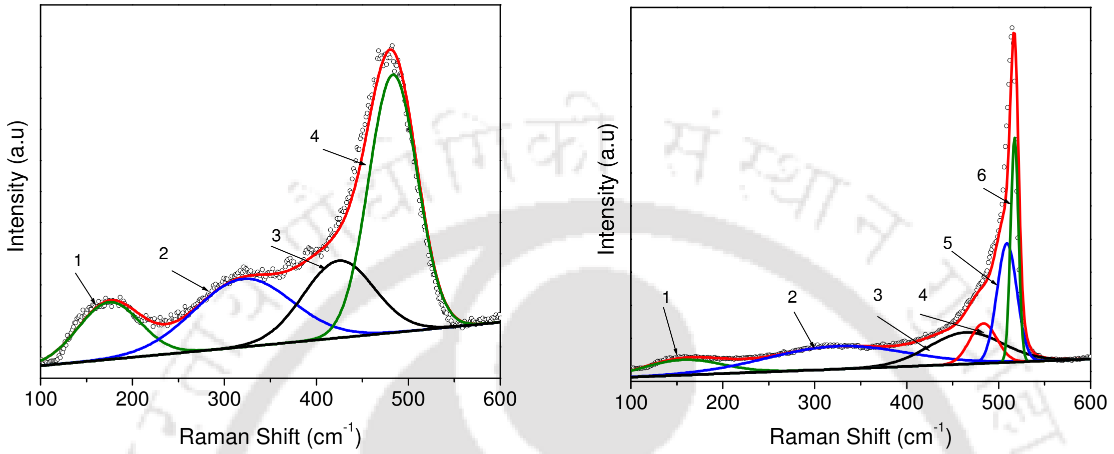

(a) (b)

Figure 9.3: Deconvoluted Raman scattering spectra for (a) amorphous film (HW_TF_1, T_F 1600°C) (b) nanocrystallites embedded film (HW_TF_4, T_F 1900°C).). Black circles are raw data while the red line is for fitted data. The peaks 1, 2, 3 and 4 correspond to amorphous TA, LA, LO and TO peak respectively while peak 5 and 6 correspond to grain boundary and nanocrystalline peak.

Table 9.2: Total crystalline fraction (X_c), grain boundary fraction (XG_B), rms deviation of tetrahedral bond angle ($\Delta\theta_B$), medium range order parameter (I_{TA}/I_{TO}), crystallite size calculated from Raman and XRD data (d_R and d_{XRD}) respectively.

Sample No.	T_F (°C)	X_c (%)	X_{GB} (%)	$\Delta\theta_B$ (°)	MRO (I_{TA}/I_{TO})	d_R (nm)	d_{XRD} (nm)
HW_TF_1	1600	------	------	8.05	0.27	------	------
HW_TF_2	1700	------	------	7.97	0.29	------	------
HW_TF_3	1800	78.7	50.3	3.13	0.2	7.68	6.83
HW_TF_4	1900	79.1	45.5	3.34	0.2	3.82	9.88

9.2.3 Transmission electron microscopy:

TEM study also supports the XRD and Raman results that the low T_F films are amorphous while crystallinity develops at high T_F. The SAD pattern for low T_F films consists of diffused diffraction rings while that for high T_F films consist of sharp rings along with the presence of bright spots on these (figure 9.4a-9.4b) This indicates that the low T_F films are amorphous, while the high T_F films contain nanocrystallites in the amorphous network.

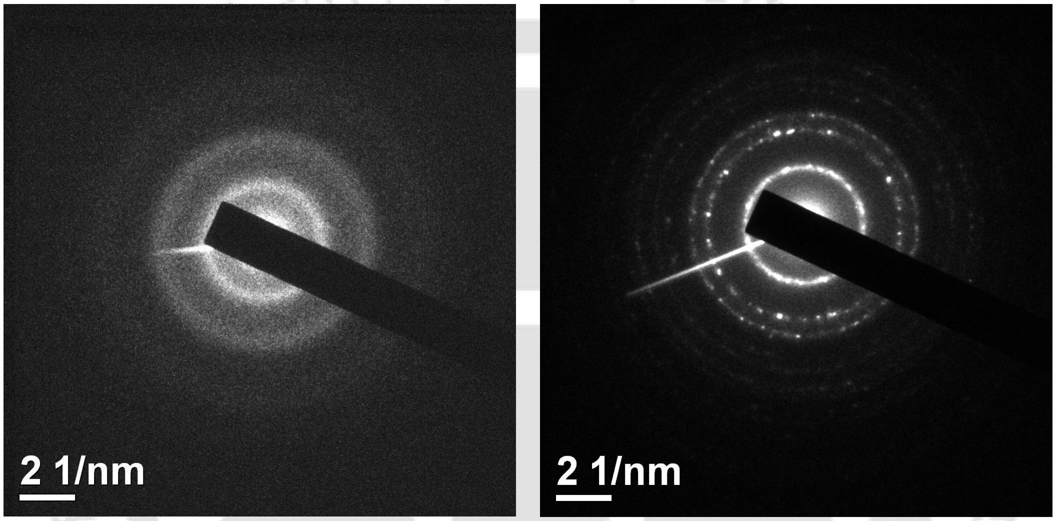

(a) (b)

Figure 9.4: SAD patterns for (a) an amorphous film (HW_TF_1, T_F 1600 ^oC) (b) nanocrystallites embedded amorphous film (HW_TF_4, T_F 1900 ^oC)

Figure 9.5 shows the low resolution TEM images for an amorphous film with T_F 1600^oC and a nanocrystallites embedded amorphous film with T_F 1900^oC. It is observed that the films with low T_F contain some dark regions scattered randomly in the homogeneous bright matrix. These dark regions are sometimes surrounded by little lighter patches as also observed by Das *et al.* [9]. The sizes of dark regions increase as the T_F is increased. In the films with high T_F white thread like structures surrounding the brighter regions of about 20nm diameter are observed in addition. These white thread like structures are believed to be low density amorphous tissues, mainly surrounding the grain boundaries [10]. The dark regions in the high T_F films show the nanocrystallites with the lattice spacing of silicon under high resolution (Figure 9.6) which is not observed in the films with low T_F (amorphous films). Probably these dark regions are the nucleation sites with more ordered and dense network which transform to crystalline nature with appropriate deposition parameters. These features are also observed for the films prepared by varying other parameters such as silane flow rate, substrate temperature etc.

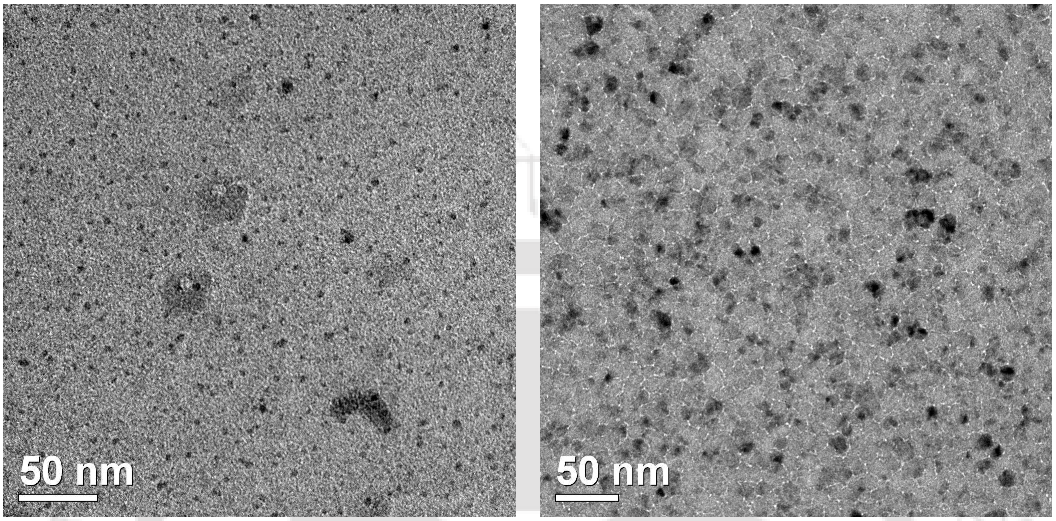

(a) (b)

Figure 9.5: Low resolution TEM images for (a) an amorphous (HW_TF_1) and (b) a nanocrystallites embedded amorphous (HW_TF_4) film.

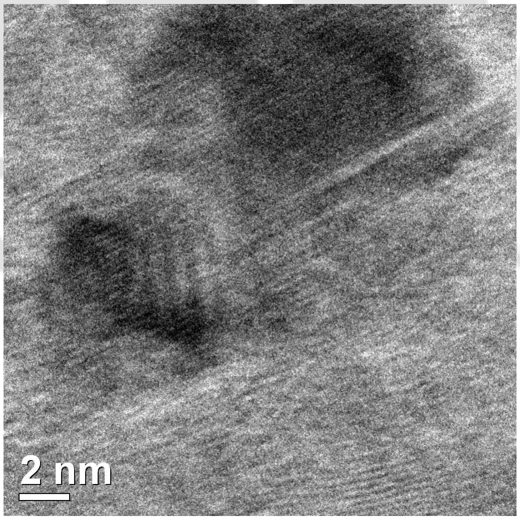

Figure 9.6: HRTEM image for film HW_TF_4 (T_F 1900°C) showing nanocrystallite formation.

Further, the films are found be free from impurities like incorporation of filament material. The EDS measurements attached to the TEM reveal that there is no signature of filament material (tungsten) in the films even for the film prepared at highest T_F (1900^oC).

9.2.4 Atomic force microscopy:

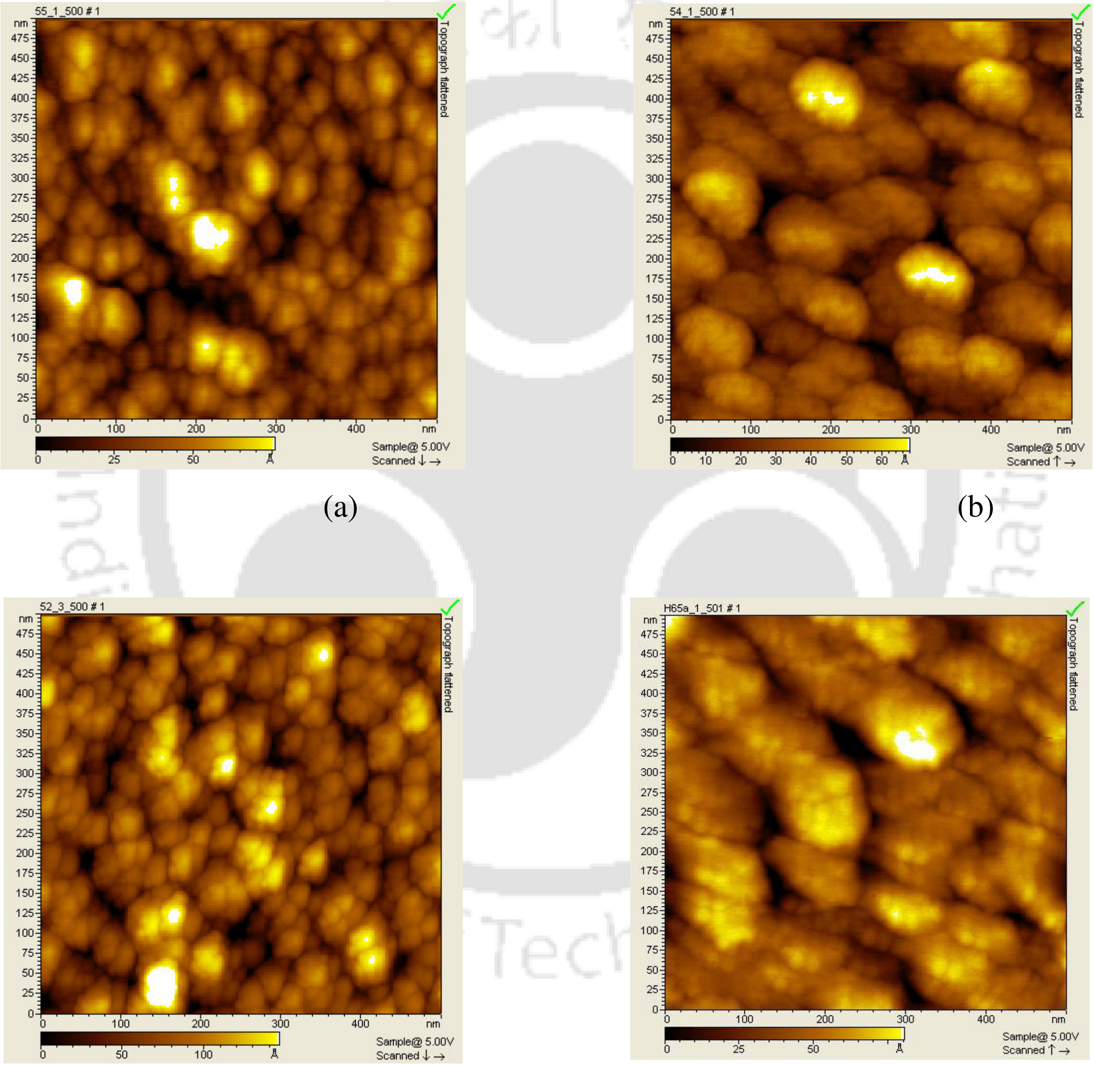

(a) (b)

(b) (d)

Figure 9.7: AFM images showing the surface topography of the films (a) HW_TF_1 (1600 °C) (b) HW_TF_2 (1700 °C) (c) HW_TF_3 (1800 °C) and (d) HW_TF_4 (1900 °C)

Figures 9.7a- 9.7d show the surface morphology of the films reported in the present chapter as obtained from AFM studies. Though the film microstructure varies from amorphous to nanocrystalline in nature, the surface morphology remains almost similar. The films are densely packed with small grains grouped into bigger clusters. It is observed that the films possess very small rms roughness (r_{rms}) of about 3-4.5 nm. There is slight decrease in the roughness as the T_F is increased up to 1800°C. Further increase in T_F results in small increase in r_{rms}, which may be within the error bars. The r_{rms} for the films are listed in Table 9.3.

Table 9.3: rms roughness (r_{rms}) of the films estimated from AFM data.

T_F (°C)	1600	1700	1800	1900
r_{rms} (nm)	4.5	3.7	2.8	3.0

9.2.5 Thickness, optical constants and optical band gap calculation:

Figure 9.8 shows the UV-Vis-NIR transmission spectra of the films reported in the present chapter. The thickness, optical constants and deposition rate (r_d) of the films as estimated from the interference fringes in the UV-Vis-NIR transmission spectra are listed in table 9.4. The r_d calculated from the thickness and deposition time of the films is found to be in the range of 8.1-12.4 Å/Sec, which is good enough for cost effective device applications. The r_d increases with the increase in T_F. As the T_F is increased, the source gas is cracked more efficiently into the film forming radicals and hence the deposition rate increases with the increase in T_F. The optical E_G of the films are calculated from the plot of $\sqrt{\alpha h\nu}\ vs\ h\nu$ in the high absorption region as shown in the figure 9.9. The E_G, thus estimated for the present films are found to be 1.9-2.2 eV, slightly higher than the E_G of 1.7-1.8eV for the regular PECVD films. However there are reports of high band gap of the films prepared by HWCVD [11-12] and also by PECVD methods [13].

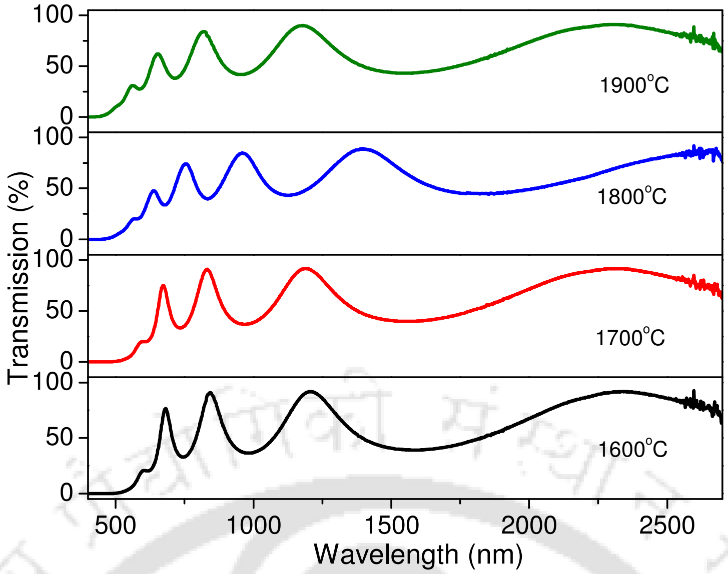

Figure 9.8: UV-Vis-NIR transmission spectra for the films reported in the present chapter.

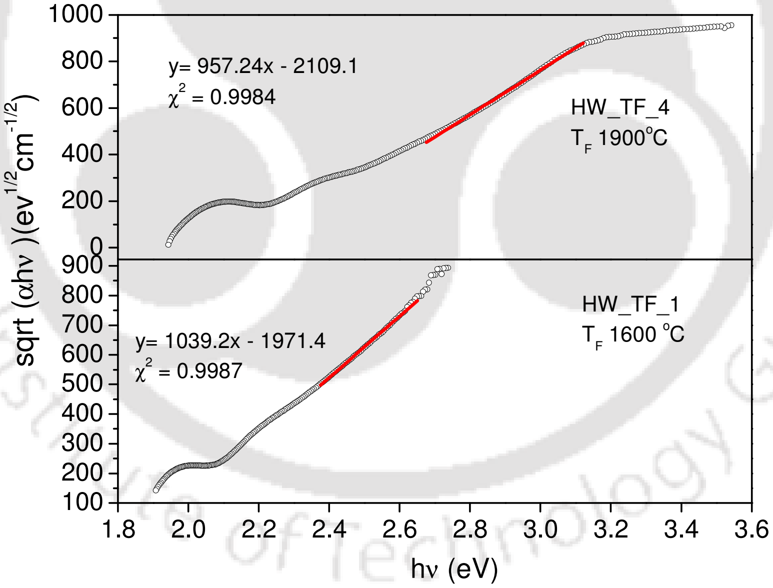

Figure 9.9: Plot of $\sqrt{\alpha h\nu}$ *vs* $h\nu$ for the calculation of optical band gap E_G of the films.

Table 9.4: Thickness, deposition rate (r_d) and optical band gap (E_G) for the films as estimated from UV-Vis-NIR transmission data.

Sample No.	Thickness (nm)	r_d (Å/Sec)	E_G (eV)
HW_TF_1	342	8.14	1.90
HW_TF_2	340	8.10	1.89
HW_TF_3	442	10.5	1.98
HW_TF_4	372	12.4	2.20

Various researchers attributed the high band gap to the alloying due to presence of hydrogen, improvement of short and medium range order and also to the presence of the nanocrystallites. Furukawa *et al.* [14] reported microcrystalline Si:H films with band gap lying in the range of 2.4 eV prepared using magnetron sputtering technique and associated the high band gap in the light of quantum confinement occurring due to small sized crystallites. It is interesting to note that in the case of HWCVD films, where the hydrogen content is relatively much less compared to the PECVD films, the band gap is higher when the films have improved SRO and the formation of nanocrystallites. Mahan *et al.* [11] reported high band gap of HWCVD films (1.8-1.99 eV) and attributed the increased band gap to the improvement in both SRO and MRO which results in narrowing of band tail width, after subtracting the effect of alloying due to hydrogenation. Among the films under present study, the one at T_F 1900°C has much higher E_G (2.2eV) than reported by Mahan *et al.* We believe that though Raman studies show improvement in order, this cannot be the only reason for the higher E_G. It is found in literature that the nanocrystallites embedded amorphous films show high band gap [12, 15]. The highly defective GB regions possess higher band gap compared to amorphous phase and prevalent contribution in the overall band gap of the mixed phase [12]. For the films reported here, the E_G is below 2eV for T_F up to 1800°C and increases suddenly at T_F 1900°C. If we compare the two films deposited at 1800 and 1900 °C, they possess almost similar hydrogen concentration, crystalline fraction as well as short and medium range order but band gap differs by 0.2eV. This difference in band gap is probably due to the presence of more low density amorphous tissues and microvoids in the film prepared at T_F 1900°C as supported by higher R* and the TEM micrographs. Microvoids reduce the effective density of the material and increase the average Si-Si distance. This lowers the absorption in the film and shifts the transmission spectrum towards higher photon energy, which manifests itself into higher band gap [16-17]. Hence we attribute the high band gap values to the improved order, formation of nanocrystallites and the existence of low density amorphous tissues surrounding the grain boundary regions as supported by TEM studies. Especially, for the film at 1900°C the abrupt increase in E_G is possibly due to the existence of larger fraction of low density amorphous tissues and voids.

9.2.6 Infrared absorption studies:

Figure 9.10 shows the IR transmission spectra of the films reported in the present chapter. The spectra show the wagging and stretching mode of vibrations of silicon hydrogen bonds near 630 and 2000 cm^{-1} respectively. Poly hydride bonding $(SiH_2)_n$ in the films is almost absent as can be seen from the absence of any absorption in the range 750-850cm^{-1}. The films free from oxygen except for the film deposited at T_F 1900 °C, where little dip in the transmission spectrum near 1050 cm^{-1} corresponding to SiO bond is observed.

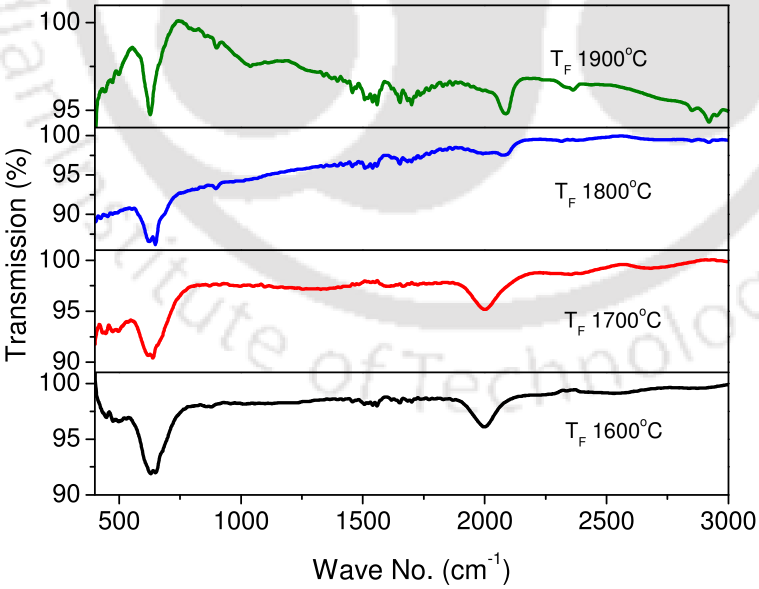

Figure 9.10: Infrared transmission spectra of the films prepared with varying T_F

The hydrogen content, C_H in the films is estimated from the total IR absorption intensity under the peak corresponding to the wagging mode of silicon hydrogen bond occurring near 630cm^{-1} whereas the microstructure factor R* is calculated from the intensity ratio between the stretching mode absorption band near 2000 cm^{-1} (monohydride) [18] and 2100cm^{-1} (dihydride as well as clustered monohydride in the grain boundary regions) [19-20] as discussed in the Section 2.2.2.2. The estimated values are listed in table 9.5. Figures 9.11a and 9.11b show the absorption coefficients of wagging mode and stretching mode respectively. The hydrogen content C_H, as estimated from wagging mode, varies from 8 to 4.5 atomic %, typical values for HWCVD films [21]. It is observed that films with low T_F, which are also amorphous in nature, contain more hydrogen while C_H decreases with increase in T_F. This implies that probably the concentration of hydrogen atom reaching the growing film surface is more at low T_F. This may happen due to the low evolution of Si containing radical from the filament at lower T_F. Above 1800^{o}C, the number of Si radicals coming out of the filament levels off the amount of Si radicals absorbed in it; SiH_3 and Si_2H_6 concentrations also increase to some extent and become significant at much higher temperatures [4]. Hence there is sharp decrease in C_H up to 1800^{o}C with a little decrease above 1800^{o}C, as can be seen from figure 9.12. The nanocrystalline nature of the films at high T_F may also be responsible for the low C_H of the films. With the increase in T_F the films become more ordered and develop crystallinty. The hydrogen atoms are pushed out of the crystallites and the more ordered amorphous regions, thus forming hydrogen deficient regions. Like some other films presented in earlier chapters of this thesis, the wagging mode peak is not symmetric around the peak position. This might be due to the presence of nanocrystallites embedded in amorphous matrix and resulting variations in local bonding configurations. For the estimation of microstructure factor the absorption band near 2000-2100 cm^{-1} is deconvoluted into two bands, one centered at 2000 cm^{-1} and the other at 2100 cm^{-1} as shown in the figure 9.13. The microstructure factor R* is found to be lower for low T_F films and increases with T_F. As the crystallinity increases with T_F and the films become more ordered, hydrogen atoms are pushed out of the ordered region to the grain boundary or less ordered regions as mentioned above, where they passivate the dangling bonds. According to Shim *et al.* [22], the nanocrystallites with size 2-8 nm are passivated mostly with Si-H bonds, whereas for the crystallite size < 2nm, Si-H_3 bonding dominates. The Si-H bonding in the grain boundary region may remain in clustered mode which gives stretching modes near 2100 cm^{-1}. Hence higher R* need not always indicate dihydride bonding, it may arise also due to the clustered monohydride mode on the internal surfaces of voids or grain boundaries [19- 20, 23].

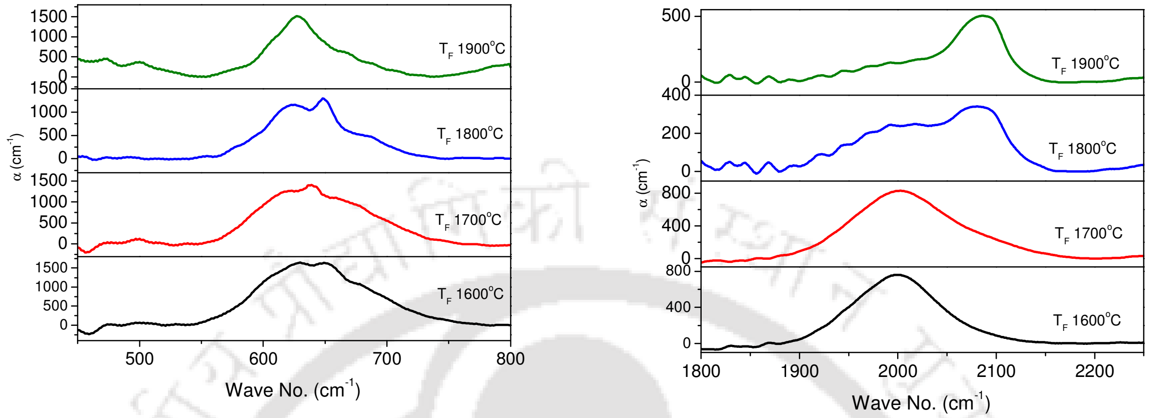

(a) (b)

Figure 9.11: The absorption coefficients of the films in (a) wagging mode and (b) stretching mode of vibrations.

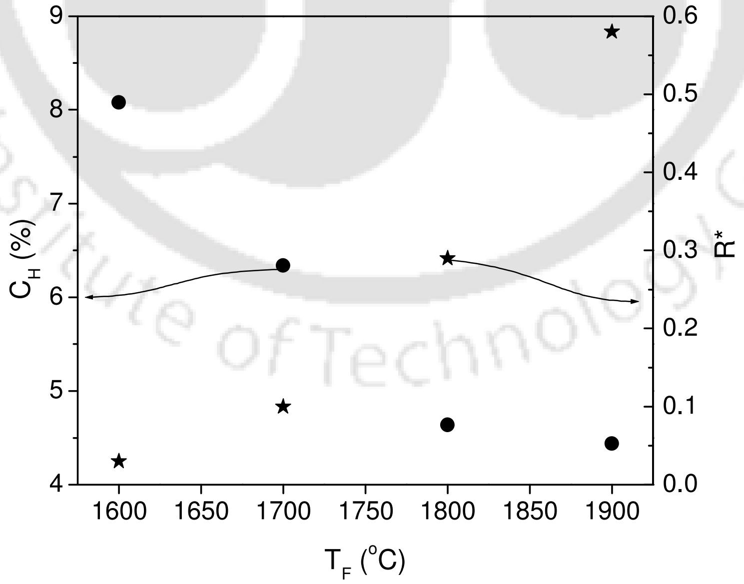

Figure 9.12: The variation of hydrogen content (C_H) and microstructure factor (R*) as a function of filament temperature.

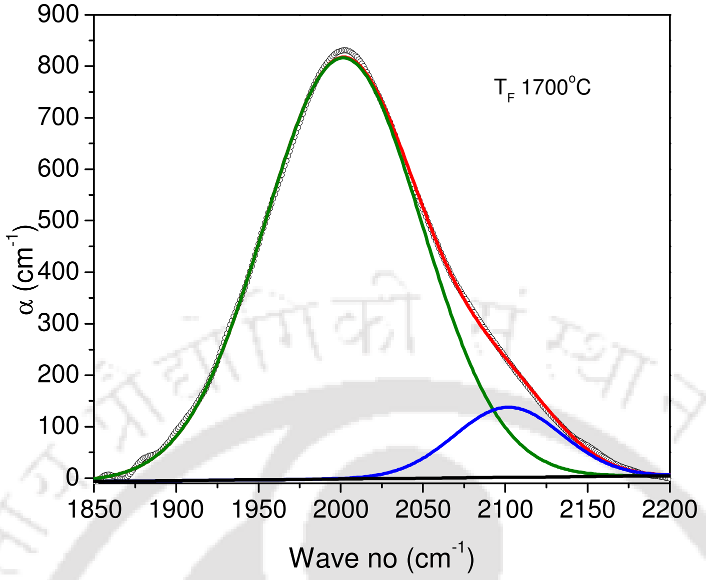

Figure 9.13: The deconvoluted absorption coefficients in the stretching mode of a film for the estimation of microstructure factor.

Table 9.5: Atomic percentage of hydrogen content (C_H) and microstructure factor (R*) for the films as estimated from IR transmission data.

Sample No.	T_F (°C)	C_H (%)	R*
HW_TF_1	1600	8.08	0.03
HW_TF_2	1700	6.34	0.10
HW_TF_3	1800	4.64	0.29
HW_TF_4	1900	4.44	0.58

9.2.7 Temperature dependent Conductivity and Stability studies:

Figures 9.14a and figure 9.14b show the temperature dependent conductivity and stability studies data of one amorphous and one nanocrystallites embedded amorphous film in the temperature range of room temperature (25 or 30°C) to 200°C. The room temperature dark conductivity for the as deposited amorphous films (with T_F 1600 and 1700°C) is below $10^{-11}\Omega^{-1}cm^{-1}$, while photo conductivity is about $5x10^{-7}$ cm^{-1}, yielding a high photosensitivity ratio of $>10^4$. The nanocrystallites embedded films show an increased dark conductivity with the T_F; $4x10^{-7}$ $\Omega^{-1}cm^{-1}$ and $4x10^{-6}$ $\Omega^{-1}cm^{-1}$ for films prepared at T_F of 1800 and 1900°C respectively, while the photoconductivity is only 6 and 2 times more than the dark conductivities. Annealing at 200°C for 2 hours increases the dark conductivity for all the films and photoconductivity of the nanocrystallites embedded films. For the amorphous films, the photoconductivity remains same (film at 1700°C), or there is a little decrease (film at 1600°C) due to annealing. The room temperature conductivity values for the as deposited, annealed and light soaked states are plotted against the filament temperature in figure 9.15. In general, the photosensitivity decreases after annealing, the decrease being more for the amorphous films. Table 9.6 shows the summarized result of conductivity studies. The films show thermally activated behaviour with different activation energies (E_d) in different temperature ranges. The amorphous films show single activation energy while the nanocrystallites embedded films show high E_d at low temperature range (room temperature to 100°C) and low E_d at high temperature range. The nanocrystallites embedded films show more than one activation energy because of the complex microstructure. The material is composed of nanocrystallites embedded in the amorphous matrix, the two phases separated by grain boundaries. Hence nanocrystallites embedded films can be regarded as three phase system, each phase contributing to the conductivity separately. Overall activation energy is the result of all these conduction paths depending on the contribution from each. Das *et al.* [12] explained the low activation energy at high temperature and high activation energy at low temperature of mixed phase films considering the system as a three phase one, consisting of amorphous tissues, grain boundaries and micro/nano crystallites. In their model, the crystallites (nano/ micro) are considered as single crystals) separated from amorphous tissues by highly disordered grain boundaries which act as trapping centers for charge carriers. In the course of trapping the charge carriers these grain boundaries become electrically charged and start opposing the passage of similar charge carriers from one crystallite to another, thus creating a potential energy barrier. These highly defective grain boundary regions possess higher optical gap compared to amorphous phase. Figure 9.16 shows the energy band diagram of the model. Here L is the average crystallite size and S is the barrier width between two crystallites including grain boundary and amorphous phase. At low temperature, the thermally activated carriers are less in number and a large fraction of these are trapped in the grain boundaries. Hence conduction through amorphous region is relatively prominent. At higher temperature, thermally activated carriers are high in concentration, eventually saturating the traps and reducing the barrier height. Hence barriers are not serious obstacle for current and carrier transport is dominantly controlled by crystalline components, thereby giving low activation energy.

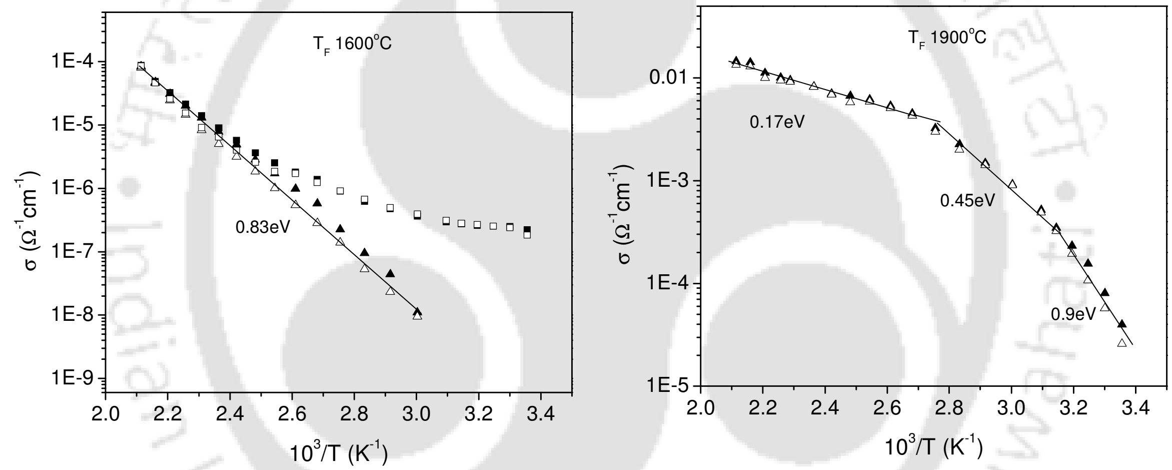

(a) (b)

Figure 9.14: Temperature dependent conductivity data for (a) an amorphous (T_F 1600^{o}C) (b) a nanocrystallites embedded amorphous (T_F 1900^{o}C) film. The filled symbols denote annealed state conductivities and the empty symbols denote the light soaked state conductivities, while dark and photoconductivity are denoted by triangles and rectangles respectively.

All the films under present study show very less light induced degradation under exposure of 100Watt light for 12 hours. We attribute the less light induced degradation to the improved order as supported by Raman studies and also hydrogen preferably bonded in the monohydride mode like the films reported in previous chapters. The better ordered (crystalline or crystalline like) regions can tolerate the recombination events without much damage than the regions which are less ordered and hence suffer less light induced degradation [24]. Also, monohydride bonding ensures stronger bonding than the higher hydrides, and hence is less likely to be broken. This makes the films containing monohydride bonding less prone to light induced degradation. The stability of the films is also contributed by the low hydrogen content. Among the films reported in this chapter, the film deposited at 1700°C is found to have the highest photosensitivity. So this film is considered as the best among all. This film is prepared in the protocrystalline regime.

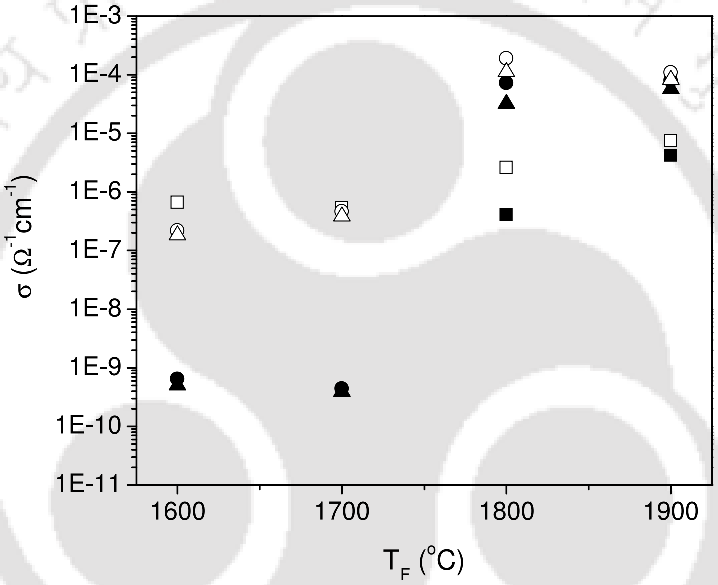

Figure 9.15: Variation of room temperature dark (filled symbols) and photo (empty symbols) conductivities with the filament temperature (T_F) for the films reported in this chapter. The filled rectangles are for as deposited state, circles are for annealed state and the triangles are for light soaked state of the films.

Table 9.6: Summarized results of temperature dependent conductivity and stability studies.

Sample No (HW_TF_)	σ_d (30°) ($\Omega^{-1}cm^{-1}$)			σ_{ph} (30°) ($\Omega^{-1}cm^{-1}$)			σ_{ph}/σ_d (As dep)	σ_{ph}/σ_d (Annld)	E_d (eV)	
	As Dep	Annld	LS	As Dep	Annld	LS			High Tmp	Low Tmp
1	<10^{-11}	6.5x10^{-10} (extrpl)	5x10^{-10} (extrpl)	6.7x10^{-7}	2.19x10^{-7}	1.83x10^{-7}	>10^4	3.34x10^2	0.83	
2	<10^{-11}	4.45x10^{-10} (extrpl)	3.92x10^{-10} (extrpl)	5.4x10^{-7}	4.67 x10^{-7}	3.82x10^{-7}	>10^4	1.05x10^3	0.74	
3	4.1 x10^{-7}	7.28x10^{-5}	3.18x10^{-5}	2.63x10^{-6}	1.9x10^{-4}	1.11x10^{-4}	6.4	2.6	0.21	0.53
4	4.2x10^{-6}	8.02x10^{-5}	5.72x10^{-5}	7.53x10^{-6}	1.1x10^{-4}	8.21x10^{-5}	1.7	1.37	0.17	0.45

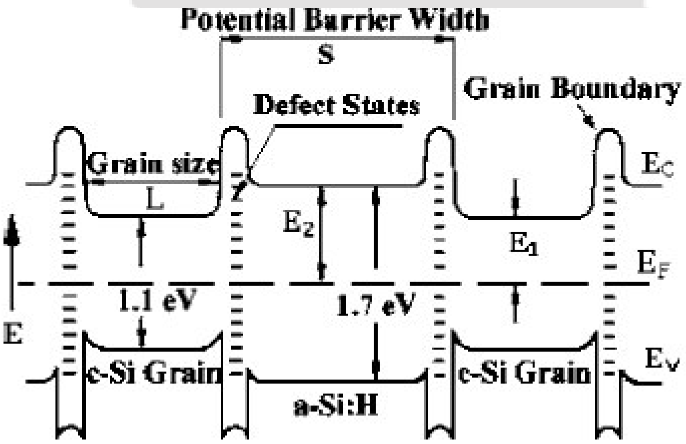

Figure 9.16: Potential energy structure for the three phase model of nanocrystallites embedded amorphous silicon [12]

9.3 Conclusion:

In this chapter the effect of filament temperature (T_F) on film microstructure and optoelectronic properties are reported. The films are prepared at reasonably good deposition rates (r_d) (8.1-12.4 Å/Sec). Low T_F films are found to be amorphous while the films deposited at higher T_F contains nanocrystallites embedded in the amorphous matrix. We could achieve the transition from amorphous to nanocrystalline phase without hydrogen dilution. Raman studies reveal good SRO ($\Delta\theta_B$~ 3 for nanocrystalline films and ~8^o for amorphous films) and MRO (I_{TA}/I_{TO} ~ 0.2 for nanocrystalline films and ~0.3 for amorphous films) for the studied films. The optical band gap E_G observed for these films is slightly higher than the regular PECVD films and can be varied in the range of 1.9-2.2eV; the higher value being attributed to improved order and existence of low density amorphous tissues surrounding the grain boundaries. The hydrogen is preferably bonded in the monohydride mode. The amorphous films are found to possess good photosensitivity. Both the amorphous and nanocrystallites embedded amorphous films are stable against prolonged light soaking. We attribute the stability of the films to the improved order, monohydride bonding and also to low hydrogen content in the films. The stability and variation of band gap makes these films suitable for multijunction solar cells and other optoelectronic devices.

9.4 References:

1. C. Horbach, W. Beyer and H. Wagner, J. Non-Cryst. Solids **137-138** (1991) 661.
2. P. Brogueira, J. P. Conde, S. Arekat and V. Chu, J. Appl. Phys. **79** (1996) 8748.
3. J. Doyle, R. Robertson, G.H. Lin, M. Z. He, A. Gallagher, J. Appl. Phys. **64** (1988) 3215.
4. H. L. Duan, G. A. Zaharias and S. F. Bent, Thin Solid Films **395** (2001) 36.
5. D. Beeman, R.Tsu and M. F. Thorpe, Phys. Rev. **B 32** (1985) 874.
6. M. Stutzman, Handbook of semiconductors (Ed. S. Mahajan) North Holland Vol 3a (1994) 657.
7. M. Ito and M. Kondo, J. J. Appl. Phys. **45** (2006) L230.

8. G. Morell, R. S. Katiyar, S. Z. Weisz, H. Jia, J. Shinar and I. Balberg, J. Appl. Phys. **78** (1995) 5120.
9. U. K. Das, P. Chaudhuri and S. T. Kshirsagar, J. Appl. Phys. **80** (1996) 5389.
10. M. Fonrodona, D Soler, J.M. Asensi, J. Bertomeu and J. Andreu, J. Non-Cryst. Solids **299-302** (2002) 14.
11. A. H. Mahan, R. Biswas, L. M. Gedvilas, G. D. Williamson and B. C. Pan J. Appl. Phys. **96** (2004) 3818.
12. D. Das and K. Bhattacharya, J. Appl. Phys. **100** (2006) 103701.
13. D. Das, M. Jana and A. K. Barua, J. Appl. Phys. **89** (2001) 3041.
14. S. Furukawa and T. Miyasato, Phys. Rev. B **38** (1988) 5726.
15. R. O. Dusane, S. R. Dusane, V. G. Bhide and S. T. Kshirsagar, Appl. Phys. Lett. **63** (1993) 2201.
16. S. R. Jadkar, J. V. Sali, A. M. Funde, N. A. Bakr, P. B. Vidyasagar, R. R. Hawaldar and D. P. Amalnerkar, Sol. Energy Mater. Sol. Cells **91** (2007) 714.
17. K. F. Feenstra, R. E. I. Schropp and W. F. Van der Weg, J. Appl. Phys. **85** (1999) 6843.
18. R.A. Street, Hydrogenated Amorphous Silicon, Cambridge University Press, (1992).
19. D. Han, K. Wang, J. M. Owens, L. Gedvilas, B. Nelson, H. Habuchi and M. Tanaka, J. Appl. Phys. **93** (2003) 3776.
20. T. Itoh, K. Yamamoto, K. Ushikoshi, S. Nonomura and S. Nitta, J. Non-Cryst. Solids **266-269** (2000) 201.
21. A. H. Mahan, J. Carapella, B. P. Nelson, R. S. Crandall and I. Balberg, J. Appl. Phys. **69** (1991) 6728.
22. J. H. Shim, S. Im and N. H. Cho, Appl. Surf. Sci. **234**(2004) 268.
23. J. K. Rath, H. Meiling, R. E. I. Schropp, Jpn. J. Appl. Phys. **36** (1997) 5436.
24. A.H. Mahan, J. Yang, S. Guha and D. L. Williamson, Phys. Rev. B **61** (2000) 1677.

Chapter -10

Conclusion and Scope for future work

Chapter 10

Conclusion and Scope for future work

10.1 Conclusion:

In this thesis work amorphous and nanocrystallites embedded amorphous silicon films are prepared by two different deposition methods *viz.* plasma enhanced chemical vapour deposition (PECVD) method and hot wire chemical vapour deposition (HWCVD) method. A systematic study on the influence of different process parameters on the microstructure and optoelectronic properties as well as stability of the films are carried out. As a part of the thesis work, a few systems including HWCVD deposition system and characterization set ups are also fabricated in house. Keeping the current issues in the material research of amorphous silicon in mind, the motivation of the thesis work was set to deposit good quality films at a reasonably high deposition rate. During the thesis work, six series of films are prepared; one series by PECVD using argon and hydrogen dilution of silane and others by HWCVD method by varying different deposition parameters such as, substrate temperature, filament temperature, gas flow rate etc., one at a time. The HWCVD technique is new and less extensively studied in comparison to the PECVD technique. Hence, in this thesis work more interest is paid for the deposition and optimization of process parameters for making device quality films by HWCVD method. It has been observed that the microstructure of the films could be varied from pure amorphous to nanocrystallites embedded amorphous just by varying a single deposition parameter at one time. This will be useful in making multi-junction solar cells just by varying a single parameter.

In the present work, good quality PECVD films ranging from amorphous to nanocrystallites embedded amorphous are prepared using combined argon and hydrogen dilution of silane. These films are found to be free from columnar growth which is a major concern for the films prepared with argon dilution of silane. At the same time good deposition rate is also observed. The good deposition rate is due to argon dilution while absence of columnar growth is attributed to the combined effect of hydrogen and argon. Presence of excited argon atoms (Ar*) helps in efficient dissociation of source gas while hydrogen increases the surface reaction thus improving the order of the films and avoiding column formation. Ar* also releases energy that is used for breaking weak Si-Si bonds and reconstructing strong Si-Si bonds thus further improving the medium range order. The best quality films are obtained with argon dilution (argon flow rate/ silane flow rate) of about 400. The key achievements in these films are high growth rate, high band gap (1.84-2.16eV) compared to regular PECVD films and better stability against exposure to light. The better stability against light soaking is attributed to the improvement in order.

Next we have studied the films prepared by HWCVD method. By the variation of hydrogen as well as silane flow rate, films ranging from amorphous to nanocrystallites embedded amorphous are prepared by HWCVD method at low substrate temperature (200^{o}C) with reasonably good deposition rates (0.64-3.22 Å/Sec). The films without hydrogen dilution are amorphous and the microstructure can be tailored by increasing the hydrogen flow rate or decreasing the silane flow rate i. e., by increasing hydrogen dilution. These films show good optoelectronic properties along with very less light induced degradation. We associate the stability of the films to improved order and hydrogen in the monohydride mode as suggested by Raman and IR measurements.

A few films are prepared from heavily hydrogen diluted silane (10 % silane in hydrogen) by varying the substrate temperature in the range of $100\text{-}350^{o}$C keeping other parameters fixed. The films show transition from amorphous to nanocrystallites embedded amorphous when the T_s is raised from 150 to 200^{o}C. These films have very good deposition rate (8-14 Å/Sec) and possess good short and medium range order with (rms deviation of tetrahedral angle $\Delta\theta_B \sim 6.5\text{-}7.5^{o}$, I_{TA}/ I_{TO}~0.27-0.45). Hydrogen content in these films ranges from 2.5-7.5 atomic %. These films possess strikingly high band gap (2.02-2.34eV). Good quality films at T_s as low as 100 ^{o}C at a deposition rate of 14 Å/Sec is a major achievement towards the cost effectiveness of film preparation as well as the feasibility of using the low cost flexible substrates. Another series of films are prepared from the same source gas by varying the process pressure in the range of 0.02 -0.8 mbar. All these films are nanocrystallites embedded amorphous in nature with good short and medium range order ($\Delta\theta_B$ ~4.4-$6.7^{o,}$ I_{TA}/ I_{TO}~0.3-0.5). The films are prepared with a good deposition rate (5 to11 Å/Sec). These films also possess very high band gap (2.2-2.4eV) and hence can be used in multi-junction solar cells to explore wide range of solar spectrum. We attribute the high band gap of both the series of films to the improvement of order and presence of low density amorphous tissues and microvoids surrounding the nanocrystallites. Stability studies show that the films suffer less light induced degradation. However photosensitivity of both the series of films are not very good.

Then films prepared from pure silane by varying the silane flow rate and filament temperature are studied. Silane flow rate variation shows that the film microstructure changes from amorphous to nanocrystallites embedded amorphous as the flow rate is decreased. The deposition rates are very high (6.5-27.3 Å/Sec). The band gap is little higher (1.8-1.98 eV) compared to the regular PECVD films. The other series of films deposited by varying the filament temperature shows transition from amorphous to nanocrystallites embedded nature when the T_F is increased from 1700 to1800°C. These films are also deposited at high rate (8.1-12.4 Å/Sec). The band gaps of the films high (1.9-2.2 eV), though the films possess 4.5-8 atomic % of hydrogen. Both the series of films possess good SRO and MRO along with hydrogen mostly in the monohydride mode. Both the series of films show good photosensitivity and less light induce degradation, useful for stable device applications. We attribute the stability of the films to improved order and hydrogen mainly bonded in monohydride mode.

It is inferred from the work on HWCVD films that unlike PECVD this method requires less hydrogen dilution for good quality films. The best quality amorphous silicon films are obtained from pure silane or with weakly hydrogen diluted silane. Heavily hydrogen diluted silane do not yield highly photosensitive films. We could achieve nanocrystalline transition at low temperature like 200°C. Also amorphous films with good homogeneity and adhesion to the substrate could be obtained at substrate temperature as low as 100°C. The films reported under present work show wide variation of band gap and very good stability, this wide variation of band gap will allow to explore a broad component of solar spectrum for photovoltaic application. Also, this will be helpful in making multijunction solar cell by varying a single deposition parameter. Further, these films possess medium to high deposition rate and hence can be viable candidate for stable and cost effective devices. The process parameters can be fine tuned for further improvement in material quality.

10.2 Scope for future work:

The present thesis work on the amorphous and nanocrystalline silicon films prepared by PECVD and HWCVD method has revealed several interesting aspects of these materials. To name in the first place, columnar growth of the films could be inhibited while maintaining a good deposition rate if argon dilution of silane is used in combination with hydrogen dilution. Hence this recipe can be used for the preparation of these materials for solar cells and other device applications. Secondly, present work shows that HWCVD method stands as viable contender to the highly used PECVD for the deposition of device quality films with higher growth rate. Though we have achieved good quality films at high growth rate from preliminary studies, the process parameters can be fine tuned for further improvement in material quality. Some additional parameters such as filament to substrate distance, change in gas flow scheme, different filament material and filament assembly etc. could also be tried to see their effect in the material properties and the deposition rate. These studies could also be performed on the doped layers. Some interesting studies including hydrogen effusion measurements, PES measurements, NMR measurements etc. could also be performed on the films to get more information. Though IR measurements give the amount of bonded hydrogen in the films, the actual hydrogen content may be more because of its presence in molecular state, effusion measurements will enable to estimate molecular hydrogen also.

The ultimate aim in the research of photovoltaic technology and other devices is to enhance the device performance. Improvement of material quality is one way to achieve better device performance. Hence the incorporation of these good quality films into devices and study the effect of device performance will be an exciting topic of research.

List of Publications:

A. Refereed Journals:

1. "Amorphous silicon films with high deposition rate prepared using argon and hydrogen diluted silane for stable solar cells", **Purabi Gogoi**, P. N. Dixit and Pratima Agarwal, *Solar Energy Materials and Solar Cells* **91** (2007) 1253-1257.
2. "Steady state photo carrier grating technique for measurement of charge carrier diffusion length", **Purabi Gogoi**, Taufique A. Ansari and Pratima Agarwal, *Indian Journal of Physics* **82** (2008) 179-84.
3. "Transport and stability studies on high band gap a-Si:H prepared by argon dilution", **Purabi Gogoi**, P. N. Dixit and Pratima Agarwal, *Pramana – Journal of Physics,* **70** (2008) 351-358.
4. "Structural and optical studies on Hot Wire CVD prepared hydrogenated silicon films at low substrate temperature", **Purabi Gogoi** and Pratima Agarwal, *Solar Energy Materials and Solar Cells* **93** (2009) 199-205.
5. "Amorphous to nanocrystalline transition in HWCVD Si:H films by substrate temperature variation", **Purabi Gogoi,** Himanshu S. Jha and Pratima Agarwal, accepted for publication in *Physica Status Solidi C*.
6. "High band gap nano-crystallite embedded amorphous silicon prepared by hot-wire chemical vapour deposition" **Purabi Gogoi,** Himanshu S. Jha and Pratima Agarwal, communicated.

B. Published in International Conference proceedings/ abstract books:

1. "Effect of argon dilution on growth and stability of amorphous silicon films" **Purabi Gogoi,** B. Kalita, P. N. Dixit, D. Deva and Pratima Agarwal, Abstract book of *21st*

International Conference on Amorphous and Nanocrystalline Semiconductors (ICANS21, Sept 04-09, 2005, Lisbon, Portugal) P115.

2. "Transport and stability studies on high band gap a-Si:H prepared by argon dilution" **Purabi Gogoi,** P. N. Dixit and Pratima Agarwal, Abstract book of *International Workshop on Physics of Mesoscopic and Disordered Materials (MESODIS 06*, Dec 04-08, 2006, IIT Kanpur) P 154.
3. "Structural and transport studies on HWCVD deposited nanomorph silicon films" **Purabi Gogoi,** H. S. Jha, A. Kumbhar and Pratima Agarwal, Abstract book of *22nd International Conference on Amorphous and Nanocrystalline Semiconductors (ICANS22*, Aug 19-24, 2007, Breckenridge, Colorado, USA) No. ThP14.4.
4. "Nanocrystallite embedded amorphous silicon prepared by hot wire chemical vapour deposition" **Purabi Gogoi,** H. S. Jha and Pratima Agarwal, Abstract book of *18th International Photovoltaic Science and Engineering Conference* (PVSEC18, Jan 19-23, 2009, IACS, Kolkata) P63.
5. "Nanocrystalline silicon films by HWCVD method" **Purabi Gogoi,** H. S. Jha and Pratima Agarwal, Abstract book of *American Physical Society March Meeting* (Mar 16–20, 2009; Pittsburgh, Pennsylvania, USA) Abstract no BAPS. 2009.MAR.V21.12.
6. "High band gap nano-crystalline silicon deposited by HWCVD" **Purabi Gogoi,** Himanshu S. Jha, D. Deva and Pratima Agarwal, Abstract book of *23rd International Conference on Amorphous and Nanocrystalline Semiconductors (ICANS23*, Aug 23-28, 2009, Utrecht, the Netherlands) P220.
7. "Microstructure investigation of Si:H films by photoelectron spectroscopy" **Purabi Gogoi,** Himanshu S. Jha, Pratima Agarwal, D. M. Phase and S. Kumar, Abstract book of *23rd International Conference on Amorphous and Nanocrystalline Semiconductors (ICANS23*, Aug 23-28, 2009, Utrecht, the Netherlands) P222.

C. National Conference/workshop/ symposium attended and/or published in proceedings/ abstract books:

1. "Metastable changes in electrical conductivity of a-SiGe:H film after annealing", **Purabi Gogoi,** Bulumoni Kalita and Pratima Agarwal, Proceedings of 49th DAE Solid State Physics Symposium, Vol 49 (2004) 542-543**.**
2. "Transport studies on high band gap a-Si:H thin films" Bulumoni Kalita, **Purabi Gogoi**, Sushil Kumar, P.N. Dixit and Pratima Agarwal, *Proceedings of 49th DAE Solid State Physics Symposium*, Vol 49 (2004) 544-545.
3. "Modeling of amorphous silicon based single junction solar cells", Rupanjan Das, **Purabi Gogoi** and Pratima Agarwal, *Proceedings of 50th DAE Solid State Physics Symposium*, Vol 50 (2005) 291-292.
4. "Photoconductivity studies on amorphous silicon germanium thin films", **P. Gogoi**, B. Kalita, J. Anto Pradeep, B. Bhattacharyya and Pratima Agarwal, *Proceedings of 50th DAE Solid State Physics Symposium*, Vol 50 (2005) 385-386.
5. "Steady State Photo carrier grating technique for measurement of charge carrier diffusion length" **Purabi Gogoi**, Taufique A. Ansari and Pratima Agarwal, Abstract book of Condensed Matter Days 06 (Tezpur University Aug 29-31, 2006) P 29.
6. "Steady state photo carrier grating technique: a powerful tool for measurement of charge carrier diffusion length", **Purabi Gogoi**, Taufique A. Ansari and Pratima Agarwal, *Proceedings of 51st DAE Solid State Physics Symposium*, Vol 51 (2006) 821-822.
7. "Stable hydrogenated amorphous silicon films with high deposition rate prepared by argon dilution for cost effective application" *Physics Academy of North East -07,* (Gauhati University, Mar 01-02, 2007) P67.
8. "Structural Studies on amorphous silicon films deposited by Hot Wire CVD technique", **Purabi Gogoi,** H.S. Jha and Pratima Agarwal, *Proceedings of 52nd DAE Solid State Physics Symposium,* Vol 52 (2007) 997-998.
9. "Fabrication of Hot Wire Chemical Vapor deposition set up for preparation of hydrogenated silicon", **Purabi Gogoi,** H.S. Jha and Pratima Agarwal, *Proceedings of 53rd DAE Solid State Physics Symposium,* Vol 53 (2008) 543-544.

10. “Amorphous to Nano crystalline transition in HWCVD silicon: Effect of filament temperature and gas flow rate” **Purabi Gogoi,** Himanshu S. Jha and Pratima Agarwal, *Proceedings of 54th DAE Solid State Physics Symposium,* Vol 54 (2009) 567-568..
11. “Photoelectron Spectroscopy Studies on Si:H films prepared by HWCVD” P. Anand Kumar, **P. Gogoi**, H.S. Jha, D.M. Phase, S. Kumar and P. Agarwal *Proceedings of 54th DAE Solid State Physics Symposium,* Vol 54 (2009) 639-640.